Springer Series in Optical Sciences 181

Valerii (Vartan) Ter-Mikirtychev

Fundamentals of Fiber Lasers and Fiber Amplifiers

Springer

Springer Series in Optical Sciences

Volume 181

For further volumes:
http://www.springer.com/series/624

Springer Series in Optical Sciences

The Springer Series in Optical Sciences, under the leadership of Editor-in-Chief William T. Rhodes, Georgia Institute of Technology, USA, provides an expanding selection of research monographs in all major areas of optics: lasers and quantum optics, ultrafast phenomena, optical spectroscopy techniques, optoelectronics, quantum information, information optics, applied laser technology, industrial applications, and other topics of contemporary interest.

With this broad coverage of topics, the series is of use to all research scientists and engineers who need up-to-date reference books.

The editors encourage prospective authors to correspond with them in advance of submitting a manuscript. Submission of manuscripts should be made to the Editor-in-Chief or one of the Editors. See also www.springer.com/series/624

Valerii (Vartan) Ter-Mikirtychev

Fundamentals of Fiber Lasers and Fiber Amplifiers

Springer

Valerii (Vartan) Ter-Mikirtychev
Mountain View, CA
USA

ISSN 0342-4111 ISSN 1556-1534 (electronic)
ISBN 978-3-319-02337-3 ISBN 978-3-319-02338-0 (eBook)
DOI 10.1007/978-3-319-02338-0
Springer Cham Heidelberg New York Dordrecht London

Library of Congress Control Number: 2013948738

Printed on acid-free paper

Springer is part of Springer Science+Business Media (www.springer.com)

Dedicated in memory of my parents Vartan and Vera,
and to my wife Katerina
and my children William and Daria

Acknowledgments

I would like to thank my former and current colleagues in Russia, Japan, and USA for useful discussion on many topics of laser physics in general and fiber optics and fiber lasers in particular. I am indebted to Dr. P. Silfsten, Prof. T. Kurobori, Prof. K. Ueda, Dr. V. Kozlov, Prof. E. Sviridenkov, Dr. M. Dubinskii, Dr. V. Fromzel, Dr. J. Zhang, Dr. N. Klaus, Dr. S. Fuerstenau, Dr. I. McKinnie, Mr. P. Ishkanian, and Prof. J.-W. Ryu, for useful and interesting discussions. I am also glad to have an opportunity to thank Mr. M. O'Connor of IPG, Mr. W. Wilson of Liekki/nLight, and Mr. D. Beiko of CorActive for many useful discussions on commercially available fibers.

I am thankful to my teachers and former colleagues at Moscow Physics and Engineering Institute (MEPhI), P. N. Lebedev Physical Institute (LPI) of the Russian Academy of Sciences, and A. M. Prokhorov General Physics Institute (GPI) of the Russian Academy of Sciences (RAS), namely: the late Prof. Yu. A. Bykovskii, Prof. E. D. Protcenko, Prof. E. A. Sviridenkov, late Prof. A. N. Oraevsky, Prof. Yu. M. Popov, the late Prof. A. P. Shotov, Prof. V. G. Sheretov (Tver State University), and late Prof. A. G. Avanesov (Krasnodar State University). Also, Prof. V. P. Danilov, Prof. V. A. Smirnov. and Academician Prof. I. A. Shcherbakov, President of A. M. Prokhorov GPI RAS.

Further, I would like to express my personal gratitude to the organizer of the Special Physics Department of MEPhI where I had a privilege to be educated and what in turn made several important changes in my life and who served as a board Chair of my graduation exams, i.e., former director of P. N. Lebedev Physical Institute the late Academician Prof. N. G. Basov, 1964 Nobel Prize Laureate in Physics (together with the late Academician Prof. A. M. Prokhorov and Prof. C. H. Townes).

Special thanks go to Mr. Stuart McLean, a fiber laser engineer, who did the hard work of proofreading the whole manuscript and whose suggestions definitely improved the material presentation. Additionally, I give thanks to Mr. William Terson for partial proofreading of the manuscript. I also highly appreciate the help of Springer Physics Editor Mr. Christopher Caughlin, and Mr. Ho Ying Fan, both from Springer for their constant help and assistance throughout the whole project including manuscript preparation and publication.

Finally, but not less importantly, I would like to thank my wife Katerina who is a Fiber-Optic engineer herself for her helpful suggestions including technical and stylistic, constant support and encouraging. Appearance of this book without Katerina's support would be impossible.

Contents

1 Introduction 1
References 5

2 Optical Properties and Optical Spectroscopy of Rare Earth Ions in Solids 7
2.1 Electron–Phonon Coupling in Solids 7
2.2 Phonon Sidebands of Optical Transition in Solids 9
2.3 Optical Center Transitions: Spontaneous and Stimulated Emission 10
2.4 Rare Earth Centers in Solids 13
2.5 Homogeneous and Inhomogeneous Line Broadening. 14
2.5.1 Homogeneous Broadening 14
2.5.2 Inhomogeneous Broadening 16
2.6 Spectroscopic Parameters of the Optical Transition: A Brief Introduction to the Main Theories. 17
2.6.1 Judd–Ofelt Theory 18
2.6.2 McCumber Theory 19
2.6.3 Füchtbauer–Ladenburg Theory and Einstein Coefficients 21
2.7 Sensitization of Laser-Active Centers 23
References 25

3 Physical and Optical Properties of Laser Glass 27
3.1 Mechanical and Thermal Properties of Glass 28
3.2 Optical Properties of Fibers (Attenuation) 30
3.2.1 Intrinsic Glass Material Properties 30
3.2.2 Waveguide Properties 31
3.2.3 Optical Connection Loss 32
3.3 Different Glass Types Used in Fiber Lasers and Amplifiers. . . 32
3.3.1 Silicate Glass 33
3.3.2 Phosphate Glass 34
3.3.3 Tellurite Glass 34
3.3.4 Fluoride Glass and ZBLAN 34
References 36

4 Fiber Fabrication and High-Quality Glasses for Gain Fibers 37
4.1 Materials 37
4.2 Fabrication of Fiber Preforms 37
4.3 Fiber Fabrication from the Preform 39
4.4 Laser-Active Fiber Fabrication 39
4.5 MCVD Technology for Rare-Earth Doped Fiber Production 40
4.6 DND Technology 42
References 42

5 Spectroscopic Properties of Nd^{3+}, Yb^{3+}, Er^{3+}, and Tm^{3+} Doped Fibers 43
5.1 Spectroscopic Notations 43
5.2 Energy Levels of Trivalent Rare Earth Ions 44
5.3 Neodymium 45
5.3.1 Nd^{3+} Fiber Laser Challenges 49
5.4 Ytterbium 50
5.4.1 Yb^{3+} Fiber Laser Challenges 51
5.5 Erbium 53
5.5.1 Er^{3+} Fiber Laser Challenges 56
5.6 Thulium 57
5.6.1 Tm^{3+} Fiber Laser Challenges 59
References 62

6 Propagation of Light and Modes in Optical Fibers 65
6.1 V Number of the Fiber 66
6.2 Fiber Dispersion 68
6.3 Polarization-Maintaining Fibers 72
6.4 Laser Beam Quality (M^2 Parameter) 73
6.4.1 Practical Recommendations on Beam Quality Measurements Using the M^2 Approach 75
References 77

7 Fiber Laser Physics Fundamentals 79
7.1 Population Inversion: Three- and Four-EnergyLevel Systems 79
7.1.1 Four-Level Laser Operational Scheme 80
7.1.2 Three-Level Laser Operational Scheme 81
7.2 Optical Fiber Amplifiers 82
7.2.1 Fiber Amplifier (General Consideration) 82
7.3 Fiber Laser Thresholds and Efficiency 90
7.4 Gain and Loss in Laser Resonators 93

7.5 Fiber Laser Resonators 93
7.5.1 Linear Laser Resonators 93
7.5.2 Ring Laser Resonators. 96
References 98

8 Main Operating Regimes of Fiber Lasers 99
8.1 Temporal Regimes 99
8.1.1 CW and Free-Running Operation of Fiber Lasers . . . 100
8.1.2 Q-Switched Operation of Fiber Lasers. 102
8.1.3 Mode-Locking of Fiber Lasers 109
8.2 Spectral Regimes 118
8.2.1 Wavelength Tunable Lasers 118
8.2.2 Single Longitudinal Mode Lasers 124
References 131

9 Main Optical Components for Fiber Laser/Amplifier Design 133
9.1 Laser Diodes 133
9.1.1 Principles of Operation 133
9.1.2 Main Types of Diode Lasers Used in Fiber Laser Technology 141
9.1.3 High-Power Diode Lasers 144
9.1.4 Fiber-Coupled Diode Lasers. 148
9.2 Fiber-Coupled Polarization-Maintained and Non-polarization-Maintained Optical Components 149
9.2.1 Polarization-Dependent Optical Isolators 152
9.2.2 Polarization-Independent Optical Isolators 153
9.2.3 High-Power Fiber-Coupled Isolators 154
9.2.4 Polarization-Dependent Circulator. 155
9.2.5 Polarization-Independent Circulator. 156
9.2.6 Chirped FBG as a Self-Phase Modulation Compensator 157
9.2.7 A Few Words About Fiber Endface Preparation 159
References 160

10 High-Power Fiber Lasers 161
10.1 Gain Fiber Pumping Technology for High-Power Fiber Lasers. 163
10.2 Double-Clad Fibers and Clad-Pumping Technology 164
10.2.1 Clad-Pumping Schemes. 165
10.2.2 Clad-Pumping and Triple-Clad Fibers 167
10.2.3 Free Space. 167
10.2.4 Fused-Pump Combiners. 169
10.3 Large-Mode Area Fibers for High-Power, Diffraction-Limited Operation 170

10.4 Nonlinear Processes in Optical Fibers and Their Role in Fiber Laser and Fiber Amplifiers Technology Development 172
10.4.1 Threshold Power of the Stimulated Scattering Process 173
10.4.2 Stimulated Raman Scattering 174
10.4.3 Continuous-Wave SRS 176
10.4.4 Pulsed SRS 176
10.4.5 Stimulated Brillouin Scattering 177
10.4.6 Continuous-Wave SBS 178
10.4.7 Pulsed SBS 180
10.4.8 Optical Kerr Effect 180
10.4.9 Self-Phase Modulation 180
10.4.10 Cross-Phase Modulation 182
10.4.11 Four-Wave Mixing 183
10.5 Self-Focusing and Self-Trapping in Optical Fibers 185
10.6 High-Power Fiber Laser Oscillators Versus Low-Power Master Oscillator–Power Fiber Amplifier Geometry 186
10.6.1 High-Power Fiber Laser Single Oscillators 187
10.6.2 High-Power Master Oscillator–Power Fiber Amplifiers 189
10.7 Beam Combining of High-Power Fiber Lasers 195
10.7.1 Spectral Beam Combining 196
10.7.2 Volume Holographic Grating 197
10.7.3 Coherent Beam Combining 200
References 206

11 Fiber Industrial Applications of Fiber Lasers 209
11.1 Laser–Material Interaction for Material Processing 210
11.2 Important Laser Parameters for Industrial Application 212
11.2.1 Wavelength 212
11.2.2 Pulse Energy 212
11.2.3 Pulse Width and Pulse Repetition Rate 213
11.2.4 Power 213
11.2.5 Power Density 214
11.2.6 Laser Beam Quality 214
11.2.7 Spot Diameter 215
11.3 Fiber-Optic Power Delivery Systems 215
11.4 Main Structure of Fiber-Optic Delivery Systems 224
11.5 Main Industrial Applications of Fiber Lasers 225
11.5.1 Welding 225
11.5.2 Cutting 226
11.5.3 Drilling 226
11.5.4 Soldering 226

11.5.5 Marking . . . 227
11.5.6 Heat Treating . . . 227
11.5.7 Metal Deposition . . . 227
11.5.8 Paint Stripping and Surface Removal . . . 227
11.5.9 Micromachining . . . 228
11.5.10 Semiconductor Processing with a Laser Beam . . . 228
11.5.11 Main Competitors of Fiber Lasers in Industrial Laser Applications . . . 229
11.5.12 Summary of Challenges for Fiber Lasers in Industrial Applications . . . 230
11.5.13 Future of Fiber Lasers in Material Processing . . . 231
References . . . 231

12 Conclusion . . . 233

Index . . . 235

Symbols

A_{21}	Einstein A coefficient (probability of spontaneous decay)
B_{12}, B_{21}	Einstein B coefficients
b	Normalized propagation constant
A_{eff}	Effective cross-section area of the fiber core
D_{chrom}	Chromatic dispersion
d_{np}	Depletion region of p-n junction
$d_n,\ d_p$	Depletion regions in n- and p-type side of the junction
E	Energy
E_F	Fermi energy
F	Energy fluence
f	Oscillator strength of the transition
$f_{F-D}(E,T)$	Fermi function (Fermi–Dirac probability)
F_{etalon}	Finesse of the etalon
g	Gain coefficient
G	Gain factor
h	Planck constant
$\hbar = \frac{h}{2\pi}$	Reduced Planck constant (or Dirac's constant)
I	Laser intensity
k_B	Boltzmann constant
L	Length
L_{eff}	Effective length of the fiber
L_{lss}	Large-scale self-focusing characteristic length
L_{sss}	Small-scale self-focusing characteristic length
L_{loss}	Intracavity incidental loss
M	Number of modes
M_{lens}	Magnification of the lens system
N	Concentration
$N_a,\ N_d$	Concentration of acceptor and donor impurity
ΔN	Population inversion
$\bar{n}_i,\ \bar{n}_f$	Normalized population inversions
$\overline{n}_{th}$	Threshold population inversion

n	Refractive index
n_0	Linear refractive index
n_2	Nonlinear refractive index
$\Delta n = n_{core} - n_{clad}$	Refractive index difference
P	Laser power
P_{cr}	Critical power of self focusing
P_p	Pump power
P_a	Absorbed pump power
P_{pcr}	Critical pump power required to achieve transparency of the signal wavelength
P_{out}	Output power
P_{th}	Laser power threshold
R	Reflectivity
$S_{core/clad}$	Cross-sectional area of the core or of the cladding
T	Transmission
T_g	Group delay
t_p	Laser pulse width
V_g	Group velocity
V_{ph}	Phase velocity
V	Volume
V	V-number
$V_{PCF}(\lambda)$	V- parameter for photonics crystal fiber
β	Propagation constant
β_{ph}	Phase constant (real part of the wavenumber k)
Δ	Relative (or fractional) refractive index difference
Γ	Spontaneous relaxation line-width of the process
Γ^{-1}	Phonon lifetime
Γ_{tot}	Total, single pass logarithmic loss of the laser cavity
μ or α	Absorption coefficient
σ	Cross-section of the transition
v or ω	Optical frequency
v_0 or ω_0	Central frequency of the transition
v_p	Pump frequency
Δv, $\Delta\omega$	Spectral line-width
λ	Wavelength
τ	Upper-level lifetime
η_{slope}	Laser slope efficiency
$\Delta\beta_{FWM}$	Phase mismatch in four-wave mixing process
Θ_B	Brillouin angle (angle between the scattered wave vector and the initial pump wave vector)
Θ_{BR}	Brewster angle
Ω	Effective phonon frequency

$\Omega_{2,4,6}$	Judd–Ofelt parameters
γ	Nonlinear interaction constant
Λ	Fiber Bragg grating period
σ_{DC}	Material DC conductivity

Abbreviations

ASE	Amplified spontaneous emission
ATR	Attenuated total reflectance
BEL	Broad area laser
CW	Continuous-wave
XPM	Cross-phase modulation
DC	Double clad
FWM	Four-wave mixing
FBG	Fiber Bragg grating
FSR	Free spectral range
LD	Laser diode
LMA	Large mode area
LP	Notation for modes in optical fibers (linearly polarized)
MCVD	Modified chemical vapor deposition
MM	Multi mode
MOPA	Master oscillator power amplifier
NA	Numerical aperture
NCPM	Noncritical phase matching
PM	Polarization maintained
PPLN	Periodically poled lithium niobate
QPM	Quasi-phase matching
SBS	Stimulated Brillouin scattering
SHB	Spectral hole burning
SM	Single mode
SPM	Self-phase modulation
SRS	Stimulated Raman scattering
TIR	Total internal reflection
TC	Triple clad

Some of the Most Important Fundamental Optical Constants

$k_B = 1.3806488 \times 10^{-23} \frac{J}{K}$

$h = 6.62606957 \times 10^{-34} J \times \text{sec}$

$\hbar = 1.054571726 \times 10^{-34} J \times \text{sec}$

$c_0 = 2.99729458 \times 10^{8} \frac{m}{\text{sec}}$

Chapter 1
Introduction

The field of fiber lasers was born in 1961—almost simultaneously with the achievement of the first laser action in Ruby [1]—when Snitzer first published his famous paper on laser oscillation in glass [2] and then on the possibility of fiber laser operation [3]. A few years later, in 1964, Koester and Snitzer experimentally demonstrated amplification and observed fiber laser oscillation in a gain fiber [4]. This important work was followed by other research groups who further studied fiber lasers. However, great success in the development of other laser-active media during the 1960s and 1970s, such as laser crystals and liquid-dye lasers, as well as lack of availability of diode lasers (the first operation of a diode laser was published in 1962) put serious fiber laser research on hold for several decades. In the 1980s and 1990s, fiber lasers had their second birth due to the appearance of reasonably powerful and reliable diode lasers and diode-pumped laser technology. This was accompanied by the application of fiber laser technology in optical telecommunication, which used a fiber amplifier rather than a fiber laser concept. The basic ideas and discoveries made during the early telecommunication age played—and are still playing—a key role in the development of fiber laser and fiber amplifier systems. The following milestones or achievements should be mentioned in the field of fiber lasers and fiber amplifiers as a stand-alone field of optics in general and laser physics in particular:

1. First operation of a fiber laser.
2. First operation of a fiber amplifier.
3. First operation of a diode laser.
4. Chemical vapor deposition (and its modifications) fiber fabrication technology, which allowed optical fibers to be achieved with extremely low loss.
5. Sensitization of some acceptor ions (e.g., Er^{3+}) with donors (e.g., Yb^{3+}).
6. Double-clad (DC) fibers and clad pumping technology.
7. Development of highly efficient, room-temperature, and cost-effective diode lasers.
8. Development of highly efficient and cost-effective single-frequency diode lasers.

V. Ter-Mikirtychev, *Fundamentals of Fiber Lasers and Fiber Amplifiers*,
Springer Series in Optical Sciences 181, DOI: 10.1007/978-3-319-02338-0_1,

9. Significant progress in fiber coupling technology, such as fiber-coupled diode lasers.
10. Development of highly doped gain fibers.
11. Commercialization of cost-effective fiber-coupled and all-fiber optical components.
12. Discovery and development of photonic crystal fibers.
13. Achievement and development of efficient Raman fiber lasers.
14. Development of polarization-maintaining fiber structures.
15. Fundamental spatial mode filtering in fibers and coiling technology.

From this list of milestones, one can observe that success in fiber lasers as a technical field is a result of joint success in the field of solid-state lasers (especially diode-pumped lasers) and fiber technology. Accordingly, fiber lasers adopted technological solutions from both of these areas. Today, fiber lasers compete with and threaten to replace most of high-power, bulk solid-state lasers and some gas lasers. The most developed fiber laser systems are based on laser glasses with the following rare earth ions: Yb^{3+}, Er^{3+}, $-Yb^{3+}$, Tm^{3+}, and Nd^{3+}. Note, however, that historically the first ion to be used in fiber laser was the Nd^{3+} ion; therefore, a lot of work has been done using Nd^{3+} as a laser active ion in fiber laser research, including new operational schemes for unique spectral and temporal fiber laser characteristics. Nevertheless, researchers and engineers soon shifted their attention to Yb^{3+} and Er^{3+}. Compared with Nd^{3+}, Yb^{3+} offers higher conversion efficiency, much broader tunability in the 1 μm spectral range, and higher energy storage time. Later, the advantages of Yb^{3+} were also magnified by the performance and availability of the more technological and reliable 9XXnm indium gallium arsenide (InGaAs) laser diodes used as pumping sources of Yb^{3+} fiber lasers.

With further advances in the development of diode pump laser technology and optical telecommunication, other ions such as Er^{3+} and later Tm^{3+} received significant attention from researchers and engineers. This eventually brought power of the fiber lasers based on these rare earth ions to hundreds of Watts, with more than 30 % conversion efficiency for Er^{3+}–Yb^{3+} systems and more than 50 % for Er^{3+}-doped and Tm^{3+}-doped fibers.

Meanwhile, scientists and engineers were investigating ways to significantly reduce optical loss in fibers. In this direction, the most important technological breakthrough was the discovery of a so-called modified chemical vapor deposition (MCVD, or just CVD) fiber manufacturing technique, which eventually allowed the achievement of optical fibers with extremely low loss ($<\sim 0.2$ dB/km in the 1.5 μm wavelength range for undoped fibers and 0.01–0.1 dB/m for the rare-earth doped fibers; i.e., gain fibers). Most fiber preparation processes use MCVD technology (or its modifications) as a core process, including gain fiber preparation.

The next fundamental step towards the development of highly efficient fiber lasers was a proposal to use sensitization of Er^{3+} laser active ions in glass by Yb^{3+} ions. Note that in early years of laser research mentioned previously, the Nd^{3+} ion also was considered to be a sensitizing ion itself (in this case, for the Yb^{3+} ion).

This interest, however, was replaced by direct excitation of Yb^{3+} with the appearance of 9XXnm InGaAs laser diodes. For the Er^{3+}–Yb^{3+} co-doped system, sensitization makes use of broad absorption of Yb^{3+} ions in glass at $\sim$915 and $\sim$976 nm wavelengths, which are accessible by well-developed InGaAs laser diodes as well as achievable high Yb^{3+} doping concentration of the laser glass. In Er^{3+}–Yb^{3+} co-doped material, excited Yb^{3+} ions in its absorption band have a highly efficient energy transfer to the Er^{3+} ions to its upper laser energy level; in turn, this creates a condition for efficient creation of population inversion in Er^{3+} with subsequent laser action in the $\sim$1.5 μm spectral range. The Er^{3+}–Yb^{3+} system also plays an important role in double-clad fibers, where achievement of effective pump absorption requires longer gain fibers. High concentration of Yb^{3+} (which in Er^{3+}–Yb^{3+} laser glass is more than 10 times bigger than that of Er^{3+}) enables efficient high-power pump absorption of the 915 or 976 nm spectral range in a clad pump geometry, resulting in the achievement of reasonably short DC gain fiber lengths.

As one can imagine, the most technological and scientific efforts (as in the case of other laser types) have been and are still being placed on the development of single transverse mode fiber lasers and amplifiers operating with close to diffraction-limited beam quality. In the early years of fiber laser development, gain fibers that support only the fundamental mode had a laser active ion-doped core that was several microns in diameter and an undoped cladding surrounding the core, which was usually about 100 μm in diameter. The pump and the signal radiation were launched inside the same volume—that is, each into the core from the same or opposite directions of the gain fiber with perfect beam overlap. Although it is a good solution and has several advantages, such core pumping geometry has very limited power scalability because of the strict requirement for brightness (i.e., optical power density per divergent solid angle $[W/\mathrm{cm}^2 \times \mathrm{steradian}]$) of the pump diode lasers in order for it to be efficiently launched into the fiber core. This circumstance limited fiber laser power to about a 1 W level at their time, which corresponded to the power of single-mode emitter pump diode lasers.

To increase pump power coupled into the gain fiber, in the mid-1980s, several research groups almost simultaneously proposed to launch pump radiation into a larger area of cladding that surrounds a doped core, thus significantly expanding the capability of launched pump power scaling in fiber lasers. Special fibers have been developed for such clad-pump propagation technology. With an external polymer coating of a lower refractive index, such fibers allowed simultaneous propagation of signal radiation inside the core and pump radiation to be guided inside cladding. Because of this dual wave-guiding property, such fibers are called double-clad fibers—that is, having extra cladding for pump radiation. Note that because of the reduced overlap between the pump area in the clad and the absorbing area of the core, DC fibers require a longer length for effective pump absorption compared with that of core pump fibers with the same core absorption coefficient at the pump wavelength. Nevertheless, for high peak power and low average power applications, where nonlinear optical processes create real design

and development issues, core pump fiber technology (which uses very short gain fibers) is a powerful and often better approach.

Among the milestones listed previously, we should also emphasize coiled-fiber mode filtering technology (proposed in 2000), which seems to be the simplest and least expensive among several existing mode filtering techniques. Making use of the high discrimination factor between bending loss of the fundamental transverse mode and that of higher order modes in large mode area fibers (LMAs), which have a reduced difference in refractive indices between core and cladding, researchers achieved diffraction-limited high-power laser emission from a multimode gain fiber by coiling the fiber to a certain radius of curvature. Note that several other techniques have been suggested for single transverse mode filtering in fibers. However, coiled technology is currently the most efficient and rugged, allowing practical and commercial high-power fiber laser systems to be built with diffraction-limited beam quality.

Currently, after rapid progress in DC fibers, high-power diode lasers and mode filtering technology (based on the previously mentioned fiber coiling approach) achieved continuous wave power levels greater than 10 kW for infrared fiber lasers with close to diffraction-limited beam quality (greater than 50 kW for multimode operation). These numbers continue to increase quickly. In the near future, it is likely that fiber lasers will not only penetrate several traditional laser markets deeper, but they will also replace several other laser types used in these markets.

The main goal of this book is to create a reasonably self-contained, single standpoint introduction to the field of fiber lasers and fiber amplifiers. The book consists of 12 chapters, including introduction and conclusion. The first several chapters introduce the reader to the fields of lasers physics, optical spectroscopy of rare earth ions in solids and glasses, and the basics of fiber optics and technology. This is followed by a review of the general principles of light propagation in fibers and a description of the main operational regimes of fiber lasers. The second half of the book discusses the physics and technology of fiber lasers, including the state of the art for components and systems. Chapter 10 is dedicated to high-power fiber lasers, fundamental physical processes that have to be addressed during research and development, technical challenges, and important available solutions.

Chapter 11 describes the industrial applications of fiber lasers. Most chapters on the fundamental principles of laser operation, as well as processes which take place in optical fibers in the field of high-power optical radiation, were written after original journal publications. Because of the introductory nature of the book, I do not describe systems such as photonic crystal fiber lasers, Raman lasers, Raman amplifiers, upconversion lasers, supercontinuum oscillation, or nonlinear frequency conversion. (Photonic crystal fibers will be briefly introduced in Chap. 11 in relation to the optical power delivery systems.) Whenever possible throughout the book (except for certain subsystems, such as tunable laser operation, some fiber laser cavities, or examples of high-power fiber laser design), I tried to keep descriptions general in nature and minimize presentation of the material, which includes certain fiber laser structures or designs targeted on restricting their numbers. Therefore, the reader can use general fundamental principles, theory, available

components, and approach modes to develop their own unique fiber lasers and fiber amplifier systems from the technical material given in the book. At the same time, available journal articles and conference presentations can be a priceless source for more detailed study of particular fiber laser schematics.

I hope this book will be helpful to students, engineers, teachers, and researchers in their daily work. The book is certainly not intended to cover all aspects of fiber laser science and technology. Rather than the applications of fiber lasers, it will cover the fundamentals of this interesting, important, and fast-growing field of laser physics.

References

1. T.H. Maiman, Stimulated optical radiation in ruby. Nature **187**, 493–494 (1960)
2. E. Snitzer, Optical maser action of Nd^{3+}in a barium crown glass. Phys. Rev. **7**(12), 444–446 (1961)
3. E. Snitzer, Proposed fiber cavities for optical masers. J. Appl. Phys. **32**(1), 36–39 (1961)
4. Ch.J. Koester, E. Snitzer, Amplification in a fiber laser. Appl. Optics. **3**(10), 1182–1186 (1964)

Recommended General Literature on Lasers

5. A. Siegman, *Lasers* (University Science Books, Mill Valley, California, 1986), pp. 1283
6. O. Svelto, *Principles of Lasers*, 4th edn. (Plenum Press, 2004), pp. 605
7. W. Koechner, *Solid-State Laser Engineering* (Springer, 2006), pp. 706
8. B.E.A. Saleh, M.C. Teich, *Fundamentals of Photonics* (Wiley, 1991), pp. 966
9. R. Diehl, R.D. Diehl, *High-power Diode Lasers: Fundamentals, Technology, Applications* (Springer, 2000), p. 416
10. Yu.M. Popov, Semiconductor lasers. Appl. Opt. **6**(11), 1818–1824 (1967)
11. V.G. Dmitriev, G.G. Gurzadyan, D.N. Nikogosyan, *Handbook of Nonlinear Optical Crystals* (Springer, 1999), p. 413

Recommended Literature on Optical Fibers

12. S. Nagel et al., An overview of the modified chemical vapor deposition (MCVD) process and performance. IEEE J. Quantum Electron. **18**(4), 459 (1982)
13. A.W. Snyder, J. Love, *Optical Waveguide Theory* (Springer, 1983), p. 734
14. G.P. Agrawal, *Nonlinear Fiber Optics*, 3rd edn, p.466, 2201
15. M. Bass, E.W. Van Stryland, Fiber Optics Handbook: Fiber, Devices, and Systems for optical communications. Optical Society of America (2001), p. 416
16. D. Marcuse, *Theory of Dielectric Optical Waveguides* (Academic Press, 1974), p. 257
17. W.A. Gambling, The rise and rise of optical fibers. IEEE J. Sel. Topics Quantum Electron. **6**(6), 1084 (2000)
18. L.B. Jeunhomme, *Single Mode Fiber Optics: Principles And Applications* (CRC Press, 1990), p. 339
19. N.S. Kapany, J.J. Burke, *Optical Waveguides* (Academic Press, 1972), p. 328
20. J. Hecht, *Understanding Fiber Optics* (Prentice Hall, 2002), p. 773

Recommended Literature on Fiber Lasers and Fiber Amplifiers

21. M.J.F. Digonnet (ed.) *Rare-Earth-Doped Fiber Lasers and Amplifiers*, 2nd edn. (Marcel Dekker, Inc., New York, 2001), p. 777
22. H.M. Pask et al., Ytterbium-doped silica fiber lasers: versatile sources for 1–1.2 μm region. IEEE J. Sel. Top. QE **1**(1), 2–13 (1995)
23. E.M. Dianov, Advances in Raman Fibers. J. Lightwave Technol. **20**(8), 1457–1462 (2002)
24. J.C. Yong, L. Thévenaz, B.Y. Kim, Brillouin fiber laser pumped by a DFB laser diode. J. Lightwave Technol. **21**, 546–554 (2003)
25. S.A. Vasil'ev et al., Fibre gratings and their applications. Quantum Electron. **35**(12), 1085–1103 (2005)
26. J.C. Knight, Photonics crystal fibers and fiber lasers. J. Opt. Soc. Am. B. **24**(8), 1661–1668 (2007)
27. M. Young, *Optics and Lasers Including Fibers and Optical Waveguides* (Springer, 2000), p. 528
28. E. Desurvire, *Erbium-Doped Fiber Amplifiers, Principles and Applications* (Wiley Series in Telecommunications and Signal Processing, 2002), p. 804
29. F. Kan, F. Gan, Laser materials. World Scientific (1995), p. 354
30. A. Bellemare, Continuous-wave silica-based erbium-doped fiber lasers. Prog. Quantum Electron. **27**(4), 211–266 (2003)
31. M.E. Fermann, A. Galvanauskas, G. Sucha (eds.), *Ultrafast Lasers: Technology and Applications* (CRC Press, 2003), p. 784
32. D. Hewak, *Properties, Processing and Applications of Glass and Rare Earth-Doped Glasses for Optical Fibers* (IET Press, 1998), p. 376
33. P.C. Becker, N.A. Olsson, J.R. Simpson, *Erbium-doped Fiber Amplifiers: Fundamentals and Technology* (Academic Press, 1999), p. 460
34. H.M. Pask, The design and operation of solid-state Raman lasers. Prog. Quantum Electron. **27**(1), 3 (2003)
35. S.D. Jackson, T.A. King, Theoretical modelling of Tm^{3+}-doped silica fiber lasers. IEEE J. Lightwave Technol. **17**(5), 948–956 (1999)
36. P.F. Moulton, G.A. Rines, E.V. Slobodtchikov, K.F. Wall, G. Frith, B. Samson, A.L.G. Carter, Tm-Doped fiber lasers: fundamentals and power scaling. IEEE J. Sel. Top. Quantum Electron. **15**(1), 85–92 (2009)
37. M.E. Fermann, I. Hartl, Ultrafast fiber laser technology. IEEE J. Sel. Top. Quantum Electron. **15**(1), 191–206 (2009)
38. R.A. Motes, R.W. Berdine, Introduction to high power fiber lasers. Directed Energy Professional Society (2009), p. 233
39. M. Kimura, X. Liu, F. Adler, F. Sotier, D. Trautlein, A. Sell, *Fiber Lasers: Research, Technology and Applications* (Lasers and Electro-Optics Research and Technology, Nova Science Pub Inc, 2009), p. 225

Chapter 2
Optical Properties and Optical Spectroscopy of Rare Earth Ions in Solids

2.1 Electron–Phonon Coupling in Solids

The Franck-Condon principle plays an important role in understanding the nature of optical transitions in laser-active ions in solids. According to this principle, absorption of a photon is an instantaneous process during which the nuclei are enormously heavy as compared to the electrons. In other words, the electronic transition occurs on a time scale that is short compared to nuclear motion, so the transition probability can be calculated at a fixed nuclear position. An electronic transition is therefore considered to be a vertical transition. Thus, during light absorption, which occurs in femtoseconds to nanoseconds, electrons can move but nuclei cannot. The much heavier atomic nuclei have no time to readjust themselves during the absorption act; instead, they readjust after the absorption process is over, which in turn creates vibrations. This occurrence is best illustrated by potential energy diagrams. Figure 2.1 is an expanded energy-level diagram with the abscissa representing the distance between the nuclei, Q. The two potential curves show the potential energy of the optical center as a function of this distance for ground and excited states. Excitation is represented, according to the Franck-Condon principle, by a vertical (i.e., instantaneous) arrow (arrow A in Fig. 2.1). This arrow crosses the upper curve, higher than the lowest point. Appearance of the optical center after the absorption process in the excited state means that the center enters a nonequilibrium configuration and needs to relax into the lower state. This relaxation process involves radiation of phonons, which is a characteristic of the lattice vibration mode. Note that there is an exception: the case of 0–0 transition, in which the resultant absorption and emission lines are called zero-phonon lines (ZPLs). ZPLs result from transitions between the lowest vibration state of the ground electronic level and that of the excited state (not indicated in the figure).

In a Franck-Condon diagram, the relaxation process is usually denoted by a down arrow inside the individual potential curve of the electronic state (not shown in Fig. 2.1). Such relaxation processes usually take place in femtoseconds to nanoseconds. During the relaxation process, almost all of the vibration energy in

V. Ter-Mikirtychev, *Fundamentals of Fiber Lasers and Fiber Amplifiers*,
Springer Series in Optical Sciences 181, DOI: 10.1007/978-3-319-02338-0_2,

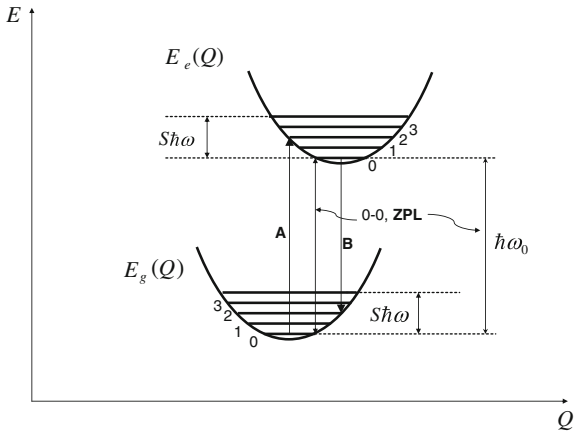

Fig. 2.1 Franck-Condon diagram of the ground and excited states of the optical center in solids. The *vertical axis* represents energy and the *horizontal axis* denotes the value proportional to the distance (i.e., normal coordinate). $E_e(Q)$ and $E_g(Q)$ are the excited and ground state energies, respectively. S is the Huang-Rhys factor (see text) and $\hbar\omega$ is an effective phonon energy of the host material (i.e., the medium in which the optical center is put). *Arrow A* denotes the absorption and *arrow B* denotes emission transitions

the excited center is lost by the energy exchange with the phonon reservoir (i.e., lattice of the host material), producing heat in the system. After the relaxation, the center needs to relax further through the electron transition between excited and ground electron levels. This process is called *luminescence*, starting from near the bottom of the upper potential curve and following a vertical arrow down (arrow *B* in Fig. 2.1), until it crosses the lower potential curve. Similar to the absorption process described previously, the luminescence transition (down arrow) does not cross the deepest point of the ground state (again, except for the previously mentioned 0–0 transition), and some excitation energy gets converted to the vibration energy. As shown in the diagram, the absorption–emission process contains two periods of energy dissipation; this phenomenon in turn creates a Stokes shift—a process during which the emission spectrum has a luminescence frequency lower than the related absorption frequency. (This phenomenon is also called a "red shift" because wavelengths of the emission are longer than of the absorption). Note that in the case of a nonlinear absorption process, such as up-conversion (i.e., the process in which two or more pump photons are used to get an ion to its high exciting level with subsequent emission of photons with higher than the original energy), the wavelength of luminescence is shorter than that of absorption. Such phenomena are widely used for the development of short-wavelength lasers for the visible spectral range (up-conversion lasers), but they are beyond the scope of this book.

2.2 Phonon Sidebands of Optical Transition in Solids

During electronic transitions in solids, an optical center (usually an imperfection in the lattice of the crystal or glass structure) may demonstrate a change in its center-to-lattice bonding configuration in the vicinity of the optical center, which in turn affects the vibration characteristics of the host material. These modified vibration characteristics of the host solid material contribute to the nature of the pure electronic transition and create a vibronic transition of the center. Therefore, most optical defects in solids, especially those that do not have a screening electronic shell (e.g., color centers, some ions of transition metals), demonstrate not only purely electronic transitions but also a vibronic transition or what is known as a "phonon sideband." Note, however, that the strength of this center-to-lattice bonding affects the visibility of the purely electronic transition, which sometimes is visible only at cryogenic temperatures; for example, F-centers have a very strong electron–phonon coupling (which will be discussed in detail later). In contrast to this, in trivalent rare earth ions, the laser-active electronic transitions are screened from the lattice environment by an electronic shell of the ion. In these optical systems, a well-resolved and intense electronic transition is evident already at room temperature with very weak electron–phonon couplings (i.e., phonon sideband). Therefore, trivalent rare earth ions, such as Er^{3+}, Yb^{3+}, and Nd^{3+}, are examples of optical systems with weak electron–phonon couplings.

To quantitatively characterize an electron–phonon coupling and its strength, let us again consider the Franck-Condon diagram shown in Fig. 2.1. In this figure, the excited and ground states have energies $E_e(Q)$ and $E_g(Q)$, respectively, with separation between the lowest vibration states of the upper and lower levels of $E_0 = hv_0$. Absorption and emission spectra commonly comprise of a number of peaks (which are usually resolved very well at cryogenic temperatures) corresponding to the number of phonons involved in the transition and thus reflecting a vibronic structure of the final electronic level (i.e., where the transition is terminated). The probability of such a multiphonon transition can be expressed as follows:

$$P_n = \frac{S^n}{n!}\exp(-S) \tag{2.1}$$

where n is number of phonons involved in the transition and S is the Huang-Rhys factor, the physical meaning of which is in the strength of the electron–phonon coupling. This expression in turn reflects the schematic shape of the phonon sideband of the optical transition. In the spectrum of optical transition, the phonon sideband is a spectral band adjacent to the line of the pure electronic transition.

The most probable transition (emission or absorption) takes place with emission or absorption of the energy equal to the following:

$$E_{\substack{\text{em}\\\text{abs}}} = hv_0 \mp Shv \tag{2.2}$$

where S (the same Huang-Rhys factor) indicates the number of phonons involved in the corresponding transition process, h is the Planck constant and v is the frequency.

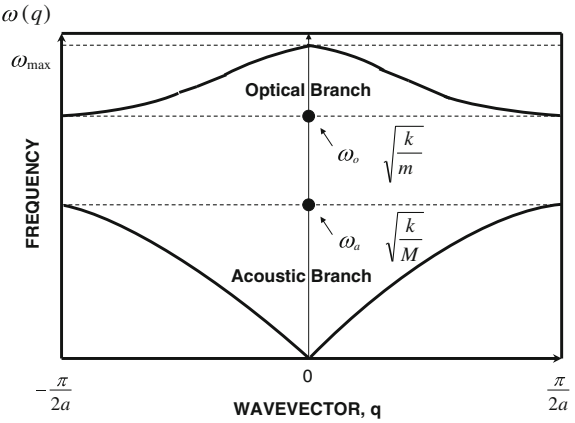

Fig. 2.2 One-dimensional phonon dispersion *curves* for a linear diatomic chain structure. The *top line* corresponds to the optical branch and the *lower curve* corresponds to the acoustic branch. See text for details

It is also useful to mention two types of lattice vibration modes in solids that have a direct relationship with some nonlinear scattering processes. In the case of a one-dimensional chain of atoms with a unit cell of two atoms, a phonon dispersion shows only one acoustic and one optical branch:

$$\omega^2(q) = \frac{k}{m^*} \pm k\sqrt{\frac{1}{(m^*)^2} - \frac{4\sin^2(qa)}{mM}} \tag{2.3}$$

where q is a wave vector, k is the force constant (i.e., elastic constant, measured in units $\left[\frac{H}{m} = \frac{\text{kg}}{\text{sec}^2}\right]$), a is the interatomic distance, m and M are the atomic masses, and $1/m^* = 1/m + 1/M$, where m^* is the effective mass. The acoustic and optic branches are specified by "±", with minus (−) for acoustical and plus (+) for optical. The two phonon branches can be seen in Fig. 2.2. The higher energy branch is optical and the lower energy branch is acoustical.

Later in the book, nonlinear scattering processes that take place in fibers will be discussed. These processes play an important role in the power scaling of fiber lasers. Each of the phonon branches described previously participates in different stimulated scattering processes, namely optical (stimulated Raman scattering) and acoustical (stimulated Brillouin scattering).

2.3 Optical Center Transitions: Spontaneous and Stimulated Emission

Consider an atomic system with discrete energy levels, which are annotated here as 1 and 2. The corresponding energy states of the levels are E_1 and E_2. E_2 is assigned a higher level, as follows:

$$E_1 < E_2 \tag{2.4}$$

In the case of thermal equilibrium, the population density of each energy level follows the Boltzmann statistics, according to which

$$N_2 = N_1 \exp\left(-\frac{E_2 - E_1}{k_B T}\right) \tag{2.5}$$

where k_B is the Boltzmann constant and T is the absolute temperature of the system. It is evident from Eq. 2.5 that the density population of the higher energy level E_2 is less than that of the lower energy level E_1 in thermal equilibrium. When an atom absorbs light with photon energy equal to the energy separation between two levels, the particle goes from lower level E_1 to higher level E_2. The absorbed photon energy is as follows:

$$h\nu_a = E_2 - E_1 \tag{2.6}$$

where h is the Planck constant and ν_a is the frequency of the absorbed light quantum. Once the atom appears in excited state E_2 (which is the nonequilibrium state of the atom), the atom has a few options to relax back into its original, equilibrium state E_1. In the absence of any existing external photons, the first way is to emit the energy through a so-called spontaneous decay, which can be done by either emitting a light quantum or nonradiatively by exchanging energy with the host material (which is usually done by emitting phonons that are vibration modes of the host material). The light-emitting part of the spontaneous decay into the lower energy level (i.e., spontaneous light emission) is represented by the A_{21} coefficient, which is called the Einstein coefficient after Albert Einstein, who studied these processes in the early 20th century. The physical meaning of the Einstein coefficient A_{21} is the probability at which the atom decays spontaneously from E_2 to E_1 and is obviously related to lifetime of the excited state of the atom.

However, if there is an external light photon with energy close to the separation $E_2 - E_1$ while the atomic system is in the excited state E_2, the excited atoms can decay to the lower energy level E_1 through so-called stimulated emission. This channel of this atomic decay was introduced by Einstein. The distinctive features of the stimulated emission is that the emission produces photons that have the same energy (or frequency) as the original external photon and also have the same phase. In other words, the incident photon stimulates an emission by forcing (or inducing) the atom to relax into its lower state by producing a stimulated emission of photons at the original (i.e., incident to the atom) photon energy and its original phase.

Because of the external inducing force, the stimulated processes can drive the atom not only from the higher energy state to the lower but also from the lower energy state to the higher (i.e., through stimulated emission and absorption). The probability of each of these processes (i.e., W_{21} or W_{12}) is proportional to the density of the incident electromagnetic radiation energy in the unit of spectral interval $\rho_\nu(\nu)$ (spectral energy density). The coefficient of proportionality for such

probabilities in this relationship is the so-called Einstein B coefficient (B_{21} and B_{12}, for emission and absorption, respectively). In the general case, $B_{21} = \frac{g_1}{g_2} \cdot B_{12}$, where g_1 and g_2 are degeneracy terms for the lower and upper energy levels. The expression for the stimulated process probabilities, which hold for nondegenerated levels, with $g_1 = g_2 = 1$, becomes the following:

$$W_{ij} = B_{ij}\rho_v(v) \tag{2.7}$$

Note that the function $\rho_v(v)$ is a radiation density per unit frequency interval that describes the number of photons with frequencies between v and $v + \Delta v$. The total energy density ρ therefore can be obtained by integrating the spectral distribution over the whole spectral range.

Another function that has to be introduced here is the spectral line profile shape $g(v)$, which is normalized over the whole spectral range of consideration as follows:

$$\int g(v)\mathrm{d}v = 1 \tag{2.8}$$

Consider the rate of the atomic energy level population exchange in units of number of atoms per unit volume per unit time. The number of atoms leaving the level will be negative and the number of atoms entering the level will be positive.

Using notations for all three processes in the case of the nondegenerated levels ($g_1 = g_2 = 1$) introduced previously, Eq. 2.9 gives a balance of emission and absorption processes for level E_2:

$$\frac{\mathrm{d}N_2}{\mathrm{d}t} = N_1 B_{12}\rho_v(v_0) - N_2 B_{21}\rho_v(v_0) - N_2 A_{21} \tag{2.9}$$

In the case of thermal equilibrium when $\mathrm{d}N_2/\mathrm{d}t = 0$, using an expression for population densities in equilibrium within Boltzmann statistics results in the following:

$$\exp(-hv_0/(k_B T)) = \frac{B_{12}\rho_v(v_0)}{B_{21}\rho_v(v_0) + A_{21}} \tag{2.10}$$

Therefore, resolving Eq. 2.10 for $\rho_v(v_0)$ gives the following expression for the energy spectral density for blackbody radiation:

$$\rho_v(v_0) = \frac{A_{21}}{B_{21}} \frac{1}{\left(\frac{B_{12}}{B_{21}}\right)\exp\left(hv_0/(k_B T)\right) - 1} \tag{2.11}$$

Again, it must be stressed that Eq. 2.11 for blackbody radiation spectral density is for the case of thermal equilibrium.

Equation 2.12 was derived by Planck for blackbody radiation for the case of absence of nonradiative processes:

$$\rho_v(v_0) = \frac{8\pi h v^3}{\left(\frac{c}{n}\right)^3} \frac{1}{\exp\left(hv_0/k_B T\right) - 1} \tag{2.12}$$

where c is the speed of light and n is the refractive index of the medium.

Using the Planck and Einstein relationships, the following expressions are ready for Einstein coefficients:

$$B_{21} = B_{12} \tag{2.13}$$

and

$$A_{21} = \frac{8\pi h n^3 v^3}{c^3} B_{21} \tag{2.14}$$

Equations 2.13 and 2.14 are very important for laser physics because they relate fundamental parameters of the laser material, such as spontaneous and stimulated emission probabilities, which in turn determine the laser gain.

2.4 Rare Earth Centers in Solids

This section reviews the basic properties of the most interesting rare earth ions for fiber lasers. The physics of rare earth ions is very interesting. However, in solid-state laser materials such as doped crystals and glasses, the most interesting rare earth ions are those in the lanthanum group—that is, the lanthanides. These ions usually appear in a trivalent state. The 4f electron shell determines the optical properties of lanthanides; it is almost insensitive to the surrounding atom of the host environment because of screening by 5s and 5p electron shells. This is the reason for weak interaction between optical centers and the crystalline field (weak electron–phonon coupling). Such weak interactions between the 4f electrons and the crystalline field produce a very well-resolved Stark structure of the levels, which varies slightly (compared with 3d ions, for example) from host to host. For the same reason, electronic transitions in trivalent rare earth ions are very narrow and demonstrate very weak phonon bands.

The spectral shape of the optical transitions of lanthanides in glasses is determined mostly by the following factors:

1. Stark splitting of the degenerated energy levels of the free ion, determining the number of Stark levels.
2. Magnitude of the splitting, which is determined by the host material.
3. Different line broadening mechanisms, such as homogeneous and inhomogeneous broadening.

Optical transitions between individual Stark levels contribute to the total absorption and emission line shape. Typical spectral line width of the lanthanide in

glass is approximately a few hundred wave-numbers. As an example of host material influence, oxide glasses demonstrate larger spectral line widths for lanthanides compared with that of fluoride glasses.

2.5 Homogeneous and Inhomogeneous Line Broadening

The nature of spectral line broadening plays a very important role in the performance of the solid-state laser. In particular, pump conversion efficiencies of certain laser regimes, such as single-frequency operation, heavily depend on the type of broadening of the laser line. This section reviews the basic properties of optical transition line broadening. The determination of whether the transition line shape is homogeneously or inhomogeneously broadened is based on whether the lines are from the same type of centers or from different types. In the case of rare earth ions in glasses, homogeneous and inhomogeneous broadening are the two main mechanisms of optical transition line broadening. These two mechanisms contribute almost equally to the resultant spectral line width, with an individual contribution of up to several hundred wave-numbers at 300 K. The spectral line broadening at room temperature smooths the overall line shape, which becomes resolved only at low temperatures. With a temperature decrease, Stark level structure becomes more and more evident and determines the line shape characteristic profile.

2.5.1 Homogeneous Broadening

Purely radiative decay (i.e., spontaneous decay) is described by an exponential function; the corresponding spectral line has the shape of a delta function. A good example of such radiative transition is a low-temperature zero-phonon line that occurs between the lowest vibration level of the excited state and the lowest vibration level of the lower electronic level. In the case of rare earth ions (especially in crystals), such zero-phonon transitions occur between electronic states of the Stark systems of energy levels because the strength of an electron–phonon interaction in this case is low.

Usually, a homogeneous broadening of optical centers in solids is defined by the random perturbation of the optical centers, such as the interaction with lattice phonons or an interaction with optical centers of a similar type. Such types of interactions result in shortening of the excited state lifetime of the optical center. The optical transition line shape in the case of homogeneous broadening is described by a Lorentzian function g_L (see Fig. 2.3), which is expressed as follows:

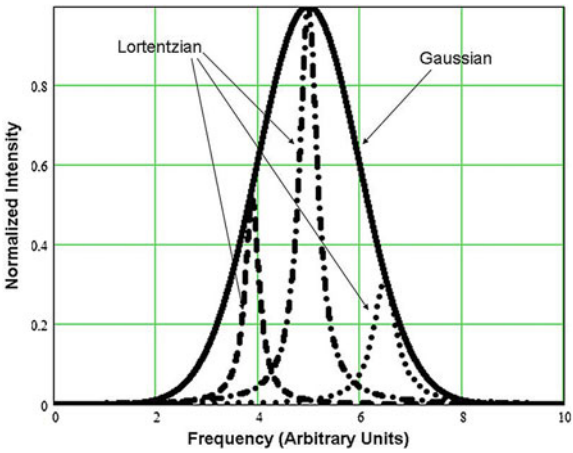

Fig. 2.3 Inhomogeneously broadened emission line spectral profile (*Gaussian shape*) and homogeneously broadened lines inside the Gaussian envelope (*Lorentzian shape*)

$$g_L(v) = \frac{\Delta v_H/(2\pi)}{(v - v_0)^2 - \left(\frac{\Delta v_H}{2}\right)^2} \tag{2.15}$$

where v_0 is the central frequency of the optical transition and Δv_H is the transition spectral line full width at half maximum (FWHM). Equation 2.15 for the Lorentzian function g_L is normalized by $\int_{-\infty}^{+\infty} g_L(v)\mathrm{d}v$.

The optical center lifetime is determined by the probability of transition from the upper level to the lower level of the optical center. This probability in turn is a sum of several process probabilities related to radiative and nonradiative transitions in the optical center. A general analytical expression for the optical center lifetime τ can be written as follows:

$$\frac{1}{\tau} = W_R + W_{\mathrm{NR}} \tag{2.16}$$

where W_R is the probability of radiative transition, which is equal to the Einstein A coefficient $A_{21} = \frac{1}{\tau_R}$. W_{NR} is the probability of all nonradiative processes of the optical center when it relaxes from the upper energy level to the lower energy level; it includes the probability of the ion interaction with phonons of the lattice, probability of ion–ion interaction, etc. In many cases, measurement of the luminescence decay time at low temperatures, such as liquid nitrogen temperatures (~77 K) or close to helium temperatures (<10 K), produces longer measured decay time by eliminating phonon interaction and therefore giving a value of purely radiative lifetime τ_R. Knowing radiative lifetime and decay time at given elevated temperature, one can determine a luminescence quantum yield—a parameter that shows a fraction of overall probability of the center transition from the higher to lower energy level, which is radiative. The luminescence quantum yield is determined by the following expression:

$$\eta_{\mathrm{LQE}} = \frac{W_R}{W_R + W_{\mathrm{NR}}} \tag{2.17}$$

Typical values of the room temperature luminescence decay in rare earth ions in solids (which is a result of the radiative and nonradiative transitions occurring in these optical centers) span from microseconds to milliseconds and are dependent on the particular ion and the host material. For example, in glass at room temperature, the lifetime of Yb^{3+} and Er^{3+} ions in their most important laser transitions are typically 1 and 10 ms, respectively.

Because of the higher phonon energy in silica glass than in phosphate glass, the probability of a nonradiative transition for a given gap between higher and lower energy levels is higher in silica glass because it requires a smaller number of participating phonons to fill the gap during relaxation from the upper level; this demonstrates the influence of the host material (energy gap law will be described in detail later in the book). In turn, this fact explains why homogeneous broadening in silica glass is usually greater than in phosphate glass. At low levels of doping, the ion–ion interaction between rare earth ions is very low; nonradiative transition probabilities originate mostly from electron exchange with lattice phonons. However, with an increase of the doping level, ion–ion interaction becomes more and more significant and may result in concentration quenching of luminescence, which affects the optical center luminescence quantum yield. In turn, this sets a limit for doping concentration levels in fibers and laser hosts in general. Other factors may also affect the decision to limit concentration of the laser-active ions at a certain concentration level.

2.5.2 Inhomogeneous Broadening

Inhomogeneous broadening of the optical center's line shape during a transition between energy levels originates from a local site-to-site variation in the optical center's surrounding field in the lattice environment. The strength and symmetry of the field around the rare earth ion determine the spectral properties of the optical transitions, as well as the transition strength. In the case of inhomogeneous broadening, the overall shape of the spectral line is a superposition of all individual, homogenously broadened lines corresponding to different types of the optical center. The line shape of the inhomogeneously broadened optical transition is described by the Gaussian line profile (see Fig. 2.3), which can be expressed as the following function of frequency:

$$g_G(\nu) = \frac{1}{\Delta\nu_{\mathrm{INH}}}\sqrt{\frac{4\ln 2}{\pi}}\exp\left[-4\ln 2\left(\frac{\nu-\nu_0}{\Delta\nu_{\mathrm{INH}}}\right)^2\right] \tag{2.18}$$

Table 2.1 Homogenous and inhomogeneous line widths for several rare earth ions in different glass hosts measured at 300 K

Rare earth ion	Glass matrix	$\Delta\nu_H$ (cm^{-1})	$\Delta\nu_{INH}$ (cm^{-1})	Source
Nd^{3+}	Silicate	110	50	[1]
Yb^{3+}	Phosphate	80	66	[2]
Er^{3+}	Germanium silicate	17	30	[3–5]
Tm^{3+}	ZBLAN (ZrF_4-BaF_2-LaF_3-AlF_3-NaF)	32	450	[6]

where $\Delta\nu_{INH}$ is the FWHM of the inhomogeneously broadened line. Determined by the optical center surrounding fields, the inhomogeneous line width is insensitive to the temperature of the host material.

In a real situation at room temperature, the individual contribution to the optical transition overall line shape by homogeneous and inhomogeneous broadening may be different or even comparable, such as in the case of most rare earth ions in glasses. In this general case, the resultant overall line shape is best described by the so-called Voigt function, which is a convolution between Lorentzian and Gaussian profiles:

$$g_{VOIGT}(\nu) = \int g_G(\xi) g_L(\nu - \xi) \mathrm{d}\xi$$

Table 2.1 demonstrates several examples of homogeneous and inhomogeneous line widths for widely used rare earth ions in some glasses at room temperature.

Note that the homogeneous and inhomogeneous line width contribution varies for the same rare earth center in different glasses. For example, it has been shown that inhomogeneous broadening of the ${}^4I_{13/2} \rightarrow {}^4I_{15/2}$ in Er^{3+}-doped silica glass was greater in alumino-silicate glasses compared to germano-silicate glass [3–5].

In optical spectroscopic research, to get information regarding the inhomogeneous broadening nature of the spectral line, one needs to cool down the host material to low temperatures (usually <77 K) in order to "freeze" phonons and eliminate contributions from homogeneous broadening. In this way, one may determine several important parameters of optical centers, such as the Stark structure of the energy levels.

2.6 Spectroscopic Parameters of the Optical Transition: A Brief Introduction to the Main Theories

Determining the spectral parameters of laser-active ions in solids is a very important task in laser physics. Several theories have been developed to calculate emission and absorption cross-sections using some of the measured spectral parameters. Existing theories reflect practical situations that appear in real solids doped with laser-active ions. This section briefly reviews each of the main theories.

2.6.1 Judd-Ofelt Theory

The Judd-Ofelt theory [7, 8] allows one to predict the stimulated emission cross-section peaks and integrated values for transitions between any level of the ion. The theory is based on the assumption that the average energy difference between the 4f levels is much larger than the energy spread of the excited configuration. The radiative transition rates and the radiative lifetimes can be obtained from the oscillator strengths of the transition. The theory gives the following expression for the oscillator strength of the electric dipole transition (f^{ed}) [7]:

$$f_{ij}^{ed} = \frac{8\pi^2 mv}{3h(2J+1)} \times \frac{(n^2+2)^2}{9n} \times \sum_{\lambda=2,4,6} \Omega_\lambda \left| \left\langle f^N J \middle| \middle| U_\lambda \middle| \middle| f^N J' \right\rangle \right|^2 \tag{2.19}$$

where i is the initial state of the transition, j is the final state of the transition, v is the transition frequency, n is the refractive index of the host material, m is the electron mass, and $\langle f^N J||U_\lambda||f^N J'\rangle$ are the reduced matrix elements, tabulated in [9].

Within this theory, the strength of any transition f can be determined by a set of three parameters: Ω_i ($i = 2, 4, 6$; see Eq. 2.19 for the oscillator strength). This set of parameters completely defines and parameterizes the effect of the host on the absorption and fluorescence properties of the ion's transitions between different multiplets of the $4f^N$ configuration. These parameters are calculated by performing a least-squares fit of the measured oscillator strengths to the theoretical ones. The more transitions that are taken into account during the fitting procedure, the more accurately determined and reliable the Judd-Ofelt coefficients appear to be (although this is not the case for Yb^{3+}, where the only transition between essentially two levels is presented in the electronic structure of the ion; see below). The complete set of Judd-Ofelt coefficients allows the calculation of the strength of any integrated cross-section. Judd-Ofelt parameters are presently tabulated for practically all rare earth ions in different solid materials. Table 2.2 presents the Judd-Ofelt parameters for Er^{3+} in different glass hosts (a detailed spectroscopic analysis of this ion will be done in Chap. 5).

For glasses, the calculated Judd-Ofelt parameters are average values of the parameters for each given site of the Er^{3+} ion because there is great variation of the sites that can be occupied by the ion (compared with crystals).

The Judd-Ofelt theory gives the total oscillator strength for the transition between two multiplets. The theory estimates only the integrated electric dipole oscillator strength for the particular transition (not the individual transitions between different states of the multiplet). Determination of the individual transitions' strength or cross-sections (spectral shapes) requires determination of the spectral distribution measurements of the relative emission spectra. This theory is particularly valuable for predicting strengths of transitions for which direct measurements are difficult. Accuracy of the Judd-Ofelt analysis is about 10–15 % for

Table 2.2 Judd-Ofelt parameters for Er^{3+} in different glass hosts

Glass matrix	$\Omega_2 \times 10^{-20}$ (cm^2)	$\Omega_4 \times 10^{-20}$ (cm^2)	$\Omega_6 \times 10^{-20}$ (cm^2)	Source
Germanate	6.4	0.75	0.34	[10]
Phosphate	9.92	3.74	7.36	[10]
Fluoride	1.54	1.13	1.19	[11]
	1.47	1.51	1.69	[23]
Borate	11.36	3.66	2.24	[10]
Tellurite	7.84	1.37	1.14	[10]
Gallium tellurite	6.46	1.64	1.47	[26]
ZBLAN (ZrF_4-BaF_2-LaF_3-AlF_3-NaF)	2.3	0.9	1.7	[12]
PKBAEr	8.05	1.46	2.28	[22]
NaTFP	5.92	1.07	1.44	[23]
Lead borate	3.31	1.63	1.29	[24]
ZTE	3.14	1.19	1.43	[25]
Oxyfluoride	2.75	1.25	0.76	[26]
Silica	8.15	1.43	1.22	[28]

most rare earth ions [13, 14]. Detailed treatments of the theory for the case of rare earth ions, including its successes and limitations, are available elsewhere [12, 15].

On a practical note, for fiber laser development in which Yb^{3+} glass plays a central role, it is practically impossible to perform a calculation of the Judd-Ofelt parameters and therefore calculate cross-section values using Judd-Ofelt theory because there is only a ${}^2F_{5/2} \rightarrow {}^2F_{7/2}$ transition (i.e., essentially a two-level transition) for Yb^{3+}. Other theoretical methods (described later) are used in the case of Yb^{3+} to determine cross-section values of optical transitions.

2.6.2 McCumber Theory

In a glass environment, rare earth ions demonstrate broad emission and absorption spectra; therefore, the previously introduced Einstein relationships need to be adjusted. For this important application, the McCumber theory can be used. The McCumber theory shows that all three processes described by Einstein in his theory—absorption, stimulated emission, and spontaneous decay—their cross-sections, and the radiative lifetime of an optical center in thermal equilibrium are related to each other at every single frequency using a set of theoretical formulas. These formulas are also sometimes called a generalized Einstein relationship.

Following McCumber [16], the theory assumes that the time required to establish a thermal distribution within each manifold is short compared with the lifetime of the manifold. The main theoretical conclusion of the McCumber theory is the following formula, which relates absorption and emission cross-sections at a

given frequency (unlike the Füchtbauer-Ladenburg theory, which gives the relationship between integrated cross-sections):

$$\sigma_{21}(\nu) = \sigma_{12}(\nu)\exp\left[\frac{E_{\text{ex}} - h\nu}{kT}\right] \tag{2.20}$$

where E_{ex} is the excitation energy, which is temperature dependent and is the net free energy required to excite an ion from its lower energy level to the upper level at temperature T. At room temperature, $kT \approx 161\ \text{cm}^{-1}$. According to the McCumber analysis, the emission and absorption cross-sections are equal at a certain frequency:

$$\nu_{\text{center}} = \frac{E_{\text{ex}}}{h} \tag{2.21}$$

All one needs to know is E_{ex}. To determine this important value following McCumber, another definition of this energy parameter is introduced:

$$\frac{N_+^0}{N_-^0} = \exp\left(-\frac{E_{\text{ex}}}{kT}\right) \tag{2.22}$$

where $N_\pm^0$ is the population of the upper and lower levels in unpumped material at temperature T.

However, if one knows the positions and number of all Stark components in the lower and upper energy levels, the same concentration ratio can be determined as follows:

$$\frac{N_+^0}{N_-^0} = \frac{\exp(-E_0/kT) \times \left(1 + \sum_{i=2}^{p} \exp\left(-E_{+i}/kT\right)\right)}{1 + \sum_{j=2}^{q} \exp\left(-E_{-j}/kT\right)} \tag{2.23}$$

where q and p are the number of Stark components at the ground and excited levels, respectively; E_0 is the energy separation between the lowest energy levels of the two manifolds (zero-phonon energy); and E_{+i} and E_{-j} are the energy differences between ith and jth levels.

The system of Eqs. 2.22 and 2.23 gives a path to calculate excitation energy E_{ex}, which in turn gives an opportunity to calculate absolute values of the emission and absorption cross-sections. As an example, for the case of Er^{3+} ions, Fig. 2.4 shows a spectral profile of the calculated stimulated-emission cross-section in low-fluorine fluorophosphate glass [17].

Figure 2.4 demonstrates a good fit with experimental data obtained for the same glass sample. The McCumber theory provides not only absolute values of the cross-section but its spectral distribution as well, thus giving the complete picture of the cross-section. This theory allows one to determine emission cross-section from the measured absorption cross-section and radiative lifetime. However, the McCumber theory requires knowledge of the electronic structure of the ion.

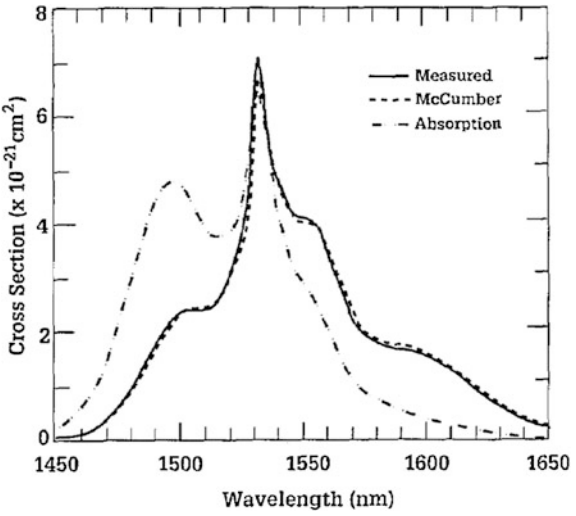

Fig. 2.4 Comparison of the shape of the measured stimulated-emission cross-section with that calculated from the absorption cross-section using the McCumber theory [17]. (Image courtesy of the optical Society of America)

Overall, the McCumber theory is a powerful instrument in hands of researchers for calculating important spectroscopic parameters of laser-active optical centers and is often used in laser physics.

2.6.3 Füchtbauer-Ladenburg Theory and Einstein Coefficients

The Füchtbauer-Ladenburg theory [18, 19] provides a relationship between the absorption coefficient and Einstein A and B coefficients for a system with two degenerate levels, using degeneracy terms g_1 and g_2 for the lower and upper energy levels. This theory assumes that in the spectral range of interest (i.e., where the optical transitions under consideration are taking place), the host material refractive index remains unchanged—an assumption that is reasonable for trivalent rare earth ions, which are being used as laser-active optical centers. The most important and probably most well-known conclusion of the Füchtbauer-Ladenburg theory is an obtained relationship between the upper-state lifetime of the laser-active ion to its emission cross-section. The corresponding Füchtbauer-Ladenburg relationship is given by:

$$\int v^2 \sigma_{21}(v) \mathrm{d}v = \frac{A_{21} c^2}{8\pi n^2} \tag{2.24}$$

where n is the refractive index; A_{21} is the Einstein coefficient, which is determined by radiative lifetime, $A_{21} = {}^1/_{\tau_{\mathrm{rad}}}$; c is the speed of light in a vacuum; v is

frequency; and $\sigma_{21}(\nu)$ is the spectral component of the emission cross-section. A similar equation can be written for the absorption cross-section:

$$\int \nu^2 \sigma_{12}(\nu) \mathrm{d}\nu = \frac{A_{21} c^2}{8\pi n^2} \frac{g_2}{g_1} \tag{2.25}$$

The relationships in Eqs. 2.24 and 2.25 give a well-known relationship between absorption and emission cross-sections:

$$g_1 \int \nu^2 \sigma_{12}(\nu) \mathrm{d}\nu = g_2 \int \nu^2 \sigma_{21}(\nu) \mathrm{d}\nu \tag{2.26}$$

A comparison of the theories presented in this chapter for calculating emission cross-sections are illustrated in Fig. 2.5 [17]. According to Fig. 2.5, the McCumber theory shows very good agreement with measured cross-section values, whereas the Einstein analysis overestimates these values.

Another example of using the Füchtbauer-Ladenburg theory for stimulated-emission cross-section calculations is illustrated in Fig. 2.6 [20]. Dong et al. [20] determined stimulated-emission cross-sections for the 3 % Nd-doped phosphate glass at both room and liquid-nitrogen temperatures using this theory.

Figure 2.6 shows variations with temperature in the stimulated-emission cross-sections of Nd:phosphate glasses calculated using the Füchtbauer-Ladenburg theory. The results show that the stimulated-emission cross-section is nearly independent of Nd^{3+} concentration. These results are important because dependence of the emission cross-section on the temperature has a significant effect on the performance of high-power Nd:glass-based lasers.

In addition to giving a path to calculate cross-sections, the Füchtbauer-Ladenburg theory shows that large emission cross-sections and therefore a

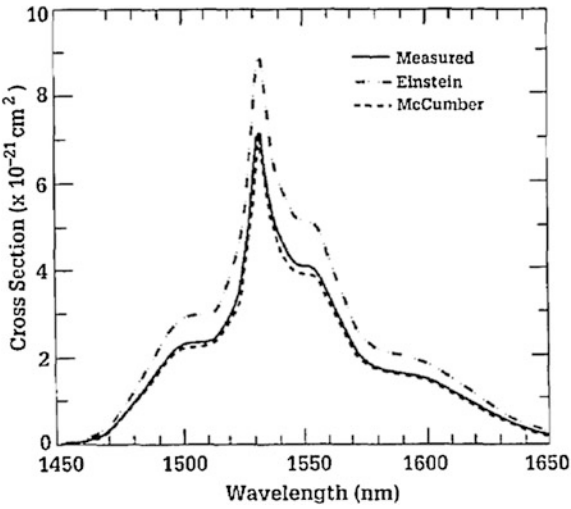

Fig. 2.5 Comparison of stimulated-emission cross-sections of Er^{3+} obtained using the radiative lifetime (measured), the Einstein relationship, and the McCumber theory with an estimated $\varepsilon \equiv E_{ex}$ for the case of fluorophosphates glass [17]. (Image courtesy of the optical Society of America.)

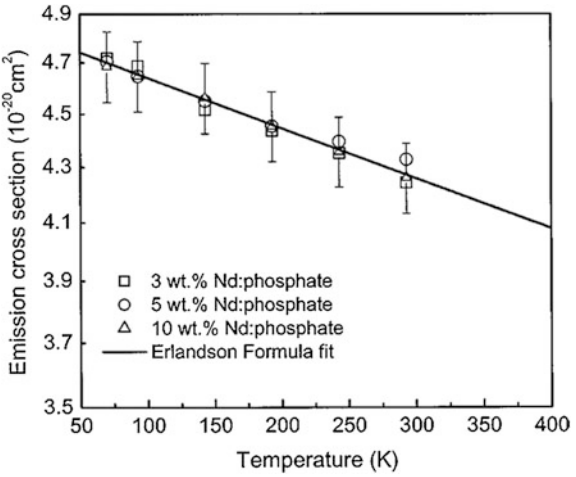

Fig. 2.6 Stimulated-emission cross-sections versus temperature for differently doped glasses. The straight line represents the model described in Ref. [20], which predicts the variation of the stimulated-emission cross-section of Nd:phosphate glasses with temperature [20, 21]. (Image courtesy of the optical Society of America.)

large-gain bandwidth of laser transitions are leading to a short radiative lifetime. This helps researchers to determine the laser-active optical centers that are required for broad-wavelength tunable laser operation and ultrashort pulse generation.

2.7 Sensitization of Laser-Active Centers

Trivalent rare earth ions used as laser-active centers in solids have several spectroscopic properties that restrict effective optical excitation for creating inversion populations. The most important spectroscopic properties that have been taken into account during rare-earth-doped gain fiber development for laser/amplifier applications are spectral line width, accessibility of the absorption band for exciting with pump-diode laser wavelengths, and absorption coefficients at the pump wavelength for reasonable gain of fiber length.

If only the most widely used laser-active rare earth centers in fiber lasers (i.e., Nd^{3+}, Yb^{3+}, Er^{3+}, and Tm) and their absorption bands are considered, we can see that all ions except for Er^{3+} require well-developed diode laser pump wavelengths of 808, 915, 976 and 792 nm when using common high-intensity excitation bands with high absorption coefficients (e.g., for Liekki Yb^{3+} [nLIGHT, Vancouver, WA], >1,200 dB/m of core absorption). Unlike the other ions mentioned, Er^{3+} demonstrates intense absorption near 1,530 nm with ~70–110 dB/m absorption coefficient and another absorption band near 980 nm with approximately one-third of that at 1,530 nm absorption band intensity. On the other hand, for high-power applications when pump-diode lasers are fiber coupled into 100–600 μm core fibers, a technology called clad pumping has been developed to make it possible to couple high-power diode lasers into the gain fibers (reviewed in detail later in this book). To use the clad pumping technique. The gain fiber consists of a doped core

and undoped cladding where the pump is coupled. However, because of the low ratio of core to clad diameter, the effective absorption of the pump light is reduced from the core absorption coefficient to the value:

$$\alpha_{\text{clad}} = \alpha_{\text{core}} \frac{S_{\text{core}}}{S_{\text{clad}}} \tag{2.27}$$

where S_{core} and S_{clad} are cross-section areas of the core and cladding, respectively. For typical true single-mode fibers with a core diameter of 9 μm and clad diameter of 125 μm, the cross-section area ratio is 0.005. Therefore, the clad pumping absorption coefficient reduces from 110 to 0.55 dB/m, which in turn requires an increase of the fiber length by a factor of 200.

One of the well-known techniques that is used to increase absorption of laser-active ions and enhance efficiency of rare-earth ion excitation is co-doping the laser active ion with another ion, using a more suitable pumping spectral location, a high doping concentration, and an efficient pumping excitation transfer to the lasing ion. Therefore, this technique is very important in clad pumping geometry in which, as mentioned above, effective absorption of the active laser center in the cladding is reduced significantly. As an example, in the case of Er^{3+}, it was suggested that Yb^{3+}, which has an intense and broad absorption band at 980 nm, can be a very good sensitizer. Experimental and theoretical research of the energy transfer between Yb^{3+} and Er^{3+} in different materials showed that direct excitation of Yb^{3+} produces a very efficient energy transfer to Er^{3+} in several laser glass hosts (see Fig. 2.7). In the case of the Yb^{3+}–Er^{3+} system, Yb^{3+} ions absorb pumping light in their broad absorption band at 980 nm, which follows an efficient energy transfer from the $^2F_{5/2}$ level of Yb^{3+} to the $^4I_{11/2}$ level of Er^{3+}. This is followed by fast nonradiative relaxation from the $^4I_{11/2}$ energy level to the metastable $^4I_{13/2}$ energy level. The $^4I_{13/2}$ energy level is an upper energy level of the 1,550 nm Er^{3+} fiber laser (see Fig. 2.7).

Concentration of Yb^{3+} is usually much higher than the concentration of Er^{3+} in such co-doped systems, which make pump absorption higher and give reasonable gain fiber lengths in case of clad-pumping geometry. In addition, 980 nm indium gallium arsenide (InGaAs) laser diodes are available with higher power models

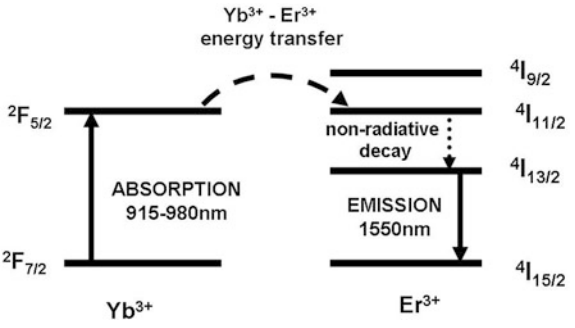

Fig. 2.7 Simplified excitation and energy transfer process in an Er^{3+}-doped glass sensitized with Yb^{3+}

and demonstrate much higher electrical to optical efficiency (>60 %) compared to ~25–30 % for 1,470–1,530 nm diode lasers used for direct Er^{3+} excitation. Unlike the case of Yb^{3+} sensitization, however, where there is a big quantum defect between pump and lasing photon energies, Er^{3+} fiber lasers with direct (i.e., resonant) excitation in the 1,450–1,550 nm spectral range may demonstrate high fiber-laser energy efficiency, high slope efficiency, and low quantum defects, which in turn reduce the heat generated by the laser medium. For high-power Er^{3+}-doped fiber laser systems, such resonant excitation plays a crucial role in solving the problem of thermal management of the laser system. However, when this approach is applied to clad pumping geometry, it requires achievement of high laser-active Er^{3+} concentration in laser glass with absent of luminescence quenching, which in turn is a challenging task. Because of the quasi-three-energy level (i.e., resonant nature) of the direct excitation of Er^{3+} when pumped directly into the 1,450–1,530 nm band, this approach requires higher pump power densities to reach transparency of the resonant Er^{3+} absorption in order to eliminate reabsorption of signal power and achieve positive net gain.

References

1. J.M. Pellegrino, W.M. Yen, M.J. Weber, Composition dependence of Nd^{3+} homogeneous line widths in glasses. J. Appl. Phys. **51**, 6332 (1980)
2. J.T. Fournier, R.H. Bartram, Inhomogeneous broadening of the optical spectra of Yb^{3+} in phosphate glass. J. Phys. Chem. Solids **31**, 2615–2624 (1970)
3. R.I. Laming, L. Reekie, P.R. Morkel, D.N. Payne, Multichannel cross talk and pump noise characterization of Er^{3+} doped fiber amplifiers pumped at 980 nm. Electron Lett. **25**, 455–456 (1989)
4. E. Desurvire, J.L. Zyskind, J.R. Simpson, Spectral gain hole-burning at 1.53 um in erbium-doped fiber amplifiers. IEEE Photon. Technol. Lett. **2**(4), 246–248 (1990)
5. J.L. Zyskind, E. Desurvive, J.W. Sulho, D. DiGiovanni, Determination of homogeneous line width by spectral gain hole-burning in an erbium-doped fiber amplifier with a GeO2-SiO2 core. IEEE Photon. Technol. Lett. **2**(12), 869–871 (1990)
6. F. Roy, D. Bayart, C. Heerdt, A.L. Sauze, P. Baniel, Spectral hole burning measurement thulium-doped fiber amplifiers. Opt. Lett. **27**(1), 10–12 (2002)
7. B.R. Judd, Optical absorption intensities of rare-earth ions. Phys. Rev. **127**, 750–761 (1962)
8. G.S. Ofelt, Intensities of crystal spectra of rare-earth ions. J. Chem. Phys. **37**, 511–520 (1962)
9. C.W. Nielson, G.F. Koster, *Spectroscopic Coefficients for the p^n, d^n and f^n Configurations* (MIT Press, Cambridge, MA, 1963)
10. R. Reisfeld, in *Spectroscopy of Solid-State Laser-Type Materials*, ed. by B.D. Bartolo (Plenum Press, New York, 1987), pp. 343–396
11. R. Reisfeld, G. Katz, N. Spector, C.K. Jorgensen, C. Jacohoni, R. de Pape, J. Sol. St. Chem. **41**, 253 (1982)
12. F. Auzel, Risita della statz. Sper. Vetro **5**, 49 (1990)
13. M.J. Weber, T.E. Varitimos, B.H. Matsinger, Optical intensities of rare-earth ions in yttrium orthoaluminate. Phys. Rev. B **8**, 47 (1973)
14. W.J. Miniscalco, *Rare Earth Doped Fiber Lasers and Amplifiers* (Marcel Dekker, Inc., New York, 1993), p. 33

15. C. Gorrller-Walrand, K. Binnemans, *Handbook on the Physics and Chemistry of Rare Earths*, vol. 25 (Elsevier Science, 1998), p. 167
16. D.E. McCumber, Theory of phonon-terminated optical lasers. Phys. Rev. **134**(2A), A299–A306 (1964)
17. W.J. Miniscalco, R.S. Quimby, General procedure for the analysis of Er^{3+} cross sections. Opt. Lett. **16**(4), 258–260 (1991)
18. P.H. Sarkies, J.N. Sandoe, S. Parke, Variations of Nd^{3+} cross section for stimulated emission with glass composition. J. Phys. D: Appl. Phys. **4**(10), 1642–1649 (1971)
19. J.N. Sandoe, P.H. Sarkies, S. Parke, Variation of Er^{3+} cross section for stimulated emission with glass composition. J. Phys. D: Appl. Phys. **5**, 1788–1799 (1972)
20. J. Dong, M. Bass, C. Walters, Temperature-dependent stimulated-emission cross section and concentration quenching in Nd^{3+}-doped phosphate glasses. J. Opt. Soc. Am. B **21**, 454–457 (2004)
21. A. C. Erlandson, G. F. Albrecht, S. E. Stokowski, Model predicting the temperature dependence of the gain coefficient and the extractable stored energy density in Nd:phosphate glass lasers. J. Opt. Soc. Am. B **9**, 214–222 (1992).
22. P. Babu, H.J. Seo, K.H. Jang, R. Balakrishnaiah, C.K. Jayasankar, K.-S. Lim, V. Lavín, Optical spectroscopy, 1.5 μm emission, and upconversion properties of Er^{3+}-doped metaphosphate laser glasses. J. Opt. Soc. Am. B **24**, 2218–2228 (2007)
23. M. Jayasimhadri, L.R. Moorthy, K. Kojima, K. Yamamoto, N. Wada, Er-doped tellurofluorophosphate glasses for lasers and optical amplifiers. J. Phys. Condens. Matter. **17**, 7705–7717 (2005)
24. W.A. Pisarski, Spectroscopic analysis of praseodymium and erbium ions in heavy metal fluoride and oxide glasses. J. Mol. Struct. **744–747**, 473–479 (2005)
25. C. Laxmi kanth, B.V. Ragavaiah, B. Appa Rao, N. Veeraiah, Optical absorption, fluorescence and thermoluminescence properties of ZnF2-MO-TeO2 (MO = ZnO, CdO and PbO) glasses doped with Er ions. J. Lumin **109**, 193–205 (2004)
26. X. Qiao, X. Fan, M. Wang, X. Zhang, Up-conversion luminescence and near infrared luminescence of Er^{3+} in transparent oxyfluoride glass-ceramics. Opt. Mater. **27**, 597–603 (2004)
27. H. Lin, K. Liu, E.Y.B. Pun, T.C. Ma, X. Peng, Q.D. An, J.Y. Yu, S.B. Jiang, Infrared and visible fluorescence in Er-doped gallium tellurite glasses. Chem. Phys. Lett. **398**, 146–150 (2004)
28. D. Ning, Y. Iv-yun, P. Ming-ying, Z. Qing-ling, C. Dan-ping, T. Akai, K. Kadono, Preparation and spectroscopic properties of Er^{3+}-doped high silica glass by sintering nanoporous glass. Mater. Lett. **60**, 1987–1989 (2006)

Chapter 3
Physical and Optical Properties of Laser Glass

Glass is an amorphic material that is highly isotropic and demonstrates a high degree of homogeneity. Unlike crystals, glass molecules are disordered but are rigidly bound. The structure of the glass shows bounds of several molecules: matrix molecules such as $(SiO_4)^{4-}$ or $(PO_4)^{3-}$ for silicate or phosphate glasses, respectively, and molecules of different metals or other chemical elements (usually their oxides). Optical properties of optically clear glass, particularly laser glass, are characterized by the spectrally dependent refractive index $n = f(\lambda)$. For most laser glasses, the value of the refractive index in the vicinity of a 1 μm wavelength is close to 1.5. This value depends on the particular laser glass structure and doping of the material. Table 3.1 demonstrates several examples of the glass composition for several of the most commonly used laser glasses.

An important characteristic of the host material for a gain medium is its principal optical phonon energy. Large phonon energy is associated with short carrier lifetimes arising from a large nonradiative relaxation rate. The phonons that are participating in the nonradiative relaxation process are the highest energy phonons in the phonon spectrum of the host material, which have a big value of density of states. There active phonons that are responsible for nonradiative relaxation are called effective phonons, with individual phonon energy equal to $h\Omega$. If the number of effective phonons involved in the multiphonon relaxation process is designated as p, then the corresponding energy gap ΔE can be expressed by effective phonon energy as follows:

$$p = \frac{\Delta E}{\hbar\Omega} \tag{3.1}$$

The so-called energy gap law is:

$$W_{nr} = A_{nr} \times \exp[-\chi \times \hbar\Omega \times p] \tag{3.2}$$

where A_{nr} and χ are constant parameters of the host material and $\hbar$ is the reduced Planck constant. Parameter A_{nr} is inversely proportional to the characteristic nonradiative decay time τ_0, while constant χ is related to the details of the

V. Ter-Mikirtychev, *Fundamentals of Fiber Lasers and Fiber Amplifiers*,
Springer Series in Optical Sciences 181, DOI: 10.1007/978-3-319-02338-0_3,

Table 3.1 Composition of several commonly used optical fiber glasses [1] (Courtesy of the Optical Society of America)

Glass	Composition (mol. %)
Phosphate	$50(P_2O_5)$–$16.66(MgO)$–$33.34(Li_2O)$
Germanate	$66(GeO_2)$–$17(BaO)$–$17(K_2O)$
Tellurite	$80(TeO_2)$–$20(Li_2O)$
ZBLAN	$57.35(ZrF_4)$–$29.63(BaF_2)$–$3.54(LaF_3)$ $-1.78(NaF)$–$5.16(InF_3)$–$2.54(AlF_3)$

electron–phonon coupling and is a function of phonon energy and the electron–phonon coupling constant:

$$\chi = \frac{\ln(\varepsilon)}{\hbar\Omega} \tag{3.3}$$

where $\varepsilon \ll 1$ is the ratio of the multiphonon relaxation rate for a p-phonon process to that for a $(p - 1)$ phonon process [2]. In glasses, the value of parameter ε is in the range between 0.012 and 0.007, which is less than the value of the same parameter in crystals. This fact motivates some researchers to conclude that that the strength of electron–phonon coupling in glasses is weaker than that in crystals. In general, if one considers same value of the energy gap, the probability of multiphonon nonradiative decay in glasses is higher compared with that in crystals, which in turn can be explained by a bigger span of available phonons with different energies in the phonon spectrum of glasses.

It is important to note that this simple form of the energy gap law (i.e., nonradiative rate law) is only valid for rare earth (RE^{3+}) ions that demonstrate the case of weak electron–phonon coupling with a Huang-Rhys parameter S close to zero.

As you can see from this analysis, the nonradiative relaxation rate is a very strong function of the lasing transition energy (the gap) to phonon energy ratio: The higher this ratio, the lower is the probability of nonradiative relaxation from laser-active level because more phonons have to be involved into the relaxation process between separated energy levels. Note that nonradiative relaxation from the upper energy level of the laser transition reduces the luminescence quantum yield of the optical center and therefore is critical for laser efficiency. Therefore, host materials with low phonon energies are required, especially for infrared (IR) laser materials with relatively small lasing photon energy.

3.1 Mechanical and Thermal Properties of Glass

This section briefly reviews the main thermomechanical properties of fiber glass and compares them to that of crystalline materials used for laser applications. As in the case of volume glass, the following advantageous properties of the glass can be defined, which make a difference in optical fibers:

1. High degree of optical uniformity over a long length.
2. Susceptibility of the glass matrix to change its nonlinear, mechanical, thermal, and spectral parameters by appropriate doping of the glass matrix in wide range of doping levels.
3. Possibility of achieving required photosensitivity to the ultraviolet (UV) light in the laser-active fiber for fiber grating recording.
4. Manufacturing optical fibers of long length with cost-effective production lines.
5. Relatively easy ways of connecting different pieces of fibers with low connection loss (using commercially available splicing machines).

When one cools down the glass that is in liquid phase (after melting), the temperature point that corresponds to the transition from a liquid to a brittle glass condition is called the glass transition temperature, T_g. The same temperature is responsible for the transition from solid to soft phase during the heating process. More accurately, the glass transition temperature is responsible for the so-called phase transition in glass, in which a super-cooled melt during cooling becomes a glassy structure. Below T_g, an amorphous glass is in a solid glass state and internal glass structure is mostly restored. During cooling from the liquid phase, the glass transition is a result of increased viscosity, which in turn depends on the cooling rate. During slow cooling, there is enough time for the glass liquid to restore its local atomic structure, whereas during rapid cooling, this process results in an increase in viscosity. Local atomic structure is not restored, which in turn results in an increase of the transition temperature T_g. Rapid and slow cooling result in different glass structures. These circumstances are taken into account in the glass manufacturing process. T_g plays an important role in high-power fiber laser design because it determines the upper limit of the allowed local temperatures of the fiber components, as well as that of gain fibers.

Table 3.2 highlights some of the most important thermomechanical properties of glass in comparison with yttrium aluminium garnet (YAG) crystal, which is widely used in laser physics (host of Nd:YAG laser material).

It is also useful here to present data on material density for several of the most popular glasses used in fiber laser technology (see Table 3.3).

Table 3.2 Thermomechanical properties of yttrium aluminium garnet (YAG) crystal and glass (fused silica)

Parameter	YAG crystal	Glass (fused silica)
Refractive index at 1,000 nm	1.83	1.47
Thermal conductivity, W/(m K)	14	0.3–1.3
dn/dT ($10^{-6}/K^{-1}$)	9.8	−20 to +10
Hardness (Moh)	8.5	7
Linear coefficient of thermal expansion ($10^{-5}/K$)	0.8−0.9	0.5
Melting point, °C (for glass: transition temperature T_g)	1,970	500[a]
Density (g/cm^3)	4.57	2.5

[a] Transition point temperature is listed. Melting point is ~1,600 °C

Table 3.3 Material density of several glasses [3]

Glasses	Density (g/cm^3)
Silicate	2.5–2.7
Borate	2.4–2.5
Phosphate	~2.6
Fluoride	~6–7

Crystalline solid-state laser materials such as YAG are superior to glasses in thermal conductivity and mechanical strength. Glasses, because of the extremely large lengths of material used when making use of distributed heat along their surface, create great opportunities for solving many thermal management issues existing in crystalline lasers. In addition, some spectroscopic parameters of the laser glass, such as broad absorption lines, make them superior for many diode pump applications (reviewed in later chapters).

3.2 Optical Properties of Fibers (Attenuation)

Because attenuation plays a very important role in the light propagation characteristics of fiber, this section provides a brief review of factors affecting this physical parameter of the glass. The physical reasons that are responsible for attenuation in optical fibers can be divided into three main categories: intrinsic glass material properties, waveguide properties, and optical connection loss.

3.2.1 Intrinsic Glass Material Properties

Intrinsic glass attenuation arises from absorption and scattering. Like in crystals, optical transmission properties of the glass reflect the degree of material purity and the method of its manufacture.

Fiber attenuation is caused by bonds between hydrogen atoms and oxygen in the glass material. The hydrogen atoms attach to oxygen sites and form hydroxyl ions. These oxygen and fundamental vibration bands are the most important and common impurities in undoped (laser-inactive) glasses, which in turn determine the UV cutoff and the presence or absence of bands in the vicinity of 250, 1,400, and 2,700 nm. The IR edge is between 4.5 and 5.0 μm, corresponding to fundamental inter zone optical transitions. Because of the great variety of glass composition used for different fibers, no single glass composition provides continuous transparency from the visible spectral region through the mid-infrared spectral region. Note that intentionally introduced dopants, such as GeO_2 and P_2O_5, which modify the fiber refractive index profile and change the manufacturing process, also affect material attenuation.

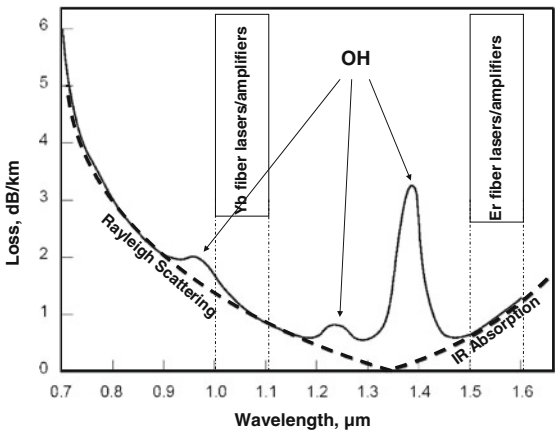

Fig. 3.1 Typical attenuation profile in optical fiber (permission to use granted by Newport Corporation. All rights reserved)

Another important physical process that determines the quality of the fiber glass is Rayleigh scattering, which is due to microscopic inhomogeneities of the glass matrix. This process demonstrates λ^{-4} wavelength dependence. The corresponding curve of the loss versus wavelength (i.e., combined losses due to impurities and Rayleigh scattering) has two major minimums in near-IR at wavelengths of approximately 1,300 and 1,580 nm wavelengths (see Fig. 3.1).

3.2.2 Waveguide Properties

Waveguide attenuation results from power leakage due to propagation with wavelengths much longer than the cutoff due to bending losses. Bending losses in turn include macrobends and microbends. A macrobend is usually a large-scale bend that is visible, like a fiber coiled around a pencil or any cylinder. Macrobending loss is usually reversible once the bend is released. Microbending is a small-scale fiber structure distortion that produces pressure over the fiber. Temperature or direct crushing force is a typical example of microbending. Microbending is usually hardly visible upon fiber inspection but still causes scattering and loss of propagating optical power. Depending on the nature and the used force, microbending may or may not be reversible. Microbending usually occurs due to distortion of the core cladding interface and is a result of poor fiber design or defective manufacturing.

With regards to power leakage in the cladding, increasing the cladding thickness usually decreases the LP_{01} (waveguide fundamental transverse mode) leakage loss. However, the overall sensitivity of the leakage losses depends on the particular fiber design and may be determined experimentally. As a guideline, however, the inner cladding diameter should be at least 10 times larger than the core diameter. This ratio is considered to be a threshold of leakage loss sensitivity.

A detailed description of waveguide properties (i.e., fiber mode structure) is covered in Chap. 6.

3.2.3 Optical Connection Loss

Two pieces of fiber spliced together demonstrate so-called joint losses. Currently, the commercially available splicing machines demonstrate down to 0.01–0.02 dB splicing loss for identical fibers. If there is mode field diameter mismatch for single-mode fibers, the optical connection (splicing) loss can be calculated using following formula:

$$L_{cl} = -20\log\left(\frac{2w_1w_2}{w_1^2 + w_2^2}\right) \tag{3.4}$$

where w_1 and w_2 are mode field radii of the two spliced fibers. The mode field radius is defined as half of the spatial extend of the fundamental mode through a larger volume, including the inner fiber cladding, where the mode intensity drops to the level of $1/e^2$.

3.3 Different Glass Types Used in Fiber Lasers and Amplifiers

Glasses differ by their principal phonon energy, which in turn affects the probability of nonradiative relaxation in these glasses. Nonradiative relaxation plays an important role in laser efficiency and therefore is a crucial parameter of the solid-state gain material.

Different chemical compounds added to the glass matrix—such as germanium, phosphorus, borate, and tellurite—can be used to create germinate, phosphate, borate, and tellurite glasses, respectively. Currently, the most widely used materials for fiber laser applications are silicate, germano-silicate, tellurite, and phosphate glasses doped with rare earth laser-active ions. Table 3.4 shows the principal

Table 3.4 Principal phonon energies in the most widely used laser glasses [4–6]

Glass system	Phonon energy ($\hbar\Omega$, 1/cm)
Borate	1,400
Phosphate	1,200
Silicate	1,100
Germanate	900
Tellurite	700
Fluorozirconate	500
Chalcogenide	350

phonon energies for the most widely used glasses [4–6]. Borate glass demonstrates the highest phonon energy, whereas chalcogenide glass shows the lowest phonon energy. The following sections briefly review several examples of important glasses used in fiber laser development.

3.3.1 Silicate Glass

Silica-based optical fibers are composed primarily of silicon dioxide (SiO_2) and certain amounts of other chemicals that are added for different applications. Currently, liquid silicon tetrachloride ($SiCl_4$) in a gaseous stream of pure oxygen is the principal source of silicon for the vapor deposition method (which will be reviewed later). Glass medium modifiers, such as Na^{3+} and Al^{3+}, are often added to facilitate the incorporation of rare earth ions because their size is greater than the basic network positions. The main purpose of the modifying impurities is to break the bridging oxygen to form non-bridging oxygen, which can later be used to coordinate the rare earth ions. The most effective glass modifier studied in silica glass is aluminum because it shows the most favorable characteristics. The incorporation of 2.87 mol % of Al_2O_3 in Nd^{3+}-doped silica glass has been shown to lead to elimination of Nd^{3+} clustering [7]. In the case of Er^{3+}, aluminum co-doping improves the efficiency of Er^{3+}-doped fiber amplifiers by eliminating the quenching effects [8].

Silica-based fibers have several advantages over other glass types used in fiber manufacturing. One of the main properties of the silicate glass is its manufacturability, which allows one to obtain high-quality fibers of long length. The next property that distinguishes this fiber type is the wide range of optical transparency, thus permitting the lowest loss for optical communication. Silicate fibers are mechanically robust, demonstrating impressive tolerance to bending. Silicate glass is not hydroscopic (i.e., highly resistive to water absorption) and demonstrates a high degree of chemical resistance, which makes it an irreplaceable candidate for many applications where a chemically aggressive environment is present. These fibers have very high damage thresholds and relatively low optical nonlinearity. Probably the most serious disadvantage of the silicate glass is its high phonon energy of ~1,100 cm^{-1}, which has to be taken into consideration when nonradiative multiphonon relaxation challenges development of gain fibers.

From all glass matrixes used for fiber laser applications, silicate glasses are probably the most widely used. They are used in several high-power fiber laser applications and currently are commercially available from a number of companies.

3.3.2 Phosphate Glass

Phosphate glasses have advantages over silicate glasses in the entire set of parameters important for laser applications. The most important advantage, particularly for fiber laser applications, is that phosphate glasses allow a significant amount of doping of laser-active ions to be introduced into the glass matrix with no substantial reduction of the luminescence quantum yield. Also, phosphate glasses are stable against the action of UV radiation but have poor chemical durability. Only mechanical strength and thermal stability make phosphate glass inferior to silicate glass. The principal phonon energy in most phosphate glasses is ~1,100–1,300 cm^{-1}. However, the ability to be doped with a significantly higher concentration of laser-active ions promotes the usage of phosphate glass in high peak power, pulse lasers, and short-cavity distributed feedback fiber lasers.

3.3.3 Tellurite Glass

Tellurite glasses are the focus of a growing number of studies due to their reduced phonon energy (principal phonon energy is ~700 cm^{-1}) and high linear and nonlinear refractive index. Tellurite glasses demonstrate good mechanical stability and quite wide optical transmission, ranging from 400 to 6,000 nm. Table 3.5 provides the typical intrinsic loss parameters of tellurite glass.

3.3.4 Fluoride Glass and ZBLAN

ZBLAN is an abbreviation of fluorozirconate glass system composition ($ZrFM_4$-BaF_2-LaF_3-AlF_3-NaF) and is the basis of most fluoride fibers. It is one of many fluoride glass compositions used to make fluoride glass and fiber. The principal phonon energy in typical fluoride glass is ~500–600 cm^{-1}. The properties of

Table 3.5 Intrinsic loss parameters in tellurite glass [9]

UV absorption	$A_{UV} = 10 \times 10^6$ dB/km
	$\lambda_{UV} = 13.0 \pm 0.3$ μm
Rayleigh scattering	R = 0.29 dB/km (Ref. [12])
IR absorption	$A_{IR} = 1{,}000$ dB/km
	$\lambda_{IR} = 4.1$ μm
Minimum loss	$(5.0 \pm 0.2) \times 10^{-3}$ dB/km
Minimum loss wavelength	2.8 ± 0.1 μm
Loss at 1.5 μm	0.06 dB/km

A_{UV} and A_{IR} are the ultraviolet (UV) and infrared (IR) absorption coefficients at corresponding wavelengths of λ_{UV} and λ_{IR}, respectively. Courtesy of the Optical Society of America

fluoride glass enable fibers to transmit light from the UV (as short as 250 nm) to the mid-IR, where application of other glass types is transmission limited, especially at wavelengths longer than 2 μm.

There are numerous families of fluoride glass with unique physical properties, including fluorozirconate, fluoraluminate, fluorindate, and fluorogallate. Fluoride glass has a refractive index ranging from 1.46 to 1.57, which provides low Fresnel losses of less than 4 % per end face for normal incidence on the glass surface. Fluoride glass also has the very unusual property of exhibiting a negative dn/dT of approximately -1×10^{-5} K^{-1}, which minimizes the thermal lens when the glass is heated.

Unlike silica-based fibers, fluoride glass preforms cannot be prepared by modified chemical-vapor deposition (MCVD; described in detail later). Fluoride glass preforms, therefore, are typically prepared by melting and casting. The resulting preforms are smaller than silica ones, but they can still be drawn into fiber samples with core diameters from 20 to 900 μm and be of a significant length. Fiber lasers have been made from fluoride glass fiber using different rare earth ions, such as Er^{3+}, Tm^{3+}, Nd^{3+}, and Pr^{3+}. Fiber lasers based on ER^{3+}-doped glass with power levels of more than 10 W at 2,740 nm have been demonstrated using a ZBLAN fiber.

Up-conversion lasers based on rare-earth-doped ZBLAN fibers have been in development since the early 1990s, when several CW and room-temperature visible-fiber lasers of this type were demonstrated. Up-conversion lasers usually use low-phonon glass fiber materials with effective phonon energy less than 600 cm^{-1}. Due to the fact that up-conversion lasers produce visible light (i.e., operate on high-energy gap transitions of rare earth ions, with visible light corresponding to ~20,000 cm^{-1}), they require two- or three-photon excitation of the laser transition using IR laser diodes. In turn, this dictates the limitations for allowed nonradiative relaxation on laser transition for efficient laser operation, which narrows selection of fiber host glasses to those with low phonon energies.

Today, up-conversion lasers based on ZBLAN fibers are efficient sources of tunable, room-temperature radiation. They are superior in many ways to other laser types with similar characteristics due to their simplicity and compactness. Up-conversion lasers presently demonstrate up to 50 % of slope efficiency. These lasers continue to be developed by many research groups and eventually may occupy a stable position in the laser market.

Despite several mechanical and optical properties that make fluoride glasses unique for fiber laser applications, these glasses demonstrate several serious disadvantages, such as reduced chemical stability, reduced humidity tolerance, and fragility.

References

1. F. Pellé, N. Gardant, F. Auzel, Effect of excited-state population density on nonradiative multiphonon relaxation rates of rare-earth ions. J. Opt. Soc. Am. B **15**, 667–679 (1998)
2. C.B. Layne, W.H. Lowdermilk, M.J. Weber, Multi-phonon relaxation of rare-earth ions in oxide glasses. Phys.Rev. B, **16**(1), 10–20 (1977)
3. M.J. Weber, The role of lanthanides in optical materials. American Ceramic Society annual meeting and exposition, Cincinnati, OH, USA, 1–5 May 1995, pp. 1–18
4. R. Reisfeld, *Spectroscopy of Solid-State Type Laser Materials*, ed. by B. DiBartolo (Plenum Press, New York, 1987), pp. 343–396
5. C.B. Layne, M.J. Weber, Multiphonon relaxation of rare-earth ions in beryllium-fluoride glass. Phys. Rev. **B16**, 3259–3261 (1977)
6. D. Lezal, J. Pedlikova, J. Zavadil, Chalcogenide glasses for optical and photonics applications. Calcogenide Lett. **1**(1), 11–15 (2004)
7. K. Arai, H. Namikawa, K. Kumata, T. Honda, Y. Ishii, T. Handa, Aluminium or phosphorus co-doping effects on the fluorescence and structural properties of neodymium-doped silica glass. J. Appl. Phys. **59**(10), 3430–3436 (1986)
8. S.P. Craig-Ryan, J.F. Massicott, M. Wilson, B.J. Ainslie, R. Wyatt, Optical study of low concentration Er^{3+} fibers for efficient power amplifiers, in *Proceeding of ECOC'90*, vol. 1 (OSA, Washington DC, USA, 1990), pp. 571–574
9. M. Naftaly, S. Shen, A. Jha, Tm^{3+}-doped tellurite glass for a broadband amplifier at 1.47 μm. Appl. Opt. **39**, 4979–4984 (2000)

Chapter 4
Fiber Fabrication and High-Quality Glasses for Gain Fibers

4.1 Materials

Glass optical fibers are almost always made from silica; however, some other materials, such as fluorozirconate, fluoroaluminate, and chalcogenide glasses, are used for longer-wavelength infrared applications. Most glasses demonstrate a refractive index of about 1.5. Typically, the difference between core and cladding is less than 1 %.

The core of a fiber is usually doped with laser-active ions. The most widely used laser active ions for fiber laser applications are rare earth ions such as erbium, neodymium, ytterbium, and thulium. Each of the ions has its own absorption bands, from which one can obtain optical gain; in turn, this creates the condition for optical amplification and oscillation. More detailed information on spectroscopic characteristics of the main laser active ions in fibers are given in a later chapter.

4.2 Fabrication of Fiber Preforms

A fiber preform is a piece of glass from which a fiber waveguide may be manufactured by pulling it into a long length using various techniques. Most fiber preforms are fabricated by modified chemical vapor deposition (MCVD) or outside vapor deposition (OVD), which is a modification of MCVD. These techniques, which allow the achievement of optical fibers with essentially reduced losses, revolutionized long-distance optical communications.

In the MCVD process (see Fig. 4.1), a mixture of oxygen, silicon chloride ($SiCl_4$), and other substances [e.g., germanium chloride ($GeCl_4$), aluminum oxide (Al_2O_3), rare earth dopants] are passed through a rotating silica glass tube, which is heated from the outside to about 1,600 °C with a traversing flame.

Under high temperatures, chemical reactions in the gas take place, eventually creating a clear glass layer through deposition. Ingredients such as $SiCl_4$ and

V. Ter-Mikirtychev, *Fundamentals of Fiber Lasers and Fiber Amplifiers*,
Springer Series in Optical Sciences 181, DOI: 10.1007/978-3-319-02338-0_4,

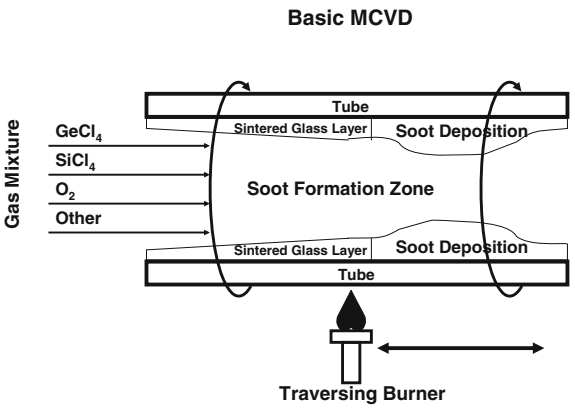

Fig. 4.1 Schematic illustration of modified chemical vapor deposition (MCVD) process

$GeCl_4$ are easily purified by distillation because they are in liquid state at room temperature. Near the end of the process, the gas mixture is modified to form a layer with a higher refractive index, the precursor of the fiber core. Finally, the tube is collapsed when heated to $\sim$2,000 °C. The MCVD technique allows for the achievement of extremely low losses (<0.2 dB/km) because high-purity materials are used during deposition and all contaminations are eliminated. Because of the absence of hydrogen, the water content of such preforms is very small, and therefore a strong loss peak at 1.4 μm decreases. Such a small absorption in this spectral range is critical for optical communication applications.

An alternative to MCVD is its modification, the OVD process. Using this technique, a doped rod of a glass with higher refractive index is inserted into a glass tube with a lower index. Deposition occurs on the outside surface of the rod (or mandrel). When deposition is completed, the rod is removed, leaving a void that is collapsed after heating, eventually creating a preform. The resultant preform is a glass rod of a few centimeters diameter and roughly a meter in length.

The preforms for multimode fibers, particularly large-core fibers, are often fabricated with plasma outside deposition (POD), in which an outer fluorine-doped layer with depressed refractive index (later forming the fiber cladding) is made with a plasma torch. The core can then be made of pure silica without any dopant. The fabrication of rare-earth-doped fibers involves various special aspects, including co-doping with other ions such as Al in special concentration ratios with laser-active ions, as well as modification of the fiber geometry (e.g., in the cases of triple-clad fibers).

Note that preforms for photonic crystal fibers, in which a core is surrounded by small holes in the cladding, are fabricated basically by stacking capillary tubes or rods that are mostly made of pure silica. However, this fiber type is outside the scope of this book.

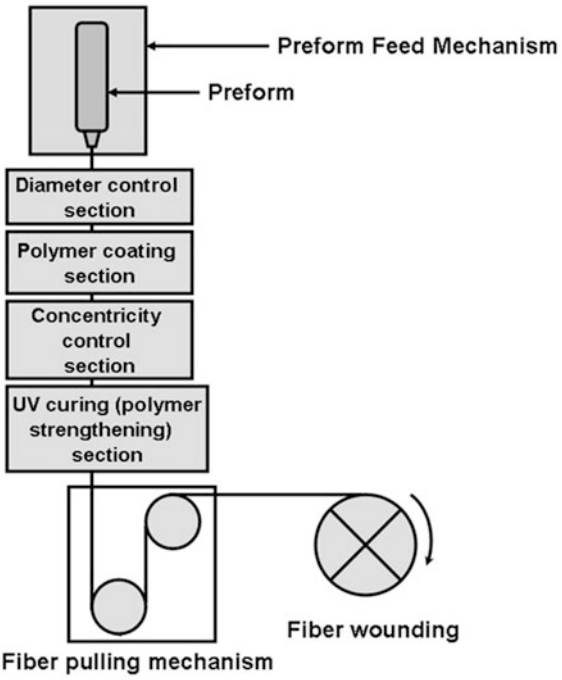

Fig. 4.2 Schematic illustration of the fiber fabrication process from a preform. *UV* Ultraviolet

4.3 Fiber Fabrication from the Preform

Most optical fibers are currently fabricated by pulling from a preform. Along its axis, the preform contains a region with increased refractive index, which forms the fiber core. When heated close to the melting point in an oven at the top of the drawing tower (Fig. 4.2), the preform allows a thin fiber to be pulled out of the bottom side of the furnace.

The fiber from a single preform can be many kilometers long. During the pulling process, the fiber diameter is held constant by automatically adjusting the pulling speed and the furnace temperature. Before the fiber is wound up, it usually gets a polymer coating for mechanical and chemical protection. Such coatings often consist of two or more different layers for optimum suppression of microbends. The resultant fiber structure is schematically shown in Fig. 4.3.

4.4 Laser-Active Fiber Fabrication

In laser-active fibers (i.e., gain fibers), the core is doped with laser-active ions. Typical rare-earth doping ions commonly used in fiber lasers are Yb^{3+}, Er^{3+}, Nd^{3+}, and Tm^{3+}. Co-doping laser-active fiber core with other dopants can affect the core

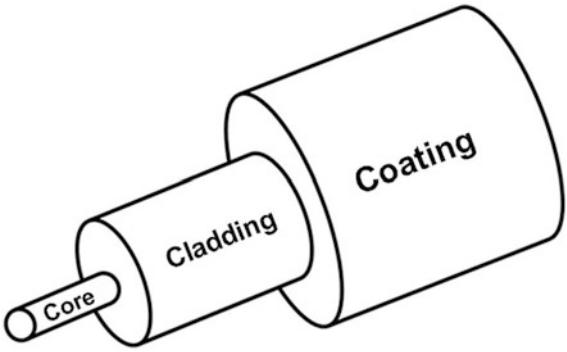

Fig. 4.3 Schematic diagram of the simplest fiber structure

refractive index as well as the solubility of the laser-active ions themselves. Therefore, although major fiber fabrication techniques described in the previous section are widely used for the fabrication of undoped fibers, doped (i.e., gain) fibers require modified techniques to incorporate laser-active rare earth ions into the fiber core at certain levels of doping and distribution [1]. Currently, two major techniques are used in laser active (gain) fiber manufacturing: MCVD (and in some cases, OVD) with solution doping of solution-phase rare earth ions and direct nanoparticle deposition (DND). This section reviews each of the techniques.

4.5 MCVD Technology for Rare-Earth Doped Fiber Production

For rare-earth doped fiber manufacturing techniques based on MCVD technology, one of the main problems is that the rare earth dopants in a gas reactant should be delivered to an oxidation reaction region together with other refractive index controlling dopants. However, the rare earth reactants have a reduced vapor pressure and therefore complicate such delivery via convective transport. To overcome this issue, one may heat the source of rare earth ions to intensify the convection.

In MCVD, one of the most commonly used techniques for heating rare earth reactants is solution doping. In solution doping, an undoped (with rare earth ions) porous silica frit (i.e., a porous layer of silica soot) is deposited on the inner side of a silica tube (see Fig. 4.4).

The tube is then dipped into a solution containing the rare earth ion salt. Then, the solution diffuses into the porous layer. The tube is removed from the solution, dried, and sintered into a solid glass rod, which later leads to a preform.

Figure 4.5 demonstrates the importance of Al co-doping during gain fiber manufacturing [2]. Co-doping Yb^{3+}-doped gain fiber with Al reduces background loss up to 50 times and maintains this low background loss up to a Yb^{3+} concentration of 10^{20} cm^{-3} [2]. Adding Al_2O_3 achieved a minimum loss of

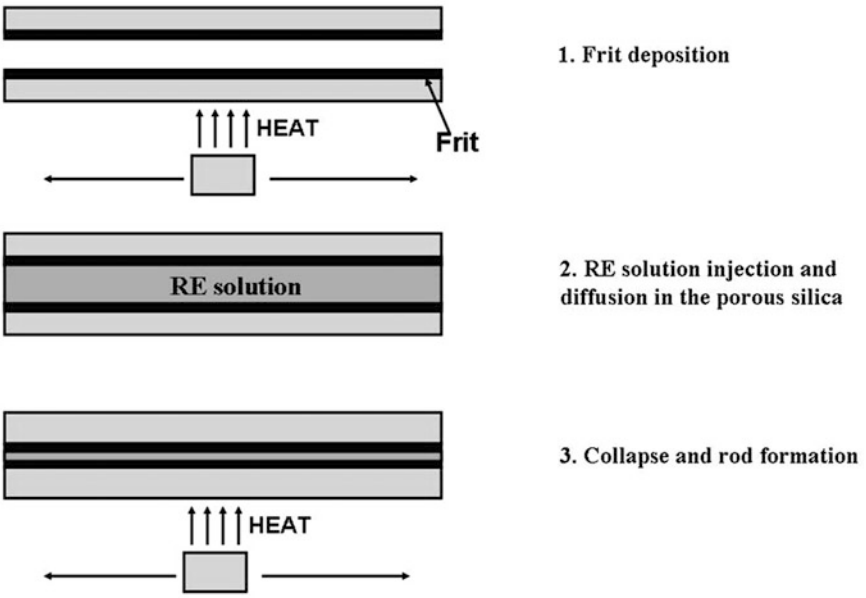

Fig. 4.4 Schematic view of the solution doping technique used in the modified chemical vapor deposition process for rare-earth doped fiber manufacturing. *RE* Rare earth

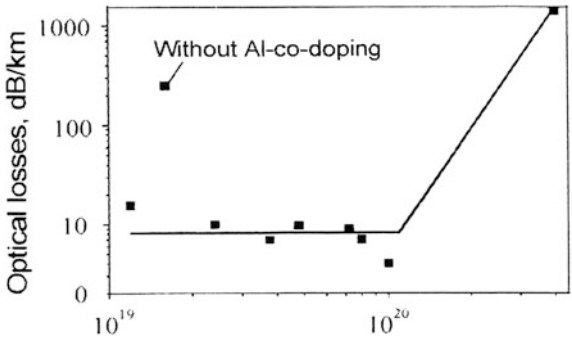

Fig. 4.5 Background loss versus Yb^{3+} concentration in alumosilicate glass [2]. Concentration is measured in cm^{-3}. (Image courtesy of SPIE)

5–20 dB/km in alumosilicate Yb^{3+}-doped glass [2]. Increasing Al_2O_3 doping level to more than 4×10^{20} cm^{-3} led to an increased level of background loss, reaching 1,400 dB/km.

Note that MCVD-based doping of rare earth ions to silica-based glasses is slow. Therefore, the rare earth ions are prone to clustering, which in turn negatively affects optical and gain performance of the active fibers used in fiber lasers and fiber amplifiers. Nevertheless, the MCVD technique (or its modifications) is used for most gain fibers available on the market.

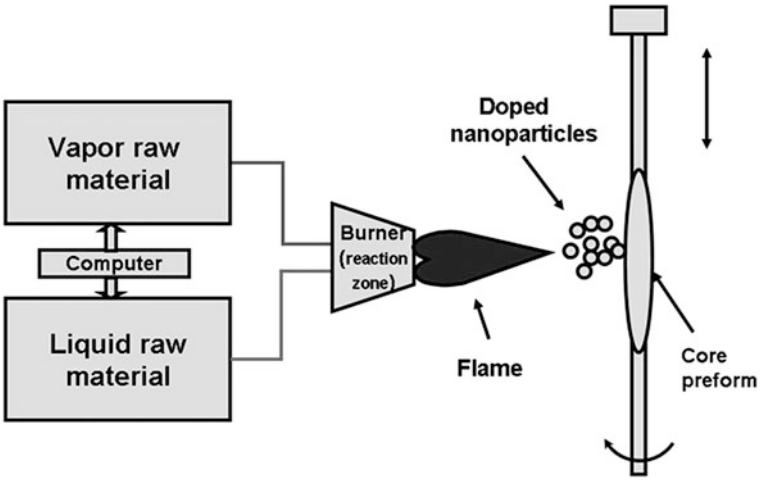

Fig. 4.6 Schematic view of the direct nanoparticle deposition technique

4.6 DND Technology

For Liekki, nLight (Vancouver, WA) developed the DND technique [3]. Unlike MCVD, DND technology directly and simultaneously (i.e., using a single step) deposits all the elements in nanoparticle size to create preforms (Fig. 4.6).

As a result, one obtains a highly doped fiber core composed of hundreds of deposited layers of particles with accurately controlled spatial composition. This is important for large mode area fibers (described in Chap. 10), which are used widely in high-power fiber lasers. The doping and refractive-index profile are independently controlled, which makes it possible to achieve gain fibers with optimized parameters.

References

1. J. Simpson, Fabrication of rare-earth doped fibers. Proc. SPIE **1171**, 2–7 (1989)
2. A.S. Kurkov, A.Y. Laptev, E.M. Dianov, A.N. Guryanov, V.I. karpov, V.M. Paramonov, O.I. Medvedkov, A.A. Umnikov, V.N. protopopov, N.N. Vechkanov, S.A. Vasiliev, E.V. Pershina, Yb^{3+}-doped double-clad fibers and lasers. Proc. SPIE **4083**, 118–126 (2000)
3. S. Tammela, M. Söderlund, J. Koponen, V. Philippov, P. Stenius, The potential of direct nanoparticle deposition for the next generation of optical fibers. Proc. SPIE **6116**, 6116.16–6116.24 (2006)

Chapter 5
Spectroscopic Properties of Nd^{3+}, Yb^{3+}, Er^{3+}, and Tm^{3+} Doped Fibers

5.1 Spectroscopic Notations

Rare earth $(RE)^{3+}$ ion transitions show up in the optical spectrum as sharp lines that vary little in energy position from host to host (either in glass or crystals). The corresponding energy level positions are designated by the following spectroscopic notations:

$$^{2S+1}L_J \tag{5.1}$$

where $(2S + 1)$ is the multiplicity and L is the term. The quantum number S is a total spin and is always an integer. J is the total angular momentum, which is either an integer or a half-integer. L is the total orbital angular momentum, which is assigned a letter (S, P, D, F, G, H, I, K, L, M, N, etc.) that corresponds to an integer (0, 1, 2, 3, 4, 5, 6, 7, 8, 9, 10, etc.).

Because L, S, and J are all quantized vectors, they can have more than one orientation in space. In addition, the z-components of these vectors are also quantized. This has several implications. First, a single L term consists of $(2L + 1)$ states. Due to spin–orbit interactions, these states do not necessarily have the same energy. Second, for any value of S, there are $(2S + 1)$ states. For instance, two electrons with the same spin can be in three different states (with three different orientations), whereas two electrons with opposite spins have only one possible state.

Finally, each value of J represents $(2J + 1)$ separate states. Normally, because there is no preferred direction for atoms, the energies of each of the $(2J + 1)$ states are equivalent. However, this degeneracy can be split by giving the atom a preferred direction, such as with an electric field (Stark effect) or magnetic field (Zeeman effect). For manifolds that demonstrate half-integer values of J, the corresponding state is at least doubly degenerated; that is, there are at most $J + 1/2$ energetically distinct levels. The total number of degeneracy with regard to total angular momentum is determined by the following expression:

$$L - S < J < L + S \tag{5.2}$$

Any further degeneracy is dictated by particular symmetry of the host material.

V. Ter-Mikirtychev, *Fundamentals of Fiber Lasers and Fiber Amplifiers*,
Springer Series in Optical Sciences 181, DOI: 10.1007/978-3-319-02338-0_5,

Note that when a shell is filled, the electrons occupy all possible orientations; therefore, the net L and S of the shell is zero. Thus, only unfilled shells contribute to the L and S of an atom. Similarly, from symmetry, a shell with all the orbitals filled except one looks and acts the same as a shell with only one electron, and shells that are missing two electrons are equivalent to shells that contain two electrons. For example, the upper laser level of the Nd^{3+} ion, ^4F_J ($S = 3/2$; $L = 3$; $J = 3/2$ or 5/2), consists of four states and two energetically distinct levels. The lower laser levels of Nd^{3+}, ^4I_J ($S = 3/2$; $L = 6$; $J = 9/2$, 11/2, 13/2, or 15/2), has four levels.

5.2 Energy Levels of Trivalent Rare Earth Ions

Rare-earth-doped glasses are currently the most promising and widely used active media of fiber lasers. Figure 5.1 shows the energy level positions of the individual rare earth ions. With a reasonable degree of accuracy, the level positions in Fig. 5.1 reflect observed absorption and emission spectra of rare earth ions in different laser glasses.

This section presents the main spectroscopic characteristics of the most widely used RE ions in gain fibers.

In glasses, which are the gain media of fiber lasers, RE^{3+} ions possess spectroscopic parameters that are very similar to crystals. However, they demonstrate some principal differences associated with the glass nature of the environment where the ion is located. Also, like in most crystals, positions of the RE^{3+} ions energy levels do not vary drastically from glass to glass, which is due to screening of the ion by 5s and 5p electron shells. That said, the similarity in energy level positions does not necessarily mean there is similarity in most spectroscopic parameters of the same rare earth ion in different glasses.

Unlike crystals, glass is a disordered material that demonstrates an inhomogenously broadened structure of the spectral lines; therefore, it shows broad absorption and emission spectra of individual absorption and emission transitions. The following sections review the major spectroscopic parameters of the most used RE ions in the design and development of modern fiber lasers. Different glass hosts are intentionally reviewed when describing different rare earth ions for two reasons. First, it would be impossible within the introductory scope of this book to review all reported laser glass materials where fiber laser action has been observed. In addition, not only does the description cover a particular type of laser glass, but it gives examples of the different host materials that have been used for fiber laser gain media. This is intended to give the reader an impression of existing diversity, as well as the similarity of the reviewed spectroscopic parameters in different laser glasses.

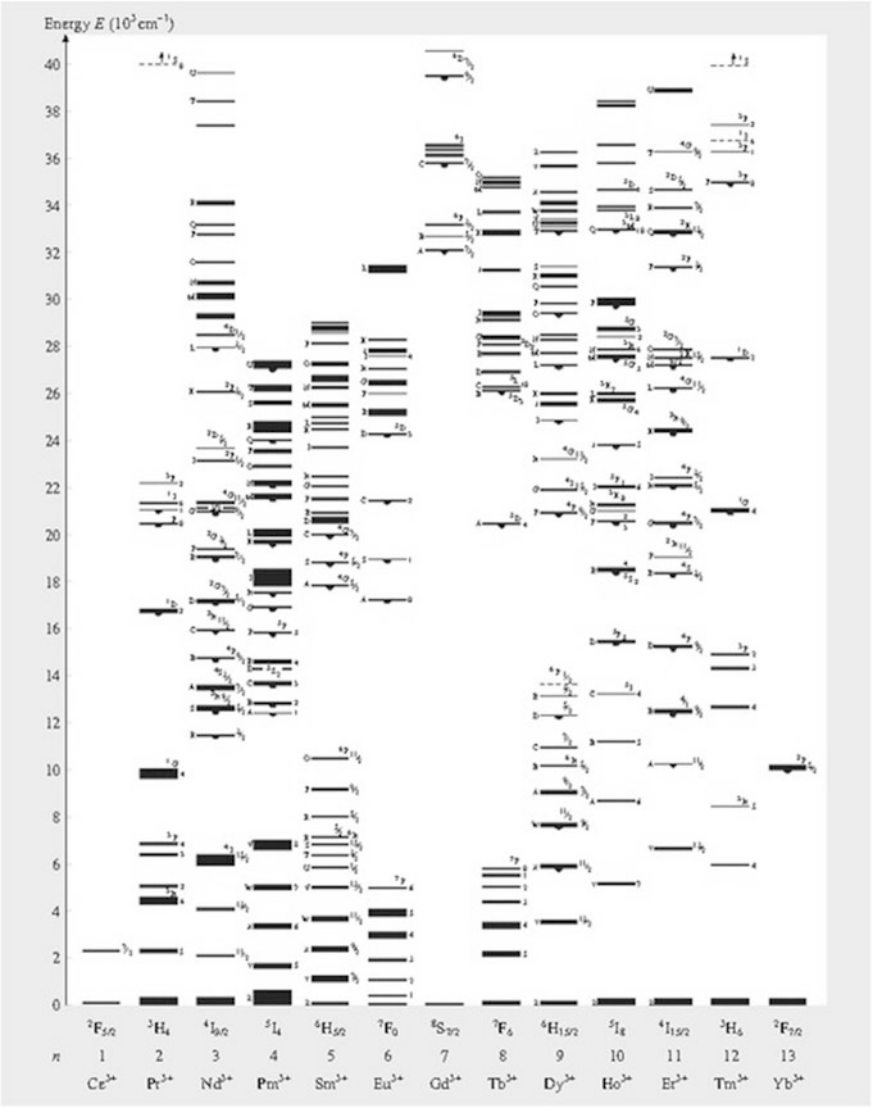

Fig. 5.1 Energy level diagrams of rare earth $(RE)^{3+}$ level diagrams of trivalent rare earth ions of RE^{3+} in $LaCl_3$ [1] (Image courtesy of Springer)

5.3 Neodymium

Since the invention of lasers and the first demonstration of fiber laser action, Nd^{3+} attracted the very close attention of researchers and engineers. Both in crystals and glasses, the Nd^{3+} ion has been the focus of many scientific publications, mostly

because of Nd:YAG lasers, which became the main solid-state laser used for many industrial and scientific applications. Being a major active medium during the era of nuclear fusion, the scientific study of Nd^{3+} in glasses is enormous. Taking into account the similarity in energy-level positions of Nd^{3+} in different glass matrices, this section presents the spectroscopic information for Nd^{3+} in one of the most developed, most studied, and most widely used glass active media: phosphate glass. An energy-level diagram of the most important laser transitions for this ion is shown in Fig. 5.2.

In Fig. 5.3, the absorption spectra of the Nd^{3+} ion in phosphate glass are shown. Strong absorption bands are shown at 583, 750, 802 and 873 nm, which correspond to the following transitions between Nd^{3+} energy levels:

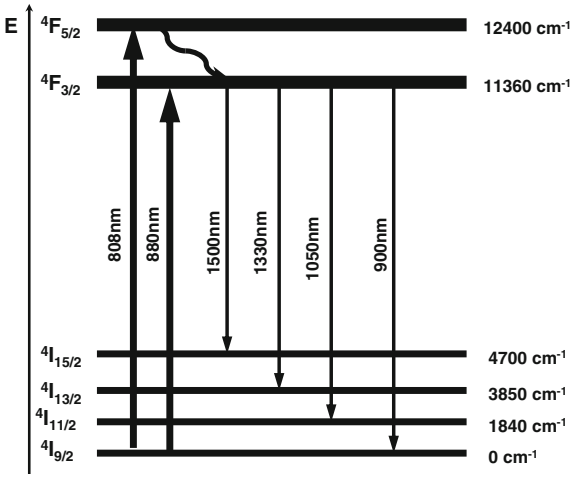

Fig. 5.2 Energy-level diagram of the most important laser transitions of Nd^{3+}

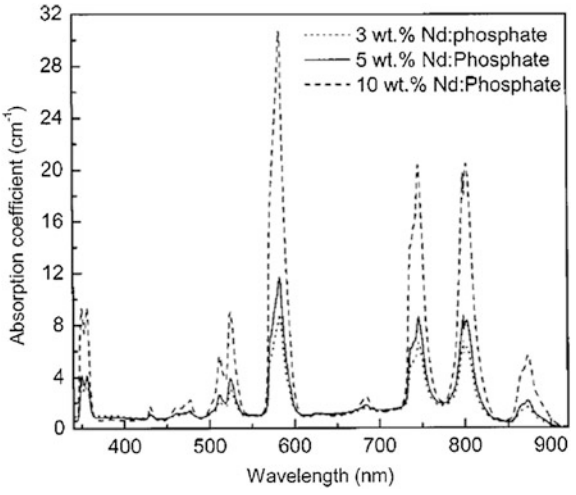

Fig. 5.3 Absorption spectrum of Nd^{3+} in phosphate glasses at room temperature [2] (Image courtesy of the Optical Society of America)

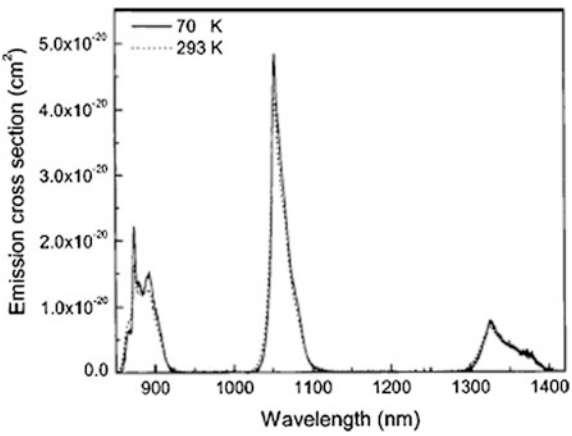

Fig. 5.4 Stimulated emission cross-section of 3 % doped Nd-phosphate glass [2] (Image courtesy of Optical Society of America)

$^4I_{9/2} \rightarrow {}^2G_{7/2}, {}^4G_{5/2}$; $^4I_{9/2} \rightarrow {}^4S_{3/2}, {}^4F_{7/2}$; $^4I_{9/2} \rightarrow {}^2H_{9/2}, {}^4F_{5/2}$ and $^4I_{9/2} \rightarrow {}^4F_{3/2}$, respectively (see Fig. 5.3) [2]. Absorption transitions at ~802 nm (as in crystals) are the most widely used for pumping of the Nd^{3+}-doped fiber laser because of the matured and widely available AlGaAs laser diodes in the 805 and 810 nm spectral range.

Figure 5.4 shows the stimulated emission spectrum of the Nd^{3+} ion in phosphate glass. The strongest emission peaks are located at 900, 1,053, and 1,330 nm, which correspond to the following transitions between Nd^{3+} energy levels: $^4F_{3/2} \rightarrow {}^4I_{9/2}$; $^4F_{3/2} \rightarrow {}^4I_{11/2}$ and $^4F_{3/2} \rightarrow {}^4I_{13/2}$, respectively (see Fig. 5.1). At 300 K, the measured and radiative lifetimes of the Nd^{3+} ion in phosphate glass doped with less than 3 wt % are 300 and 330 μs, respectively. The stimulated emission cross-section was calculated using the Fuchtbauer-Ladenburg formula (see Chap. 2), giving the following values for 900, 1,053, and 1,330 nm emission lines at 300 K: 1.5×10^{-20}, 5×10^{-20}, and 0.75×10^{-20} cm^2, respectively. Luminescence of Nd^{3+} ions starts quenching seriously in this glass at an Nd^{3+} doping level exceeding 5 wt % (5.36×10^{20} ions/cm^3). The stimulated emission cross section is almost independent of Nd^{3+} concentration and has the following temperature dependence [2]:

$$\sigma_{32}(T) = \sigma_{32}(T_0) \times \exp[b \times (T_0 - T)] \tag{5.3}$$

where T_0 is the temperature at which the stimulated emission cross-section is known. $\sigma_{32}(T_0)$, the stimulated cross-section (between laser upper level 3 and lower level 2), is measured or known, $b = 4.3 \times 10^{-4}$ K^{-1}.

For completeness of representation and for comparison, it is useful to provide here absorption and emission spectra of Nd^{3+}-doped silicate glass, which is widely used in gain fibers. Figures 5.5 and 5.6 show the room temperature absorption and emission spectra of the Nd-doped silicate glass [3].

As shown in Figs. 5.5 and 5.6, Nd-doped silica glass (similarly to other Nd-doped glasses) demonstrates absorption bands at 590, 750, 805, and 890 nm. The

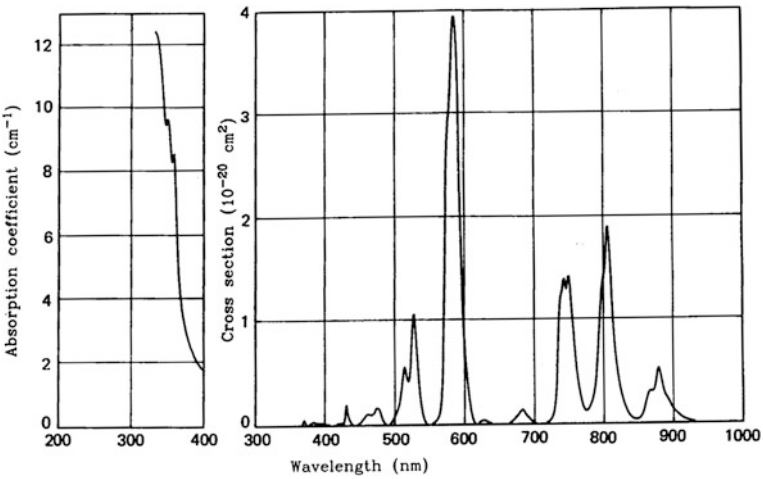

Fig. 5.5 Room temperature absorption spectrum of Nd-doped silicate glass [3]

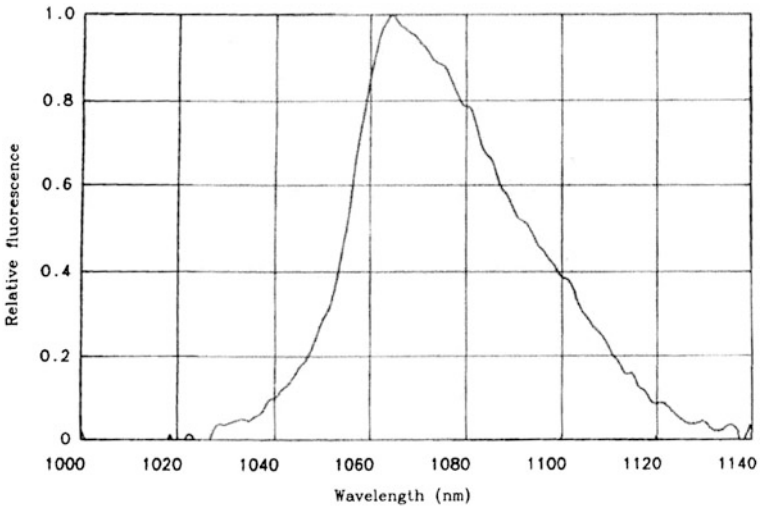

Fig. 5.6 Room temperature fluorescence spectrum of the Nd-doped silicate glass on the $^4F_{3/2} \rightarrow {}^4I_{11/2}$ transition [3]

absorption bands most used for diode pumped laser applications are 805 and 890 nm. Fluorescence spectra demonstrate the strongest lines at 950, 1,065, and 1,320 nm. Figure 5.6 shows the most widely used emission line near 1,065 nm, which corresponds to the $^4F_{3/2} \rightarrow {}^4I_{11/2}$ optical transition of Nd^{3+}. Table 5.1 shows the Judd-Ofelt parameters of the Nd^{3+} ion in different glasses.

Table 5.1 Judd-Ofelt parameters for Nd^{3+} in different glass hosts

Glass matrix	$\Omega_2 \times 10^{-20}\,cm^2$	$\Omega_4 \times 10^{-20}\,cm^2$	$\Omega_6 \times 10^{-20}\,cm^2$	Source
Silicate ($Li_2O - 2SiO_2$)	3.4	4.5	4.6	[4]
Phosphate ($Na_2O - MgO - 2P_2O_5$)	3.5	3.6	5.0	[5]
Borate ($Na_2O - MgO - 2Ba_2O_5$)	5.9	6.1	7.5	[5]
Tellurite (composition is not available from the source)	4.2	3.1	3.5	[5]

5.3.1 Nd^{3+} Fiber Laser Challenges

Similar to the situation in Nd^{3+}-doped laser crystals, one of the most important and challenging tasks in Nd-doped glasses (and therefore, in fiber lasers and amplifiers) is to achieve high-power laser or amplifier oscillation of the $^4F_{3/2} \rightarrow {}^4I_{9/2}$ transition (900–950 nm). Such importance is dictated by the possibility to achieve blue laser operation if the fundamental frequency of such oscillator can be doubled as a result of nonlinear frequency conversion. The main challenge comes from the three-energy level nature of the $^4F_{3/2} \rightarrow {}^4I_{9/2}$ transition (Fig. 5.7) and its competition with the four-energy level $^4F_{3/2} \rightarrow {}^4I_{11/2}$ (1,050–1,150 nm) and $^4F_{3/2} \rightarrow {}^4I_{13/2}$ (1,330 nm) transitions. Another challenge is related to the desired best branching ratio into the $^4F_{3/2} \rightarrow {}^4I_{9/2}$ transition—usually the ones with low solubility of Nd^{3+} (e.g., pure fused silica). Therefore, a low concentration of Nd^{3+} is an expense for desired spectroscopic parameters. However, this is partly compensated for by the naturally long length of the gain fibers in fiber lasers and amplifiers, which may require hundreds of meters in the case of cladding pumped Nd^{3+} lasers.

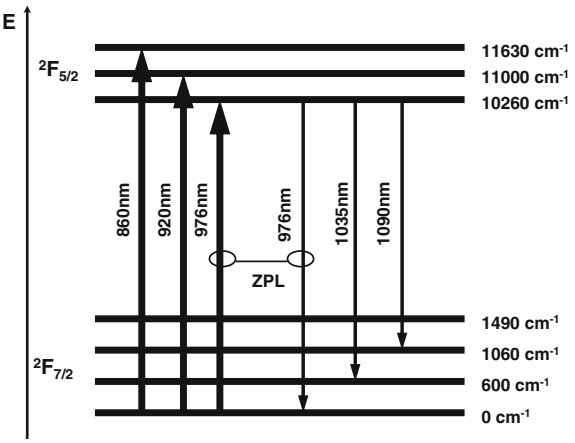

Fig. 5.7 Energy level diagram of the most important laser transitions of Yb^{3+}

5.4 Ytterbium

As a laser-active ion in solids, such as crystals and glasses, Yb^{3+} can offer several advantages compared with traditional Nd^{3+} ions. These advantages include a longer upper-state lifetime, a small quantum defect (which results in lower thermal load per unit of pump power), and absence of the excited state absorption and upconversion losses because of a simple energy-level diagram (see Fig. 5.4). Yb^{3+}-doped laser-active glasses have strong and wide absorption bands near 915 and 976 nm and are suitable for diode pumping by the robust InGaAs laser diodes. In addition, Yb^{3+}-doped laser glasses have broad and sufficiently intense emission bands in the spectral range between 950 and 1,200 nm, with a zero-phonon line at 976 nm. Room-temperature excited state lifetime is $\sim$1 ms. Due to broad emission lines, Yb^{3+}-doped laser glasses (in particular, fiber lasers) demonstrate tunable laser action in a wide spectral range, from 980 to >1,150 nm.

The energy-level diagram of the Yb^{3+} ion has two manifolds: the ground $^2F_{7/2}$ state and the excited $^2F_{5/2}$ state. An energy-level diagram of the most important laser transitions of this ion is shown in Fig. 5.7. Absorption and emission spectra of the Yb^{3+}-doped silica glass are shown in Fig. 5.8.

There are two main absorption peaks of Yb^{3+} in glass at 915 and 976 nm, which correspond to the transition from the lowest Stark sublevel of the ground $^2F_{7/2}$ state to the second and the first (the lowest) Stark sublevels of the $^2F_{5/2}$ manifold, respectively (see Fig. 5.8) [6–8]. It can be seen that Yb^{3+}-doped glass laser is a quasi-three-level laser at room temperature.

Table 5.2 summarizes experimentally measured oscillator strengths of Yb^{3+} in three of the most commonly used glass matrices, increasing in the order of silicate to germanate to phosphate. Robinson and Fournier [9] determined the oscillator strengths of Yb^{3+} ions in several glasses from room-temperature absorption spectra. They found that Yb^{3+} spectra (except for the line width) are almost identical, including relative intensities of the bands. The authors therefore

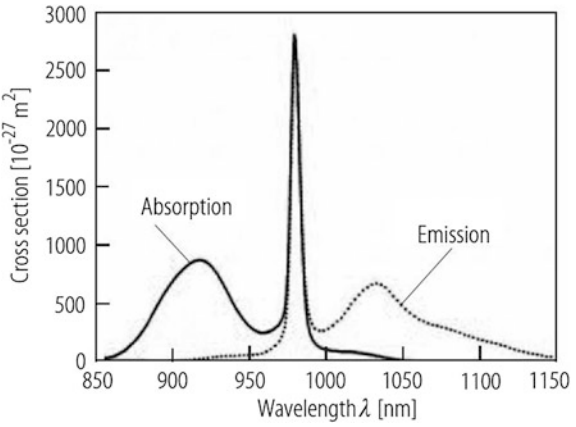

Fig. 5.8 Absorption and luminescence spectra of Yb^{3+}-doped glass [6–8] (Image courtesy of Springer)

Table 5.2 Experimentally determined values of oscillator strength of Yb^{3+} in glass

Glass matrix	$f(Yb^{3+}) \times 10^{-6}$	Source
Silicate	1.82	[9]
Germanate	2.83	[9]
Phosphate	3.66	[9]

concluded that Yb^{3+} ions reside in similar sites in these three glass types (i.e., silicate, germinate, and phosphate).

5.4.1 Yb^{3+} Fiber Laser Challenges

All challenges existing in the field of Yb^{3+}-doped fiber lasers and amplifiers can be divided into two main categories: (1) challenges associated with obtaining efficient lasing at a certain wavelengths at the associated spectroscopic transitions of the lasing optical center and (2) challenges related to operation of Yb^{3+}-doped fibers at high power levels as well as high-power density pumping conditions.

With regard to obtaining a certain wavelength of operation at challenging wavelengths, a good example is lasing in the 980 nm spectral range (i.e., where the pumping scheme is quasi-three level) or extension of the laser operation range to more than 1,100 nm, where the gain is much lower than in the maximum of the gain band. Scaling power in both the 980 and >1,100 nm spectral ranges requires pump wavelength and gain fiber length optimization. Both directions have been studied by researchers, and there has been progress in scaling power as well as achieving unique spectral range of the laser.

Challenges related to the operation of Yb^{3+}-doped fibers at high power levels and high-power density pumping conditions are mostly associated with so-called photodarkening of Yb^{3+}-doped silica fibers, which has been attributed to the formation of color centers in the rare-earth-doped glass [10].

Photodarkening appears as a temporal increase in broadband absorption with a maximum in the visible range of the fiber absorption spectrum. The manifestation of the photodarkening process varies depending on the fiber manufacturing process. The absorption band of the centers created as a result of photodarkening tails to $\sim$1,000 nm spectral region and often affects the gain fiber efficiency. Mechanisms of these photodarkening processes are yet to be fully understood and is complicated by the huge variety of laser operation regimes and conditions. However, good progress has been achieved in characterizing photodarkening in different types of fibers and pumping conditions, which in turn may eventually give more light to the understanding of the RE-doped fibers photodarkening process.

Koponen et al. [11] found that formation of color centers in the fibers undergoing photodarkening fit into to either a simple biexponential kinetic function or a stretched exponential fit. Figure 5.9 shows a normalized photodarkening rate as a function of the level of inversion population. The authors observed that the

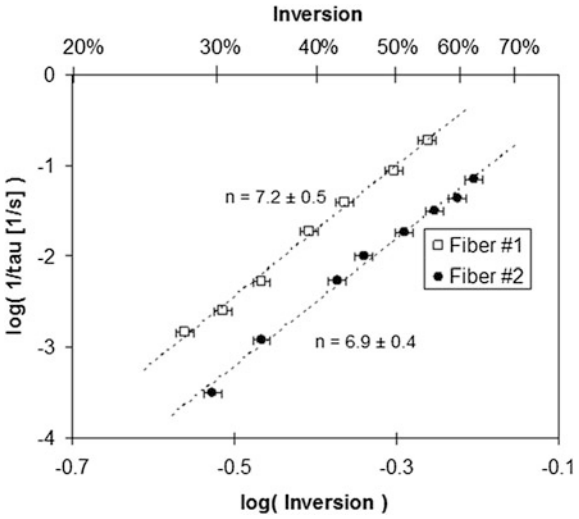

Fig. 5.9 Measured photodarkening rate constant as a function of inversion. The *slope* of the log/log plot indicates a seventh-order power dependence [11] (Image courtesy of SPIE)

photodarkening rate follows a seventh-order power dependency on the level of inversion, as shown in Fig. 5.9. From studying two fibers with different levels of Yb^{3+} doping, the authors made preliminary conclusions on the photodarkening process that takes place in the gain fiber. In particularly, it was suggested that the discovered inversion dependence of the photodarkening process may be an indication of a single mechanism (color-center formation) [11]. Seventh-order dependence on population inversion may have significant influence on the fiber laser operation. A pulse fiber amplifier may photodarken up to 105–107 times faster than even high-power CW fiber laser, where the level of inversion may be significantly lower compared with a pulse regime [11]. Figures 5.9 and 5.10 demonstrate the relative photodarkening rate versus level of inversion for different operational regimes of gain fiber operation.

Companies such as nLight (Liekki) and Nufern (East Granby, CT) achieved certain success in developing highly photostable and highly Yb^{3+}-doped fibers, which are commercially available.

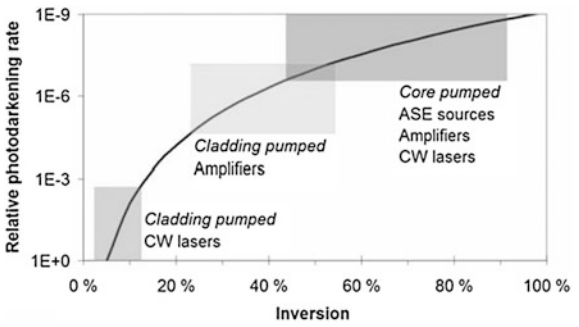

Fig. 5.10 Normalized photodarkening rate as a function of inversion, assuming a seventh-order power dependency. Device application regions with different inversion levels are highlighted [11] (Image courtesy of SPIE)

5.5 Erbium

Er-doped fiber amplifiers and lasers are probably the most extensively studied because of their importance in optical communication. Demand for 1.5 μm in-fiber laser sources and amplifiers for optical signal transmission triggered an enormous number of research papers and successful commercial development. Several laser glasses have been developed as host materials for the Er^{3+} fiber lasers. Like other trivalent rare earth ions, the spectroscopic properties of Er^{3+} in glass vary slightly from one glass host to another. An energy-level diagram of the most important laser transitions of this ion is shown in Fig. 5.11.

Because RE^{3+} ions have similar spectroscopic properties within different glass hosts, consider the main spectroscopic properties of Er^{3+} in a metaphosphate glass host as an example [12]. Metaphosphate glass is a variation of phosphate glass. Er^{3+}-doped metaphosphate glass was prepared with the following composition: mol. % of $(59 - x/2)P_2O_5$–$17K_2O$–$(15 - x/2)BaO$–$9Al_2O_3$–xEr_2O_3, where $x = 0.01, 0.1, 1.0, 2.0$, and 3.0 [12] (abbreviated glass notation is PKBAEr). We note here that phosphate glasses are regarded as better hosts for Er^{3+} ions compared to silicate glasses due to their higher phonon energy, more solubility of RE ions (which allows the creation of highly concentrated fibers with short gain length), and smaller upconversion coefficient of the $^4I_{13/2}$ level [13]. In particular, this is very important for Er^{3+}-only doped gain fibers [14], in which high Er^{3+} concentration along with a low upconversion rate are desired.

Figure 5.12 shows the absorption spectrum of Er^{3+}-doped metaphosphate glass, which is typical for all Er^{3+}-doped glasses [12]. The spectrum demonstrates number of absorption lines spanning from 350 to 1,600 nm, which correspond to the transition from ground energy level $^4I_{15/2}$ to the upper levels of the Er^{3+} energy-level diagram. For fiber laser and fiber amplifiers applications, the most important absorption bands are those located in the vicinity of 980 and 1,530 nm

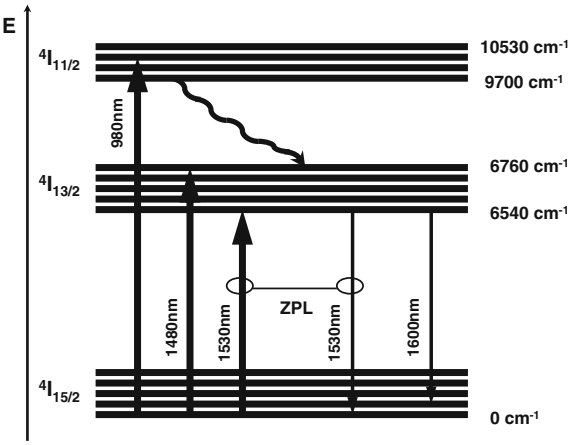

Fig. 5.11 Energy level diagram of the most important laser transitions of Er^{3+}

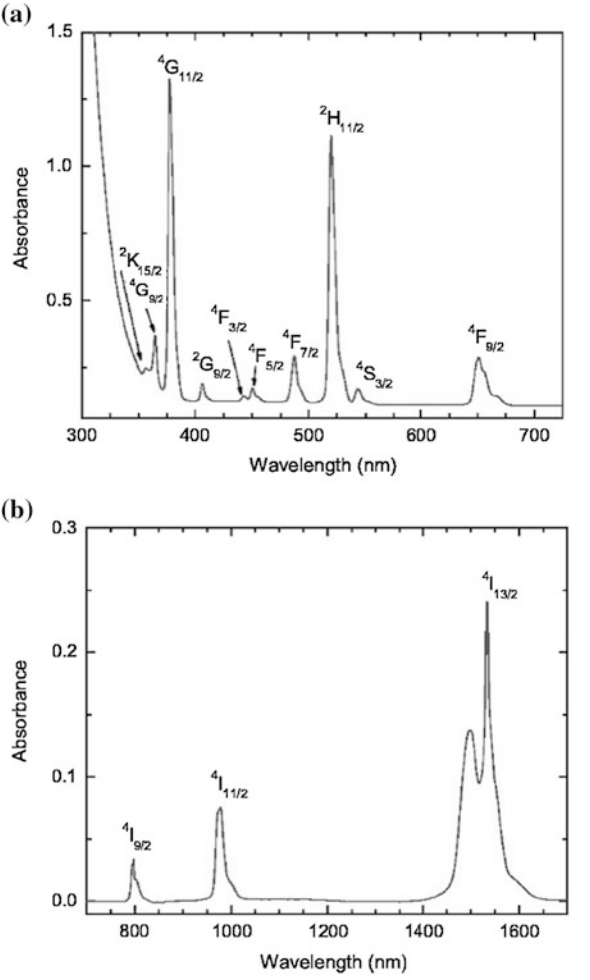

Fig. 5.12 Absorption spectra (measured in arbitrary units) of 1 mol % Er^{3+}-doped PKBAEr glass in the ultraviolet–visible (**a**) and near-infrared (**b**) spectral ranges. The band assignments over individual peaks are transitions from the ground state $^4I_{15/2}$ [12] (Image courtesy of the Optical Society of America)

spectral positions. Optical pumping into these absorption bands has been studied widely, especially using a core pumping approach, which is often used for telecommunication applications.

Figure 5.13 shows the absorption and luminescence spectra and cross-sections measured at room temperature in the 1.5 μm spectral range. Although the figure is given for Er^{3+} in metaphosphate glass, it is typical for Er^{3+} in a glass host. The strong line in the vicinity of 1530 nm is a zero-phonon line of the $^4I_{13/2} \rightarrow {}^4I_{15/2}$ transition. Luminescence is broad spanning, from 1,450 to 1,650 nm. Room-temperature decay of Er^{3+} in fiber in the 1.55 μm spectral range (i.e., on the $^4I_{13/2} \rightarrow {}^4I_{15/2}$ transition) is approximately 10 ms and varies little with glass matrix for the level of Er^{3+} doping that corresponds to the absence of luminescence concentration quenching. For comparison, Fig. 5.14 demonstrates absorption and

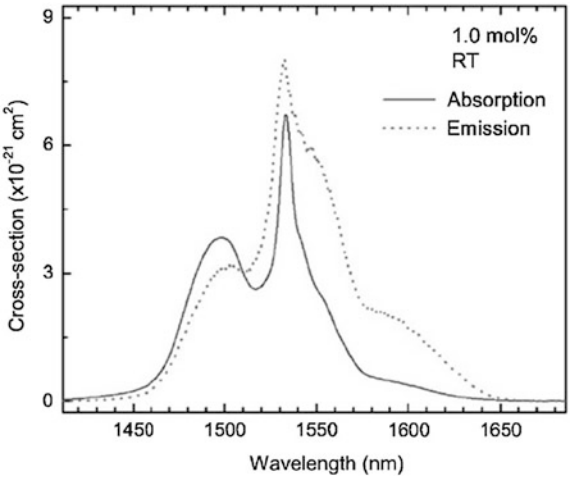

Fig. 5.13 Absorption and emission cross-sections of the $^4I_{15/2} \rightarrow {}^4I_{13/2}$ and $^4I_{13/2} \rightarrow {}^4I_{15/2}$ transitions, respectively, in the 1 mol. % Er^{3+}-doped PKBAEr glass at 300 K [12] (Image courtesy of the Optical Society of America)

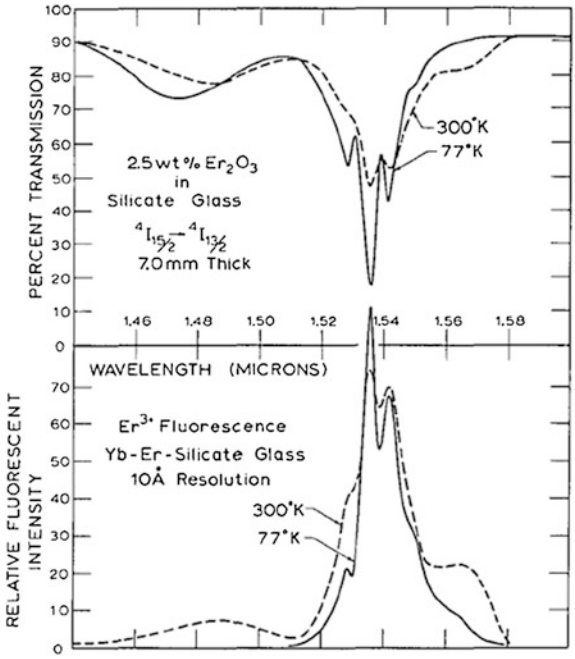

Fig. 5.14 Absorption and emission spectra of Er^{3+} in silicate glass [15] (Image courtesy of the Optical Society of America)

emission spectra of the Er^{3+} ion in silicate glass [15], which is one of the most widely used gain fiber materials.

In the field of Er^{3+} fiber laser research, the first stage lasted until the late 1980s, when so-called double-clad fibers were introduced. These fibers made it possible to use low-brightness, low-cost, and high-power laser diodes as a pumping source for Er^{3+} fiber lasers and amplifiers. Clad pumping technology allows significant

scaling of the power of Er^{3+} fiber lasers, with currently demonstrated hundreds of Watts of coherent emission in the 1.5–1.6 μm spectral range.

The introduction of clad pumping technology, especially for Er^{3+} fibers, was inspired mainly for two reasons. The first reason is related to a limited power of high-brightness diode lasers (including single-mode fiber-coupled diodes), which are used for optical pumping of laser-active ions doped into the single-mode core of the fiber. Efficient pump coupling due to the very small cross-section of the single-mode fibers requires single transverse-mode pump diode lasers. The output power of the single-emitter, single-mode diode lasers, which are used for optical pumping of Er^{3+} in fibers, are about several hundred milliWatts. Therefore, core pumping technology basically is limited to Watt-level fiber lasers (when multiple single-mode diode lasers are spectrally or polarization combined into one pumping beam or fiber pump port).

The desire to use low-brightness and low-cost multimode diode lasers for fiber laser pumping into the undoped cladding surrounding the doped core requires a high laser-active ion concentration because of the low effective absorption cross-section in clad pumping geometry. In most Er^{3+}-doped fibers that are suitable efficient lasing hosts, the concentration of Er^{3+} is low and the absorption of clad-propagating pump power requires hundreds of meters of fiber for effective pump absorption along the fiber length. Co-doping of Er^{3+} with a higher concentration of Yb^{3+} (usually more than 10 times higher than that of Er) is an effective solution to the problem. Overlapping of the Yb^{3+} and Er^{3+} absorption bands and efficient energy transfer of the absorbed in Yb^{3+} pumping radiation to the excited states of the Er^{3+} energy levels produces efficient cladding pump absorption as well as optical excitation of Er^{3+} laser-active centers. Also, because of the possibility to use shorter fibers with clad pump geometry, narrow line-width Er^{3+} fiber lasers and amplifiers became possible with scaled powers due to the reduced threshold of stimulated nonlinear scattering processes appearing in long gain fibers.

In Yb^{3+}–Er^{3+} fiber laser systems, optical pumping is taking place into the 980 nm absorption band of Yb^{3+}, with subsequent energy transfer from Yb^{3} to Er^{3+} and stimulated emission of Er^{3+} in the 1,520–1,650 nm spectral range. Therefore, using robust and high-power free space or fiber-coupled 915 or 980 nm laser diodes gives a path to significant power scaling of Er^{3+} fiber lasers and amplifiers. Typical values of optical efficiencies achieved in Yb^{3+}–Er^{3+} fiber laser systems are 30–35 %, which is as much as two times lower as that of Yb^{3+} fiber laser systems.

5.5.1 Er^{3+} Fiber Laser Challenges

There are several technical challenges in Er^{3+} fiber laser development. This section discusses what is probably the most important challenge—the low laser efficiency of the optical pumping process. Approximately 60–70 % of the coupled pump radiation has to dissipate in the form of heat. Therefore, high-power Yb^{3+}–Er^{3+}

fiber laser systems require special attention to heat management. Such a low pump-to-lasing conversion efficiency has challenged researchers to use long wavelength pumping schemes, especially those that fall into the resonant absorption band of the Er^{3+} energy level system near 1530 nm. This approach employs usage of 1,460–1,500 nm laser diodes. However, quasi-three energy level laser operation requires fulfillment of certain reabsorption bleaching conditions (i.e., a significant reduction of optical absorption); therefore, it is not trivial, especially when low-brightness diode lasers are used in clad pumping geometry. On the other hand, much higher laser efficiencies have been demonstrated, especially in core-pumping geometry due to the absence of the upconversion losses and small quantum defect for resonantly pumped Er^{3+} fiber lasers in the 1,460–1,530 nm spectral range.

Current laser diodes operating in the 1.5 μm spectral range are at least two times less efficient than 980 nm InGaAs laser diodes when calculating electrical-to-optical efficiency; therefore, overall electrical-to-optical fiber laser efficiency still requires improvements. However, less relaxed requirements for the heat management expected from resonantly pumped Er^{3+} fiber lasers is a definite advantage for power scaling to multihundred Watt to kilowatt laser power levels.

5.6 Thulium

Thulium-doped fiber lasers and amplifiers are among the most interesting fiber laser-based systems. They provide laser operation in the 1.47 and 1.8 μm spectral ranges and fall into the so-called eye-safe range of optical wavelengths.

As a side note, laser manufacturers have referred to lasers with operating wavelengths longer than 1,400 nm (mid to far infrared) as eye-safe. This eye-safe spectral range is of great importance due to numerous military and industrial applications. Wavelengths in this region are absorbed in anterior portions of the human eye (mainly the cornea) and therefore never reach the retina, which is located at the inward backside of the eye and acts as a photosensitive screen. This is in contrast to the eye-hazardous portion of the optical spectrum of 400–1,400 nm (visible and near infrared), where the anterior portions of the eye have high transmittance and refractive power. Irradiance levels are typically five orders of magnitude greater at the retina than at the cornea for visible and near infrared wavelengths. Although wavelengths longer than 1,400 nm do not interact with the retina, they can interact with the skin or cornea and cause a thermal injury. However, the eye-safe operation depends on the laser power level as well as the wavelength. High-power lasers, especially those working with high pulse energy (i.e., Q-switched or high average power lasers) may still damage the eye. Therefore, working with the laser in an eye-safe wavelength range requires often similar precautions as those outside eye-safe spectral range.

Like in other RE-doped fiber laser systems, the main problems during development of efficient Tm^{3+} fiber lasers and amplifiers are connected with selecting a

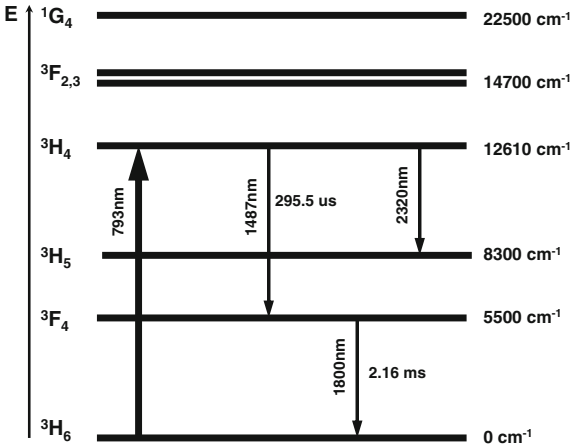

Fig. 5.15 Energy-level diagram of the most important laser transitions of Tm^{3+}

proper glass host material and Tm^{3+} ion concentration. The most efficient laser transitions in Tm^{3+} are those between the $^3H_4$ excited state and the $^3F_4$ lower level (or $^3F_4$ and $^3H_6$; see Fig. 5.15). An energy-level diagram of the most important laser transitions of this ion is shown in Fig. 5.15.

Closeness of the $^3H_5$ energy level position to the $^3H_4$ excited state level requires selection of those glass host materials that demonstrate low phonon energy to minimize nonradiative multiphonon relaxation after the excitation process. Among all glass hosts for Tm^{3+} fiber lasers, tellurite glass matrices are of great interest because they demonstrate low phonon energy (energy of the highest phonon is 780 cm^{-1}) and a high refractive index of 2.19. Without losing the general nature of the Tm^{3+} glass system review and following Ref. [16], the spectroscopic parameters of Tm^{3+} ion in tellurite glass that are important for its main laser active transitions at 1,470 and 1,800 nm wavelengths are presented here.

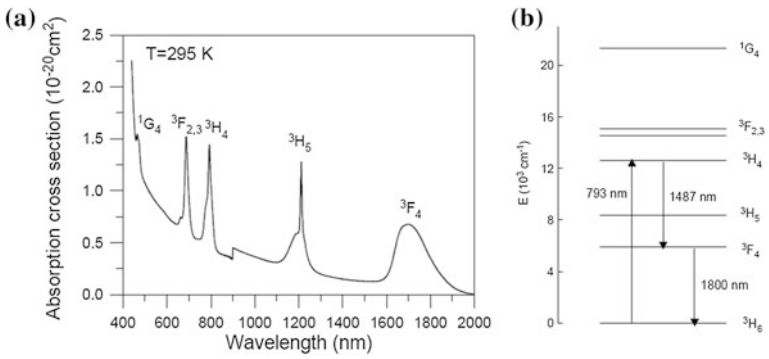

Fig. 5.16 Room-temperature absorption spectrum (**a**) and energy-level diagram (**b**) of Tm^{3+} in tellurite glass [16] (Image courtesy of the Optical Society of America)

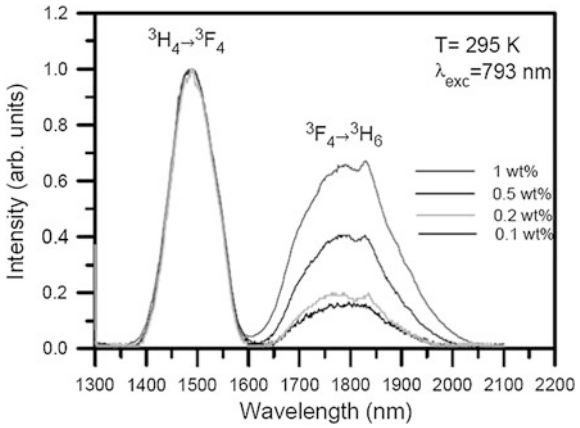

Fig. 5.17 Luminescence spectra of Tm^{3+} in tellurite glass for different dopping concentrations of Tm_2O_3 [16] (Image courtesy of the Optical Society of America)

Figure 5.16 shows an absorption spectrum and fragment of the energy-level diagram for the Tm^{3+} ion in tellurite glass. The six absorption bands (480, 675, 700, 800, 1,200, and 1,700 nm) correspond to the optical transitions from the ground $^3H_6$ level to the $^1G_4$, $^3F_2$, $^3F_3$, $^3H_4$, $^3H_5$, and $^3F_4$, upper levels, respectively.

Figure 5.17 shows a long wavelength fragment of the luminescence spectrum of Tm^{3+} in tellurite glass when excited with a 793 nm laser line at room temperature.

These spectra shows optical transitions from $^3H_4$ to $^3F_4$ (1,487 nm) and from $^3F_4$ to $^3H_6$ (1,800 nm) levels, respectively. As indicated in Ref. [16], peak positions and bandwidths of the 1,487 and 1,800 nm bands remain unchanged with Tm^{3+} concentration. Relative intensity variation of these two emission bands with changing Tm^{3+} concentration is attributed to cross-relaxation processes between these two optical transitions. Stimulated emission cross-section has been calculated and its maximum value at a 1,800 nm wavelength is 0.65×10^{-20} cm^2.

The room-temperature lifetime of Tm^{3+} ions in tellurite glass (low doping; i.e., concentration quenching free limit) measured in Ref. [16] for $^3H_4$ and $^3F_4$ energy levels are 295.5 μs and 2.16 ms, respectively.

For comparison, Fig. 5.18 shows Tm^{3+} absorption and emission spectra in other widely used glasses. Table 5.3 summarizes the Judd-Ofelt parameters as well as lifetimes of $^3F_4$ energy levels for different Tm^{3+} glasses.

5.6.1 Tm^{3+} Fiber Laser Challenges

Several challenges may determine the research and development directions of Tm^{3+}-doped fiber lasers and amplifiers. One challenge is connected with obtaining an efficient gain and laser action in the 1,487 nm spectral range, which is important in resonant pumping of Er^{3+} fiber lasers and amplifiers and also can be a good replacement of costly and more complicated Raman lasers. Another

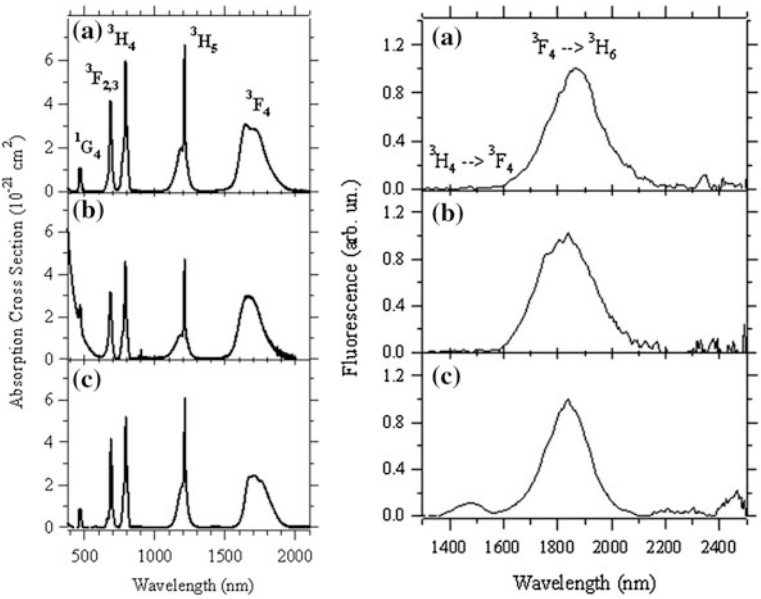

Fig. 5.18 Absorption (*left*) and fluorescence (*right*) spectra of **a** Tm^{3+}:germanate, **b** Tm^{3+}:silica, and **c** Tm^{3+}:phosphate (Reprinted with permission from [17])

Table 5.3 Results of Judd–Ofelt analysis for Tm^{3+} in four different glasses [17]

Material	Tm concentration (10^{20} ions/cm^3)	Ω_2 (10^{-20} cm^2)	Ω_4 (10^{-20} cm^2)	Ω_6 (10^{-20} cm^2)	$^3F_4$ τ_{rad} (ms)
Tm:germanate	6.24	4.4	1.2	0.9	5.3
	…	4.0	1.6	0.8	…
	2.50	…	…	…	4.97
Tm:silica	2.37	3.7	2.3	0.6	7.0
	…	6.23	1.91	1.36	4.56
	3.52	…	…	…	6.3
Tm:borophosphate	3.99	3.6	0.7	1	8.3
	…	9.8	1.9	3.4	…
Tm:fluorophosphate	…	4.12	1.47	0.72	…
Tm:phosphate	…	5.7	3.0	0.8	…
	2.35	…	…	…	5.0

Reprinted with permission from [17]

challenge is attributed to the gain and laser action in Tm^{3+} fibers under a pump wavelength of ~1,150 nm due to low quantum defect and promising values of laser efficiencies; this is an alternative to AlGaAs laser diodes operating in the 790–805 nm range, which are traditional pumping sources for Tm^{3+}-fiber lasers. A so-called two-to-one process with cross-relaxation (Fig. 5.19) has been used for power scaling of Tm^{3+}-fiber laser using clad pumping technology and 790 nm

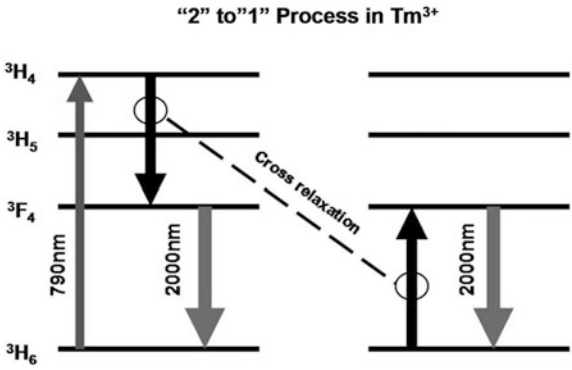

Fig. 5.19 Cross-relaxation and laser operation scheme in Tm^{3+} fiber during pumping circle with a 790 nm diode laser

high-power diode lasers; this process lead to more than 60 % of pump-to-laser efficiency, which is higher than pumping quantum efficiency for this pump wavelength [18].

Tm-fiber manufacturing technology for two-to-one process optimization has been developed by Nufern for high-power applications. However, photodarkening in the Tm^{3+} gain fiber may occur at high levels of pump power when pumping with short wavelength (790–805 nm) laser diodes. In addition, existing but less intense infrared emission near 2.3 μm in Tm^{3+} glass has been observed and laser action has been obtained [19].

Table 5.4 Spectroscopic parameters of the most widely used laser active centers in silica fibers and calculated gain saturation parameters for each ion

Laser ion and pumping scheme Q	Signal (emission) wavelength $\lambda_L \times 10^{-7}$ (cm)	Pump wavelength$\lambda_P \times 10^{-7}$ (cm)	Excited state lifetime τ (s)	Emission cross-section σ_e (cm^2)	Gain saturation parameter $I_s = \frac{hc}{\lambda_L \tau \sigma_e Q}$ (kW/cm^2)
Nd^{3+} four-energy level ($Q = 1$)	1,060	810	300×10^{-6}	5×10^{-20}	8.3
Yb^{3+} quasi-four-energy level ($Q = 1$)	1,040	976	900×10^{-6}	0.6×10^{-20}	30 [6–8]
Er^{3+} three-energy level ($Q = 2$)	1,540	1,480	0.01	0.4×10^{-20}	1.075
Tm^{3+} four-energy level ($Q = 1$)	1,900	795	250×10^{-6}	0.7×10^{-20}	39.85

Planck constant $h = 6.626 \times 10^{-34}$ J × s; speed of light in silica glass is $c_{Si} \approx c/1.5 = 2 \times 10^{10}$ cm/s

Table 5.4 summarizes important spectroscopic parameters for fiber laser development of the most widely used rare earth ions, as well as calculated gain saturation parameters for laser transitions. Note that the gain saturation parameter plays a central role in the fiber amplifier and fiber laser design.

References

1. G.H. Dieke, *Spectra and Energy Levels of Rare Earth Ions in Crystals*, 1st edn. (Wiley, New York, 1968)
2. J. Dong, M. Bass, C. Walters, Temperature-dependent stimulated-emission cross section and concentration quenching in Nd^{3+}-doped phosphate glasses. J. Opt. Soc. Am. B **21**, 454–457 (2004)
3. S.E. Stokowski, R.A. Saroyan, M.J. Weber, Nd-Doped Laser Glass Spectroscopic and Physical Properties (Technical Report) (Lawrence Livermore National Lab., Livermore, CA, USA, 2004) Nov 15, Report number: UCRL-TR-208148
4. R.R. Jacobs, M.M. Weber, IEEE J. Quantum Electron. QE-**12**, 102 (1976)
5. N.B. Brachkovskaia, A.A. Grubin, S.G. Lunter, Sov. J. Quantum Electron. **3**, 998 (1976)
6. A. Tünnermann, J. Limpert, A. Bruns, Diode-pumped fiber lasers, Chap. 4.3, Landolt-Börnstein—Group VIII Advanced Materials and Technologies, **12**, 125–139, in *Landolt-Börnstein: Numerical Data and Functional Relationships in Science and Technology*, ed. by W. Schulz (New Series, Part 12 Subseries), Advanced Materials and Technologies, vol. XV (Springer, 2008), p. 282
7. H.M. Pask et al., Ytterbium-doped silica fiber lasers: versatile sources for the 1–1.2 μm region. IEEE J. Sel. Top. Quantum Electron. **1**(1), 2–13 (1995)
8. R. Paschotta, J. Nilsson, A.C. Tropper, D.C. Hanna, Ytterbium-doped fibre amplifiers. IEEE J. Quantum Electron. **33**(7), 1049–1056 (1997)
9. ChC Robinson, J.T. Fournier, Co-ordination of Yb^{3+} in phosphate, silicate and germinate glasses. J. Phys. Chem. Solids **31**, 895–904 (1970)
10. L.B. Glebov, Linear and nonlinear photoionization of silicate glasses. Glass Sci. Technol. **75**(C2) (2002)
11. J. Koponen, M. Söderlund, H. Hoffman, D. Kliner, J. Koplow, Photodarkening measurements in LMA fibers. Proc. SPIE **6453**, 64531E.1–64531E.11 (2007)
12. P. Babu, H.J. Seo, K.H. Jang, R. Balakrishnaiah, C.K. Jayasankar, K.-S. Lim, V. Lavín, Optical spectroscopy, 1.5 μm emission, and upconversion properties of Er^{3+}-doped metaphosphate laser glasses. J. Opt. Soc. Am. B **24**, 2218–2228 (2007)
13. S. Jiang, T. Luo, B.C. Hwang, F. Smekatala, K. Seneschal, J. Lucas, N. Peyghabarian, Er^{3+}-doped phosphate glasses for fiber amplifiers with high gain per unit length. J. Non-Cryst. Solids **263–264**, 364–368 (2000)
14. M. Dubinskii, V. Ter-Mikirtychev, J. Zhang, I. Kudryashov, Yb-free, SLM EDFA: comparison of 980, 1470 and 1530 nm excitation for the core- and clad-pumping. Proc. SPIE **6952** (2008)
15. E. Snitzer, Glass lasers. Appl. Opt. **5**, 1487–1499 (1966)
16. R. Balda, J. Fernández, S. García-Revilla, J.M. Fernández Navarro, Spectroscopy and concentration quenching of the infrared emissions in Tm^{3+}-doped TeO_2-TiO_2-Nb_2O_5 glass. Opt. Express **15**, 6750–6761 (2007)
17. G. Turri, V. Sudesh, M. Richardson, M. Bass, A. Toncelli, M. Tonelli, Temperature-dependent spectroscopic properties of Tm^{3+} in germanate, silica, and phosphate glasses: a comparative study. J. Appl. Phys. **103**, 093104.1–093104.7 (2008)

18. G. Frith, B. Samson, A. Carter, D. Machewirth, J. Farroni, K. Tankala, *Power Scaling 790 nm-Pumped Tm^{3+}-Doped Devices from* 1.91 to 2.13 μm Photonics West, San Jose, 19–24 Jan 2008
19. R.G. Smart, J.N. Carter, A.C. Tropper, D.C. Hanna, CW oscillation of Tm^{3+}-doped fluorozirconate fiber lasers at around 1,470, 1,900 and 2,300 nm when pumped at 790 nm. Opt. Commun. **82**(5, 6), 563–570 (1991)

Chapter 6
Propagation of Light and Modes in Optical Fibers

Distance transfer of electromagnetic energy (i.e., energy transfer between remote points in space) in the spectral range of optical frequencies (light) can be done by propagation of an electromagnetic field in a dielectric waveguide. The main properties of this light propagation in an optical waveguide are determined by total internal reflection (TIR). TIR takes place when light that propagates in a medium with a refractive index of n_1 can be reflected from the boundary between this medium and another medium with a refractive index of n_2, which is less than n_1. The condition of TIR takes place under a certain angle (critical angle) of incidence of light. The angle of TIR is given by the following expression:

$$\sin(\Theta_{\mathrm{TIR}}) = {}^{n_2}\!/_{n_1} \tag{6.1}$$

Therefore,

$$\Theta_{\mathrm{TIR}} = \arcsin\left({}^{n_2}\!/_{n_1}\right) \tag{6.2}$$

On the other hand, the allowed distribution of electromagnetic fields across the fiber is referred to as the *modes* of the fiber. Fiber mode derivation can be determined by solving the Maxwell equation for a cylindrical waveguide. In typical silica-core, silica-clad fibers, the core refractive index is very close to that of the cladding. This condition is called a "weakly guiding approximation":

$$\Delta = \frac{(n_{\mathrm{core}} - n_{\mathrm{clad}})}{n_{\mathrm{core}}} \ll 1 \tag{6.3}$$

where $\Delta n = n_{\mathrm{core}} - n_{\mathrm{clad}}$ is the refractive index difference and Δ is the relative (or fractional) refractive index difference of the mode.

Under this condition, the modes propagating in the fiber are linearly polarized (LP) modes characterized by two subscripts, m and n. Therefore, the full notation becomes LP_{mn} (the longitudinal components of the fields are small when $\Delta \ll 1$). The LP modes are combinations of the modes found from the exact theory of the wave guide. The first subscript, *m*, gives the number of azimuthal, or angular, nodes (i.e., periodicity in the angular field distribution) in the electric field

V. Ter-Mikirtychev, *Fundamentals of Fiber Lasers and Fiber Amplifiers*,
Springer Series in Optical Sciences 181, DOI: 10.1007/978-3-319-02338-0_6,

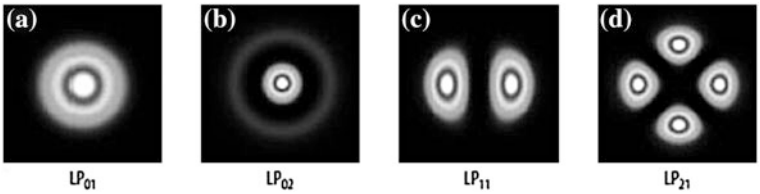

Fig. 6.1 Intensity pattern of several low-index *LP* modes in optical fiber [1] (Image courtesy of Springer)

distribution. The second subscript, n, gives the number of radial nodes (i.e., periodicity in the radial field distribution). Output field patterns are symmetric from the center of the beam and show bright regions separated by dark regions, or the nodes (the zero field point) that determine the order of numbers m and n. For example, in the case of the general waveguide, the HE_{11} mode becomes the LP_{01} mode in the weakly guiding approximation. This is the lowest order—that is, the fundamental mode of the fiber.

The fundamental LP_{01} mode intensity pattern is illustrated in Fig. 6.1. Note that the fiber fundamental mode LP_{01} creates the best beam quality condition of the light emerging from the fiber, which supports only this mode. The corresponding beam quality parameter, often called the M^2 value, is close to 1.

6.1 *V* Number of the Fiber

The V number (the normalized waveguide parameter or normalized frequency) is a very important and useful value in optical fiber theory. It defines several important fiber parameters, such as number of supported modes, mode field diameter, mode cutoff condition, and propagation constant. Theoretical definition of the V number is determined by the following expressions:

$$V = \frac{2\pi a}{\lambda}\sqrt{n_{\text{core}}^2 - n_{\text{cladding}}^2}$$

or

$$V = \frac{2\pi a}{\lambda}\text{NA} \tag{6.4}$$

Therefore, the definition of V may be restated as:

$$V = ka\text{NA} \tag{6.5}$$

where a is the radius of the fiber core, k is the wave vector, and λ is the wavelength of the core propagating light. NA is the core numerical aperture, which is determined by the following (see Fig. 6.2):

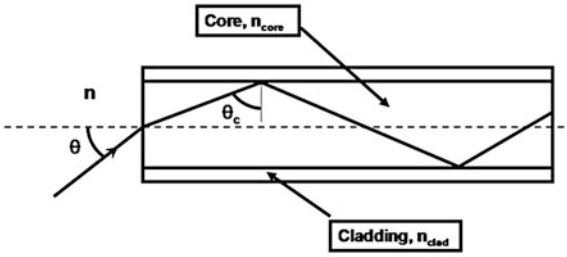

Fig. 6.2 Ray tracing in optical fiber (*schematic view*) for definition of the fiber numerical aperture (θ is the acceptance angle; θ_c is the critical angle of the TIR)

$$\mathrm{NA} = \sqrt{\left(n_{\mathrm{core}}^2 - n_{\mathrm{clad}}^2\right)} = n\sin(\theta) \tag{6.6}$$

where n stands for the refractive index of the medium from which the light is coupled into the fiber (or coupled out of the fiber) and θ is the maximum angle of incidence to couple light into the fiber (i.e., acceptance angle).

Another main fiber parameter is the normalized propagation constant b, which is defined as follows [2]:

$$b = \frac{\left(\frac{\beta^2}{k^2}\right) - n_{\mathrm{clad}}^2}{n_{\mathrm{core}}^2 - n_{\mathrm{clad}}^2} \tag{6.7}$$

where $k = 2\pi/\lambda$ and $\beta/k = \Delta$ is the effective refractive index, β is the mode propagation constant, and $0 < b < 1$. The value of k is the magnitude of the wave vector and defines number of waves per unit length. Therefore, the magnitude k is often called the *wave number*. The number of the modes the step-index fiber can support may be determined using the following expression:

$$M \approx \frac{4V^2}{\pi^2} \tag{6.8}$$

Figure 6.3 illustrates the so-called *b*–*V* diagram. If $V < 2.4048$, a fiber supports only the fundamental LP_{01} mode. Thus, one can define a cutoff wavelength, λ_c, above which only a single mode is propagating in the waveguide with certain dimensions and refractive indices. The value $b = 0$ corresponds to the cutoff condition, whereas $b = 1$ corresponds to the $\lambda = 0$ condition.

Figure 6.3 shows the number of crossings of vertical line for a given value of the V number, with each curve corresponding to an individual LP mode, which in turn gives the number of modes propagating in the fiber. When the V number is less than 2.405, only the LP_{01} mode propagates. When the V number is greater than 2.405, the next LP mode can be supported by the fiber. For example, when $V = 3$, both the LP_{01} and LP_{11} modes will propagate along the fiber (Fig. 6.3).

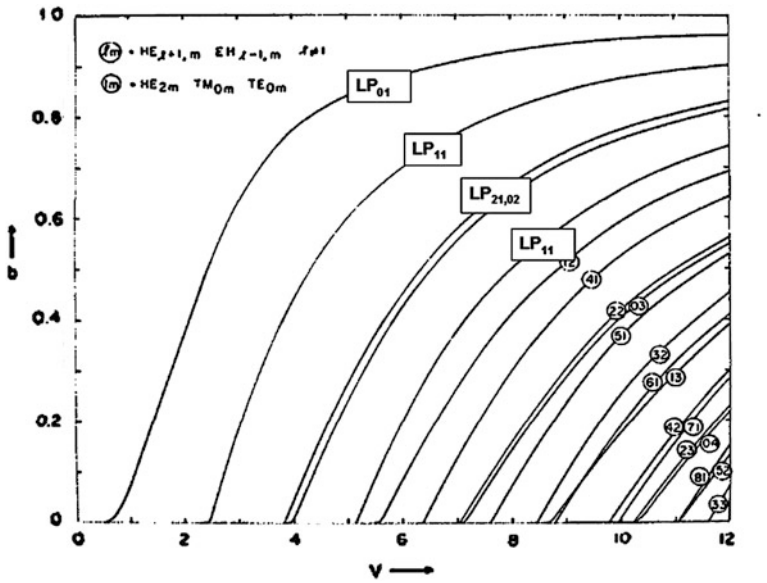

Fig. 6.3 Normalized propagation parameter $b \approx \frac{1}{2} \cdot \frac{\beta/k - n_{\text{clad}}}{n_{\text{core}} - n_{\text{clad}}}$ as a function of the normalized frequency for the case of weak guiding approximation (i.e., when $\Delta \ll 1$) [3] (Image courtesy of the Optical Society of America)

6.2 Fiber Dispersion

Dispersion in an optical fiber is the "spreading" or broadening of a light pulse during its propagation along the fiber. There are two main types of light dispersion in optical fibers: chromatic, which deals with the light spectral properties, and modal, which deals with the path (i.e., mode) of each light ray inside the fiber. The effect of the modal dispersion can be eliminated by using a single-mode fiber.

Chromatic dispersion results from a limited spectral bandwidth of the injected pulse into the fiber because different spectral components of the pulse spectrum propagate along the fiber with different speed: $v = c/n(\omega)$, which is the frequency dependence of the refractive index $n(\omega)$. Because of the light speed difference for different spectral components, the propagating pulse eventually spreads in time and the pulse become broader.

Before considering the effect of the dispersion on the propagating optical pulse, note that, in the theory of electromagnetism, the complex exponential form of the wave's electrical field can be written as follows:

$$E(z,t) = E_0 \exp(iwt) \cdot \exp(-i \cdot k \cdot z) \tag{6.9}$$

where the propagation constant (or wave vector) k is the sum of the real part and imaginary part:

$$k = \beta_{\text{ph}} + i\mu \tag{6.10}$$

where μ represents the attenuation constant and β_{ph} represents the phase constant. β_{ph} determines the change in phase per unit length along the propagation path and is equal to real part of the wave number. The phase constant is measured in units of radians per meter. Therefore:

$$k = \frac{2\pi}{\lambda} = \beta_{\text{ph}} \tag{6.11}$$

To demonstrate the effect of dispersion on the propagating pulse, consider an optical pulse with pulse width τ. Also assume that the pulse propagates in a single-mode fiber. The minimum spectral width of the pulse $\Delta\omega_{\text{min}}$ is inversely proportional to the pulse width (i.e., $1/\tau$). Then assume that the spectral width of the propagating pulse is much broader than the minimum spectral width:

$$\Delta\omega \gg \Delta\omega_{\text{min}} \tag{6.12}$$

It can be imagined that the overall spectrum of the pulse is a superposition of several individual pulses with minimum spectral width of $\Delta\omega_{\text{min}}$. Each of the individual pulses moves with group velocity:

$$V_g = \frac{\mathrm{d}\omega}{\mathrm{d}\beta_{\text{ph}}} \tag{6.13}$$

where again β_{ph} is the phase constant and group velocity V_g is a speed at which the fiber mode power propagates along the fiber. In other words, group velocity determines the speed of energy propagation.

For completeness of the discussion, consider another important parameter called phase velocity or V_{ph}, which is determined by:

$$V_{\text{ph}} = \frac{\omega}{k} = \frac{c}{n(\omega)} \tag{6.14}$$

Phase velocity determines a speed at which phase (or wave front) of the wave of certain frequency (wavelength) propagates along the fiber.

The so-called group delay [4] demonstrates the effect of the dispersion on the pulse spreading in fiber:

$$T_g = \frac{1}{V_g} \tag{6.15}$$

where T_g is the group delay time of a propagating pulse per unit length of waveguide. Due to chromatic dispersion, the group velocity depends on the frequency. Therefore:

$$d\left(\frac{1}{V_g}\right) = \left(\frac{d^2\beta_{\text{ph}}}{\mathrm{d}\omega^2}\right)\mathrm{d}\omega \tag{6.16}$$

On a scale of finite frequencies, this expression becomes:

$$\Delta\left(\frac{1}{V_g}\right) = \left(\frac{d^2\beta_{\text{ph}}}{\text{d}\omega^2}\right)\Delta\omega \tag{6.17}$$

At the fiber entrance just after injection, a pulse with spectral width $\Delta\omega$ can be considered as a pulse consisting of individual pulses with minimum duration τ. All pulses at the starting point coincide with each other and the overall pulse width has the same value of τ. When the pulse starts propagating along the fiber, individual pulses travel at different speeds and require different times t to travel distance L in the fiber. The individual pulse corresponding to given spectral component has a traveling time that can be calculated as follows:

$$t = T_g \cdot L = \frac{L}{V_g} \tag{6.18}$$

Therefore, individual pulses with different frequencies will be spread along the fiber in the following time interval:

$$\Delta t = L * \Delta\left(\frac{1}{V_g}\right) \tag{6.19}$$

In turn, Eq. 6.19 gives the value of change of the original pulse $\Delta\tau$ width over a traveling distance L:

$$\Delta t = \Delta\tau = \left(\frac{d^2\beta_{\text{ph}}}{\text{d}\omega^2}\right)\Delta\omega L = -\frac{L}{2\times\pi\times c}\left[\lambda^2\frac{d^2\beta_{\text{ph}}}{\text{d}\lambda^2} + 2\lambda\frac{\text{d}\beta_{\text{ph}}}{\text{d}\lambda}\right]\Delta\omega \tag{6.20}$$

Value $\left(d^2\beta_{\text{ph}}/\text{d}\lambda^2\right)$ is the chromatic dispersion (more accurately, $D_{\text{chrom}} = d^2\beta_{\text{ph}}/\text{d}\omega^2$), determined by the fiber material [5], whereas $\text{d}\beta_{\text{ph}}/\text{d}\lambda$ is determined by the waveguide dispersion. Waveguide dispersion is only important in single-mode fibers, where an evanescent wave of the fundamental mode propagates in the cladding. Because the refractive index in the cladding is lower than in the core, the cladding part of the mode travels faster than the part of the mode that propagates in the core. In turn, this leads to the dispersion. Waveguide dispersion depends on the waveguide structure and is a part of chromatic dispersion:

$$D_{\text{chrom}} = D_{\text{mat}} + D_{\text{wg}} \tag{6.21}$$

Material and chromatic dispersion may have different signs depending on the propagation wavelength (i.e., wavelength at which they are measured). In silica step-index fiber, material and waveguide dispersions cancel each other out and therefore lead to the minimization of chromatic dispersion near the 1,300-nm wavelength (Fig. 6.4). This fact attracts the attention of researchers in optical fiber communications to the 1,300-nm spectral range. At this range, the pulse spread caused by chromatic dispersion results in limitations on the performance of the

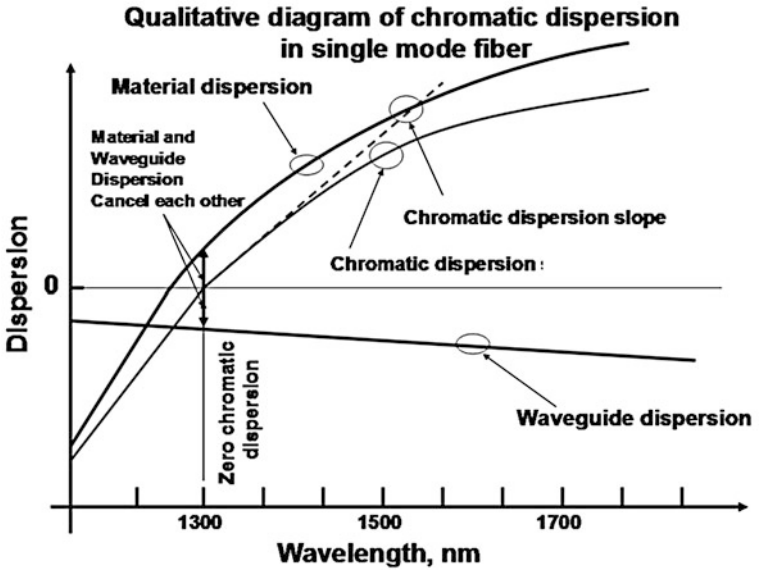

Fig. 6.4 General diagram of chromatic dispersion in a single-mode optical fiber

optical transmission line. The chromatic dispersion curve can be approximated by a straight line near the wavelength of the zero dispersion. This line is called the chromatic dispersion slope (dashed line in Fig. 6.4). However, the propagation of light with a wavelength close to 1,300 nm in silica fiber has measurable power attenuation, especially at long distances; therefore, it is called "loss limited". This attenuation in silica fiber decreases at the 1,550 nm wavelength, where chromatic dispersion rises. Nevertheless, most optical communication systems operate in the vicinity of 1,550 nm because of a developed Er^{3+}-doped fiber amplifier (its gain band covers the 1.55 μm range) and low attenuation. Therefore, operation in this spectral range is chromatic dispersion limited.

Another dispersion type that needs to be mentioned is called the *polarization mode dispersion*. This parameter is related to the fact that even an ideal single-mode fiber (i.e., the fiber that allows the propagation of only one fundamental transverse mode) actually supports two orthogonally polarized components of the same fundamental mode. Note that an ideal single-mode fiber has the ideal cylindrical symmetry and is stress free. However, such polarization degeneracy breaks in real life due to slight deviations from the fiber's ideal cylindrical shape as well as from stress introduced into the fiber in some cases, such as polarization-maintaining (PM) fibers. This deviation from the cylindrical symmetry and stress-induced anisotropy causes modal birefringence in the fiber, which in turn leads to slightly different propagation constants for two orthogonally polarized modes. This effect also results in pulse broadening in optical fibers.

6.3 Polarization-Maintaining Fibers

In PM optical fiber, the plane of propagation light polarization is maintained unchanged. This PM property of PM fiber is conditional, however. The condition requires the light polarization plane to be aligned at certain angle to the fiber stress gradient direction during coupling into the fiber. PM fibers are very important—not only in fiber laser applications, but also in optical telecommunications and instrumentation. Usually, the PM property of the fiber is achieved by inducing a certain amount of stress in the core. This can be done through either elliptical core geometry, a noncircular cladding profile, or so-called stress rods introduced into the cladding surrounding the core. Accordingly, there are four main types of PM fiber geometries commonly used in current fiber laser technology: elliptical core, elliptical cladding, Panda profile, and Bow-tie profile (see Fig. 6.5). These PM fiber structures differ in the way that stress is introduced inside the waveguide to suppress the cross-coupling of propagating power along two perpendicularly polarized fiber modes.

Among all existing PM fiber types, the most widely used are Panda geometry-based fibers [6]. This geometry provides low loss, high optical quality, and superior uniformity along the whole length of the fiber. Commercial Panda fibers have been developed in different configurations, including large core (>30–35 μm). Preservation of the circular core geometry gives the Panda-type structure an additional advantage in the case of gain fibers. Technology of introducing Panda stress rods into the cladding involves careful design, including cladding space requirements. For gain fibers, technologists usually grow non-PM core-doped fiber with a cladding diameter sufficient for introduced Panda stress rods. Later, after the laser/gain test is successful, stress rods are added during the next run into the cladding surrounding the core, creating a PM fiber structure of Panda type. The direction along the line where Panda rods and the core are located is called the slow axis; the perpendicular direction is called the fast axis.

PM fiber does not work as a polarizer (as it may seem to) but rather as a PM waveguide transmitter of optical waves. Only light coupled into the fiber along slow or fast axes will maintain its polarization plane. Launching the light into the fiber along planes other than those of slow or fast axes will not lead to the PM

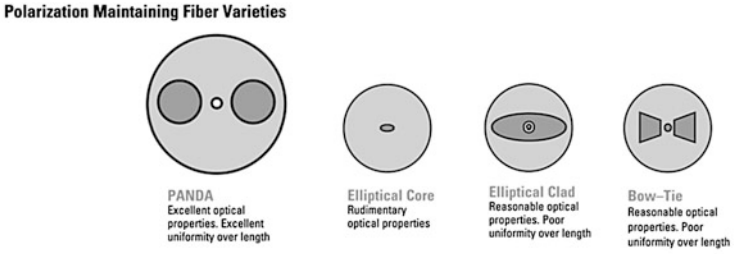

Fig. 6.5 Different types of polarization-maintaining fibers (Image courtesy of Nufern)

property of the waveguide. This is why careful angle alignment during PM fiber splicing is critical. In current PM splicing machines, the angle between the stress rods of two fibers needs to be aligned by less than 1–2°. With the recent development of photonics crystal fibers, in which cladding consists of a periodic air/solid structure, Panda-like configurations have been successfully implemented.

6.4 Laser Beam Quality (M^2 Parameter)

The beam quality is an important parameter of the laser, although it has been defined in different ways. For most laser industrial applications, it is a measure of the focusing capability of the beam. Comparing two different laser beams with the same focusing optics, the beams with better quality will allow tighter focusing. However, different kinds of aberrations or diffraction effects, existing either in focusing optics or in the laser oscillator active media, may affect the focus ability of the system as they alter the laser beam wavefront.

All laser beam quality definitions can be divided into two major categories. Historically, the first method was based on the comparison of the product of laser beam radius at the beam waist and the far-field beam divergence angle of the beam [called beam parameter products (BPP)] with that of the fundamental mode Gaussian beam. The BPP is expressed in units of mm·mrad. Another method is based on the second moment of the laser beam intensity profile. This method defines beam quality using the so-called M^2 parameter.

By definition, a Gaussian beam with diffraction limited divergence (i.e., TEM_{00} mode in open laser resonators or LP_{01} mode in circular optical fiber) has the highest beam quality. Correspondingly, high-order Gaussian modes demonstrate poor beam quality. Other beams, such as those originating from unstable resonators, may not be Gaussian in nature but may also demonstrate high beam-quality parameters. This topic, however, is beyond the scope of this book.

Introduced by Siegman [7, 8], the M^2 parameter has become a major beam-quality standard. It has been widely used since the early 1990s, both by laser researchers as well as in laser applications in industry. Following Siegman [9] (with these relationships holding in the main axes system of the beam), consider the second moment of the beam intensity profile $I(x, y)$ in the rectangular coordinates x and y, which can be expressed as follows:

$$\sigma_x^2 = 4 \cdot \frac{\iint (x - x_0)^2 I(x,y) \mathrm{d}x\mathrm{d}y}{\iint I(x,y) \mathrm{d}x\mathrm{d}y} \tag{6.22}$$

where x_0 is the center of gravity of the beam. For symmetrical beams, the gravity center usually is along the beam propagation line.

Following the expression for the variation of the Gaussian beam spot size $w(z)$ along the distance of propagation:

$$w^2(z) = w_0^2 + \left(\frac{\lambda}{\pi w_0}\right)^2 \cdot (z - z_0)^2 \tag{6.23}$$

where z_0 is the Gaussian beam waist location and w_0 is the beam waist. It can be shown that the analogous expression (i.e., the quadratic free-space propagation rule) can be written for the second moment of the intensity, which is then:

$$\sigma_x^2(z) = \sigma_{x0}^2 + \sigma_{\theta X}^2 \cdot (z - z_0)^2 \tag{6.24}$$

and

$$\sigma_{\theta X}^2 = 4 \cdot \frac{\int\int (\theta_x - \theta_{x0})^2 \cdot I_{FF}(\theta_x, \theta_y) \mathrm{d}\theta_x \mathrm{d}\theta_y}{\int\int I_{FF}(\theta_x, \theta_y) \mathrm{d}\theta_x \mathrm{d}\theta_y} \tag{6.25}$$

where σ_{x0} and σ_θ are the variance at the beam waist and the variance of the angular spread of the beam departing from the waist, respectively; z_0 is the location of the beam waist along the z axis (i.e., along the axis of propagation); $I_{FF}(\theta_x, \theta_y)$ is the far field intensity distribution and θ_x, θ_y are angular coordinates of its center of gravity. The quadratic propagation dependence is valid for any real laser beam (Gaussian or not, coherent or partially incoherent, single mode or multiple transverse mode). It is also important to note that the quadratic dependence of beam width given above is valid only for the second-moment beam width definition.

As it is known, the Gaussian beam intensity profile can be expressed as:

$$I(x) = \exp\left[-2x^2/w_x^2\right] \tag{6.26}$$

By defining $w_x \equiv 2\sigma_x$ the expression for intensity becomes:

$$I(x) = \exp\left[-x^2/2\sigma_x^2\right] \tag{6.27}$$

From the above intensity profile, Siegman defined the spot size or beam width of an arbitrary, non-Gaussian beam (i.e., beam from real life) as the following:

$$W_x \equiv 2\sigma_x \quad \text{and} \quad W_y \equiv 2\sigma_y \tag{6.28}$$

where W stands for a general beam width for arbitrary real beams. Note that for the ideal Gaussian TEM_{00} beam, the corresponding Gaussian beam parameter is w.

With above definition, the beam width W will propagate in free space following the same rule as the Gaussian spot size $w(z)$ does if one multiplies the far-field spreading of the beam by the factor M^2. Therefore, one can write for any arbitrary beam the following width propagation rule, taking into account introduced definition of the second moment width:

$$W_{x,y}^2(z) = W_{0x,0y}^2 + \left(M_{x,y}^2 \times \frac{\lambda}{\pi W_{0x,0y}}\right)^2 \left(z - z_{0x,0y}\right)^2 \tag{6.29}$$

where M_x and M_y are parameters of the arbitrary beam under consideration and

$$\theta_{x,y} = M_{x,y}^2 \frac{\lambda}{\pi W_{0x,0y}} \tag{6.30}$$

is the divergence of the arbitrary beam. One can see that $M_{x,y}^2$ shows how many times the arbitrary beam divergence is bigger than that of the fundamental mode Gaussian beam:

$$\theta_0 = \frac{\lambda}{\pi w_0} \tag{6.31}$$

Consequently, the near-field far-field product for an arbitrary beam can be written as follows:

$$W_{0x,0y} \times W_{x,y}(z) \approx M_{x,y}^2 \times \frac{z\lambda}{\pi}, \quad z \to \infty \tag{6.32}$$

As can be seen from Eq. 6.32, parameters $M_{x,y}^2$ may be interpreted as a value or a measure of the propagating beam quality. It is natural to conclude from the above expression that $M^2 \equiv 1$ characterizes a single, fundamental-mode Gaussian beam (i.e., TEM_{00} mode or, in the case of optical fiber, LP_{01} mode). It is also natural to conclude that the M^2 parameter defined above shows how many times the real beam divergence is larger than that of a diffraction-limited beam.

Despite that the M^2 approach is not ideal and does have limitations, it works quite well and is presently considered as a standard in the laser industry.

6.4.1 *Practical Recommendations on Beam Quality Measurements Using the* M^2 *Approach*

Beam quality, defined by the M^2 parameter, ranges from 1 (the case of a diffraction-limited TEM_{00} laser beam) and >1 (for the arbitrary beam with high-order or distorted modes). The National Institute for Standards and Technology and the International Standards Organization established standards [10] for laser beam quality measurements based on the M^2 parameter, which can be implemented by a set of beam diameter measurements. An interesting and detailed discussion of different aspects of the laser beam quality can be found in Ref. [11].

The previously mentioned formalism can be reduced to practical formulas to calculate the M^2 parameter through measurements. If the M^2 parameter is expressed as a ratio of the diameter-divergence product of the laser beam under consideration (arbitrary beam) to the ideal diffraction-limited (TEM_{00}) beam diameter-divergence product. It can also be given by the square of the ratio of the multimode beam diameter to the diffraction-limited beam diameter:

$$M^2 = \left(\frac{W_{0\text{meas}}\theta_{\text{meas}}}{w_0\theta_0}\right) = \left(\frac{W_{0\text{meas}}}{w_0}\right)^2 \tag{6.33}$$

where $W_{0\text{meas}}$ is the measured beam waist diameter, θ_{meas} is the measured full-angle divergence, w_0 is the calculated (i.e., theoretical) diffraction-limited Gaussian beam waist, and θ_0 is the diffraction-limited Gaussian beam divergence. Recall also the Rayleigh range of the Gaussian beam, which is defined as the distance a beam propagates from its waist to grow its diameter by a factor of $\sqrt{2}$, denoted as z_R. For the diffraction-limited Gaussian beams, the Rayleigh range is related to the beam waist as follows:

$$w_0 = \sqrt{\frac{z_R\lambda}{\pi}} \tag{6.34}$$

Therefore, by measuring the arbitrary beam's Rayleigh range, one can calculate the beam waist for so-called imbedded fundamental mode Gaussian beams. Using an expression for the M^2 parameter, where this value is defined as a square of the ratio of the multimode (i.e., unknown) beam diameter to the diffraction-limited beam diameter, one can calculate the unknown beam M^2 parameter. Figure 6.6 demonstrates an experimental setup for M^2 measurement using the Rayleigh range approach.

The following procedure can be used for M^2 parameter measurement:

1. Insert a focusing lens in the beam under consideration. Locate and measure the beam focus by moving an available charge-coupled device (CCD) camera along the beam propagating axis and estimate the smallest spot size (initially along one axis; i.e., x diameter).
2. Locate the positions of the spot size where it is twice the estimated waist (i.e., minimum) size on either side of the focus.
3. The actual focus position lies exactly halfway between these two points. Locate the position of the waist.
4. Move the CCD camera to the actual focus position and measure the focus diameter, which becomes the $W_{0\text{meas}}$ value.

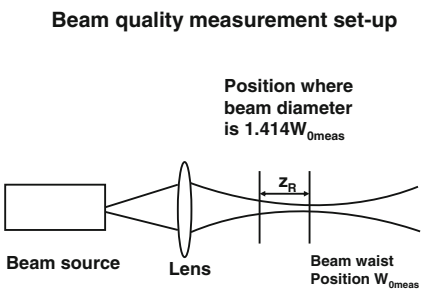

Fig. 6.6 Experimental setup for beam quality measurement

5. Measure the Rayleigh range, Z_R, by finding the place along the beam propagation axis where the spot size grows to $\sqrt{2} = 1.414$ times the focused (i.e., minimum) spot size. Do this by moving the CCD camera toward the lens until such spot size is found. The distance between the beam waist location (minimum size) and the location of the beam where the beam size is $\sqrt{2}$ larger is the Rayleigh range Z_R.
6. Using the beam waist and Rayleigh range relationship for the diffraction-limited Gaussian beam, calculate the imbedded Gaussian beam diameter, which has the same Rayleigh range as that of the beam under consideration:

$$w_0 = \sqrt{\frac{z_R \lambda}{\pi}}$$

7. Calculate M^2 parameter using the following above given formula, inserting the calculated imbedded beam waist diameter and measured diameter of the beam under consideration (focal spot size):

$$M^2 = \left(\frac{W_{0\text{meas}}}{w_0}\right)^2 \tag{6.35}$$

   This value defines the M^2 parameter along the x axis (i.e., M_x^2).

8. Repeat this procedure for the y axis and determine the M^2 parameter along the perpendicular direction (i.e., M_y^2).

For better measurement accuracy, one may consider measuring two Rayleigh ranges instead of one Rayleigh range (as is demonstrated here) and calculate the M^2 parameter from there. The typical value of M^2 for diffraction-limited or close to diffraction-limited laser beams is between 1 and 1.5. M^2 values of more than 1.5 typically point to a multimode beam.

References

1. A. Tünnermann, J. Limpert, A. Bruns, Diode-pumped fiber lasers, Chap. 4.3 in Laser Systems, Part 2, Landolt-Börnstein—Group VIII Advanced Materials and Technologies, vol. 12 (Springer, New York, 2008), pp 125–139
2. L.B. Jeunhomme, *Single mode fiber optics: principles and applications* (CRC Press, 1990), p. 339
3. D. Gloge, Weakly guiding fibers. Appl. Opt. **10**(10), 2252–2258 (1971)
4. R.B. Dyott, J.R. Stern, Group delay in fiber waveguides. Electron. Lett. **l7**, 82–84 (1971)
5. M. DiDomenico Jr, Material dispersion in optical fiber waveguides. Appl. Opt. **11**(3), 652–654 (1972)
6. K. Okamoto, T. Edahiro, N. Shibota, Polarization properties of single-polarization fibers. Opt. Lett. **7**(11), 569–571 (1982)
7. A.E. Siegman, New developments in laser resonators. Proc. SPIE **1224**, 2 (1990)

8. A.E. Siegman, Defining, measuring, and optimizing laser beam quality. Proc. SPIE **1868**, 2 (1993)
9. A.E. Siegman, How to (Maybe) measure laser beam quality, in *DPSS Lasers: Applications and Issues* (OSA TOPS vol. 17) ed. by M.W. Dowley, OSA, Washington D.C. (1998), pp. 184–199
10. Lasers and laser-related equipment—Test methods for laser beam widths, divergence angles and beam propagation ratios. ISO Standard 11146 (2005)
11. T.S. Ross, W.P. Latham, Appropriate measures and consistent standard for high energy laser beam quality. J. Directed Energy **2**(1), 22–58 (2006)

Chapter 7
Fiber Laser Physics Fundamentals

After reviewing the basics of solid-state physics and spectroscopy as related to fiber laser gain media, this chapter shifts the focus to the general aspects of laser physics—especially the branches that are very important for understanding the principles of fiber laser operation.

7.1 Population Inversion: Three- and Four-Energy Level Systems

Population inversion plays a central role in the field of laser physics because it provides a means for electromagnetic wave amplification and oscillation. To understand the phenomenon of population inversion, it is important to briefly review the basic statistics of the particles' distribution at thermal equilibrium.

As was described in Chap. 2, the number of particles at two neighboring non-degenerated energy levels in thermal equilibrium follows the Boltzmann distribution:

$$N_2 = N_1 \exp\left(-\frac{E_2 - E_1}{k_B T}\right) = N_1 \exp\left(-\frac{h \cdot v_0}{k_B T}\right) \tag{7.1}$$

where $E_2 > E_1$ (and $E_2 - E_1 = hv_0$) and v_0 is the resonant frequency of the transition between these two energy levels. Particles are able to occupy either level 1 with population N_1 or level 2 with population N_2. The total number of particles therefore is:

$$N = N_1 + N_2 \tag{7.2}$$

As already shown in Chap. 2, in thermal equilibrium the lower energy level is more populated than the higher energy level; therefore, the atomic system does not emit light and is naturally relaxed. Even at elevated temperatures, the number of atoms occupying high-energy level 2 increases, but it never exceeds population of the lower level. As can be seen from the Boltzmann distribution formula in

V. Ter-Mikirtychev, *Fundamentals of Fiber Lasers and Fiber Amplifiers*,
Springer Series in Optical Sciences 181, DOI: 10.1007/978-3-319-02338-0_7,

Eq. (7.1), levels 2 and 1 may become equally populated only at infinite temperatures. However, to achieve an optical gain through stimulated emission, one needs to achieve a non-equilibrium situation when the number of particles at the upper level is higher than that at the lower energy level. This non-equilibrium condition (or inverted population condition) has been suggested to achieve amplification of electromagnetic waves. During the early years of laser physics, atomic states with inverted populations were called states with absolute negative temperatures because, from the classic viewpoint of Boltzmann distribution, such a situation corresponds to absolute negative temperatures (which, in thermodynamic theory, is known as an unachievable condition). This consideration shows that, thermodynamically, the laser is an example of a system where optical emission occurs with a very small value of entropy [1].

Several ways have been suggested to achieve such non-equilibrium conditions (i.e., population inversion). There are two basic pumping schemes of laser operation within the concept of creation of population inversion, which in turn divide all active media into corresponding two classes (or types): the so-called four-level and three-level laser systems. Historically speaking, the three-energy-level system was the first to demonstrate laser action (Ruby laser). However, for most practical applications, the four-energy-level scheme found much wider applications in laser development and commercialization. This chapter reviews each of these laser pumping schemes in detail because they are very important for all types of lasers, especially fiber lasers and amplifiers. In these applications, energy-level diagrams and the nature of line broadening of optical transitions can often be described by intermediate situations (i.e., so-called quasi-three-level or quasi-four-level schemes, rather than purely three- or four-energy level schemes).

7.1.1 Four-Level Laser Operational Scheme

Figure 7.1 demonstrates the four-energy-level scheme of laser operation, which is ideal for most laser applications requiring the highest efficiency along with the lowest laser threshold. As one can see from Fig. 7.1, during the pumping process, atoms are excited from the ground level 1 to the excited level 2. Then, after fast nonradiative relaxation to energy level 3 (usually within sub-nanosecond to picosecond timescale), atoms decay spontaneously to level 4 and then again through nonradiative relaxation from level 4, returning to the original ground level 1. This is the full excitation circle of the four-energy-level scheme. Note that spontaneous decay from level 3 to level 4 (which is a slow process, with durations spanning from nano-seconds to milliseconds) is exactly the transition where laser action is expected. After fast non-radiative relaxation from level 2, particles start accumulating at level 3, while level 4 remains unpopulated because of fast relaxation from it to ground level 1. Therefore, to create inversion population between levels 3 and 4, only one particle needs to appear at level 3. Thus, the basic requirement for creation of the population inversion is that relaxation from level 4 to level 1 has to be faster than spontaneous decay from level 3 to level 4.

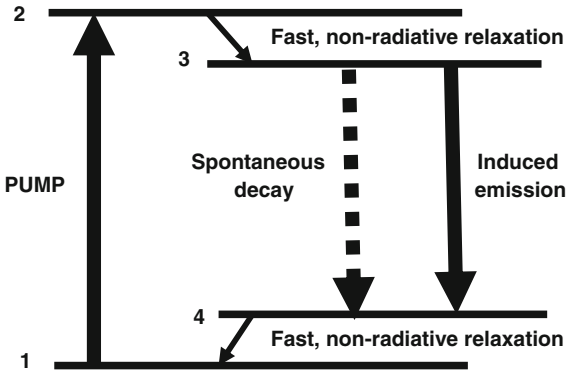

Fig. 7.1 Four-energy-level diagram of laser operation

7.1.2 Three-Level Laser Operational Scheme

Figure 7.2 shows the three-energy-level scheme of laser excitation. The principal difference between the three-energy-level scheme and the four-energy-level scheme is that the lower laser level (i.e., level 4 in Fig. 7.1) and the lowest level (i.e., ground state; level 1 in Fig. 7.1) becomes a single level (Level 1 in Fig. 7.2). Therefore, after spontaneous decay, particles do not return to the unpopulated terminal level, as was the case in the four-energy-level scheme, but they appear to return to the original, populated ground state instead. In other words, within the three-energy level scheme, the laser-terminating level is always populated. Therefore, the requirements for creating inversion population between the two laser levels are very strict.

More than half of the total particles have to be excited to the laser's upper level in the three-energy-level laser operation scheme in order to create population inversion. This condition requires much higher excitation intensities as well as special care to eliminate re-absorption of the amplified light while it travels along the laser medium. All of these factors contribute to an increased laser threshold

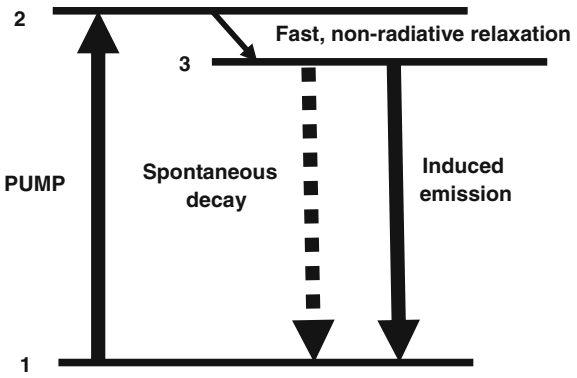

Fig. 7.2 Three-energy-level diagram of laser operation

and complicate the achievement of high laser efficiencies. Nevertheless, the three-energy-level laser operation scheme is very important and has many applications in fiber lasers and amplifiers.

In commonly used laser excitation conditions, when the laser medium is excited by another laser or flash lamp, it is fundamentally impossible to create population inversion in a two-energy-level scheme. However, while exciting an isolated two-energy-level scheme using a resonant pump light with a very strong electromagnetic field, one can create a condition in which the probability of the particle to appear in the upper or lower energy level becomes a time-dependent parameter. Oscillation of the population at each of the two levels begins at the so-called Rabi frequency [2, 3]. Broadening of the spectral lines and deviation of the real energy-level systems from two-level systems (due to Stark splitting) prevents easy observation of this phenomenon in solid-state laser media.

7.2 Optical Fiber Amplifiers

7.2.1 Fiber Amplifier (General Consideration)

A fiber amplifier basically works on same physical principles as its bulk solid-state analogs. The purpose of the fiber amplifier is to amplify a less powerful optical beam, which is propagating either inside another fiber or in free space. In this way, the amplifier is "seeded" with a low-power laser beam; such an optical beam is called a seed. There are two fundamental types of fiber laser amplifiers: those based on doped cores and those based on doped cladding. Doped-cladding fiber amplifiers use the evanescent field amplification principle; although they exist, they are not commonly used. Therefore, this review concentrates on core-doped fiber amplifiers.

In core-doped fiber amplifiers, the amplifying light propagates in the same volume where laser-active centers are located. The next subclassification is usually done based on the way the pump is coupled and propagates inside the gain fiber. This pump propagation classification divides all amplifiers into core-pumped and cladding-pumped fiber amplifiers. Note that the same classification is valid for fiber laser oscillators. As it is known from main principles of laser physics, the laser oscillator is a device that contains a laser amplifier put inside an optical resonator. The laser resonator fundamental function provides positive feedback.

This chapter considers a laser amplifier (i.e., optical amplifier) based on the stimulated emission amplification principle only. Information on other fiber optical amplifiers, such as those based on optical nonlinearities (e.g., optical parametric amplifiers and Raman or Brillouin amplifiers) is available elsewhere. In this introduction, the main physical processes that take place in optical amplifiers are briefly reviewed. A theoretical consideration of the CW and pulse amplifiers are then presented, followed by the derived main formulas that are important for practical design.

7.2.1.1 Gain Saturation

As will be shown by analytical expression later in this section, high-input optical fluence does not increase indefinitely in an amplifier but rather saturates, leading to amplifier gain reduction. Obviously, even from the general consideration of energy conservation, the gain of the amplifier has to saturate because one cannot extract more power from the amplifier than it was excited (pumped) with. Gain saturation plays an important role in theory and practice of optical amplification and oscillation. The gain saturation parameter (I_s), which will be introduced later in this section, is a very important and unique parameter of the gain medium; it is often used to analyze and compare different gain media for certain applications. This parameter also plays an important role in the calculation and design of laser systems, including amplifiers.

The advantages of operating an optical fiber amplifier in the gain saturation regime are mainly the following:

1. Small power fluctuations in the input signal do not reflect to the same extent in the output amplified signal
2. The fiber amplifier, which has multiple spectrally close input signals with varied intensity, may work as a gain equalizer because smaller input signal powers have higher gain (because of less saturation) and higher input powers have lower gain (because of a higher degree of saturation)
3. A saturated optical amplifier demonstrates a high energy extraction efficiency; therefore, the overall efficiency of the system is high.

7.2.1.2 Gain Narrowing

Gain narrowing is an effect that takes place in fiber amplifiers and lasers; it is responsible for light bandwidth reduction during amplification process. The process is a result of the fact that, due to limited gain bandwidth (usually with a bell-like gain spectral profile) of the amplifier material, the central region of the signal optical spectrum is a subject of higher gain than the spectral wings.

For the single-pass laser amplifier, the seed line width decreases with increasing gain. For the Lorentzian atomic line shape (see Chap. 2), the optical amplifier full-width, half-maximum (FWHM) gain spectral bandwidth can be written as [2, 3]:

$$\Delta\omega_{3\mathrm{dB=FWHM}} = \Delta\omega_a \times \sqrt{\frac{3}{G_{\mathrm{dB}}(\omega_0) - 3}} \tag{7.3}$$

where ω_0 is the central frequency of the atomic transition, $G(\omega_a) = \frac{I(L)}{I(0)} = \exp\left[2 \cdot g(\omega) \cdot L - 2 \cdot \mu \cdot L\right]$ is the amplifier gain factor expressed in units of dB, $\Delta\omega_0$ is the natural line width of the atomic transition, $g(\omega)$ is the gain coefficient, and μ is the loss coefficient.

Amplifier losses and laser intracavity losses have to be taken into consideration when analyzing the gain narrowing effect. In the field of fiber lasers, the gain narrowing effect may play a positive role (when a smaller spectral line width is required) or a negative role (when designing so-called Amplified spontaneous emission (ASE) sources with a flattened spectral distribution of output power across the emission spectrum).

7.2.1.3 Amplified Spontaneous Emission

Being an incoherent process, ASE extracts stored energy from the fiber amplifier by depleting the inversion population by spontaneous emission amplification. The physical reason for the ASE is as follows. Once excited during the pumping process, electrons in the upper energy level are decaying not only through stimulated emission but also through spontaneous emission, which in turn is a random process that depends on the level of inversion created in gain fiber. Only a fraction of the photons emitted spontaneously in all directions falls within the Numerical aperture (NA) of the fiber and therefore will be guided inside the core where the seed propagates. While propagating along the core, the amplified portion of captured ASE photons interact with other laser active centers and, as other photons, these spontaneous photons are amplified by the stimulated emission process. Because ASE is mostly confined in the core, it is one of the major phenomena that saturates the fiber amplifier power scaling in the case of telecom type fibers (NA = 0.12, $D_{\text{core}} = 5$ μm).

The power spectral density of the spontaneous emission induced noise $S_{\text{sp}}(v)$ is a function of the frequency and amplifier gain [2, 3]:

$$S_{\text{sp}}(v) = (G - 1) \times n_{\text{sp}} \times hv \tag{7.4}$$

Total integrated ASE noise power is:

$$P_{\text{ASE}} = S_{\text{sp}}(v) \times \Delta v \tag{7.5}$$

The optical power of the ASE light at the output of the fiber amplifier is therefore determined by the following expression [2, 3]:

$$P_{\text{ASE}} = n_{\text{sp}} \times (G - 1) \times hv \times \Delta v \tag{7.6}$$

where Δv stands for FWHM of the output spectrum and G is the absolute amplifier gain (see details later in this chapter). n_{sp} is the spontaneous emission factor, which is determined by:

$$n_{\text{sp}} = \frac{\overline{N_2}}{\left(\overline{N_2} - \overline{N_1}\right)} \tag{7.7}$$

where $\overline{N_i}$ is the average population of level i over the whole fiber length. It is evident from the expression for n_{sp} that output ASE power in the fiber amplifier is

large when population inversion is low. When the population inversion is high, seed can only be amplified. When the population inversion is low, the seed photons cannot only be amplified but also can be absorbed on the same transition. Therefore, the seed photons that get absorbed in the low inversion amplifier can produce not only stimulated emission but spontaneous emission as well.

Using large mode area fibers with core diameters of 30 μm in conjunction with low NA of ~0.06, one can significantly suppress the ASE process in high-power fiber amplifiers.

7.2.1.4 Laser Amplifier Noise

The main source of noise in fiber optical amplifiers is ASE, which has a spectrum close to that of the amplifier gain spectrum. The noise arising from forward-propagating ASE is only a direct concern to the amplifier system because it strikes the detector along with useful signals. The backward-propagating ASE can still deplete the amplifier inversion and reduce the gain.

The existence of ASE in the amplifier (or laser) system is often a major factor restricting output power scaling with increase of the pump. Although in solid-state and other laser systems there are several approaches to suppress ASE, such as laser-active medium geometry and surface profile optimization, fighting ASE in gain fiber is still a big challenge because of the long lengths and small core sizes. To achieve minimum noise, optical fiber amplifiers are usually operated in a gain saturation regime with gain between 8 and 10 dB, leaving little room for ASE and increasing depleted stored energy.

The noise figure in a optical amplifier is defined as:

$$F_n = \frac{\mathrm{SNR}_{\mathrm{input}}}{\mathrm{SNR}_{\mathrm{output}}} \approx 2n_i = 2\frac{N_2}{N_2 - N_1} \tag{7.8}$$

where $\mathrm{SNR}_{\mathrm{input/output}}$ stands for the signal-to-noise ratio at the input/output of the amplifier, n_i is the population inversion factor (which is equal to 1 for an ideal amplifier; i.e., four-level amplifier, where the population of the lower laser level is zero). Therefore, from Eq. (7.8), one can see that the noise figure of the ideal amplifier is:

$$F_n \approx 2 \text{ or } 3\,\mathrm{dB} \tag{7.9}$$

In practical fiber amplifiers, the noise figure usually falls into the range of 6–8 dB.

7.2.1.5 Laser Amplifier Phase Shift

Qualitatively speaking, the phase shift in a single-pass laser amplifier has two main contributors: (1) the so-called free-space phase shift, which is linearly proportional

to the optical frequency; and (2) the phase shift due to atomic transition. Following Siegman [2, 3], the total phase shift in a single-pass laser amplifier can be expressed as follows:

$$\exp[-i \times (\beta(v) + \Delta\beta_{\text{at}}(v))L] \equiv \exp[-i \times \varphi_{\text{tot}}(v)] \tag{7.10}$$

and

$$\varphi_{\text{tot}}(v) = \beta(v)L + \Delta\beta_{\text{at}}(v)L = \frac{2\pi v}{c} + \frac{\beta L}{2}\chi(v)' \tag{7.11}$$

where $\chi(v)$ is the real part of the material susceptibility (sometimes called a dispersive part of the atomic response) of the gain medium. The first term in the expression for the total phase shift is the basic free-space phase shift $\beta(v)L = (2\pi vL)/c = 2\pi L/\lambda$, which appears while the wave propagates through the laser medium. As mentioned, the free-space phase shift is linearly proportional to the frequency. The second term in the expression for the total phase shift is the phase shift due to atomic transition, $\Delta\beta_{at}(v)L$. The magnitude of the added phase shift due to atomic transition is proportional to the net gain (or absorption) of the optical wave propagating through the gain medium. It can be shown that for a Lorentzian shape of the atomic transition, the added phase shift is related to the optical gain by the following expression [2, 3]:

$$\Delta\beta_{\text{at}}(v)L = 2\frac{v - v_0}{\Delta v_0} \cdot g(v)L = 2\frac{(v - v_0)}{\Delta v_0}L \cdot g(v_0)\frac{(\Delta v/2)^2}{(v - v_0)^2 + (\Delta v/2)^2} \tag{7.12}$$

where $g(v_0)$ is the gain coefficient at the center of the emission line. Note that at the resonance frequency, when $v = v_0$, the gain is maximum but the phase shift is equal to zero. The phase shift is negative for frequencies below the resonance frequency and positive for frequencies above the resonance frequency. The free-space phase shift usually is a major contributing factor to the amplifier phase shift.

7.2.1.6 Other Processes in Optical Amplifiers

In addition to the previously mentioned phenomena, a few other processes have to be considered during the design and development of practical fiber amplifiers, especially at elevated optical powers. The first and probably most challenging process is the parasitic reflections from end surfaces of the amplifier material (poor splicing; i.e., poor optical contacts) or other surfaces of free space optics in an amplifier system, which can cause parasitic lasing or self-pulsing (i.e., amplifier pulsing without a seed). Started oscillation obviously depletes inversion and reduces achievable gain. Self-pulsing plays an important role in stability and creating a damage-free condition of CW fiber lasers and amplifiers. The output instabilities of a CW pumped three-level fiber laser, with sustained self-pulsing or self-mode-locking [4, 5], have been investigated extensively. Instability may follow from the nonlinear dynamics of the laser signal and from population

inversion. It was demonstrated that higher output coupler reflectivity and suppressed nonlinear scattering processes, such as SBS and SRS yield to substantially suppressed self-pulsing, which in turn creates a condition for damage-free CW operation.

Other processes that take place during short pulse amplification and happen under high pulse intensity are spectral broadening (due to some nonlinear effects) and amplifying pulse distortion.

7.2.1.7 Fiber Amplifier Gains and Losses

When dealing with three-energy-level systems or quasi-three-energy-level systems (as in the case of most widely used fiber lasers, such as Yb^{3+} and Er^{3+}), one needs to take into account reabsorption losses of laser radiation at the oscillation wavelength. Following Pask et al. [6], this section provides a detailed description of the gains and losses in fiber amplifiers. First, consider the critical pump power P_{pcr} required to achieve a gain coefficient of zero at a particular point in the fiber (i.e., to reach transparency for the signal/laser wavelength), which is given by [6]:

$$P_{\text{pcr}} = Ahv_p \frac{1}{\tau} \frac{\sigma_{\text{al}}}{(\sigma_{\text{el}}\sigma_{\text{ap}} - \sigma_{\text{ep}}\sigma_{\text{al}})} \tag{7.13}$$

where A is the core area cross section, h is the Planck's constant, v_p is the pump laser frequency, τ is the upper-level lifetime, σ is the cross-section of the quantum transition, and e, a, p, and l denote to the emission, absorption, pump, and laser wavelengths, respectively (i.e., σ_{ap} stands for the absorption cross-section at the pumping wavelength).

It is assumed in this analysis that the only loss mechanism in the fiber doped with laser-active ions is related to the absorption transition of the laser-active center and any other sources of loss-like scattering are absent. However, modern optical fibers demonstrate measurable scattering loss (although this loss is small due to advanced modified chemical vapor deposition [MCVD] technology). Typical loss in modern fibers, especially those used for telecommunication applications (i.e., undoped), is on the order of $\sim$0.2 dB/km; for doped fibers, the loss varies from 0.01–0.1 dB/m, depending on the wavelength of laser operation and the gain fiber under consideration. Because typical fiber amplifier gain is in the order of 10–30 dB/m, today's state-of-the art MCVD or DND technology provide very efficient gain fibers, offering more than 75 % power conversion efficiencies (in the case of Yb^{3+} amplifiers and lasers).

The pump saturation power of the absorption transition of the optical center can be expressed as:

$$P_s = \frac{hv_p A}{(\sigma_{\text{ep}} + \sigma_{\text{ap}})\tau\phi_p} \tag{7.14}$$

where ϕ_p is the pumping quantum efficiency (for the Yb^{3+} ion, it is ~ 0.92 when the seed wavelength is 1,064 nm and pump wavelength is 976 nm—a typical example of this type of amplifier).

The small-signal (unsaturated) gain for the whole length of the fiber amplifier is given by:

$$G_0 = g_0 L = \frac{\phi_p(\sigma_{\mathrm{el}} + \sigma_{\mathrm{al}})\tau P_a}{A h v_p} - N\sigma_{\mathrm{al}} L \tag{7.15}$$

In an approximation of the constant inversion along the fiber length, the absolute gain factor of the fiber amplifier of the length L is therefore:

$$G = \frac{P(L)}{P(0)} = \exp[G_0] \tag{7.16}$$

where P_a is the absorbed pump power, N is the laser-active center concentration, and L is the gain medium length. Note that expression $N\sigma_{\mathrm{al}}L$ indicates total absorption loss in the whole length of the gain fiber at laser oscillation wavelength. In the general case of the varied inversion along the gain fiber, the absolute gain factor should be integrated along the whole fiber length:

$$G = \exp[\int_0^L g_0(z)\mathrm{d}z]. \tag{7.17}$$

For a high pumping level when gain coefficient g_0 cannot be considered, a small value saturated gain coefficient, g, can be expressed as follows:

$$g = \frac{g_0}{1 + I/I_s} \tag{7.18}$$

where I is the amplified light intensity and I_s is a so-called gain saturation parameter, defined as an intensity of the amplifying beam in active medium at which the small-signal (unsaturated) gain coefficient g_0 is reduced by 50 % (i.e., half). In turn, the gain saturation parameter with good approximation can be defined as the following general formula:

$$I_s = \frac{h v_L}{(\sigma_{\mathrm{el}} + \sigma_{\mathrm{ea}})\tau} = \frac{h v_L}{\sigma_{\mathrm{el}} \tau Q} \tag{7.19}$$

where $Q = 1 + {}^{\sigma_{\mathrm{ea}}}/_{\sigma_{\mathrm{el}}}$, and with good degree of accuracy $Q = 1$ for four-energy-level systems (i.e., when $\sigma_{\mathrm{el}} \gg \sigma_{\mathrm{ea}}$) and $Q = 2$ for three-energy-level systems (i.e., when $\sigma_{\mathrm{el}} \approx \sigma_{\mathrm{ea}}$).

The stored energy in the four-level solid-state laser amplifier can be defined by the following expression [2, 3]:

$$E_{\mathrm{st}} = h v_L N V = g_0 I_s V \tag{7.20}$$

where V is the amplifier gain volume and N is the concentration of laser-active centers created during the pumping process.

Note that the expressions for gain saturation parameters have been originally derived for homogenously broadened lines, such as those appearing in crystals (e.g., YAG, ruby). However, in glass host materials, such as Yb^{3+} or Nd^{3+}-doped glasses, cross-relaxation processes are very fast (i.e., those processes responsible for excitation energy transfer between individual homogeneously broadened spectral components within inhomogeneously broadened envelopes). For fast cross-relaxation in-homogeneously broadened host materials, it was shown that the previous formulas are valid with good degree of accuracy. It is also evident from these expressions that, in three-energy-level transitions, gain saturates faster than that of four-energy level scheme.

The single-pass gain in fiber amplifiers, expressed in units of dB, can be calculated using following formula:

$$\begin{aligned} g(\lambda) &= 10\log\left(\frac{I}{I_0}\right) = 10\log e^{\int_0^l g(z)\mathrm{d}z} \\ &= 10\log\left\{\exp\left[\frac{\phi_p(\sigma_{\mathrm{el}}+\sigma_{\mathrm{al}})\tau P_a}{Ahv_p} - N\sigma_{\mathrm{al}}l\right]\right\} \end{aligned} \tag{7.21}$$

7.2.1.8 Pulse Amplification

Frantz and Nodvik [7] reviewed two important practical application cases of pulse amplification in laser amplifiers: (a) the square pulse shape and (b) the Lorentzian pulse shape. The details of the analytical expressions for each of these cases can be found in Ref. [7].

(a) **Square pulse shape**

Figure 7.3 illustrates how the ratio of the output photon density (fluence) to input photon density changes versus time in units of pulse width τ when the square pulse has been injected into the amplifier.

Figure 7.3 is typical for pulse fiber amplifiers with "chopped" seeds, boosted in the high-power amplification stages of the system. One can see clear temporal narrowing of the output pulse, which is evident from Frantz–Nodvik analyses. Due to difficulties associated with Q-switched fiber laser master oscillators, the seed chopping approach is widely used. The Frantz−Nodvik theory provides a direct path for pulse profile analysis in such fiber amplifier systems.

(b) **Lorentzian pulse**

The fiber amplifier seeded with a Q-switched pulse from a master oscillator, as illustrated in Fig. 7.4, does not have a square shape. One can use the above expression to calculate the gain. Unlike the square-pulse seeded optical amplifier,

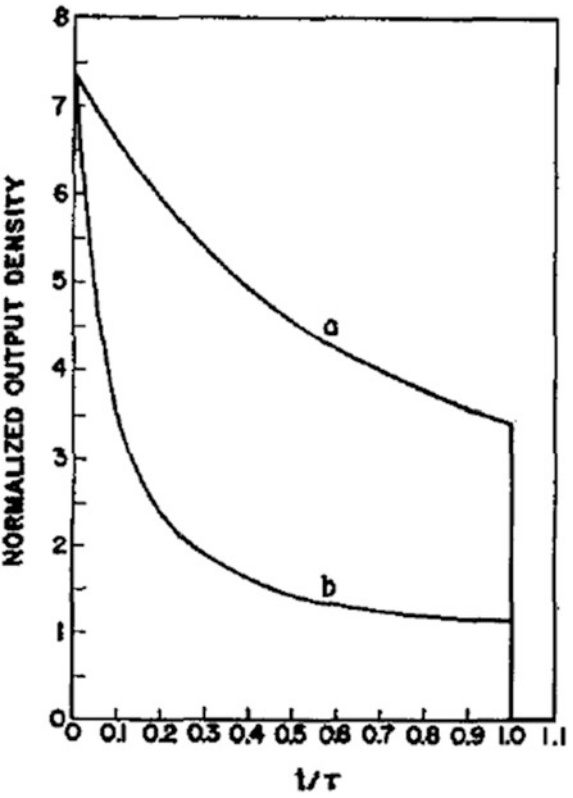

Fig. 7.3 Ratio of the output photon density to input photon density versus time in units of pulse width for an initially *square-shaped* pulse [7]. *Curve* (*a*) shows that the total number of photons per unit area in the traveling pulse is 4×10^{18} cm^{-2}. *Curve* (*b*) shows that the total number of photons per unit area in the traveling pulse is 4×10^{19} cm^{-2}. (Reprinted with permission from Frantz and Nodvik [7], COPYRIGHT AIP PUBLISHING LLC.)

in which the square shape changes and the front of the pulse narrows significantly, the Lorentzian pulse preserves its bell-shaped profile (Fig. 7.4). Absence of a steep front can be useful for some considerations of the pulse propagation in fiber amplifiers with respect to damage mechanisms of the fiber amplifier material.

7.3 Fiber Laser Thresholds and Efficiency

The laser threshold is one of the most important parameters of the laser oscillator. It reflects not only the gain properties of the active medium but also all active and passive losses in the laser cavity. Calculated laser threshold and laser slope efficiency give the researcher a full set of parameters to calculate laser output power at any level of pump power.

In this section, for simplicity, the basic formulas for fiber laser threshold and laser efficiency are presented [8, 9]. In most cases, fiber laser is a longitudinally pumped system; therefore, the theoretical expressions for this type of excitation are used.

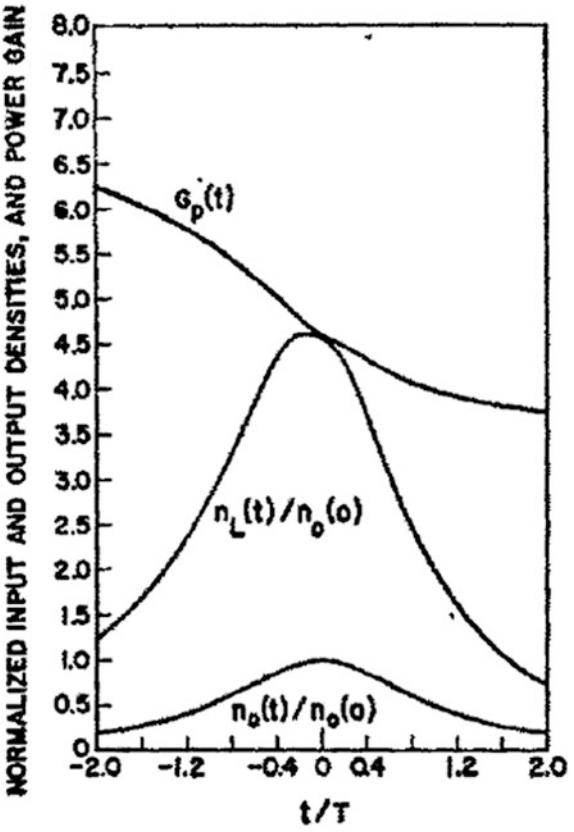

Fig. 7.4 Ratio of the output photon density to input photon density versus time in units of the pulse width for an initially Lorentzian-shaped pulse. (Reprinted with permission from Frantz and Nodvik [7], COPYRIGHT AIP PUBLISHING LLC.)

Following Risk [8], consider the general energy-level scheme shown in Fig. 7.5, in which the population density of the lower laser level N_1 is not zero (as in a classic four-energy-level system) but has a small thermally induced population. If the total population density residing in the relaxed excited state component of the upper lasing level is N_U and the population density residing in the lower laser level is N_L, then the relationship between the actual population density in the corresponding levels 1 and 2 can be expressed as follows (see Fig. 7.5):

$$N_1 = f_1 N_L \text{ and } N_2 = f_2 N_U$$

where f_1 and f_2 are fractional parameters of total inversion. Accordingly, $\Delta N^0 = N_2^0 - N_1^0$ is the unpumped population inversion.

Then, the absorbed pump power (or threshold power) in a quasi-three-level laser system is given by:

$$P_{\text{th}} = \frac{\pi h \nu_p \left(w_L^2 + w_P^2\right) \times \left(L_{\text{rt}} + T + 2\sigma_{\text{al}} N_1^0 L\right)}{4\sigma_{\text{el}} \tau \eta_a (f_1 + f_2)} \tag{7.22}$$

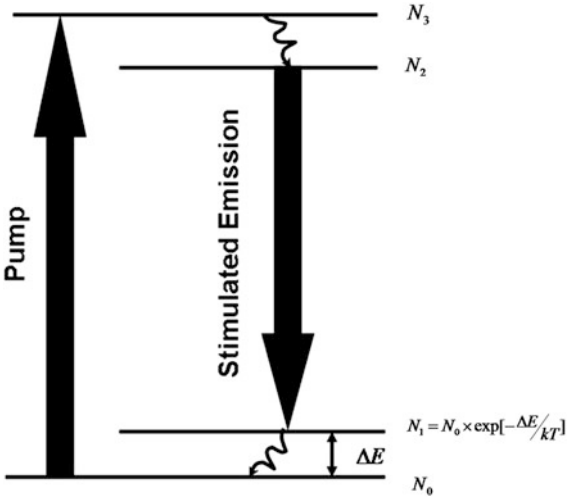

Fig. 7.5 General energy-level diagram [8]. (Image courtesy of the Optical Society of America)

where w_L and w_P are the laser and pump beam waists, respectively; τ is the fluorescence lifetime; T is the output mirror transmittance; and L_{rt} is the round-trip loss, except for output coupling.

In the case of core-pumped fiber lasers, in which pump and laser beam waists are similar, the following expression can be used to determine the laser slope efficiency in the absence of excited state absorption:

$$\eta_{\text{slope}} = \frac{\mathrm{d}P_{\text{out}}}{\mathrm{d}P_p} = \frac{T}{(L_{\text{rt}} + T)} \frac{\lambda_P}{\lambda_L} \eta_a \frac{\mathrm{d}S}{\mathrm{d}F} \tag{7.23}$$

where η_a is the efficiency with which the pump photons are absorbed, $\mathrm{d}S/\mathrm{d}F$ is the efficiency with which absorbed pump photons are converted to laser photons, and $T/(L_{rt} + T)$ is the fraction of the laser photons that have been lost during round-trip due to emission through output coupler from total loss. If we simplify the above formula for slope efficiency for the case when all absorbed pump photons are converted to lasing photons and all pump photons have been absorbed, we can obtain a commonly used simplified expression for the laser slope efficiency, namely:

$$\eta_{\text{slope}} = \frac{T}{(L_{\text{rt}} + T)} \frac{\lambda_P}{\lambda_L} \tag{7.24}$$

Summarizing all analyses presented in this section, we can give an analytical expression for the laser output power in quasi-three-level case, which is the most common case of fiber laser and fiber amplifiers energy-level configurations:

$$P_{\text{out}} = \eta_{\text{slope}} \left(P_p - P_{\text{th}} \right) \tag{7.25}$$

Note that in the case of Yb^{3+} fiber laser, where pumping can be accomplished using 976 nm excitation wavelength and laser can be observed at 1,030 nm

wavelength, the quantum defect ratio is $\lambda_P/\lambda_L \approx 0.95$, which in turn determines the maximum value of the laser slope efficiency. Typical Yb^{3+} fiber laser optical efficiency is 70–80 %; slope efficiencies as high as 90 % have been achieved.

7.4 Gain and Loss in Laser Resonators

Knowing the amount of loss in the laser resonator is very important for understanding the laser operation. There are several ways of measuring such losses. One of the most widely used techniques for four-energy-level lasers is based on the measured laser threshold power as a function of varying output couplers. This technique was first suggested by Findlay and Clay [10].

By measuring threshold pump power, P_{th}, and output coupler reflectivity, R, one can use the Findlay and Clay technique [10] to obtain the round-trip intracavity loss and small storage efficiency, η_{st} (pump efficiency), which in turn gives the value of small signal gain. By measuring the plot of $\ln(R)$ versus P_{th}, one can readily derive these two important laser parameters using the following function:

$$-\ln(R) = \left(\frac{2 \cdot \eta_{\text{st}}}{A \times I_s}\right) \cdot P_{\text{th}} - L_{\text{loss}} \tag{7.26}$$

where the intercept of the y-axis yields $-L_{\text{loss}}$ (loss), and the slope is proportional to η_{st}. Note that $-L_{\text{loss}} = 2\mu L$, where L is the length of the gain medium and μ is the total internal loss coefficient due to absorption, scattering, and optical inhomogeneity. The Findlay and Clay technique is valid for all systems and gives loss measurements independent of pump geometry, pulse shape, and pulse duration [10].

7.5 Fiber Laser Resonators

The physics of optical resonators used in fiber lasers is similar to the physics of traditional laser resonators. The main differences are in intracavity components and geometry of the active medium. Intracavity optical components of fiber laser resonators have certain features, mostly related to the tolerance for optical damages and fiber coupling. The active medium of fiber lasers is an optical waveguide usually with significantly longer length than in traditional lasers and very small diameter of the optical wave propagating medium. Long length and small fiber diameters are the reasons for optical nonlinearities, which require special attention in fiber laser development. The long length of the gain fiber in most fiber laser resonators is also the cause of challenges related to achieving short Q-switch pulse durations. This section briefly reviews two fundamental types of laser resonators, which (as in other laser types) play an important role in practical fiber lasers.

7.5.1 Linear Laser Resonators

A linear fiber laser resonator consists of two reflectors (usually mirror or fiber Bragg gratings) set at the opposite ends of the optical cavity, gain medium in the form of laser-active ion-doped fiber, and other intracavity laser components to control temporal and spectral properties of the fiber laser. In linear laser resonators, the resonator modes are usually considered as a superposition of two electromagnetic waves traveling in opposite directions between cavity reflectors. Resonant frequencies of the linear resonator are given by the following expression:

$$v = M \times \left(\frac{c_0}{2 \times n \times L}\right) \tag{7.27}$$

where M is the integer. Therefore, the frequency difference between two consecutive (i.e., longitudinal) modes is given by:

$$\Delta v = \frac{c_0}{2 \times n \times L} \tag{7.28}$$

where n is the refractive index of the medium where light propagates inside the laser cavity.

Because light waves inside a linear laser resonator propagate in directions opposite to each other, standing waves are created, which in turn have minimum and maximum interfering intensities. The minimum intensities of the standing-wave pattern of the intracavity laser field in the laser resonator are responsible for the so-called spatial hole-burning effect; this affects the laser spatial gain distribution, which in turn favors the multispectral mode oscillation of the laser. On the other hand, because of the roundtrip nature of the light path inside the laser resonator and because the light propagates twice through the active medium during the cavity roundtrip, the laser gain (and loss) is accounted twice. This is a fundamental feature of the linear laser resonator, differentiating it from the unidirectional ring laser resonator, which demonstrates no spatial hole burning effect. Ring laser resonators are described next.

Barnard et al. [11] developed an analytical model for rare-earth-doped fiber lasers. What makes this model appealing is that it provides formulas for the main laser parameters expressed in relatively easy measurable optical parameters of the system. According to Barnard et al. [11], in the case of a linear fiber laser cavity, the total fiber gain can be expressed as:

$$G = \exp\left[\left(\frac{P_p \mu_p P_p^{\mathrm{IS}}}{P_s^{\mathrm{CS}}\left(P_p^{\mathrm{IS}} + P_p\right)} - \mu_s\right) \times L\right] \tag{7.29}$$

Here, the small signal gain coefficient is:

$$g = \frac{P_p \mu_p P_p^{\mathrm{IS}}}{P_s^{\mathrm{CS}}\left(P_p^{\mathrm{IS}} + P_p\right)} - \mu_s \tag{7.30}$$

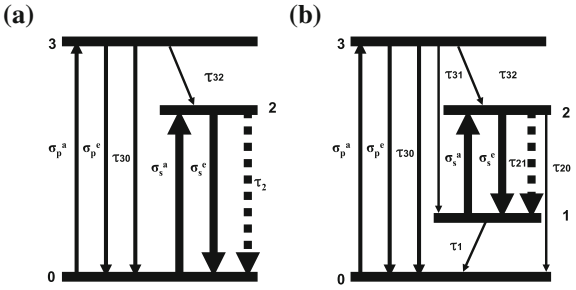

Fig. 7.6 Three-(**a**) and four-(**b**) energy-level laser operation schemes

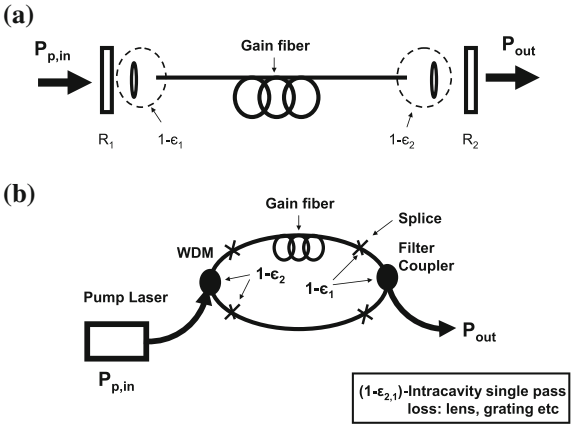

Fig. 7.7 Linear (**a**) and ring (**b**) fiber laser cavities

For the high pump level, the maximum gain is:

$$G_{\max} = \exp\left[\left(\mu_p/\delta - \mu_s\right)L\right] \tag{7.31}$$

The laser threshold is determined by the following expression (see Figs. 7.6 and 7.7):

$$P_{\text{th}}^{L} = \frac{h\nu_p P_s^{\text{CS}}[\mu_s L - \ln(\varepsilon R)]}{1 - (G_{\max}\varepsilon R)^{-\delta}} \quad \text{Linear laser cavity} \tag{7.32}$$

where $\tau = (\tau_2$ or $\tau_{21})$ is the laser metastable level lifetime, ν_p is the pumping photon frequency, $\varepsilon = \varepsilon_1\ \varepsilon_2$ is the effective cavity transmission (with ε_1 and ε_2 as the intracavity component single-pass transmissions), $R = \sqrt{R_1 R_2}$ is the effective laser cavity mirror reflectivity, $\delta = P_s^{\text{CS}}/P_p^{\text{IS}}$ is the ratio of the signal cross-saturation power parameter and the pump intrinsic saturation power parameter, μ_s is the small signal absorption coefficient at the signal wavelength and μ_p is the small signal pump absorption coefficient.

The signal cross saturation power P_s^{CS} is the parameter characterizing the transfer of energy from the absorbed pump power to the signal. Parameters $P_{s,p}^{\text{CS,IS}}$ are defined as follows:

$$P_s^{\mathrm{CS}} = \frac{\beta_{2e}}{\eta_p \tau} \frac{A_{\mathrm{eff}}}{(\sigma_{\mathrm{al}} + \beta_{2e}\sigma_{\mathrm{el}})} \quad \text{(three-energy-level scheme)} \tag{7.33}$$

or

$$P_s^{\mathrm{CS}} = \frac{\beta_{2e}}{\eta_p \tau} \frac{A_{\mathrm{eff}}}{(\beta_{2e}\sigma_{\mathrm{el}} + \beta_{12}\sigma_{\mathrm{al}})} \quad \text{(four-energy-level scheme)} \tag{7.34}$$

where $\tau = (\tau_2$ or $\tau_{21})$ is the upper laser level lifetime in the gain fiber, parameter β_{2e} for the three-energy-level scheme is $N_2/N_e = \beta_{2e} = (1 + \tau_{32}/\tau_2)^{-1}$ and for the four-energy-level scheme $N_2/N_e = \beta_{2e} = (1 + \tau_{32}/\tau_2 + \tau_1/\tau_{21} + (\tau_1\tau_{32})/(\tau\tau_{31}))^{-1}$ (both at the absence of seed power $P_s = 0$); $N_1/N_2 = \beta_{12} = \tau/\tau_2 + \tau_{32}\tau_1/\tau_2\tau_{31}$ is the N_1 and N_2 energy-level population ratio at the absence of signal propagating power (i.e., $P_s = 0$); and $\beta_{12}\beta_{2e} = \beta_{1e} = {}^{N_1}/_{N_e}$, also when $P_s = 0$.

P_p^{IS} is the parameter that characterizes how pump absorption is saturated by the pump light. P_p^{IS} is the pump internal saturation parameter defined as:

$$P_p^{\mathrm{IS}} = \frac{\beta_{2e}}{\eta_p \tau} \frac{A_{\mathrm{eff}}}{(\sigma_{\mathrm{ap}} + \beta_{3e}\sigma_{\mathrm{ep}})} \quad \text{(three-energy-level scheme)} \tag{7.35}$$

or

$$P_p^{\mathrm{IS}} = \frac{\beta_{2e}}{\eta_p \tau} \frac{A_{\mathrm{eff}}}{(\sigma_{\mathrm{pa}} + \beta_{3e}\sigma_{\mathrm{ep}})} \quad \text{(four-energy-level scheme)} \tag{7.36}$$

where $\beta_{3e} = (\tau_{32}/\tau_2) \cdot \beta_{2e}$.

Fiber laser slope efficiency in linear cavity can be expressed as follows:

$$\eta_{\mathrm{linear}} = \frac{\eta_q \varepsilon_2 (1 - R_2)}{T_{\mathrm{eff,linear}}} \times \frac{P_s^{\mathrm{IS}}}{P_s^{\mathrm{CS}}} \left[1 - (G_{\max}\varepsilon R)^{-\delta}\right] \tag{7.37}$$

where $T_{\mathrm{eff,linear}} = (1 - R_2\varepsilon_2^2) + (1 - \varepsilon_1^2 R_1)\varepsilon_2^2 R_2/(\varepsilon R)$ is the effective output transmission and $R^2 = R_1 \times R_2$. One can calculate fiber laser output power in linear cavity using the following formula:

$$P_{\mathrm{out}} = \eta_{\mathrm{linear}}(P_p - P_{\mathrm{th,linear}}) \tag{7.38}$$

Optimum gain fiber length obtained in Ref. [11] for the case of linear cavity is:

$$L_{\mathrm{opt}} = \frac{1}{\mu_p - \delta \times \mu_s} \ln\left[\frac{P_p(\mu_p - \delta \times \mu_s)}{P_s^{\mathrm{CS}}\mu_s(\varepsilon R)^{\delta}}\right] \tag{7.39}$$

7.5.2 Ring Laser Resonators

The ring resonator is another important type of laser cavity. It is defined as a resonator where the intracavity light travels along the ring type configuration. The ring cavity may be realized differently (i.e., using a folded type). To achieve a condition for phase shift of the traveling light wave during roundtrip of the cavity to be equal to 2π (the same condition as in the case of linear resonators), the expression for resonant frequency can be given as follows:

$$v = M \times \frac{c_0}{n \times L_{\text{ring}}} \tag{7.40}$$

where L_{ring} is the length of the closed loop path, M is an integer, and n is the refractive index of the fiber material. Ring laser resonators can support waves propagating in opposite directions (i.e., clockwise and counterclockwise). However, unlike linear laser resonators, ring laser resonators use a unidirectional device (e.g., an optical isolator), which allows the unidirectional propagation of the light wave inside the laser cavity; the resonator becomes traveling wave because the concept of the cavity mode and cavity resonance frequency are no longer defined as the same wave (as in the case of a standing wave resonator).

Following similar consideration of the cavity gain and loss, in traveling wave (unidirectional) ring resonators, the gain and loss have to be counted once. Less cavity roundtrip gain obviously reduces laser gain; however, the absence of a hole-burning effect helps to achieve the single longitudinal mode of laser operation. Therefore, ring laser cavities are widely used for very narrow, single-longitudinal mode operation of the lasers.

However, the spatial hole-burning effect is essential for lasers in which the active medium demonstrates a homogeneously broadening case of spectral line broadening, where inversion of population is shared between different spectral components of the laser modes. In the case of inhomogeneously broadened spectral lines (e.g., glasses) spatial hole burning effect does not play a significant role. In this case, a so-called spectral hole burning effect, which is a selective bleaching of the spectral holes in the inhomogeneously broadened gain band of the optical center [12, 13], plays a more important role in the multispectral mode nature of the laser operation.

Following the results of Barnard et al. [11] and parameters introduced previously, the ring fiber laser power threshold can be expressed as follows:

$$P_{\text{th}}^{R} = \frac{h v_p P_s^{\text{CS}} [\mu_s L - \ln(\varepsilon\kappa)]}{1 - (G_{\max}\varepsilon\kappa)^{-\delta}} \text{ Ring laser cavity} \tag{7.41}$$

where κ is defined as the portion of the power that returns to the ring cavity by the output coupler. That is, if a filter coupler is used with 30:70 coupling ratio and 30 % is recouped back into the cavity, then $\kappa = 0.3$ and $1 - \kappa = 0.7$ is coupled out of the ring laser cavity. Ring fiber laser slope efficiency is defined as [11]:

$$\eta_{\text{ring}} = \frac{\eta_q \varepsilon_2 (1-\kappa)}{T_{\text{eff,ring}}} \frac{P_s^{\text{IS}}}{P_s^{\text{CS}}} \left[1 - (G_{\max}\varepsilon\kappa)^{-\delta}\right] \tag{7.42}$$

where $\eta_q = \lambda_p/\lambda_s$ is the quantum efficiency (i.e., ratio of pumping to signal wavelengths or corresponding photon energies); and $T_{\text{eff,ring}} = 1 - \kappa\varepsilon$ is the effective output transmission.

Using the formulas, one may obtain the ring laser output power using the following general expression:

$$P_{\text{out}} = \eta_{\text{ring}}\left(P_p - P_{\text{th,ring}}\right) \tag{7.43}$$

It is also important here to give an expression for optimum gain fiber length obtained in Ref. [11] for the case of ring cavity:

$$L_{\text{opt}} = \frac{1}{\mu_p - \delta \times \mu_s} \ln\left[\frac{P_p\left(\mu_p - \delta \times \mu_s\right)}{P_s^{\text{CS}}\mu_s(\varepsilon k)^{\delta}}\right] \tag{7.44}$$

References

1. N.G. Basov, Semiconductor lasers, Nobel lecture, Stockholm, Sweden, December 1964
2. A. Siegman, *Lasers* (University Science books, Mill Valley, 1986), pp. 1283
3. C.R. Giles, E. Desurvire, Propagation of signal and noise in concatenated erbium-doped fiber optical amplifiers. IEEE J. Lightwave Technol. Lett. **9**(2), 147–154 (1991)
4. A. Hideur, T. Chartier, C. Ozkul, F. Sanchez, Dynamics and stabilization of a high power, side-pumped Yb^{3+}-doped double-clad fiber laser. Opt. Commun. **186**, 311–317 (2000)
5. A. Hideur, T. Chartier, M. Brunel, M. Salhi, C. Ozkul, F. Sanchez, Mode-lock, Q-switch and CW operation of an Yb^{3+}-doped double-clad fiber ring laser. Opt. Commun. **198**, 141–146 (2001)
6. H. Pask et al, Ytterbium-doped silica fiber lasers: versatile sources for the 1–1.2 μm region. IEEE J. Sel.Topics in Quantum Electron. **1**(1), 2–13 (1995)
7. L.M. Frantz, J.S. Nodvik, Theory of pulse propagation in a laser amplifier. J. Appl. Phys. **34**(8), 2346–2349 (1963)
8. W. P. Risk, Modeling of longitudinally pumped solid-state lasers exhibiting re-absorption losses. J. Opt. Soc. Am. B **5**, 1412– (1988)
9. M.J.F. Digonnet, C.J. Gaeta, Theoretical analysis of optical fiber laser amplifiers and oscillators. Appl.Optics. **24**(3), 333–342 (1985)
10. D. Findlay, R.A. Clay, The measurement of internal losses in 4-level lasers. Phys. Lett. **20**(3), 277–278 (1966)
11. C. Barnard, P. Myslinski, J. Chrostowski, M. Kavehrad, Analytical model for rare-earth doped fiber amplifiers and lasers. IEEE J. Quantum Electron **30**(8), 1817–1830 (1994)
12. M. Bolshtyansky, Spectral hole burning in erbium-doped fiber amplifiers. J. Lightwave Technol. **21**(4), 1032–1038 (2003)
13. E. Desurvire, J.W. Sulhov, J.L. Zyskind, J.R. Simpson, Study of spectral dependence of gain saturation and effect of inhomogeneous broadening in erbium-doped aluminosilicate fiber amplifiers. IEEE Photon. Technol. Lett. **2**, 653–655 (1990)

Chapter 8
Main Operating Regimes of Fiber Lasers

8.1 Temporal Regimes

There are three main temporal regimes in laser operation:

1. Continuous-wave (CW) and free-running
2. Q-switching
3. Mode-locking.

As solid-state lasers, fiber lasers demonstrate the same types of operating regimes. However, the physical processes that take place in gain media (the fiber core) create challenges that are unique to fiber lasers, mainly because of their small cross-section dimensions compared with other active media (typical core diameter of diffraction-limited fiber lasers: 6–30 μm) and the very long length of gain material (typically in the multimeter scale). In comparison, semiconductor lasers also have gain material with very small cross-sectional dimensions, but the gain material length is on the submillimeter scale. In addition, because of the rare-earth nature of fiber lasers' active ions, energy storage in fiber laser systems is high. In addition to possibility of high energy/peak power pulse production by fiber lasers, these characteristics create challenges in nonlinear processes and damage processes, which have to be addressed during fiber laser design and development.

Like many other laser types, fiber lasers also can operate in the following operational modes:

1. *Quasi-CW operation (QCW)*: When the pump source is opened only for short period of time to prevent excessive heating of the gain medium or pump source.
2. *Gain-switched operation*: When the pump source (i.e., master laser; usually another laser with high peak power and short laser pulse) is pumping another laser (i.e., slave laser) only during short time periods within the time frame of the excited state lifetime of the slave laser source. Such excitation results in direct slave laser gain modulation. This technique is widely used for pumping of high-gain solid-state lasers, such as Ti^{3+}:sapphire, Cr^{4+}:forsterite, Cr^{4+}:YAG, as well as color center lasers.

V. Ter-Mikirtychev, *Fundamentals of Fiber Lasers and Fiber Amplifiers*,
Springer Series in Optical Sciences 181, DOI: 10.1007/978-3-319-02338-0_8,

3. *Q-switched mode-locked operation*: A combined regime when simultaneous mode locking and Q-switching of the laser takes place, such as when the Q-switched laser pulse envelope contains mode lock laser pulses, or under continuous pumping conditions the laser generates a train of such complexly modulated pulses.

This section provides a more detailed description of the three main laser regimes. It qualitatively describes the essential differences and challenges of CW and quasi-CW operational regimes and gives a detailed theoretical and qualitative analysis of the Q-switch and mode-lock operation. The motivation behind such different treatments of CW and high peak power regimes is in the different degree of challenges and issues that researchers face during laser development. For CW fiber lasers, the main challenge is usually twofold: thermal management and nonlinearities. Because of the relatively low power level (on a watt to kilowatt scale), nonlinearities that appear in CW lasers mostly affect power scaling at a very narrow laser spectral line width in the kilohertz to megahertz range. In high peak power lasers, such as Q-switched or mode-lock lasers, high peak powers of hundreds of kilowatts to megawatts not only restrict power scaling but also affect almost all fiber laser parameters, such as spectral line width, damage threshold, and power stability.

8.1.1 CW and Free-Running Operation of Fiber Lasers

8.1.1.1 Qualitative Descriptions of the Essential Differences and Challenges

Free-Running Operation

Free-running (or QCW) operation occurs when the laser-active medium is excited by the pump pulses with energies enough to sustain laser operation; no other intracavity laser components are used to control/modulate the laser pulse temporal profile. Usually, the pump pulse duration is on the order of the active medium's lifetime. Such pumping results in a chaotic number of individual pulses. Pulsed operation with significantly shorter pumping pulses and high enough peak power to modulate the pumped laser gain is called *gain switching* (reviewed later in this section).

The QCW regime of laser operation is usually applied when one needs to limit thermal effects in the laser-active medium. The pump is switched on only for a certain period of time, which is enough to reduce thermal effects, while the laser pumping process is close to its steady-state condition. For temperature-related issues, one may consider the so-called duty cycle (DC)—the parameter that shows how much time the laser is exposed to the pumping within one pumping circle:

$$\mathrm{DC} = \frac{t_p}{T_p} \tag{8.1}$$

where t_p is the laser pulse duration and T_p is the distance between pulses (i.e., period of the pulse train). For instance, if a diode laser with a pulse duration of 0.001 ms fires one periodical pulse at a frequency of 10 pulses per second (10 Hz), the diode laser DC is 0.00001 (0.001 %). The DC of CW operation is therefore equal to 100 % because there are no pulses.

Low-DC laser operation (a few percent or less) strongly reduces the thermal effects in glass material, which in turn can reduce heat-related damage. At the same time, applying techniques such as Q-switching still allows one to achieve very high peak power in a pulse-repetitive mode. When average power is not an issue and high peak power is required, the QCW operating regime is a very good solution because QCW laser diodes and laser diode arrays are able to deliver a large amount of energy into the active medium within a short pumping pulse. In the case of fiber lasers, for which thermal management requirements are relaxed compared with diode-pumped solid-state lasers, QCW operating regime is not very commonly used unless high peak power is required, and it is not limited by bulk and surface damage of the fiber laser intracavity components. Note that thermal management issues still exist in fiber lasers due to finite heat dissipation in gain fiber and thus need to be addressed. These issues usually occur in the case of high laser average power and need to be taken into consideration during design and development. Therefore, the development of new fiber lasers with small quantum defects is an important task for several applications.

CW Operation

In CW laser operation, the laser is continuously pumped and continuously oscillates in single or multiple longitudinal or transverse modes. The CW mode is applied when one requires high average power and high power stability of the laser emission. The CW (or CW-pumped) fiber laser class is one of the most important and demanded class of lasers for different industrial, military, and scientific applications.

Like in all other types of lasers, especially solid-state lasers, the CW regime of fiber lasers follows similar physics and theory. The main difference during the design and development of CW fiber lasers compared with solid-state lasers is associated mostly with nonlinear scattering processes and other nonlinear processes (some of which should be taken into consideration when designing solid-state lasers as well). The other nonlinear processes mentioned previously are associated with refractive index influence by high-power propagating inside the fiber core. These nonlinear processes include the optical Kerr effect, self-focusing, cross-phase modulation, and four-wave mixing. In addition, heat management and damage of the bulk fiber glass and end surfaces are also essential during fiber laser design. Modeling of the main nonlinear scattering processes, such as stimulated

Brillouin scattering and stimulated Raman scattering (discussed later), contributes to successful development.

Despite the widespread opinion that fiber lasers are generally a thermal problem free system is just not valid opinion without considering level of power under design. Potential thermal management issues of CW fiber lasers as important as other with other design parameters. Most development of CW fiber lasers focuses on power scaling, which is connected to the selection of high-power fiber-coupled components, such as isolators, pump couplers, and gain fibers with appropriate core and clad diameters, as well as their numerical apertures.

Presently, the most developed CW fiber lasers systems are based on Yb^{3+}, Er^{3+}–Yb^{3+}, Er^{3+}, Tm^{3+}, and Nd^{3+}. Free space and fiber-coupled laser diodes used for pumping mentioned fiber gain materials are available from a number of companies with power levels of several hundreds of watts. The main challenge in CW fiber laser commercialization is connected with the development of commercially available high-power tolerant fiber-coupled laser components. The typical diode laser wavelengths used for pumping applications are 793, 915, 980, 1,480, and 1,530 nm. Note that several impressive CW fiber laser demonstrations have been made in achieving high-power performance. Yb^{3+}-based fiber lasers operating in the 1 μm spectral range demonstrate the following highest power levels (IPG Photonics, 2011): (a) 50 kW in the MM regime, with $M^2 \approx 30$; (b) 10 kW in the SM regime (i.e., close to diffraction-limited operation) with $M^2 \approx 2$; and (c) 1.1 kW in the PM regime with $M^2 \approx 1.1$. At the same time, the highest fiber laser power for the 1.5 μm spectral range with diffraction-limited beam quality is currently in the range of several hundreds of watts, approaching the 1 kW level obtained with the Yb^{3+}–Er^{3+} system. Both Yb^{3+} and Er^{3+} fiber laser systems are pumped with InGaAs high-power diode lasers.

8.1.2 Q-Switched Operation of Fiber Lasers

Q-switched fiber lasers are currently one of the most important and challenging types of fiber lasers because they have probably highest potential (when operating at high average power levels) for different applications (including nonlinear frequency conversion). However, they suffer from bulk and surface damage resulting from high peak power pulses that interact with fiber material for nanoseconds.

This section briefly reviews the basic theory of Q-switched laser operational regimes and then mentions the challenges associated with this mode of laser operation for high peak power fiber lasers. The section begins with general Q-switch theory and then goes on to the CW-pumped, repetitive Q-switch regime in fiber lasers.

Q-switching of the laser resonator was first introduced in 1961 by Hellwarth [1] and experimentally demonstrated by McClung and Hellwarth in 1962. The main idea of laser cavity Q-switching is that the laser should produce high peak power and short pulses if the laser resonator Q factor changes rapidly from its highest

value to the lowest (i.e., when intracavity loss changes from a high to low value). Initially, laser action is disabled by introducing a high loss (low Q condition). During such a low Q condition, pump power builds up the inversion population; when the latter reaches its peak value, the laser cavity Q factor switches to its high value (i.e., intracavity loss is removed). As soon as the laser cavity Q factor is high, radiation starts to build up inside the laser resonator from its spontaneous emission. After a certain period of time (buildup time or delay), due to the high value of the inversion population, the laser dynamically (through stimulated emission) generates a high intensity pulse within a short period of time, which is called the Q-switched laser pulse or giant pulse (Fig. 8.1).

8.1.2.1 General Analyses of the Laser Q-Switched Operating Regime

Following the original work of Wagner and Lengyel [2], consider a laser cavity with two end reflectors: gain medium and Q-switch device. Here, formulas for calculating the main parameters of the laser emission in Q-switch mode of operation are outlined.

In their analyses, Wagner and Lengyel [2] introduced the normalized variables:

$$\bar{n} = \frac{N}{N_0} \tag{8.2}$$

where N is the population inversion per unit volume and N_0 is the number of active ions in the volume element (concentration).

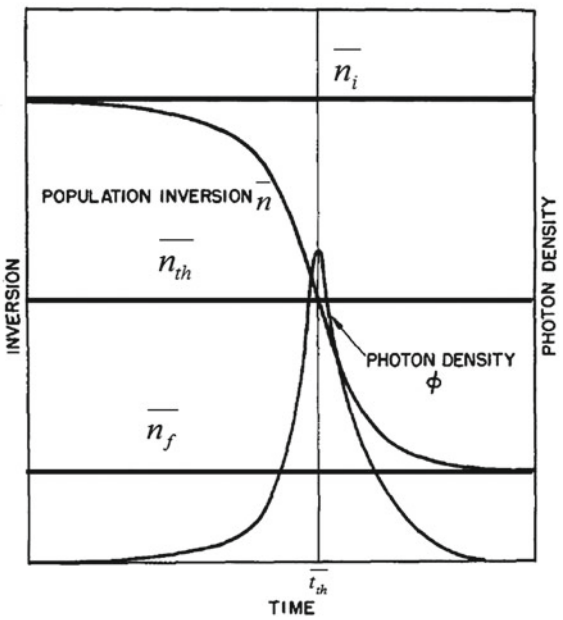

Fig. 8.1 Inversion in the Q-switched pulse (Reprinted with permission from [2])

The normalized initial and final population inversions per unit volume for the high ($\bar{n}_i$) and low ($\bar{n}_f$) Q state of the laser cavity during the pump process are related by the following transcendental equation:

$$\bar{n}_i - \bar{n}_f = \bar{n}_{\text{th}} \cdot \ln\left(\frac{\bar{n}_i}{\bar{n}_f}\right) \tag{8.3}$$

where the $\bar{n}_{\text{th}}$ population inversion density at the threshold can be expressed as:

$$\bar{n}_{\text{th}} = \frac{\ln\left[\frac{1}{R_1 R_2}\right] + N_0 \sigma_{\text{al}} L}{2N_0(\sigma_{\text{el}} + \sigma_{\text{al}})L} \tag{8.4}$$

where R_1 and R_2 are reflectivity of the laser cavity mirrors, σ_{el} and σ_{al} are the emission and absorption cross-sections of the laser-active ion at laser wavelength, N_0 is the total concentration of laser-active centers, and L is the fiber gain medium length. Output energy of the Q-switched laser pulse can be expressed as follows:

$$E_p = h\nu_L \frac{1}{\gamma} V N_0 \cdot (\bar{n}_i - \bar{n}_f) \tag{8.5}$$

where V is gain volume, N_0 is the number of active ions in the volume element (concentration), $h \times \nu_L$ is the photon energy at laser emission frequency, and $\gamma = 1 + g_2/g_1$, g_1, g_2 are degeneracies of the upper and lower laser levels. Note that for a three-energy level system with no degeneracy $g_2/g_1 = 1$, $\gamma = 2$. For a four-energy level system, $\gamma = 1$.

Consequently, the duration of the Q-switch pulse is:

$$t_p = T_{\text{res}} \frac{\bar{n}_i - \bar{n}_f}{\bar{n}_i - \bar{n}_{\text{th}}\left[1 + \ln\left(\frac{\bar{n}_i}{\bar{n}_{\text{th}}}\right)\right]} \tag{8.6}$$

where $T_{\text{res}} = L \cdot n/c \cdot \Gamma_{\text{tot}}$ is the lifetime of the laser photon in the laser resonator; Γ_{tot} is the total, single-pass logarithmic loss of the cavity (useful laser logarithmic output plus intrinsic logarithmic loss; i.e., $\ln(1 - T_{\text{int r}})$, where $T_{\text{int r}}$ is the overall intrinsic loss of the intracavity medium), and n is the intracavity refractive index. Γ_{tot} can be expressed as follows:

$$\Gamma_{\text{tot}} = -\left[\ln\left(\sqrt{R_1 R_2}\right) + \ln(1 - T_{\text{int r}})\right] \tag{8.7}$$

Therefore, the peak power of the Q-switched laser pulse is:

$$P_{\text{peak}} = \frac{E_p}{t_p} \tag{8.8}$$

or

$$P_{\text{peak}} = \frac{1}{2}\left[\bar{n}_{\text{th}} \log(\bar{n}_{\text{th}}/\bar{n}_i) + \bar{n}_i - \bar{n}_{\text{th}}\right]\left(\frac{V N_0 h\nu_L}{T_{\text{res}}}\right) \tag{8.9}$$

8.1.2.2 CW-Pumped, Repetitive Q-Switching Regime Analyses

We will start by estimating the maximum obtainable pulse energy from a CW-pumped Q-switched laser. The maximum extracted pulse energy from a CW-pumped Q-switched laser is given by [2, 3]:

$$E_p = h\nu_L \frac{1}{\gamma} V \Delta N \tag{8.10}$$

where $h\nu_L$ is the laser photon energy, V is the gain volume, and ΔN is the population inversion difference per unit volume (non-normalized) between high (N_i) and low (N_f) Q mode of operation:

$$\Delta N = N_i - N_f \tag{8.11}$$

Note that because most practical CW-pumped lasers are four-energy level (or quasi-four-energy level), we will assume that $\gamma = 1$. We also assume that $N_i \langle\langle N_T$, which is valid for four-energy-level laser systems, and $N_\infty = \sigma_{ap} \times I_p \times \tau_{21} \times N_{th}$, which is an asymptotic value of the population inversion that is reached during the time duration between laser pulses larger than the time of spontaneous decay τ_{21} under a pumping intensity I_p. Then, solving a rate equation that describes the pump circle can give us the following expression for the time-dependent population inversion:

$$N(t) = N_\infty - \left(N_\infty - N_f\right)\exp\left(-\frac{t}{\tau_{21}}\right) \tag{8.12}$$

Consequently, for the repetitive Q-switching with pulse repetition rate f, the maximum time available for the inversion population to build up between laser pulses is:

$$\Delta t = \frac{1}{f} \tag{8.13}$$

Therefore, the expression for the value of population inversion achieved during such a buildup of time becomes:

$$N_i = N_\infty - \left(N_\infty - N_f\right)\exp\left(-\frac{1}{\tau_{21} f}\right) \tag{8.14}$$

In the approximation of ASE free operation (i.e., when N_f is negligibly small) and in the case when the laser is Q-switched with repetition rate f, we can express the population inversion difference per unit volume between high (N_i) and low (N_f) Q modes as follows:

$$\Delta N = N_i - N_f \exp\left(-\frac{1}{\tau_{21} f}\right) = N_\infty \left(1 - \exp\left[-\left(\frac{1}{\tau_{21} f}\right)\right]\right) \tag{8.15}$$

The output laser power in the CW regime is proportional to the difference of population inversions in the absence of stimulated emission (N_∞) and that at the laser threshold (N_{th}) and can be expressed as follows:

$$P_{\text{CW}} = \left(\frac{T}{T + L_{\text{RT}}}\right) h\nu_L V \frac{(N_\infty - N_{\text{th}})}{\tau_{21}} \tag{8.16}$$

where τ_{21} is the upper laser level lifetime, T is the transmission of the laser output coupler, and L_{RT} is the laser cavity round-trip loss.

The threshold value of population inversion (similar to the previous paragraph) can be expressed as follows:

$$N_{\text{th}} = \frac{\ln\left[\frac{1}{R_1 R_2}\right] + N_0 \sigma_a^L L}{2\left(\sigma_e^L + \sigma_a^L\right) L} \tag{8.17}$$

Consequently, the Q-switched laser pulse energy can be expressed by:

$$E_p = h\nu_L V N_\infty \left(1 - \exp\left[\frac{1}{\tau_{21} f}\right]\right) \tag{8.18}$$

or

$$E_p = \left(P_{\text{CW}} \tau_{21} + N_{\text{th}} h\nu_L V\right) \cdot \left(1 - \exp\left[\frac{1}{\tau_{21} f}\right]\right) \tag{8.19}$$

Knowing the fiber laser output power in the CW regime and the active ion spectroscopic parameters along with the gain fiber geometrical parameters, one can calculate the Q-switched laser pulse energy.

Laser average power can be expressed as:

$$P_{\text{av}} = \left(\frac{Tf}{T + L_{\text{RT}}}\right) h\nu_L V \left(N_i - N_f\right) \tag{8.20}$$

Finally, we will give an expression for the ratio of the CW-pumped Q-switched laser average power and output power in CW operation because this is an important measure of the laser performance:

$$\frac{P_{\text{av}}}{P_{\text{cw}}} = \frac{f\tau_{21}}{T} \left(\frac{N_i - N_f}{N_\infty - N_{\text{th}}}\right) \tag{8.21}$$

where T is the transmission of the laser output coupler.

8.1.2.3 Damage Problem

In optical materials, laser damage is a complex subject because of the many factors affecting the phenomenon, such as the presence of material volume defects and surface polishing quality. Creating a single model that can describe laser-induced

damage at different power levels and different qualities of the material irradiated by the laser beam appears to be a very challenging task. Nevertheless, a few laws were found to describe fairly well the bulk and surface damage thresholds of dielectric materials, thus providing a ballpark value of the damage threshold.

The well-established square root law [3] describes the bulk damage of solid-state materials, such as crystal or glasses, and can be reasonably well applied to fiber laser systems. As is well known, the energy fluence [J/cm^2], which corresponds to the limit when bulk damage start appearing in dielectric solids such as crystals or glasses, can be expressed as follows [4]:

$$F \approx 25 \times \sqrt{t_p} \tag{8.22}$$

$$(F \approx 10 \times \sqrt{t_p} \text{ for the case of surface damage }) \tag{8.23}$$

where t_p is the laser pulse duration expressed in nanoseconds. This formula works quite well for nanosecond pulses longer than 5–10 ns, which is the case of most Q-switched fiber lasers. (For pulses close to 1 ns in duration, this formula may not be as accurate.) Assuming several meters of total fiber laser cavity roundtrip time, which gives a pulse duration of tens nanoseconds for the Q-switch pulses, we can see that if the pulse duration is 25 ns, the maximum allowed laser pulse energy fluence when the laser fiber is in bulk damage-free condition is $\sim$125 J/cm^2. If we take the gain fiber diameter of 30 μm, which is almost the highest currently commercially available for diffraction-limited operations, the allowed pulse energy is about 880 μJ, which in turn corresponds to about 30 kW of pulse peak power. For comparison, Q-switched solid-state lasers such as Nd:YAG can easily exceed tens of millijoules in pulse energies and over a megawatt of peak power in damage-free operation because of the bigger mode size of solid-state lasers. The typical damage pattern of the fiber laser output resulting from high peak power output laser pulses is illustrated in Fig. 8.2.

Another challenge of high peak power fiber lasers (which include Q-switch and mode-locked systems) is to suppress the so-called self-phase modulation (SPM), described in more detail later in the book, and in such a way to preserve the original or required spectral line width of the laser. This is usually achieved by properly designed gain fiber core diameter and length, as well as the profile of the laser pulse propagating inside the fiber. The ratio of the rise time of the laser pulse to the pulse duration is critical for SPM (and therefore the resultant laser spectral line-width), which can be minimized by using Gaussian laser pulses. The laser line broadening due to SPM is maximized with super-Gaussian laser pulses.

Note that when the pulse duration approaches the 1 ns barrier (or less), the optical breakdown processes, which include avalanche ionization and avalanche breakdown, are too slow. Therefore, the damage threshold for short laser pulses with sub nanosecond durations (or even below 10 ps) is usually higher. This fact explains why short-pulse fiber lasers (especially mode-locked fiber lasers, described in the next section) are more successful in scaling the fiber laser pulse energy up to several millijoules and peak powers of $\sim$10 MW and higher.

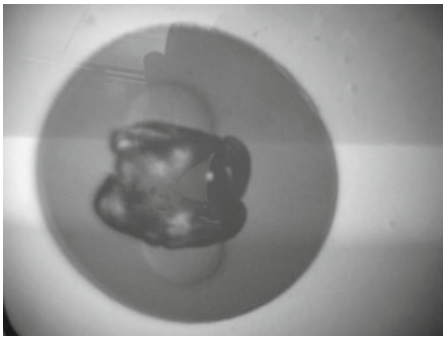

Fig. 8.2 Typical fiber core damage pattern from self-pulsing or high peak power pulse propagation inside the fiber core (Panda-type fiber is shown)

Long cavities in fiber lasers are problematic for short Q-switch pulse production directly from the fiber laser oscillator. Therefore, researchers and engineers use a master oscillator power amplifier system (MOPA; discussed later in the book) in fiber laser systems when the seed laser is amplitude/intensity modulated with a required short pulse duration; therefore, it is subsequently amplified to the necessary power level using fiber amplifiers (usually in several amplifications stages).

8.1.2.4 Surface Versus Bulk Damage

Usually, the surface damage threshold is a factor of 2–5 times lower than the bulk damage. In crystallography, the surface of the material represents a special type of crystal lattice defect; therefore, the surface damage threshold is expected to be lower than that of the bulk damage threshold. The surface damage threshold reduces by a factor of 4–5 compared with the bulk damage threshold [5]. In fibers that are mostly made of silica glass (especially those of high-power fiber lasers), surface damage on the connectors or bare fiber ends is typical. Keeping the fiber end surface clean usually extends damage-free operation.

8.1.2.5 Q-Switch Fiber Laser Example

An interesting example of a Q-switched fiber laser is shown in Fig. 8.3, which is a schematic of a laser designed by Chen et al. [6] demonstrated enhanced Q-switching in a double-clad fiber laser with increased peak power by an order of magnitude compared with conventional Q-switch operation. A pulse duration of $\sim$2 ns and peak power of $\sim$3.7 kW were achieved. As seen in Fig. 8.3, the laser employs an acousto-optical modulator (AOM) as a Q-switch intracavity device. The authors enhanced peak power by using a stimulated Brillouin scattering process, which reduced the laser pulse duration and subsequent amplification in a double-clad fiber with a high level of inversion population. An increased level of inversion population and reduced ASE level can be achieved by implementing

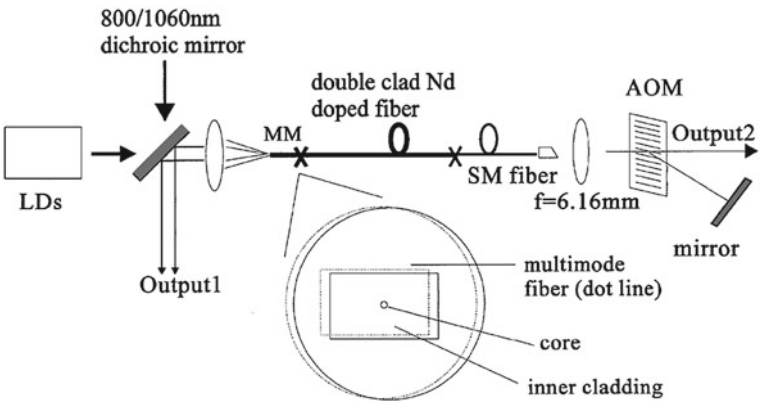

Fig. 8.3 Setup of an enhanced Q-switched Nd^{3+} fiber laser. *LD* Laser diode, *MM* Multimode fiber, *SM* Single mode [6] (Image courtesy of the Optical Society of America)

diffraction-order resonant operation of the AOM, which completely blocks the laser cavity mirror during buildup of inversion.

Unlike other solid-state lasers, fiber lasers have a very high gain. The AOM based Q-switch is often used when operating in the non-zeroth diffraction order for the feedback. In other words, the laser cavity mirror is aligned along the axes of the diffraction order (usually first) and the AOM shutter is on when the radio-frequency (RF) power is applied. In this way, when the cavity is closed (i.e., when no RF power is applied to the AOM modulator; low Q condition), the ASE is not supported by the cavity mirrors and does not get reflected back into the gain fiber. The cavity mirror is completely blocked from possible feedback during inversion buildup. When RF power is applied, the intracavity laser beam gets deflected into the diffraction order and the resonator mirror starts providing feedback to the gain fiber. The Q-switch pulse starts its buildup and eventually gets emitted.

8.1.3 Mode-Locking of Fiber Lasers

Mode-locked fiber lasers attracted the attention of researchers mainly because they can simultaneously produce several important laser parameters, such as high peak power, high average power, relatively high pulse energy, high repetition rates, and diffraction-limited beam quality. These unique properties of mode-locked fiber lasers can be explained by several properties of fiber lasers in general, as well as by mode-locked lasers themselves.

First of all, because of the nature of line broadening in laser glass, the gain band of rare-earth-doped fibers is quite broad (on the order of tens of nanometers). This in turn allows the generation of the femtosecond laser pulses. In contrast, the inhomogeneous nature of the broadening of the spectral lines in glass is

problematic for an energy-efficient narrow line-width in the glass laser oscillator. In the fiber laser, however, because of the high gain that comes from the long fiber length and small core diameter, this type of glass laser is quite power efficient. Secondly, the high gain of fiber laser material allows the the fiber lasers to operate with quite low pump powers and to use intracavity optical elements with relatively high optical losses. Several dispersion compensation elements used in mode-locked fiber lasers cannot be used in traditional bulk solid-state lasers.

8.1.3.1 General Analysis of the Laser Mode-Locking Operating Regime

The regime of so-called mode-locking in lasers has been studied since the early 1960s. In laser literature, several published reports on the mode-lock operation of the laser appeared in 1963. Since that time, laser mode-locking has been studied extensively, both experimentally and theoretically [7]. This section gives a general analysis of the mode-locking regime of the laser operation.

In a free-running regime of operation, the laser oscillation is a complex combination of transverse and longitudinal modes without phase or amplitude correlation between modes. It is interesting to consider a situation in which the adjacent longitudinal modes under passive (from passive intracavity devices) or active (from active intracavity device) modulation are forced into constant phase differences between each other. The process that leads to the establishment of such a fixed adjacent longitudinal mode phase separation is called *mode-locking*.

During the mode-locking process, the laser system starts from noise, which consists of a series of short, irregular pulses with irregular phases. These pulses are travelling back and forth between the two end mirrors of the laser resonator and are amplified by each transit in the laser-active medium. Kuizenga and Siegman [8] developed a theory describing mode-locked laser operation, predicting the mode-locked laser pulse duration and the mode-locked laser spectral bandwidth. According to Kuizenga and Siegman [8], there are two competing mechanisms affecting the creation of intracavity laser pulse width during the mode-lock regime. The first mechanism is due to the laser gain, which leads to the bandwidth-limited gain factor and thus a reduction in the spectral width of the intracavity laser pulses, therefore lengthening the pulse width in each transit. The second mechanism is related to the effect of the modulator. The modulator shortens the pulse by affecting the pulse tails due to the time-varying transmission of the modulator.

The equilibrium condition between the lengthening from the active medium and shortening due to the modulator eventually determines what the steady-state pulse width is. The pulse gets shorter per transit, and one pulse per roundtrip time is selected. In a spectral domain, the development of the mode-locked regime is related to the amplitude modulator's modulating frequency. If the amplitude is modulated with a sinusoidal modulation at a frequency $\Delta\omega_{\text{res}}$, which is equal to the inverse value of the laser resonator round trip, the sinusoidal modulation of the central mode at the modulation frequency produces sidebands at $\omega \pm \Delta\omega_{\text{res}}$. These

sideband frequencies injection-lock the adjacent modes, which in turn lock their neighbors. According to Kuizenga and Siegman [8], in the case of the amplitude modulation (AM) type of the intracavity optical modulator, the mode-locked laser pulse width and the laser pulse spectral bandwidth are as follows:

$$\Delta t_p = \frac{\sqrt{\ln 2 \cdot \sqrt{2}}}{\pi} \cdot \left(\frac{g_0 \cdot L}{\delta_l}\right)^{\frac{1}{4}} \cdot \left(\frac{1}{f_m \cdot \Delta v_g}\right)^{\frac{1}{2}} \tag{8.24}$$

$$\Delta v_p = \frac{\sqrt{2 \cdot \ln 2\sqrt{2}}}{1} \cdot \left(\frac{g_0 \cdot L}{\delta_l}\right)^{-\frac{1}{4}} \cdot \left(\frac{1}{f_m \cdot \Delta v_g}\right)^{-\frac{1}{2}} \tag{8.25}$$

where Δv_{g} is the gain bandwidth of the laser medium; f_m is the modulator frequency, which is expected to be close to the inverse value of the roundtrip time; $g_0 \cdot L$ is the laser gain, and δ_l is the modulation depth. Note that for the case of AM modulation, the pulse width–bandwidth product is $\Delta t_p \cdot \Delta v_g = 0.44$. ($\Delta v_g$ is the spectral bandwidth of the mode-locked Gaussian pulse.)

Further assume that the laser demonstrates M longitudinal modes. The electric field of an individual mode i can be expressed by the following formula [7]:

$$E_m(z,t) = E_{0m}\sin[\omega_m t + \phi_m] \cdot \sin[k_m z] \tag{8.26}$$

where z is the coordinate along the propagation direction, E_{0m} is the mode field amplitude, ω_m is the mode frequency, c is the speed of light, ϕ_m is the phase of the field of the mth mode, and $k_m = \omega_m/c$ is the wave-number of the mth mode.

If we introduce the central frequency ω_0 of the laser emission spectrum, the following formula will describe the spectral position of each of the m longitudinal modes:

$$\omega_m = \omega_0 + m\Delta\omega_{\mathrm{res}} \tag{8.27}$$

where $\Delta\omega_{\mathrm{res}}$ is a spectral separation of equidistant longitudinal modes of the Fabry–Perot interferometer located on the frequency axis (expressed in hertz):

$$\Delta\omega_{\mathrm{res}} = \frac{2\pi c}{L_{\mathrm{res}}} = 2\pi \times \Delta v_{\mathrm{res}} \tag{8.28}$$

In the case of fiber analysis, the speed of light c has to be replaced in this formula by c/n, where n is the fiber material refractive index. L_{res} is the distance between laser cavity mirrors.

The resulting time dependent electrical field at point z can be expressed as:

$$E(z,t) = \sum_{m=0}^{M-1} E_{0m}\sin(\omega_m t + \phi_m) \cdot \sin(k_m \cdot z) \tag{8.29}$$

During a free-running regime, in the case of the homogeneously broadened spectral line, individual laser modes undergo amplification during the round trip of the laser cavity across the whole gain band of the laser medium. However, because

of the limited gain bandwidth and gain distribution inside the gain band, not all modes amplify evenly. Those modes whose spectral frequencies are at the wings of the gain profile undergo much less gain and therefore join the laser oscillation with a delay, compared with a mode corresponding to the central frequency of the gain band. After a number of the round trips, the free-running laser spectral bandwidth therefore gets narrowed compared with the luminescence band and even the spectral width of the gain band. The individual spectral modes, however, are not locked, and the mode phases are not related. In the case of multilongitudinal mode oscillation, the frequency resonances appear not only at the frequencies of the longitudinal modes, but also on their nonlinear (parametric) frequency mixed modes because of the mode interaction. This in turn further complicates achieving a steady state condition of the laser.

In addition, inhomogeneously broadened spectral lines, which take place in fiber lasers, contribute additional characteristics to the laser dynamics. These contributions are related to additional frequency variations, variations of the relaxation oscillations, and frequency interactions within the inhomogeneously broadened spectral line envelope [3, 9, 10]. Mode competitions and phase variations inside the oscillating spectral band result in the variation of frequencies of each mode. The unlocked laser is therefore noisy. In general, if the laser cavity lifetime is long compared to the lifetime of the population inversion, the laser tends to be stable. If, however, the lifetime of the population inversion is long compared to the laser cavity lifetime, the laser is unstable and demonstrates spiking in its temporary profile. On the other hand, when the mode phases are locked, the field of each mode reaches the maximum at the same time. The mode competition in a locked laser therefore does not exist, and all modes are equidistantly positioned in the frequency domain. Note that the noise in mode-locked lasers is significantly reduced by several orders of magnitudes compared with a free-running (i.e., unlocked) regime.

Consider the electric field inside the laser cavity. The intracavity electric field in a standing-wave laser resonator can be expressed as:

$$E(z,t) = \sum_{m=\frac{M-1}{2}}^{\frac{M-1}{2}} E_{0m}(\exp[ik_m z] - \exp[-ik_m z])\exp(i\omega_m t) \tag{8.30}$$

and

$$E(z,t) = \sum_{m=0}^{M-1} E_{0m}(\exp[ik_m z] - \exp[-ik_m z])\exp(i(\omega_0 + m\Delta\omega_{\text{res}})t) \tag{8.31}$$

where z is the coordinate on the laser axis $0 < z < L_{\text{res}}$, L_{res} is the resonator length, k_m is the wave vector of the mth individual mode:

$$k_m = \frac{\omega_m}{c} = \frac{1}{c}(\omega_0 + m\Delta\omega_{\text{res}}) = k_0 + \frac{m2\pi}{L_{\text{res}}} \tag{8.32}$$

where $m = 0, 1, \ldots M$.

The resultant field of the M modes is the following sum [7]:

$$\begin{aligned} E(z,t) = \exp\left[i\left(\omega_0 t - k_0 z + \frac{\pi}{2}\right)\right] \sum_{m=-\frac{M-1}{2}}^{\frac{M-1}{2}} E_{0m} \exp\left[im\left(\Delta\omega_{\text{res}} t - \frac{\pi z}{L_{\text{res}}}\right)\right] \\ + \exp\left[i\left(\omega_0 t + k_0 z - \frac{\pi}{2}\right)\right] \sum_{m=0}^{M-1} E_{0m} \exp\left[im\left(\Delta\omega_{\text{res}} t + \frac{\pi z}{L_{\text{res}}}\right)\right] \end{aligned} \tag{8.33}$$

Equation 8.33 shows that the field is modulated with the frequency $\Delta\omega_{\text{res}}$ inside the pulse envelope. Therefore, the distance between individual pulses in the envelope is equal to the laser cavity roundtrip t_{rt}. The front terms in each part of the above expression describe the light inside the laser cavity travelling to the right and to the left. The terms under the expression maximize at $z = 0$ (one of the cavity mirrors) and $t = 0$, that is, in the points where the high-intensity pulse is created. The new maximum appears when $t = \pi/\Delta\omega_{\text{res}}$ at a distance of $z = L_{\text{res}}$, which corresponds to the location of the second laser cavity mirror.

When $z = 0$ (at one of the cavity mirrors), the intracavity electric field can be expressed as:

$$\begin{aligned} E(t) = \frac{1}{2} \sum_{m=0}^{M-1} E_{0m} \exp(-i(\omega_0 + m\Delta\omega_{\text{res}})t + i\phi_m) \\ + \frac{1}{2} \sum_{m=0}^{M-1} E_{0m} \exp(+i(\omega_0 + m\Delta\omega_{\text{res}}t) - i\phi_m) \end{aligned} \tag{8.34}$$

All these modes will be locked once the following condition for phase is achieved:

$$\varphi_0 = \phi_1 = \cdots = \phi_m \tag{8.35}$$

If we assume for simplicity that, for all values of m, the amplitude of the individual field is $E_{0m} = E_0$ and the phase of individual field is $\phi_m = 0$, one can obtain the following sum for total electric field value:

$$\begin{aligned} E(t) &= \frac{1}{2} \sum_{m=0}^{M-1} E_0 \exp(i(\omega_0 + m\Delta\omega_{\text{res}})t) + \frac{1}{2} \sum_{m=0}^{M-1} E_0 \exp(-i(\omega_0 + m\Delta\omega_{\text{res}})t) \\ &= \frac{1}{2} E_0 \left[\exp(-i\omega_0 t) \frac{\exp(-iM\Delta\omega_{\text{res}}t) - 1}{\exp(-i\Delta\omega_{\text{res}}t) - 1} + \exp\left(+i\omega_0 t \frac{\exp(+iM\Delta\omega_{\text{res}}t - 1)}{\exp(+i\Delta\omega_{\text{res}}t)}\right)\right] \\ &= E_0 \frac{\sin^2\left(\frac{M\Delta\omega_{\text{res}}t}{2}\right)}{\sin^2\left(\frac{\Delta\omega_{\text{res}}t}{2}\right)} \cos\left(\omega_0 + (M-1)\frac{\Delta\omega_{\text{res}}}{2}\right)t \end{aligned} \tag{8.36}$$

Therefore, the laser intensity becomes:

$$I(t) = I_0 \frac{\sin^2\left(\frac{M\Delta\omega_{\text{res}}t}{2}\right)}{\sin^2\left(\frac{\Delta\omega_{\text{res}}t}{2}\right)} = I_0 \frac{1-\cos(M\Delta\omega_{\text{res}}t)}{1-\cos(\Delta\omega_{\text{res}}t)} \tag{8.37}$$

Equation 8.37 shows that the laser field is modulated with the function $F(t)$:

$$F(t) = \frac{1-\cos(M\Delta\omega_{\text{res}}t)}{1-\cos(\Delta\omega_{\text{res}}t)} \tag{8.38}$$

where frequency $\Delta\omega_{\text{res}} = 2\pi c/L_{\text{res}}$. Therefore, the distance between individual pulses in the envelope is equal to the laser cavity roundtrip, $t_{\text{rt}} = 2L_{\text{res}}/c$ (Fig. 8.4).

The number of modes that can be locked is related to the gain bandwidth of the laser-active medium Δv_g and the distance between adjacent longitudinal modes:

$$M = \frac{\Delta v_g}{\Delta v_{\text{res}}} \tag{8.39}$$

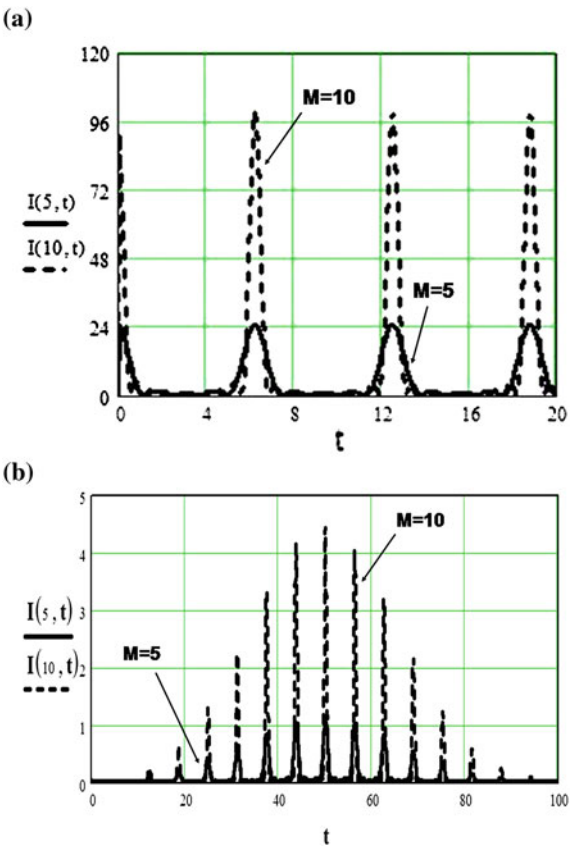

Fig. 8.4 The mode-locked laser intensity $I(t)$ for two numbers of oscillating modes: $M = 5$ and $M = 10$. **a** The pulse shape envelope is not taken into consideration. **b** The Gaussian pulse shape envelope is taken into consideration

To estimate the mode-locked laser pulse-width, we assume that it corresponds to the half of the time span between zeros of the function $F(t)$:

$$\Delta t_p = \frac{2\pi}{M\Delta\omega_{\text{res}}} = \frac{2L_{\text{res}}}{Mc} = \frac{2\pi}{\Delta\omega_L} \tag{8.40}$$

where $\Delta\omega_L = M\Delta\omega_{\text{res}}$ is the total laser spectral band width.

As a result of the uncertainty principle between the intensity of the individual laser pulse and its phase, one can obtain the following expression for the shortest pulse obtainable during mode-locking operation of the laser, which is:

$$\Delta t_p = \frac{C}{\Delta v_g} \approx \frac{t_{\text{rt}}}{M} \tag{8.41}$$

where constant C is the time bandwidth product. Constant C is equal to 0.44 for Gaussian-shaped pulses and 0.315 for sech^2-shaped pulses. The latter is very important in optical soliton laser oscillation and soliton pulse propagation. One can see from Eq. 8.41 for the minimum pulse width of the mode-locked laser that the minimum pulse duration is inversely proportional to the number of the locked longitudinal modes. In other words, under similar other laser parameters, the more longitudinal modes that are locked, the shorter pulse the laser is expected to generate. Therefore, active media with very broad emission spectra (e.g., transition metals in crystals, color centers, liquid dyes, laser-active glasses) are the most promising laser materials for ultra short pulse generation. For the same inter longitudinal mode distance for the laser resonator mentioned above, laser gain materials may cover a very big number of spectral modes.

It is interesting to compare the laser intensities for two cases: free-running (unlocked) and mode-locked lasers. Assuming the laser demonstrates M operating modes, the peak and average power of the laser depend on the locking conditions of the individual laser modes. In the case of unlocked lasers, both average and peak power are proportional to the number of modes M:

$$P_{\text{FR,AV}} \approx ME_{0m}^2 \tag{8.42}$$

$$P_{\text{peak,FR},m} \approx ME_{0m}^2 \tag{8.43}$$

In the case of mode-locked lasers:

$$P_{M-L,\text{AV}} \approx ME_{0m}^2 \tag{8.44}$$

$$P_{\text{peak},M-L,m} \approx M^2E_{0m}^2 = \frac{t_{rt}}{\Delta t_p}P_{\text{AV},M-L} \tag{8.45}$$

Therefore:

$$\frac{P_{\text{peak},M-L,m}}{P_{\text{AV},M-L}} = M \tag{8.46}$$

One can see that the ratio of the average powers for these two regimes equals to 1, whereas the ratio of the peak powers is equal to M. One can also see that the peak power of the most intense mode-locked laser pulse is M times higher than the average power of the same laser. Therefore, in mode-locked lasers, the peak power has a strong dependence on number of modes. By knowing the laser cavity's geometrical parameters, such as cavity length, the mode-locked laser average power, and pulse duration, one can estimate the individual pulse peak power.

A generalization of the expression for the mode-locked pulse duration for the case of so-called Chirped pulses (i.e., when there is a linear frequency shift during the pulse) can be written as follows:

$$\Delta t_p = \frac{1}{\Delta v_g}\left(\frac{2\ln 2}{\pi}\right)\sqrt{\left(1+\left(\frac{\beta}{\alpha}\right)^2\right)} \tag{8.47}$$

where α is the Gaussian parameter (envelope) of the pulse and β is the pulse Chirp, both of which are determined from the electrical field of the laser pulse:

$$E(t) = \frac{1}{2}E_0 \exp\left(-\alpha t^2\right)\exp\left[i\left(2\pi v_L t + \beta t^2\right)\right] \tag{8.48}$$

In the time domain (i.e., oscilloscope trace), the regime of the laser mode-lock operation is viewed as a train of ultrashort laser pulses separated by a time difference equal to the laser cavity roundtrip time. Depending on the type of mode locking, the train of mode-locked pulses may either be enclosed on the Q-switched pulse envelope (Fig. 8.5) or simply represent a traveling pulse train (Fig. 8.6).

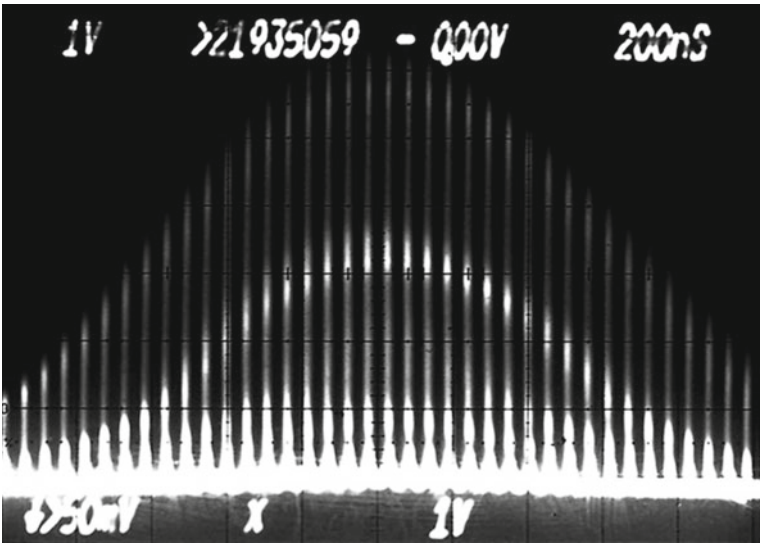

Fig. 8.5 Q-switched-mode-locked pulse train in a Yb^{3+}-doped fiber laser [26]. (Image courtesy of IOP)

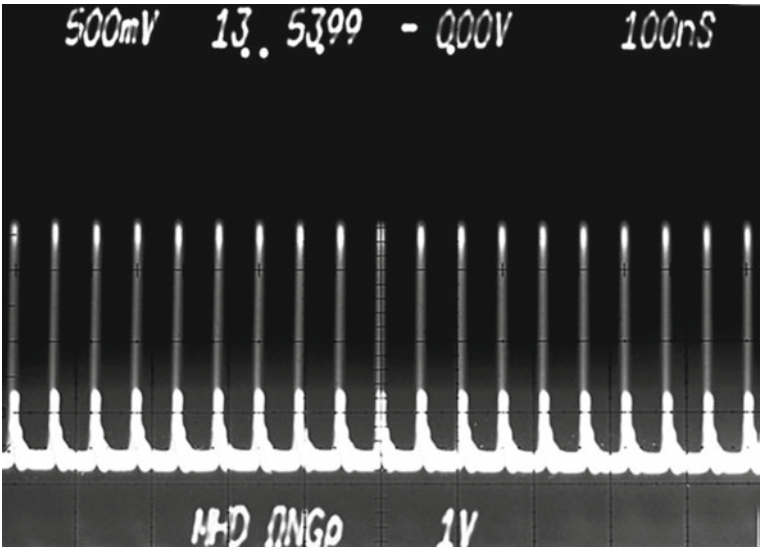

Fig. 8.6 Continuous wave mode-locking pulse train in a Yb^{3+}-doped fiber laser [26]. (Image courtesy of IOP)

(The distance between two pulses on these figures, which corresponds to the resonator roundtrip time, is approximately $t_{rt} \approx 50$ ns.)

Similar to Q-switching, mode-locking of the laser can be realized using active and passive techniques. In the case of active mode-locking, one needs to modulate the laser resonator parameters with a frequency equal to (or equal to integer number) the frequency difference between adjacent longitudinal modes. Usually this type of mode-locking is realized using acousto-optical modulators, electro-optical modulators, synchronous pumping, or optically modulated saturable absorbers. In the case of passive mode-locking, a special passive nonlinear optical element is introduced into the laser cavity. Several techniques have been developed to implement passive mode-locking of the laser. Among those the most widely used are the saturable absorber (SA), Kerr lens mode-locking (KLM), and nonlinear polarization rotation (NLPR). For extended study of the mode-lock laser regime, the reader is referred to existing textbooks on laser physics [3, 9, 11].

Fiber lasers use both active and passive techniques to achieve the mode-locked regime of operation. Similar to the case of bulk lasers, these techniques include semiconductor saturable absorbing mirrors and acousto-optical switches. Nonlinearities in fibers, such as production of solitons, are widely used in production of ultrashort laser pulses.

A typical mode-locked fiber laser cavity consists of rare-earth-doped gain fiber, an intracavity intensity modulator (passive or active), a pump-coupling device (e.g., WDM), end mirrors (in case of standing-wave cavity), and an intracavity dispersion compensating device (e.g., a grating pair). The large normal

group-velocity dispersion of the intracavity fiber is compensated for or balanced by a dispersion compensation of the grating or prism pair. A problem associated with mode-locked fiber laser systems comes from polarization dependence of the intracavity intensity modulator performance. Usually, thermal perturbations cause polarization drift in the fiber, which in turn produce an unstable fiber laser output. There have been several solutions to this problem, including the use of polarization-independent modulator technology or all intracavity fibers, such as polarization-maintained (PM) fibers.

Note that having pulse durations in the subnanosecond range (as was mentioned earlier) is not enough to develop a time-dependent avalanche process, which leads to material breakdown. Mode-locked fiber lasers, especially those with pulse durations of less than 10–20 ps, have much higher glass damage threshold than Q-switched lasers. Mode-locked fiber lasers have several important applications in fundamental research and industry. They are also successfully used for nonlinear frequency conversion to ultraviolet, visible, and infrared spectral ranges because of their high laser peak powers.

8.2 Spectral Regimes

8.2.1 Wavelength Tunable Lasers

Fiber lasers, like most solid-state lasers, demonstrate similar techniques and schemes for wavelength tunable operation. As in their solid-state laser counterparts, tunable fiber lasers consist of the following main parts: gain medium, optical resonator mirrors, and wavelength dispersive element. As in solid-state lasers, the wavelength dispersive element can be a separate part of the fiber laser resonator or it can act as one of the fiber laser resonator mirrors.

This section briefly reviews some commonly used types of dispersive elements that are used in the design and development of tunable fiber lasers: diffraction gratings, prisms, birefringence plates, and intracavity etalons or their combination (e.g., grating-prism based tunable lasers). However, this list is not limited to these wavelength dispersive elements. For example, some intracavity wavelength dispersive systems, such as acousto-optical deflectors and tilted Fabry–Perot etalons, are also used by researchers. Again, as in other solid-state lasers, both CW and Q-switched laser operation regimes can be achieved for tunable fiber lasers.

8.2.1.1 Diffraction Gratings Based Tunable Lasers

Diffraction gratings are probably the most commonly used element in solid-state laser resonators. The popularity of this tuning element is due to its high wavelength selectivity (dispersion). However, metallic gratings have a relatively low damage

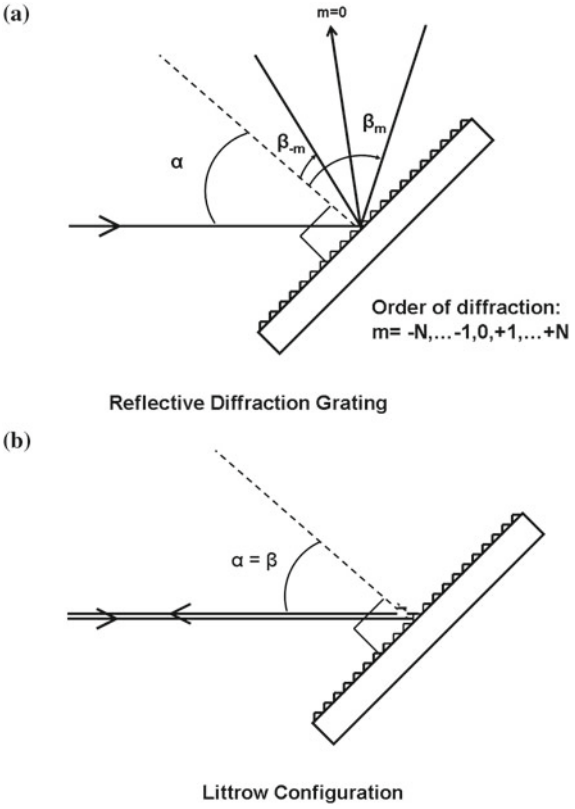

Fig. 8.7 Schematic and ray path in a plane reflective-diffraction grating

threshold, especially for the high peak power Q-switch nanosecond pulses and high pulse energies of the laser (i.e., ~ 1 J/cm^2 [12], although they withstand >150 kW/cm^2 power densities in the CW mode, as in the case of the 10.6 μm wavelength of the laser beam and power densities of more than 200 W/cm^2 [13, 14]).

Different gratings are presently used for different schemes of the tunable laser resonator and wavelength range. The groove density of the commonly used ruled gold- or aluminum-coated metallic diffraction gratings for tunable laser applications typically range from 300 to 1,200 grooves/mm. The groove density of the holographic gratings, which have greater dispersion than that of the ruled gratings, can reach 3,600 grooves/mm. Note that ruled diffraction gratings are successfully used in the infrared range of the spectrum, where their reflectivity is very high (over 95 %) in wide spectral range; holographic grating can be used in the visible and ultraviolet spectral range.

This section outlines the most important parameters of diffraction grating for laser tuning applications. In the Littrow configuration (Fig. 8.7b)—that is, when incident and diffracted rays are in autocollimation—the input and output rays propagate along the same axis (one of the most commonly used geometries, as described later).

Consider a reflective diffraction grating with the groove density d operating in the mth diffraction order, as shown in Fig. 8.7a.

Let us derive analytical expression for the diffraction grating angular dispersion because it plays an important role in the field of tunable lasers. A general, well-known relationship between the angle of incidence α and the angle of diffraction β_m in the case of reflective diffraction grating operating in the mth order of diffraction in a vacuum ($n = 1$) can be expressed as:

$$\sin\alpha + \sin\beta_m = \frac{m\lambda}{d} \tag{8.49}$$

where d is the grating period (i.e., the inverse value of the grooves' density $1/d$).

The angular spread $d\beta_m$ of the spectrum of the diffracted beam in mth order in the diffraction for wavelength span of $d\lambda$ is called the angular dispersion D_{grating}, which can be expressed as follows:

$$D_{\text{grating}} = \frac{d\beta_m}{d\lambda} = \frac{m}{d\cos\beta_m} \tag{8.50}$$

Substituting the ratio of the diffraction order to the groove period from the general diffraction grating relationship given above, one can obtain the following general formula, which relates the angular dispersion, incident angle, diffraction angle, and the wavelength:

$$D_{\text{grating}} = \frac{d\beta_m}{d\lambda} = \frac{\sin\alpha + \sin\beta_m}{\lambda\cos\beta_m} \tag{8.51}$$

In the case of Littrow configuration (Fig. 8.6b), $\alpha = \beta$, one can obtain the following expression for angular dispersion:

$$D_{\text{grating}} = 2\frac{\tan(\alpha)}{\lambda} \tag{8.52}$$

where α is the angle of incidence and λ is the wavelength.

For the diffraction gratings used in tunable laser resonators, the most important case is when the grating period produces only two working orders: zeroth and first diffraction order. In this case, intracavity losses introduced by the grating are minimal because the diffracted beam is used for the positive feedback in the laser resonator and zeroth order radiation is used for the output coupling. The diffraction grating period that corresponds to the Littrow (i.e., autocollimation) configuration can be defined as follows:

$$\frac{\lambda}{2} \le d_{\text{Littrow}} \le \frac{3\lambda}{2} \tag{8.53}$$

The minimum spectral transmission of the diffraction grating-based resonator can be calculated using the following formula:

$$\Delta\nu_{\min} = \frac{2(2\ln 2)^{0.5}}{\pi}\frac{\lambda}{D_{\text{grating}}w_0} \tag{8.54}$$

where w_0 is the radius of the intracavity laser beam on the grating surface.

As was previously mentioned, the most common way to use a diffraction grating in solid-state (or fiber) tunable laser is a first-order retroreflection (Figs. 8.7b, 8.8). In some cases, the incident power is divided between the zeroth and first diffraction-order reflections. In this case, the diffraction grating acts as one of the laser resonator mirrors (i.e., output coupler; Fig. 8.8). The collimated intracavity fiber laser beam is directed onto the diffraction grating and the first diffraction order is retroreflected back into the laser cavity. The laser output is coupled out through zeroth order of the grating diffraction. Rotating the grating around its vertical axis allows one to tune the wavelength of the radiation coupled out of the laser through the zeroth diffraction order. However, with the grating rotation, the output beam is steered; to achieve unidirectional output beam propagation, one may need to consider putting a high reflecting mirror next to the diffraction grating, which will create 90° with the mirror plane.

Another scheme, called the grazing incidence configuration, is used when more selectivity is required (Fig. 8.9). In this case, the diffraction grating is coupled with a mirror (or another grating), which returns the first diffraction-order reflection onto the grating for the zero-order output. The mirror rotation is used to achieve wavelength-tunable operation in the output beam. In this configuration, while the laser line-width gets narrower, the laser may be less power efficient due to increased intracavity loss (especially in the case of grazing incidence: double grating configuration).

Usage of the diffraction grating in a laser resonator should be realized in the location where the intracavity laser beam is collimated. This can be accomplished by placing the grating either at the end of the cavity just after the collimator (standing-wave resonator) or in one of the collimated ports of the intracavity fiber circulator (standing wave or ring cavity).

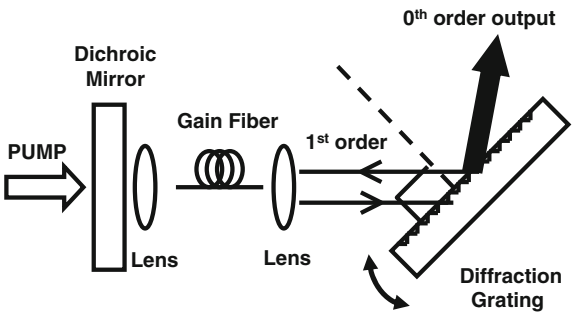

Fig. 8.8 Experimental setup of a tunable fiber laser with diffraction grating in the Littrow configuration

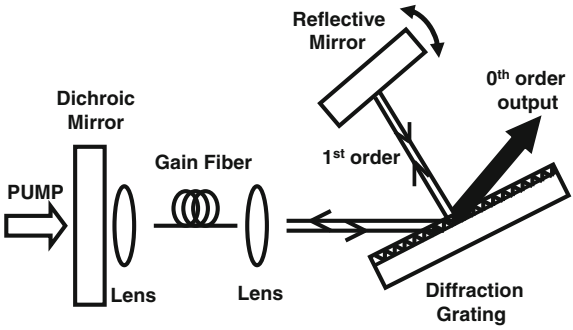

Fig. 8.9 Grazing incidence configuration with a wavelength-tuning rotating mirror

8.2.1.2 Prism-Based Tunable Lasers

The simplest and most cost-effective dispersive intracavity laser element is a simple optical prism. Material selection is usually dictated by the spectral range of operation and required dispersion, which is proportional to the prism refractive index. Fused silica is commonly used for the visible and near-infrared spectral range, where the highest possible dispersion is not required. In the same spectral range, prisms made of sapphire, YAG, or flint glass are used for higher dispersion. In the long wavelength range of the optical spectrum (i.e., near or over 3 μm), CaF_2 or similar crystals are widely used. In the ultraviolet spectral range, crystalline quartz is a good choice because it has high transmission in this spectral range. Because most laser systems are polarized, Brewster angle prisms can be used, which can provide minimal intracavity loss for *S* polarization. Note that a prism-based intracavity tuning element is one of the most power tolerant because its damage threshold is determined only by a surface and bulk damage threshold of the prism material, which is very high compared with metallic grating or even an etalon (which has reflective coatings with limited damage threshold; described later in this chapter).

Figure 8.10 shows a prism-tuned fiber laser schematic similar to that used by Hanna et al. [15]. The design employs a high-dispersion prism set consisting of three prisms (for increased dispersion) between a fiber end and feedback mirror (output coupler). The tuning is achieved by angular adjustment of the mirror close to the prism. If high reflecting mirrors are used on both resonator ends, the output radiation is coupled through the reflection from one facet of the prism. Note that a similar dispersive resonator is widely used for tunable solid-state lasers, such as Ti^{3+}:sapphire laser.

This section provides some formulas to calculate the prism-based tunable laser line-width. Dispersion of the single prism-based resonator with the prism's apex angle, which allows the incident light to enter the prism under the Brewster condition $(\tan \Theta_{BR} = n)$ on both prism facets, can be calculated by the following formula:

$$D_{\text{res}} = 4\frac{dn}{d\lambda} \tag{8.55}$$

The typical value of the dispersion $(dn/d\lambda)$ in visible spectral range for most prism materials is ~ 0.05 mrad/nm. Then, the full dispersion is $D_{\text{res}} = 2 \times 10^{-4}$ rad/nm.

For the prism-based laser resonator, the selective loss spectral distribution of the resonator has the following bandwidth:

$$\delta\lambda_{\text{res}} = \sqrt{L_{\text{loss}}}\frac{\theta_{\text{res}}}{D_{\text{res}}} \tag{8.56}$$

where L_{loss} is the total nonselective losses of the resonator at the wavelength of the laser emission and θ_{res} is laser divergence. If one assumes $\lambda_{\text{laser}} = 500\,\text{nm}$, nonselective losses of $L_{\text{loss}} = 0.01$, and laser divergence of $\theta_{\text{res}} = 0.001$, then the estimated bandwidth of the laser emission is close to: $\delta\lambda_{\text{res}} \approx 0.5\,\text{nm}$ or $\delta\nu_{\text{res}} \approx 20\ \text{cm}^{-1}$, which obviously points to a not very high selectivity of the prism-based resonator. The wavelength selectivity, however, can be improved using a sequence of prisms (Fig. 8.10) or an intracavity prism with a high index of refraction.

8.2.1.3 Birefringent Tuning Plates (Lyot Filter)-Based Lasers

The birefringent plate-based intracavity tuning element is another example of a high-power tolerant dispersive element. An intracavity wavelength filter of this type adjusts the wavelength of maximum transmission by rotation of the filter (Fig. 8.11).

Usually, a birefringent plate is cut in such way that its optical axis is in the plane of the plate [16]. Tuning of the wavelength is accomplished by rotation of the plate about its normal axes. The birefringent plate needs to be located between two polarizers or the plate has to be oriented at the Brewster angle to the laser

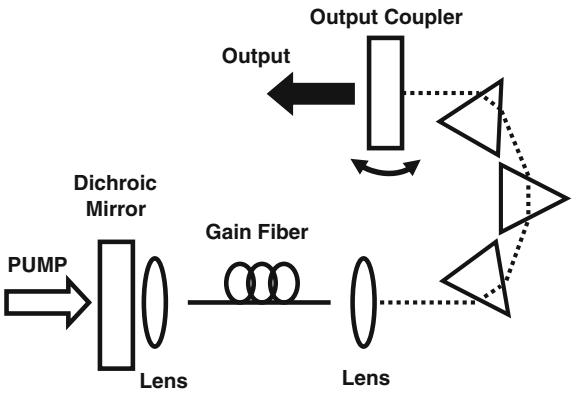

Fig. 8.10 Example of a prism-tuned fiber laser schematic

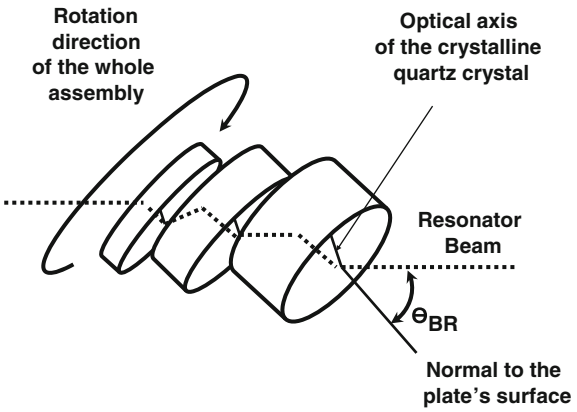

Fig. 8.11 A typical three-stage birefringent filter

resonator axis. Multiple plates are used for higher filter selectivity. Each individual plate of the so-called multistage Lyot filter is usually made of crystalline quartz. Each plate's thickness differs by an integer number.

Basic formulas are presented here to describe the operation of the birefringent tunable filter and its main parameters. For the case of the ring laser resonator (which is very important in fiber lasers), when the plate is inserted into the ring laser cavity at the Brewster angle (θ_{BR}), τ_F is defined as a transmission of the S-polarized beam through the plate as follows (assuming the P-polarized beam is transmitted through the plate without loss):

$$\tau_F = \frac{2n}{(n^2+1)} \tag{8.57}$$

where $n \approx (n_o + n_e)/2$, $(n_o + n_e)$, n_o/n_e are ordinary/extraordinary refractive indexes. Then, the ring laser resonator transmission band width can be computed as follows:

$$\delta\nu_{\mathrm{res}} \approx \frac{2(1-\tau_F)\cdot c}{\pi l_{\mathrm{plate}}(n_e - n_o)} \sqrt{-\left(\frac{\ln 2}{\ln \tau_F}\right)} \tag{8.58}$$

where l_{plate} is the plate thickness.

Figure 8.12 shows a typical linear tunable fiber laser schematic with a birefringent tunable filter as an intracavity wavelength selective element.

A more detailed description of Lyot filters for tunable laser applications can be found in Hodgkinson and Vukusic [16], Hanna e al. [17] and references therein.

8.2.2 Single Longitudinal Mode Lasers

Longitudinal laser modes (sometimes called axial modes) belong to the frequency domain of the laser mode structure. While oscillating on a single transverse mode

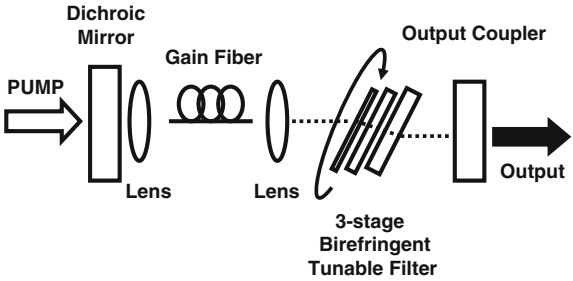

Fig. 8.12 Birefringent plate (Lyot filter)-based fiber laser

(TEM_{00} for open resonators and LP_{01} for optical fibers) with close to diffraction-limited beam quality, the laser may oscillate at the same time on several longitudinal (i.e., spectral) modes.

For a laser with the Fabry–Perot resonator length L_{res}, spacing of the laser longitudinal modes is given by:

$$\Delta v_{res} = \frac{c}{2nL_{res}} \tag{8.59}$$

where n is the refractive index of the space between laser cavity mirrors and c is the speed of light. From this formula, it is clear that the laser resonator mode structure is a sequence of periodic and equidistant discrete frequencies. If the laser gain medium has a gain band width that is wider than a longitudinal mode separation and the laser gain is high enough, several longitudinal modes that fall into the laser gain bandwidth have a chance to reach the threshold and participate in laser operation. Oscillation on several longitudinal modes is called *multi–longitudinal mode laser operation*.

The number of the longitudinal modes participating in the laser operation can usually be read as a third mode index. For open laser resonators, the general mode notation can be read as:

$$TEM_{mnq} \tag{8.60}$$

where q is the longitudinal mode index. The number of oscillating longitudinal modes in the laser depends on several factors, including (but not limited to) intracavity loss distribution at laser frequencies, length of the laser resonator, pump power, and laser medium gain band. If one is able to reduce the number of oscillating longitudinal modes to one, the laser starts oscillating on a single longitudinal mode; that is, it becomes a single-frequency (SF) laser.

8.2.2.1 Single-Frequency Laser Operation

In practice, the goal of selecting a single longitudinal mode of laser operation can be achieved using several effective and well-developed techniques:

1. Using an intra-cavity Fabry–Perot (FP) etalon, which creates its own transmission spectral profile on the background of the laser cavity mode separation and works as an intracavity axial mode filter.

2. Using a wavelength-dispersive, highly selective laser resonator, which creates high wavelength-dependent cavity losses on frequencies other than those selected for laser operation.

3. Using very short laser cavities, in which the laser resonator itself acts as a highly selective FP etalon (by frequency filter) by introducing increased separation of neighboring longitudinal modes.

4. Seeding a higher power laser by an SF seed laser, which is injection seeding based on the forced oscillation of slave (i.e., higher power laser, by injecting low power, SF master oscillator).

5. Using passive Q-switching, which uses a longer buildup time during passive Q-switch laser creation compared with that of active Q-switching (longer buildup times require more laser roundtrips of photons in the cavity, which in turn acts as a longitudinal mode discriminator).

6. Cooling of the laser gain medium, which is especially important in the case of solid-state lasers, when the gain medium emission spectral bandwidth gets narrower during cooling (this technique forces reduction of the laser gain band, which in turn reduces the number of longitudinal modes participating in laser action).

Different techniques are used in different types of lasers and at different operational conditions. This section gives a more detailed review of the techniques that are more practical and more widely used in fiber lasers.

8.2.2.2 IntraCavity Fabry-Perot Etalon

This technique is an effective method of single longitudinal mode selection in lasers and is widely used in fiber lasers for longitudinal mode selection (or tenability; e.g., with the scanning FP etalon by Micron Optics).

As mentioned previously, the laser resonator longitudinal mode separation is as follows:

$$\Delta v_{\text{res}} = \frac{c}{(2nL_{\text{res}})} \tag{8.61}$$

From this expression, one see that a thin intracavity FP etalon with a free spectral range bigger than the laser cavity mode separation can act as an efficient laser resonator axial mode filter. Here, the basic formulas for the FP etalon are given. The FP etalon mode spacing, which is also called the free spectral range (FSR), is determined by the following expression:

$$\Delta v_{\text{FSR}} = \text{FSR}_{\text{etalon}} = \frac{c}{2n_{\text{etalon}}L_{\text{etalon}}} \tag{8.62}$$

where n_{etalon} is the refractive index of the material between etalon reflecting surfaces and L_{etalon} is the distance between etalon reflecting surfaces (or base of the etalon). Another important parameter of the FP etalon is its finesse. For a loss-free etalon, finesse is determined by:

$$F_{\text{etalon}} = \frac{\pi (R_1 R_2)^{1/4}}{1 - \sqrt{(R_1 R_2)}} \tag{8.63}$$

The finesse indicates how much narrower the transmission peak of the etalon is than the spectral separation between neighboring transmission peaks (i.e., FSR).

One can deduce accordingly that individual transmission peak of the FP etalon has the following spectral width:

$$\Delta \nu_{\text{peak}} = \frac{\text{FSR}_{\text{etalon}}}{F_{\text{etalon}}} \tag{8.64}$$

As a rule of thumb to achieve a single longitudinal mode operation of the laser, the etalon $\text{FSR}_{\text{etalon}}$ should be wider than the laser medium-gain band. It also requires that FSR of the intracavity FP etalon is wider than the distance between the neighboring frequency modes of the laser resonator.

In an interesting case of so-called microchip lasers, the laser cavity itself is very short and acts as a laser resonator and FP longitudinal mode filter. Such lasers were proposed in the late 1980s and were based mostly on existing solid-state laser materials such as Nd:YVO_4, in which a high concentration of active ions allow efficient pump power absorption in a thickness of millimeter and submillimeter scales. With laser mirrors directly created on such thin crystal surfaces, the whole laser might be less than 1 mm thick and favorable conditions for SF oscillation are readily available. Microchip laser geometry is difficult to realize in the case of fiber lasers because of the long length of the fiber laser-active medium. However, SF microchip solid-state lasers can be used (and are used) as a master oscillators or seeds in high-power fiber laser MOPA systems.

Another widely used technique to achieve single-frequency oscillation in fiber lasers is based on the development of so-called fiber Bragg gratings (FBGs). FBGs can be directly written into the single-mode doped fiber core by recording a picture of periodical change of the core refractive index using an ultraviolet laser. Such a picture is a result of the interaction between two coherent ultraviolet laser beams, usually after a split of a single laser, that are then redirected to create an interference pattern on the fiber.

The fundamental physical principle behind FBG is Bragg reflection. When light travels through the region of periodically alternative regions of high and low refractive indexes, it is partly reflected at each index step. If the distance between the low and high index of refraction allows all the reflected light waves to add in phase, then the integrated reflection grows up significantly. This in-phase reflecting condition can be satisfied for certain wavelengths and is possible when the doubled distance between two reflections (grating period; i.e., the distance

between the low and high refractive index areas) is equal to an integral number of propagating light wavelengths:

$$\lambda_B = 2n\Lambda \text{ and } L_{\text{FBG}} = N\Lambda \tag{8.65}$$

where Λ is the grating period, N is the number of the FBG refractive index periodic variations, and and L_{FBG} is the FBG length.

It is useful here to give basic formulas for the calculation of the main parameters of FBG. There are two main parameters in the design of FBG and its applications: FBG reflectivity and FBG spectral bandwidth. The FBG reflectivity can be computed using the following expression [18, 19]:

$$R_{\text{FBG}} = \tan h^2\left(\frac{\pi\delta n L_{\text{FBG}}}{\lambda_B}\right) \tag{8.66}$$

where δn is the refractive index variation along the grating period.

The FBG spectral bandwidth can be expressed using following relationship:

$$\Delta\lambda_{\text{FBG}} = \left(\frac{2\delta n}{\pi}\right)\lambda_B \tag{8.67}$$

FBGs act as reflectors, and a couple of them inside the laser cavity can create an FP intracavity etalon. On the other hand, narrow spectral band reflective FBGs, used as a laser cavity mirror along with short gain fiber, allow the achievement of the single longitudinal operation of the fiber lasers. Figure 8.13 shows an example of SF fiber lasers using FBGs as a narrowband output coupler.

Another effective use of FBGs for SF fiber laser operation is a so-called distributed feedback (DFB) linear laser configuration. In this type of SF fiber laser, the Bragg grating is written into (or close to) the core of the gain fiber. For achieving single-sided output, the FBG was written on the fiber by offsetting the phase shift from the center position by half a grating period [20]. Single polarization is achieved by creating the phase-shifted FBG with ultraviolet light polarized perpendicular to the propagation axes of the gain fiber by forcing light photons with certain polarization states to be coupled into the waveguide. Using such an approach, researchers [21] achieved >20 mW of unidirectional and single polarization (PER $\sim$40 dB) fiber laser output.

Single-frequency lasers are widely used in science and technology for different applications, from optical communications and nonlinear optics to sensors of different types.

8.2.2.3 Minimum Line-Width of the Laser

When lasers operate on a single longitudinal mode, the minimum laser line-width is determined by the spontaneous emission noise. This is valid for gas and most types of solid-state lasers. Based on a semi-classical approach, the following

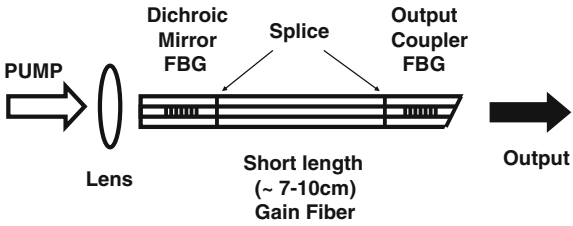

Fig. 8.13 Schematic of one of the diode-pumped single-frequency fiber lasers with fiber Bragg gratings (FBGs)

expression, called the Schawlow-Townes formula, has been obtained for the minimum laser line-width [22]:

$$\Delta v_{L\min} = \frac{4\pi h v \Delta v_{\text{res}}^2}{P} \frac{N_2}{N_2 - N_1 \frac{g_2}{g_1}} \tag{8.68}$$

where v is the laser frequency, Δv_{res} is the laser passive resonator mode spectral width, g_1 and g_2 are degeneracy factors of the lower and higher laser levels, and P is the laser output power.

In practice, however, most SF lasers demonstrate a considerably broader oscillating line-width. The main reasons for that are the fluctuations of laser cavity length and active medium length caused by mechanical and temperature perturbations, which in turn change the phase of the laser line by the laser frequency variation.

As an example of existing challenges in a route to approach minimum laser line-width, consider the single-frequency fiber laser built by Voo et al. [23]. The authors investigated the line-width behavior of an anomalous single-frequency DFB CW fiber laser in the laser configuration shown in Fig. 8.14. The Er:Yb DFB fiber laser demonstrated a 15–40 kHz line-width and up to 20 mW output power when pumped with 110 mW of 980 nm diode laser [23].

Using the line-width measurement setup shown in Fig. 8.15, Voo et al. [23] demonstrated that not only does the line-width of the laser deviate drastically from the Schawlow-Townes formula by increasing with pump and laser power, but it also has significant variation with the used pumping configuration.

Laser line-width is the perturbation to the laser phase caused by spontaneous emission into the laser cavity. Spontaneous emission results in the emission of a single photon will have less impact as the total number of photons (laser power) in the cavity gets larger. Therefore, laser line-width decreases with increasing laser power following the Schawlow-Townes $\sim 1/P$ power dependence. Voo et al. [23] observed an increase in the DFB laser output power from 1 to 10 mW when the pump power increased to about 60 mW, especially for the forward and dual pumping configurations. Therefore, Voo et al. [23] suggested that there may be different physical origins for the DFB fiber laser line-width. Similar behavior of the DBR and DFB lasers has been observed by others also [24, 25]; according to Voo et al. [23], it may be quite general in nature. This anomalous behavior is attributed by the authors to the intrinsic properties of the DFB laser coming from optimization towards higher output powers and higher efficiencies. The authors

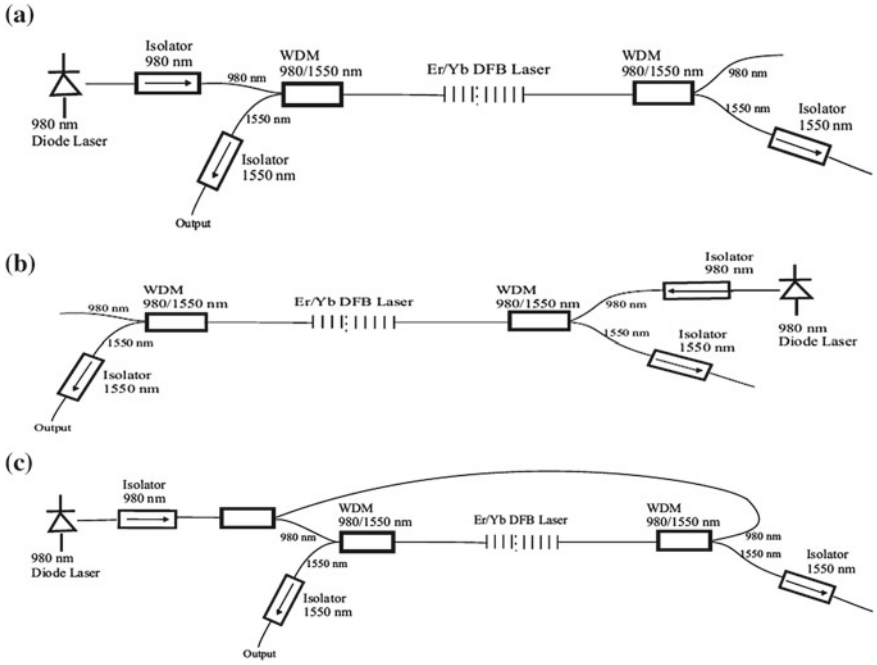

Fig. 8.14 Distributed feedback (DFB) fiber laser pumping configurations: **a** backward (counter) pumping, **b** forward (co-) pumping, and **c** dual side pumping schemes [23] (Image courtesy of SPIE)

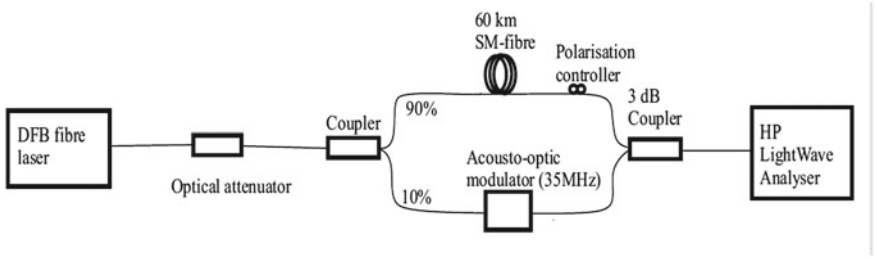

Fig. 8.15 Experimental setup for line-width measurement using a delayed self-heterodyne technique [23]. DFB, distributed feedback (Image courtesy of SPIE)

suggest that the master oscillator-power amplifier configuration is expected to produce better results in terms of line-width.

In pulsed laser systems, the laser spectral line limit is determined by the so-called transform limited condition. For Gaussian pulses, this condition can be expressed as follows:

$$\Delta v_{L\mathrm{lim}}\, t_p \approx 0.44 \tag{8.69}$$

where t_p is the laser pulse width. It is assumed that the pulse is Chirp free.

References

1. R.W. Hellwarth, Control of fluorescent pulsations, in *Advances in Quantum Electronics*, ed. by J.R. Singer (Columbia University Press, New York, 1961), pp. 334–341
2. W.G. Wagner, B.A. Lengyel, Evaluation of the giant pulse in a laser. J. Appl. Phys. **34**(7), 2040–2046 (1963)
3. W. Koechner, *Solid-State Laser Engineering*, 5th edn. (Springer, Berlin, 1999), p. 746
4. A.V. Smith, B.T. Do, Bulk and surface laser damage of silica by picosecond and nanosecond pulses at 1064 nm. Appl. Opt. **47**(26), 418–4832 (2008)
5. F.Y. Génin, A. Salleo, T.V. Pistor, L.L. Chase, Role of light intensification by cracks in optical breakdown on surfaces. J. Opt. Soc. Am. A: **18**, 2607–2616 (2001)
6. Z.J. Chen, A.B. Grudinin, J. Porta, J.D. Minelly, Enhanced *Q* switching in double-clad fiber lasers. Opt. Lett. **23**, 454–456 (1998)
7. A.M. Ratner, *Spectral, Spatial, and Temporal Properties of Lasers* (Plenum Press, New York, 1972), pp. 1–220
8. D.J. Kuizenga, A.E. Siegman, FM and AM mode locking of the homogeneous laser—Part I: Theory. IEEE J. Quantum Electron. **6**(11), 694–708 (1970)
9. A. Siegman, *Lasers* (University Science books, USA, 1986), p. 1283
10. H. Statz, G.A. deMars, *Quantum Electronics*, ed. by C.H. Townes (Columbia University Press, New York, 1960), p. 530
11. O. Svelto, *Principles of Lasers*, 4th edn. (Plenum Press, New York, 1998), p. 605
12. D.H. Gill, B.E. Newnam, Picosecond-pulse damage studies of diffraction gratings, in *Damage in Laser Materials*, vol. 727, ed. by H.E. Bennett, A.H. Guenther, D. Milam, B.E. Newnam (National Bureau of Standards Special Publication, USA, 1986), pp. 154–161
13. E.G. Loewen, E. Popov, *Diffraction Gratings and Applications* (Marcel Dekker, Inc., New York, 1997), p. 485
14. C.A. Huguley, J.S. Loomis, Optical material damage from 10.6 μm CW radiation, in *Damage in Laser Materials*, vol. 435, ed. by A.J. Glass, A.H. Guenther (National Bureau of Standards Special Publication, USA, 1975)
15. D.C. Hanna, R.M. Percival, I.R. Perry, R.G. Smart, P.J. Suni, A.C. Tropper, An Ytterbium-doped monomode fibre laser: broadly tunable operation from 1.010 μm to 1.162 μm and three level operation at 974 nm. J. Mod. Opt. **37**(4), 517–525 (1990)
16. I.J. Hodgkinson, J.I. Vukusic, Birefringent filters for tuning flashlamp-pumped dye lasers: simplified theory and design (T). Appl. Opt. **17**, 1944–1948 (1978)
17. D.C. Hanna, R.M. Percival, R.G. Smart, A.C. Tropper, Efficient and tunable operation of a Tm^{3+}-doped fibre laser. Opt. Commun. **75**, 283–286 (1989)
18. T. Erdogan, Fiber grating spectra. J. Lightwave Technol. **15**, 1227–1294 (1997)
19. A. Othonos, K. Kalli, *FBG: Fundamentals and Applications in Telecommunications and Sensing* (Artech House, Boston, 1999). Chapter 5
20. V.C. Lauridsen et al., Design of DFB fiber lasers, in *Proceedings of ECOC*, vol. 3, (Edinburgh, UK, 1997), pp. 39–42
21. M. Ibsen et al., Robust high power (> 20 mW) all-fiber DFB lasers with unidirectional and truly single polarization outputs, Conference Proceedings, CLEO' 99, (Wasgington DC, OSA, 1999), pp. 245–246
22. A.L. Schawlow, C.H. Townes, Infrared and optical masers. Phys. Rev. **112**, 1940–1949 (1958)
23. N.Y. Voo, P. Horak, M. Ibsen, W.H. Loh, Linewidth and phase noise characteristics of DFB fibre lasers, in *Proceedings SPIE*, vol. 5620, 2004, Solid State Laser Technologies and Femtosecond Phenomena, eds. by Jonathan A. C. Terry; W. Andrew Clarkson, pp. 179–186
24. NP Photonics, Scorpion' Laser Module, Product Data Sheet Rev 4. Available at: http://www.npphotonics.com/files/Laser_Module.pdf
25. W.H. Loh, S.D. Butterworth, W.A. Clarkson, Efficient distributed feedback erbium-doped germanosilicate fiber laser pumped in the 520 nm band. Electron. Lett. **32**, 2088–2089 (1996)

26. Y. Gan, W.H. Xiang, G.Z. Zhang, Studies on ytterbium-doped fibre laser operating in different regime. J. Phys: Conf. Ser. **48**, 795–799 (2006)
27. L. Reekie, R.J. Mears, S.B. Poole, D.N. Payne, Tunable single-mode fiber lasers. IEEE J. Lightwave Technol. **4**(7), 956–960 (1986)
28. K.R. German, Grazing angle tuner for CW lasers. Appl. Opt. **20**, 3168–3171 (1981)
29. J.T. Kringlebotn, P.R. Morkel, L. Reekie, J.L. Archambault, D.N. Payne, Efficient diode-pumped single-frequency erbium: ytterbium fibre laser. IEEE Photonics Technol. Lett. **5**(10), 1162–1164 (1993)

Chapter 9
Main Optical Components for Fiber Laser/Amplifier Design

9.1 Laser Diodes

9.1.1 Principles of Operation

The first reported theoretical analysis and prediction of laser action based on a semiconductor diode was published in 1959 in the USSR [1]. The first operation of a semiconductor laser (also called a "diode laser" or "laser diode") was reported in 1962 in the USA [2]. Semiconductor lasers play a very important role in the fiber laser field. Therefore, this section provides a detailed description of the physical processes that take place in these laser devices.

Unlike isolated atoms and molecules (and even some laser optical centers in doped dielectrics), semiconductors demonstrate wide energy bands. These bands are separated by a bandgap (Fig. 9.1). Typical values of the bandgap of semiconductor materials for the most commonly used and commercially available diode lasers are on the order of a few electron volts. Under certain excitation conditions, such as injecting an electrical current, optical excitation, or heating, electrons from the valence band can move from the valence band to the conduction band after absorbing energy by an excitation process. As a result of this interband electron transition, a pair of charge carriers can be created (i.e., electrons in the conduction band and holes in the valence band), which is called an electron–hole pair. If an electron undergoes reverse transition (i.e., from the conduction band to the valence band), the process is called electron–hole recombination. The result of this interband recombination is usually an extraction of energy that was received during the excitation process.

In equilibrium, electron–hole pairs can be created and recombined as a result of thermal diffusion and spontaneous emission of photons. Thermal equilibrium of electrons and holes, in this case, produces a certain concentration of electrons in the conduction band and holes in the valence band. Note that electrons are fermions (their spin equals 1/2) and thus follow so-called Fermi–Dirac statistics. Therefore, a probability of the electron occupying a certain level with energy E at

V. Ter-Mikirtychev, *Fundamentals of Fiber Lasers and Fiber Amplifiers*,
Springer Series in Optical Sciences 181, DOI: 10.1007/978-3-319-02338-0_9,

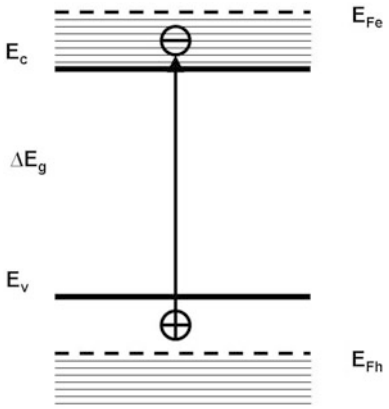

Fig. 9.1 Energy spectrum of the degenerate semiconductor

temperature T in either the conduction or valence band is described by the following Fermi–Dirac formula:

$$f_{F-D}(E,T) = \frac{1}{1+\exp\left[\frac{E-E_F}{kT}\right]} \tag{9.1}$$

where T is the absolute temperature, E_F is the Fermi energy, and k is the Boltzmann constant. The Fermi energy E_F (and, associated with it, the Fermi level in a semiconductor) is an energy that corresponds to the highest energy state occupied by a carrier (either an electron or hole; Fig 9.1). The Fermi level and Fermi energy play a very important role in the physics of the semiconductor lasers, particularly in the creation of the population inversion.

In equilibrium, the number of electrons in the valence band is essentially higher than in the conduction band; therefore, absorption of light during excitation is a major process for interband transitions. If, however, one creates a condition where electrons occupy the majority of levels at the bottom of the conduction band and holes occupy most levels at the top of the valence band, such a condition is called a degenerate condition or a degenerate state. In degenerate semiconductors, emission processes will dominate the absorption. To create a population inversion condition, one must fill more than half of the levels in the band of the order of kT near the band's edge with electrons (in the conduction band) and holes (in the valence band).

In the theory of semiconductor lasers, the condition of population inversion is expressed in terms of Fermi energy for electrons in the conduction band and holes in the valence band. As mentioned above, Fermi energy defines the energy level with the highest energy that can be occupied by an electron. The probability of the electron to occupy Fermi level is given by:

$$f_{F-D}(E_e,T)_e = \frac{1}{1+\exp\left[\frac{E_e-E_{Fe}}{kT}\right]} \tag{9.2}$$

where E_{Fe} is the Fermi energy of the electron. With increasing electron concentration in the conduction band, the Fermi energy of the electron increases; therefore, electron degeneracy increases as well (Fig. 9.1).

Similarly, the probability for holes to occupy energy levels in the valence can be determined as follows:

$$f_{F-D}(E_h, T)_h = \frac{1}{1 + \exp\left[\frac{E_{Fh} - E_h}{kT}\right]} \tag{9.3}$$

where E_{Fh} is the Fermi energy for holes. Note that:

$$f_{F-D}(E_h, T)_h = 1 - f_{F-D}(E_e, T)_e \tag{9.4}$$

If the semiconductor material demonstrates the degenerate state for both electrons and holes, then the energy gap between Fermi energy for electrons and Fermi energy for holes exceeds the bandgap of the material:

$$E_{Fe} - E_{Fh} > E_g \tag{9.5}$$

This condition in turn is required for amplification of light in a semiconductor and basically defines the condition of population inversion.

There are several ways to create a condition of inversion population in semiconductors: namely, optical pumping, excitation with an electron beam, and injection of carriers through the p-n junction of the semiconductor. Carrier injection through a p-n junction is the most popular option; this section describes its use to create the required conditions for amplification and oscillation in semiconductors. Because the first diode laser was based on a single GaAs crystal, an example of a semiconductor laser based on this material and physical processes leading to the laser action are reviewed here.

Consider a GaAs crystal doped with Zn. The dopant creates an energy level within the bandgap close to the top of the valence band (Fig 9.2b). Electrons traveling in the valence band need little thermal energy kT (kT is $\sim$0.025 eV at 300 K, while the bandgap of GaAs is $\sim$1.4 eV) to jump into the above-mentioned energy level, leaving behind positively charged holes (Fig 9.2b). In this case, the impurity level is called an acceptor level because an electron is accepted to this level.

As a result, a created hole can work as a trap for another electron still traveling in the valence band. Once trapped by this hole, the valence band propagating the electron leaves another hole behind. In this way, one can consider holes moving around in the valence band. The moving hole becomes a carrier of charge, and the material now becomes a p-type semiconductor (Fig. 9.2b). In a p-type semiconductor, holes are considered majority carriers.

On the other hand, if the same GaAs material is doped with Si, the impurity creates an energy level in the bandgap; in this case, it is very close to the bottom of the conduction band. With similar considerations as mentioned above, an impurity electron occupying an energy level in the bandgap very close to the conduction

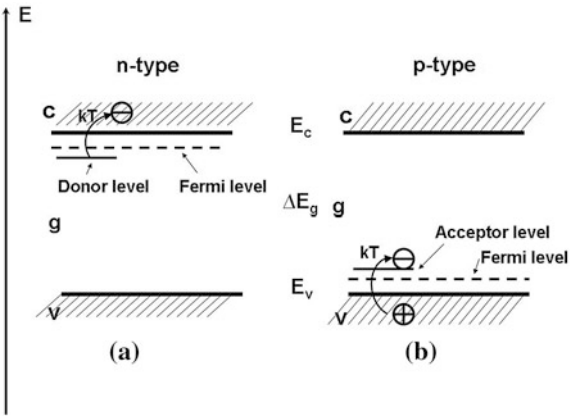

Fig. 9.2 Energy levels of the doped semiconductors of n-type (**a**) and p-type (**b**) *c* conduction band, *v* valence band, *g* bandgap, E_c edge energy of the conduction band, E_v edge energy of the valence band, ΔE_g energy of the bandgap

band can easily jump up to the conduction band with the help of a little energy (Fig 9.2a). The electron appeared in the conduction band as a result of the above-mentioned process, creating additional negative charge in the band, and the material becomes an n-type semiconductor (Fig. 9.2a). In this case, the impurity level is called a donor level because an electron is donated from this level. Electrons in n-type material are called majority carriers.

When n- and p-type semiconductors are put into contact, a boundary region is formed, which is called a p-n junction (Fig. 9.3). As mentioned, electrons in an n-type semiconductor and holes in a p-type semiconductor are called majority carriers. The small amount of holes in an n-type semiconductor and the small amount of electrons in a p-type semiconductor are called minority carriers. When a p-n junction is created, some of the electrons from the the n-region that have reached the conduction band, leaving donors, can diffuse across the junction and combine with acceptors on the p side. An acceptor filled in such a way leads to the creation of a negative ion. In doing so, electrons leave behind positive ions (i.e., donor impurities) on the n side. This process creates a space charge layer, a so-called depletion region (a region that completely lacks any charge carriers across it), which becomes a barrier for further electron and hole movement across the p-n junction. In energy space, this condition corresponds to the creation of an energy barrier (Fig. 9.4a). The size of the depletion region depends on the level of donors on the n side and acceptors on the p side. The higher the doping level, the smaller the region because elevated concentration of doping increases the probability of the carrier being trapped and creating the ion. In general, the depletion region size is a sum of the depletion regions in n (d_n) and p (d_p) sides:

$$d_{np} = d_n + d_p \tag{9.6}$$

and

$$\frac{N_d}{N_a} = \frac{d_p}{d_n} \tag{9.7}$$

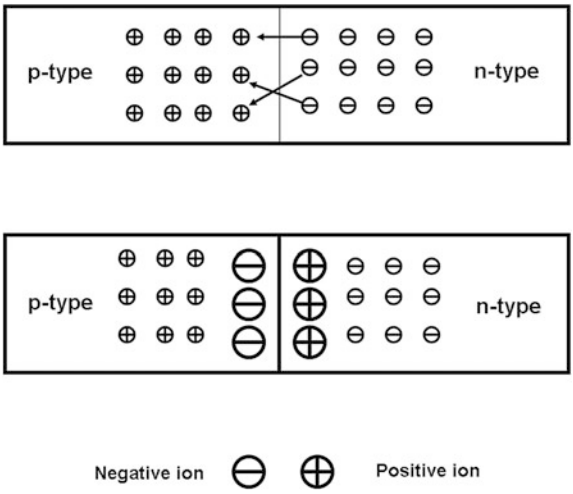

Fig. 9.3 Depletion region in the junction area of n-type and p-type semiconductors

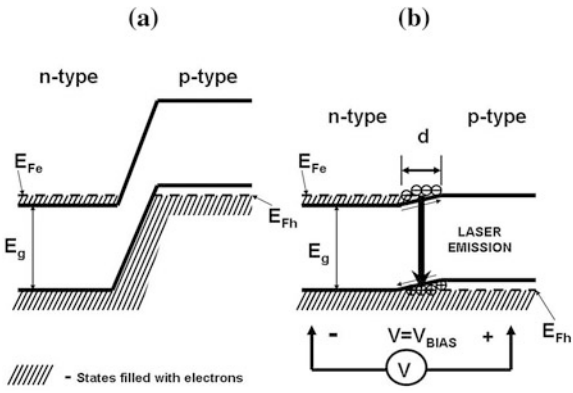

Fig. 9.4 Energy band diagram for a p-n junction: (**a**) $V = 0$; (**b**) $V > 0$. E_{Fe} and E_{Fh}, Fermi energies for electrons and holes, respectively

where N_d and N_a are concentrations of donors and acceptors, respectively. If doping level of the p-type side is higher than the n-type side (i.e., $N_d < N_a$), then $d_n > d_p$; that is, the depletion region mostly occupies the n-type of the semiconductor. The typical size of the depletion region is on the order of a fraction of the micron (i.e., ~ 0.1, ~ 0.4 μm for doping density $\sim 10^{16}$ cm^{-3}) [3].

If one applies an external electric field or so-called forward bias (forward voltage) across the p-n junction (positive to p-type and negative to n-type), it can create an additional amount of electrons following the appearance of electrical field (i.e., injected) at the n-side and holes at the p-side of the junction (Fig 9.4b). Basically, the necessary voltage (the bias voltage) is required to overcome a potential barrier created in the depletion region. As one can see from Fig. 9.4, applying forward voltage reduces the existing energy barrier. The forward voltage required to overcome the energy barrier of the p-n junction is very close to the

energy of the bandgap and is on the order of 1–2 V (for visible and infrared diode lasers). Note that when no forward voltage is applied, the two Fermi levels are aligned (Fig 9.4a). However, when the forward voltage is applied, the Fermi levels become separated by a value close to eV and the energy barrier for the carriers gets smaller. In the condition of applied forward voltage, electrons can more easily penetrate into the p-type side. During diffusion, the electron penetration depth into p-type material (i.e., a length; the carrier defuses before recombination), which is called a minority diffusion length, can be determined by the following formula:

$$d_M = \sqrt{D_M \times \tau_M} \tag{9.8}$$

where D_M is the bulk minority diffusion coefficient (for GaAs, $D_M = 10$ cm^2/s) and τ_M (for GaAs, $\tau_M = 1$ ns) is the lifetime (i.e., minority carrier recombination time) [4]. Calculated this way, penetration distance is ~ 1 μm. This distance determines the laser-active region in a semiconductor laser in the direction perpendicular to the plane of junction.

Injected electrons into the p-type and injected holes into the n-type of the semiconductor boundary can recombine and in such a way emit a light with photon energy roughly corresponding to the bandgap of the semiconductor material. If one then creates a resonator (usually two cleaves perpendicular to the plane of the junction), this may bring the system to the threshold condition, where gain due to the stimulated emission from carrier recombination overcomes losses. The current required to achieve the lasing threshold is called the *threshold current* (Fig. 9.6) and is a very important parameter of the semiconductor laser. This is the basic principle of semiconductor laser operation and in fact describes the first semiconductor lasers based on GaAs single crystals (Fig. 9.5). Such a semiconductor laser type is also called a *homojunction laser*, in which both n-type and p-type semiconductors are made of the same material. Also described was an injection type of pumping for semiconductor lasers. Other pumping architectures have been suggested, including optical pumping and electron beam pumping approaches.

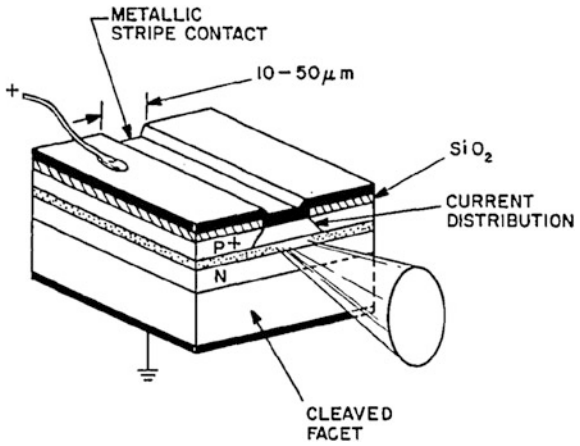

Fig. 9.5 Configuration of the edge-emitting semiconductor laser [12] (Image courtesy of the OpticalSociety of America)

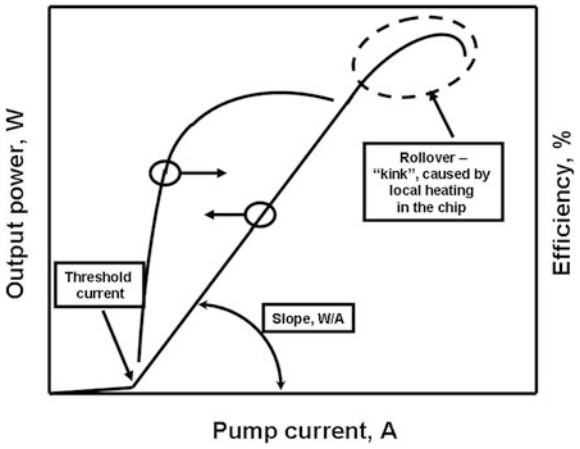

Fig. 9.6 General view of the output power versus pump current function for the diode laser

However, among the commercially available and most widely used diode lasers, injection lasers are widely used, especially as pump sources of fiber lasers and amplifiers.

One of the biggest problems in the operation of early diode lasers was heating, which in turn prevented room-temperature continuous-wave (CW) operation. To overcome this problem, an interesting method was suggested, which consisted of creating a suitable multilayered crystal of GaAs and AlGaAs. Variation in electrical and optical properties in the multilayered crystal required replacement of a large fraction of the Ga. Technological development continued in this direction in order to maintain no sizing defects in the interfaces between the layers, as caused by size match of the crystal lattices. This eventually lead to the creation of so-called heterostructure diode lasers, which allowed CW operation at room temperature. After this important discovery, the field of diode lasers grew dramatically. The following section reviews the most widely used types of diode lasers.

Figure 9.6 shows the typical function of the diode laser's output power versus pump current. Note that the diode laser's output power pump dependence curve has a rollover area, which is called a *kink*. This *kink* arises from local overheating of the chip at high pump current and should be avoided. Usually diode laser manufacturers specify a so-called *kink-free* operation, which is typically defined by a distance from the *kink* in current values. Working in a *kink-free* pump current zone prolongs the diode laser's lifetime.

9.1.1.1 Metal–Organic Vapor Deposition for Diode Laser Chip Fabrication

Several techniques have been developed for semiconductor laser material manufacturing. One of the most commonly used techniques for thin-film deposition and high-quality crystalline chip manufacturing is metal–organic vapor deposition

(MOCVD) or its variations. MOCVD is popular for several reasons, including its excellent thickness control, possibility to grow numerous thin ($\sim$1 nm) layers of complex heterostructures, good uniformity of growth structures, capabilities of patterned (i.e., localized) growth, and scalability for large area-multiple wafer growth. In addition, the MOCVD technique demonstrates high growth yield.

MOCVD uses a process of epitaxial growth, which in turn consists of depositing thin layers of material at a desired thickness and molecular composition. The general schematic of the MOCVD process is illustrated in Fig. 9.7.

For the case of GaAs-based diode laser structures, the GaAs substrate in the form of a thin disk 50–90 mm in diameter (a wafer) is placed in a reaction chamber, heated up to temperatures of 600–1100 °C (see Fig. 9.7). During the MOCVD process, source materials through mass flow control and pressure control are thermally deposited in the reaction chamber; the semiconductor material grows epitaxially on the wafer and creates crystalline layers from the gaseous phase. The SiO_2 insulation layer is deposited and contact structuring is created, then both sides of the chip are gold coated for electrical connection. The wafer is cleaved into bars and diode laser cavity mirrors are then deposited. The created bar is then soldered onto a copper heatsink (which later acts as an electrode or ground). The wired chip is then packaged into different packaging configurations, including hermetically sealed systems. For better thermal management (especially in the

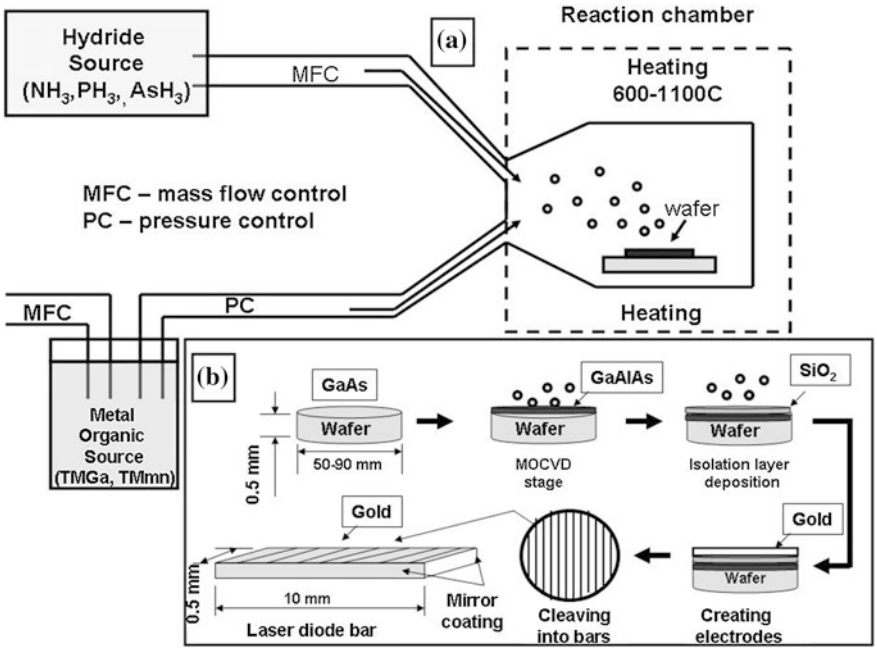

Fig. 9.7 **a** Schematic of the MOCVD technique. **b** The main steps in a simple GaAs-based diode laser emitter/bar manufacturing process

case of high-power diodes), the p-side of the chip is heatsinked and a wire is attached to the opposite side (i.e., the top of the structure that consequently becomes a negative electrode; attached to n-type of the semiconductor). Packaged diode lasers may later be fiber coupled (see details later in this chapter).

9.1.2 Main Types of Diode Lasers Used in Fiber Laser Technology

The most common semiconductors used in laser diodes are compounds based on gallium arsenide, indium gallium arsenide, phosphide, and gallium nitride. Table 9.1 shows most commonly used semiconductor laser compounds and related wavelengths of operation in applications for diode pumping of fiber lasers and fiber amplifiers.

9.1.2.1 Basic Structure of Diode Lasers (Single Emitters)

Fabry–Perot Lasers

In the simplest form of the laser diode, an optical waveguide is made on the crystal surface in such a way that the light is confined to a relatively narrow line. The two ends of the crystal are cleaved to form perfectly smooth, parallel edges, thus forming a Fabry–Perot (FP) resonator with semiconductor gain material located between reflecting surfaces. Light in the laser diode travels along the waveguide created by the p-n junction and is reflected from the end faces of the semiconductor. Because one end of the semiconductor material is cleaved the traveling light inside the diode, the laser cavity undergoes incomplete reflection from this end facet and emerges outside the diode laser resonator. When the laser threshold is reached (i.e., when more amplification than loss is achieved), the diode laser begins to oscillate.

In most types of diode lasers (edge-emitting lasers), the light is confined in a very thin layer—a waveguide. This waveguide is usually supports only a single optical mode in one direction (i.e., in the direction perpendicular to the semiconductor layers or the plane of junction). In this direction, therefore, the diode

Table 9.1 Main types of diode laser matrixes and related wavelengths of operation

Semiconductor compounds	Wavelength of operation (nm)
AlGaInP	~630–690
InGaAlAs/GaAlAs	~780–880
InGaAs	~900–1200
InGaAsP/InP	~1400–1850
InGaAsSb	~2000–2200

laser beam is close to diffraction limited. In the perpendicular direction, if the waveguide is wide compared to the wavelength of light, the laser is multimode. In this case, due to diffraction, the beam diverges rapidly after leaving the semiconductor chip, typically at ~40° vertically (fast axes) by ~10° laterally (slow axes). The typical wavelength temperature dependence is ~0.3 nm/°C. If the laser diode emitting area is strongly asymmetric, the diode laser is called a broad-area laser (BAL); this is the case for multimode edge-emitting diode lasers.

The wavelength emitted by a diode laser is a function of the bandgap of the semiconductor and the modes of the optical cavity. In the laboratory environment and product installations, spectral properties of the semiconductor laser depend on temperature and pump current (in the case of injection lasers).

9.1.2.2 Distributed Feedback Lasers and Distributed Bragg Reflector Lasers

Distributed feedback lasers (DFB) are one of the most important type of single emitter diode lasers used in the field of fiber lasers. This type of diode laser is often used as a seed source in high-power fiber amplifiers. To stabilize the lasing wavelength, a diffraction grating is etched close to the p-n junction of the diode (Fig. 9.8). This grating acts like an optical filter, causing a single wavelength to be fed back to the gain region; therefore, it affects the laser spectral parameters. Because the distributed feedback (i.e., grating) provides the feedback that is required for lasing, reflection from the facets is not required. Therefore, usually one facet of a DFB diode laser is antireflection coated.

The DFB laser has a stable wavelength that is set during manufacturing by the pitch of the grating; it can only be tuned slightly with temperature (usually ~0.06 nm/K) or by pump current (usually ~0.007 nm/mA). DFB diode lasers operate on a single longitudinal mode with extremely narrow spectral line width of less than 1 MHz. DFB diode lasers are very sensitive to optical feedback; therefore, they are usually manufactured with an optical isolator in between the semiconductor chip and fiber where the laser is coupled (in the case of fiber-coupled devices).

In distributed Bragg reflector (DBR) diode lasers, as with DFB lasers, a Bragg grating is integrated into the diode (Fig. 9.9). However, instead of being etched into the gain medium of the chip, the grating is positioned outside the active region

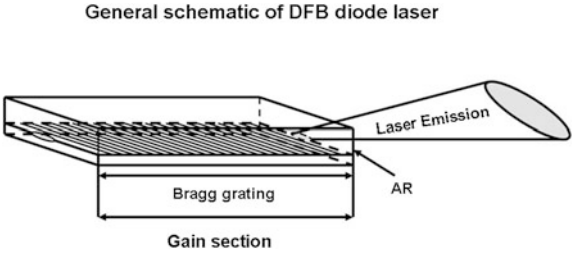

Fig. 9.8 Distributed feedback (DFB) diode laser structure (Image courtesy of Sacher Lasetechnik)

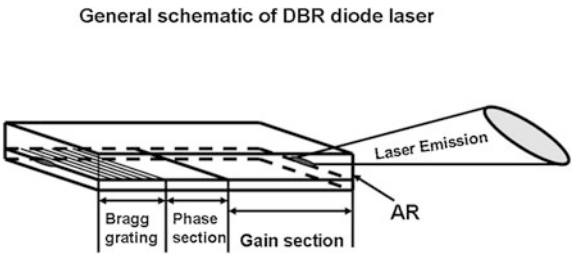

Fig. 9.9 Distributed Bragg reflector diode laser structure (Image courtesy of Sacher Lasetechnik)

of the cavity. The grating acts as a mirror and reflects a single wavelength back into the cavity. The rear facet of the laser chip has a high reflection coating, whereas the front facet has an antireflection coating. In some configurations of DBR lasers, it is possible to provide individual control of the different semiconductor chip sections. This in turn allows the achievement of certain flexibility in electrical modulation of the laser. The laser wavelength tunability of the DBR laser is achieved by synchronously changing the current of the Bragg and the phase section of the laser.

Both DFB and DBR diode lasers (similar to other diode lasers) are wavelength tunable with current and temperature. Thermally tuned DFB and DBR lasers have very large mode-hop free tuning ranges, which can span over hundreds of gigahertz.

9.1.2.3 Vertical Cavity Surface-Emitting Semiconductor Lasers

Vertical cavity surface-emitting lasers (VCSELs) have their optical cavity axis along the direction of current flow (i.e., perpendicular to the plane of junction) rather than perpendicular to the current flow as in conventional edge-emitting laser diodes (described previously). The active region length is very short compared with the lateral dimensions (Fig. 9.10). The VCSEL laser resonator consists of two

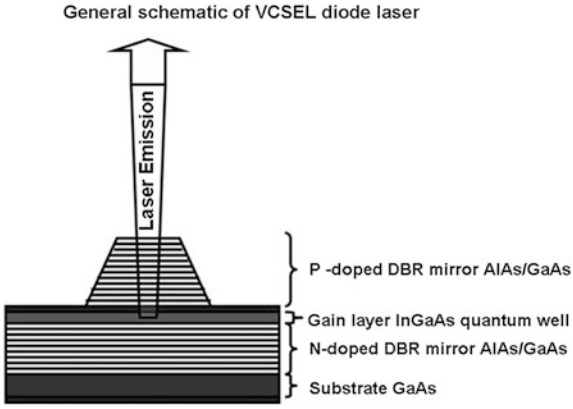

Fig. 9.10 Vertical cavity surface-emitting laser (VCSEL) structure. DBR distributed Bragg reflector

DBR mirrors parallel to the wafer surface, with an active layer consisting of one or more quantum wells of semiconductor laser-active material. The planar DBR mirrors consist of layers with alternating high and low refractive indices, creating both a high reflector and an output coupler. VCSELs have better wavelength stability, reduced temperature wavelength dependence (<0.1 nm/C), improved reliability due to the higher light intensity of the edge versus the surface geometry, and higher temperature of operation (>70 °C). Commercially available high-power VCSELs (i.e., Princeton Photonics) demonstrate more than 1 kW of optical power from the 1 mm core (0.4 NA at 975 nm).

Having relatively large mirror surfaces, dielectric mirrors may be fabricated with a high degree of wavelength-selective reflectance using a multilayer coating structure. Because of the possible high mirror reflectivity, VCSELs have lower output powers when compared to edge-emitting lasers. The main advantage of a VSCEL is its round beam shape (compared with the highly astigmatic beam emerging from edge-emitting laser diodes) and convenience of the laser inspection during fabrication. Because of their round beam structure, VCSELs also allow resonator geometries and structures that are similar to conventional solid-state lasers, along with similar thermal lensing issues and challenges concerning laser resonator stability. Because the laser resonator axis is in the same direction as the pumping current flow, the shape, size, and structure of the electrodes are essential.

9.1.3 High-Power Diode Lasers

Commercial production and development of laser diodes has been significant since the early 1990s. One of the biggest interests is in their power scaling. BALs became a focus of the commercial development of high-power diode lasers. Mainly, the diode laser power scaling included single-emitter strip-diode lasers, bars (linear arrays of single emitters), and stacks of such broad-area diode laser structures. Thus, the principal scaling roadmap is straightforward.

9.1.3.1 Single Emitters

The typically single-emitter BAL layer structure has $\sim$1 μm dimension in the direction perpendicular to the plane of junction (single transverse mode, diffraction-limited propagation) and typically 50–200 μm dimension along the plane of junction (i.e., multitransverse mode propagation; see Fig. 9.11). The edge-emitting laser cavity is about $\sim$500 μm. For comparison, the VCSEL laser cavity is typically a few micrometers long.

The wider the multimode dimension of the BAL, the higher is the power that is achievable from the single emitter. (However, there is a limitation related to the onset of the ASE process and parasitic lasing in transverse direction.) Power scaling of a single-emitter BAL is limited by $\sim$5 MW/cm^2, mainly because of the

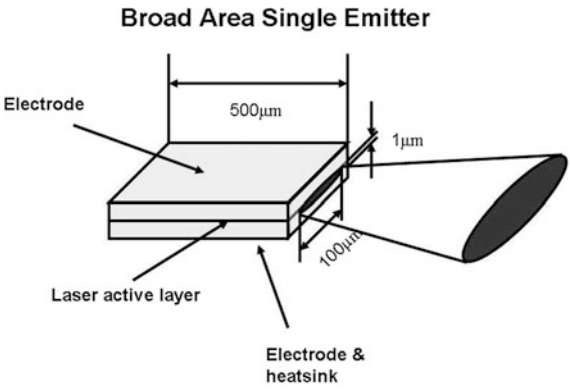

Fig. 9.11 Schematic structure of a broad-area laser diode

facet damage; therefore, it allows a 1 × 100 μm laser strip to withhold an optical power of typically ~3–5 W.

9.1.3.2 Diode Laser Linear Array (Bar)

Numerous applications, ranging from material processing to diode pumping of solid-state lasers, drive scientists and engineers to develop more powerful single-emitter BALs. However, straightforward power scaling of diode lasers is limited by the high power density of the diode laser chip front facet, which in turn produces a large thermal load and risks a diode chip failure.

Another way to scale the diode laser power is to create single-emitter linear arrays with stable and reliable performance of the individual multimode emitter. Diode arrays are created by linearly aligning a number of single diode laser emitters (during the chip manufacturing process) as a one-dimensional array of BALs (Fig. 9.12). They typically contain between 19 and 50 emitters, each being ~100–200 μm wide. A typical diode laser bar has a laser resonator length of approximately a millimeter, a 10 mm width, and has 10 × 40° of divergence at full-width half-maximum (FWHM) in the slow direction (plane of junction: multimode operation) and fast direction (perpendicular to the plane of junction: single mode, diffraction-limited operation).

Diode laser bars generate tens of watts of output power (typically 20–50 W). The power of a diode laser array depends on the wavelength, chip structure, cooling configuration, and the mode of operation. The most challenging operational mode is CW because, at 100 % duty circle, the heat load on the chip is tremendous at a high power level of operation. Currently, the most powerful CW diode laser bars have wavelengths between 780 and 980 nm, with electrical to optical conversion efficiency of more than 60 %. Figure 9.13 shows a typical view of a diode laser bar packaged in a so-called microchannel cooled heatsink and conductively cooled packages. Microchannel technology produces highly efficient heat removal capability (compared to conductively cooled systems).

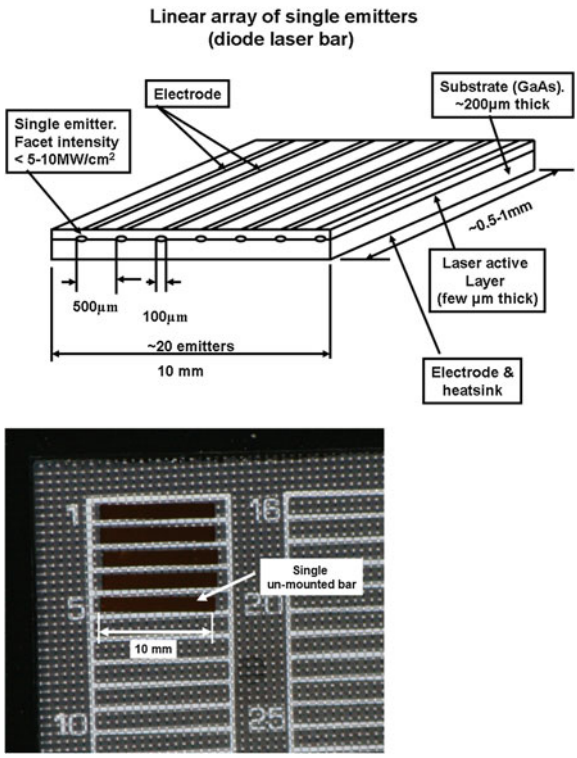

Fig. 9.12 Schematic of a chip of a semiconductor laser bar (*top*) and photograph of an unmounted diode laser bar (*bottom*)

Because of the astigmatic nature of diode laser bar emission, one usually considers so-called fast axis collimators, which typically are aspheric lenses. Fast axis collimation allows the achievement of typically ~ 1–2° of divergence of the diode laser bar in the fast direction, thus producing a powerful laser emitter with $10 \times 2^\circ$ of overall divergence and tens of Watts of output power. Note that diode laser bars typically demonstrate a "smile" phenomenon in the laser bar emission properties. The smile usually originates from a small bend of the horizontal line

Fig. 9.13 Microchannel cooled diode laser bar (vertical stack) with an array length of 1 cm (*left*) and conductively cooled (i.e., CS mount type) diode laser bar with an array length is 1 cm (*right*). Both were manufactured by Princeton Lightwave (Image courtesy of Princeton Lightwave)

where single emitters are located; it is a technological drawback that affects fast axis collimation and focusing of the diode laser bar radiation. This in turn may affect diode laser fiber-coupling efficiency, which is critical for fiber laser and fiber amplifier applications.

9.1.3.3 Diode Laser Stack of Bars

Further power scaling of the diode lasers uses one- or two-dimensional stacks of several diode bars. Usually, bars are arranged in horizontal or vertical directions, depending on applications. Most fiber laser applications require efficient fiber-coupled high-power diode laser beam delivery for optical pumping. Horizontally stacked diode laser bars are usually used in high-power diode pumping of crystalline or glass slab lasers. Vertical stacks can be manufactured from a two-dimensional wafer packaged into the heat sink. An example schematic of a water-cooled diode laser stack is shown in Fig. 9.14.

Packaging the diode laser bars close to each other provides many advantages with respect to the output beam and beam management. However, heat removal usually applies restriction to the separation of the individual bars. Because of this reason, most high-power diode laser stacks have low overall brightness, and one may consider diode stack polarization or spectral beam combining technologies. Similar to the fast axis microlensing of diode laser bars, two-dimensional diode laser stacks are microlensed by a mask (matrix) of high-aperture aspheric lenses.

Commercially available diode laser stacks may be arranged in two-dimensional structures (vertically and horizontally), providing more than several hundreds Watts of diode laser emission. A diode laser stack–beam combination allows the achievement of thousands of watts and is very important for power scaling of fiber lasers. The possibility of fiber-coupling options creates additional advantages for

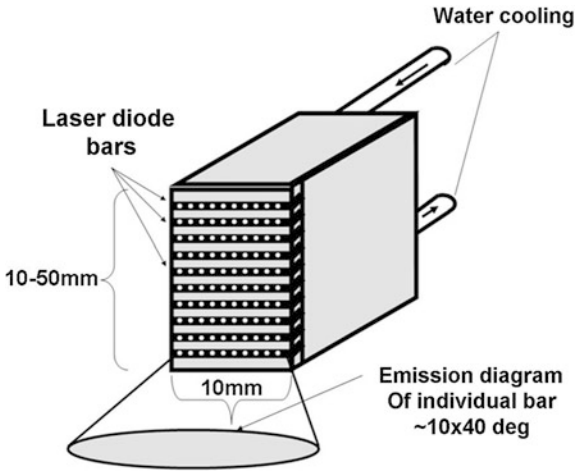

Fig. 9.14 Schematic of a high-power, water-cooled vertical laser diode stack. The laser diode stack height is typically 10–50 mm but may vary beyond this dimension, depending on several factors including power level, operational duty factor, number of bars, and bar-to-bar distance. (Permission to use granted by Newport Corporation. All rights reserved)

fiber laser technology because it gives an opportunity to build the all-fiber (no free space) high-power fiber laser systems that are required for many industrial and military applications.

9.1.4 Fiber-Coupled Diode Lasers

Although the fiber-coupled diode laser concept has existed for years, scientists and engineers started sensing a real advantage in using fiber pigtails of diode lasers with the development of fiber lasers and fiber amplifiers. The advantages of using light emerging from optical fiber compared with direct diode laser emission include the following:

1. For many applications that use direct light from a laser diode, it is convenient to use a fiber-coupled diode laser beam to deliver the laser light to the place where it is needed.
2. The fiber-coupled light has a circular geometry (unlike direct emissions from edge-emitting diode lasers), which is very convenient for many subsequent beam transformations.
3. The use of fiber-coupled laser diodes in laser pumping applications allows the achievement of easy (alignment-free) diode laser maintenance, including diode laser replacement and service.
4. The manageable fiber length of fiber-coupled diode lasers allows the achievement of separate locations for the pump and the main laser cavity. Such flexibility in the relative displacement of pump and cavity optics is especially important for high-power laser systems, in which the thermal management of both diode lasers and active laser media requires careful consideration.
5. In fiber lasers and amplifiers in which an all-fiber approach is applied, fiber-coupled diode lasers allow all-fiber solutions; together with other fiber-coupled components, the entire system is practically alignment free.

Usually, diode lasers are fiber coupled into single-mode or multimode optical fibers, depending on the mode structure of the original diode laser. Fiber coupling efficiencies depend strongly on the power level of the diode laser, the diode laser structure, and the approach of fiber coupling (i.e., lens based or fiber profiling). Power diode laser systems with high average power may create overheating conditions at the fiber entrance, which in turn may result in stress and damage of the fiber endface. Special care has to be taken with the fiber termination enclosure facing the diode laser beam.

When fiber profiling is used, the fiber tip that faces the laser diode-emitting surface is shaped by polishing for efficient, direct coupling of the diode laser radiation. Efficiencies of more than 92 % are achieved using such a fiber-coupling geometry. This high fiber-coupling efficiency is very important for high-power diode lasers, where minimization of heat dissipation plays an important role in the

reliability of the component. However, the direct coupling of the fiber laser beam into the fiber prevents the possibility of locating additional optical components between the diode laser and fiber, such as dichroic mirrors (for protection against back reflection) or optical isolators (e.g., in DFB fiber-coupled diode lasers, where optical feedback compromises DFB diode laser parameters and therefore incorporation of an optical isolator is a must).

Fiber-coupled diode lasers are characterized by power—spectral as well as optical parameters of the fiber into which the diode laser light has been coupled. Usually, optical parameters of the fiber include the fiber core diameter and core numerical aperture. The most common fiber diameters of fiber-coupled diode lasers are 6, 9, 50, 105, 200, 400, and 600 microns, whereas numerical apertures usually are 0.12, 0.15, or 0.22.

Along with obvious and important advantages, a fiber-coupling approach has several disadvantages, including the following:

- Higher cost compared with free-space diode emitters.
- Decreased output power because fiber coupling has limited efficiency, especially for high-power diode laser bars.
- Inability (at times) to insert an additional optical component, such as an optical isolator, between the diode laser output and fiber input.
- For multimode diode lasers using multimode fibers, the polarization maintaining propagation of the diode laser beam is lost.
- Fiber-coupled diode lasers are more susceptible to optical damage due to back reflections; they require special consideration for protection against optical damage using additional in-line beam splitters and filters.

9.2 Fiber-Coupled Polarization-Maintained and Non-polarization-Maintained Optical Components

This section reviews the most common fiber-optic components used in fiber lasers and fiber amplifiers. Depending on the manufacturing process used in the development process, there are two main categories of fiber-optic components: free-space components and fused components. Free-space fiber-optic components employ free-space optics, such as lenses and optical filters, in between input and output fiber ports of the device. In the case of fused components, all fiber ports are fused together to create optical contact. In either approach, however, the main principle (i.e., the principle of optical brightness preservation) has to be maintained in order to design reliable and low-loss systems. Unmatched optical brightness usually results in excess heat generated in the place of transition from one aperture to another, which in turn impact power tolerance and power transmission efficiency/loss of the device. Fiber-coupled optical components that are not brightness limited allow more than 95 % of power transmission.

Depending on the fiber type used, all fiber-optic components can be divided into two principal categories: single-mode and multimode. Single-mode fiber-based components in turn are divided into polarization-maintained (PM) and non-PM types, depending on the fiber type used during the particular component's development.

Fiber-Coupled Power Splitters: A power splitter is a passive fiber-optic coupler that divides light from a single fiber into two or more fiber ports. The target of such a component is to split the fiber propagating power without losing brightness and total power. Usually, the numerical aperture of the output fibers is the same as the input fiber. Fiber-coupled splitters need to be tolerant to high power handling because they are intended to split large fiber-coupled diodes with up to kilowatts of output power. In fiber lasers, power splitters are essential when the user has access to high-power individual diode lasers and the pump power signal/pump combiner has a limited number of ports or limited power in each individual pump port. Pump power splitters are usually brightness limited; therefore, consideration of brightness preservation is essential for low-insertion loss power splitters.

Fiber-Coupled Pump Power Combiners: A pump power combiner is a fiber-coupled device that combines several fiber pump ports into a single fiber. Pump combiners generally have several input pump ports and one fiber output port. Power pump combiners can also include one more fiber at the pump port side of the device, which is a single mode-through fiber (PM or non-PM, true single mode or large mode area); this allows the power pump combiner to not only combine power from separate fiber-coupled diode lasers, but also to inject a fiber-coupled seed laser into the core of the output fiber port of the pump combiner. Usually, pump combiners are used in clad pumping geometry when combined power from several pump ports is coupled into the cladding of the output fiber. The light propagating in the core of the seed input port of the combiner goes through the combiner and is injected into the core of the output double-clad fiber of the device. The output port of this pump/signal combiner is then spliced to the double-clad gain fiber of the fiber laser or fiber amplifier. The coupled-together pump radiation propagates further into the cladding of the gain fiber, and core-propagating signal radiation is injected into the core of the gain fiber. Pump-to-signal combiners can be PM or non-PM, depending on the through fiber used for signal propagation.

Mode-Field Adaptors: A mode field adaptor (MFA) is a fiber-coupled optical device that allows the core-propagating signal to be transferred into another fiber with a different core diameter. Commercially available MFAs are usually fused (Fig. 9.15). In the case of all-fiber MFAs (which tolerate high optical powers), there are different approaches to solve the problem of mode adaptation, including heating when the size of the mode field changes through dopant diffusion or fiber tapering when the fiber core diameter changes (Fig. 9.15b). Alternatively, one can use a combination of both approaches.

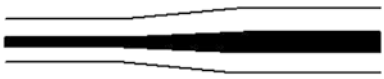

Fig. 9.15 Schematic of the fused mode-field adaptor

Because most applications deal with fundamental mode fiber lasers and amplifiers, the aim of an MFA is to preserve the energy (loss-free propagation) in the fundamental mode of the fiber; therefore, this mode transformation has to be done adiabatically. The adiabaticity criteria use an assumption that the characteristic angle of tapering should be smaller than the diffraction angle of the field at each point along the taper [5]. The analytical expression for the diffraction angle for step index fiber is as follows:

$$\theta_D = \frac{2 \times \sqrt{\ln V}}{V} \times NA \tag{9.9}$$

where V is the V-number and NA is the fiber core numerical aperture. The diffraction angle applies for the fundamental mode of the fiber only. Another way to formulate the mode-matching criteria is to require that core sizes and numerical apertures of the input and output fibers (or their V-numbers) have to be matched. This condition creates challenges in the manufacturing process.

In general, MFAs are usually low-insertion-loss devices, unless backward propagation of the optical signal takes place when they become brightness limited. MFAs play an important role in the development of high-power fiber laser systems and amplifiers, which often use multistage geometries with increased gain and fiber core diameters. MFAs can be made in a PM or non-PM configuration, depending on the fibers used in its input and output ports.

Cladding light strippers: Optical devices that strip residual cladding propagating light while preserving core propagating energy are called cladding light strippers (or cladding beam dumps). The ability to strip cladding light from double-clad fiber is required for many different reasons during fiber laser design. Cladding propagating power can reach power levels of the hundreds of Watts (note that cladding NA is typically several times higher than NA of the core). By locally changing cladding NA (e.g., by changing the refractive index of the material surrounding cladding), it is possible to achieve significant attenuation of the cladding propagating light. Figure 9.16 demonstrates an example of the use of a cladding power stripper in fiber laser [6].

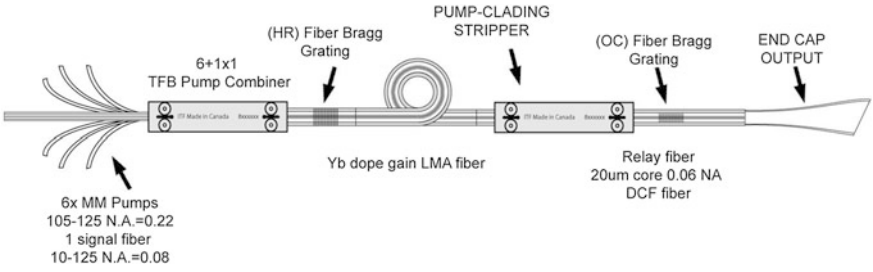

Fig. 9.16 Example of a simple fiber laser/amplifier design employing a cladding power stripper [6]. (Image courtesy of SPIE)

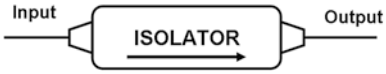

Fig. 9.17 Schematic view of a packaged two-port fiber-coupled opticalisolator

As shown in Fig. 9.15a, Wetter et al. [6] used an all-fiber 6 + 1×1 TFB spliced to a 20–400 Yb^{3+}-doped DCF gain fiber. The fiber laser resonator is formed by two fiber Bragg gratings (FBGs), which act as the laser cavity mirrors (i.e., high reflector and output coupler). A cladding light stripper is introduced after the gain fiber to strip all the unwanted light in the forward and backward direction. The authors [6] achieved attenuation of more than 20 dB in the cladding, practically without signal loss. After stripping the damped cladding, light energy has to be properly distributed along the stripper and heat sink. Cladding strippers can potentially strip tens to hundreds of Watts in high-power fiber lasers and amplifiers.

Optical Isolators: A fiber-coupled optical isolator is an optical device that allows for unidirectional core propagation of light with a high degree of optical isolation in the backward propagation direction (Fig. 9.17). Fiber-coupled optical isolators can be single or double/multistage depending on the degree of required optical isolation of the core-propagating light.

9.2.1 Polarization-Dependent Optical Isolators

Figure 9.18 shows the structure of a polarization-dependent optical isolator. The optical isolator consists of a polarizer, an analyzer, and a 45° Faraday rotator inserted between them. The polarizer and analyzer main axes are rotated at 45° relative to each other.

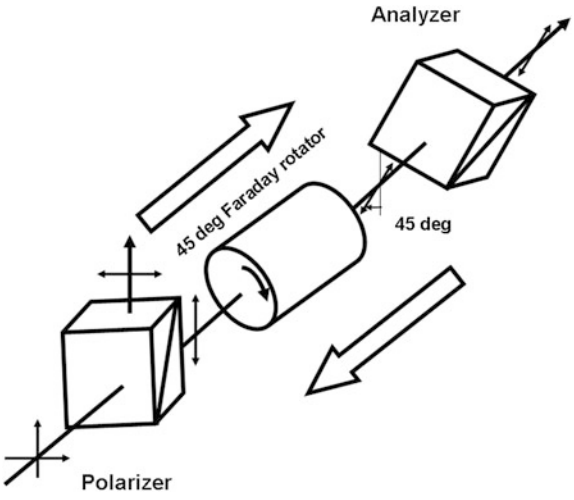

Fig. 9.18 Composition of polarization-sensitive optical isolator (Image courtesy of FDK Corporation)

When light propagates forward through the optical isolator, it first goes through the polarizer, where it is transformed into a linearly polarized light. Then, the light passes through the Faraday rotator, where the polarization plane of the light entering the rotator is rotated 45° to its original orientation. Finally, the light passes through the analyzer without loss because the analyzer is tilted in such a way that its polarization plane is set in the same direction as the light exiting the rotator. On the way back, the light first passes through the analyzer, where it is transformed into linearly polarized light. Then, it passes through the Faraday rotator, getting a 45° rotation of its polarization direction in the same rotation direction as on the way forward in the initial tilt. Finally, because the total tilt of the back-propagating light polarization plane is 90°, it is completely blocked by the polarizer.

It is important to mention the recent developed all-fiber isolators. These devices are based on 56 wt % terbium (Tb)-doped silicate fiber, and the fiber polarizers are made of Corning SP1060 single-polarization fiber [7]. Sun et al. [7] demonstrated 17 dB optical isolation at 1,053 nm. This approach shows the potential for achieving compact, high-power isolators in the near future.

Polarization-dependent isolators have wide applications, not only between stages of multistate fiber amplifiers but also in semiconductor lasers, especially the DFB type, which are very sensitive to backward-propagating light. The optical isolators are usually compared by their insertion loss and degree of isolation at the wavelength of interest.

9.2.2 Polarization-Independent Optical Isolators

Unlike polarization-dependent optical isolators, polarization-independent isolators have a 45° Faraday rotator placed between two wedge-shaped birefringent plates (Fig. 9.16a and b). Birefringent plates can be manufactured from TiO_2 single crystals (rutile), which demonstrate superior extinction ratios and big differences between ordinary and extraordinary beam refractive indexes.

When light enters a polarization-insensitive isolator, it first undergoes a polarization separation into ordinary and extraordinary beam components by the first birefringent plate (see Fig. 9.19a). The two beams then enter a Faraday rotator; the polarization planes are each rotated 45° after passing through the rotator. After that, the ordinary and extraordinary beams pass through a second wedged birefringent plate. The second birefringent plate has an optic axis oriented in such a way that the relationship between ordinary and extraordinary beams is maintained. Finally, both beams are refracted in an identical parallel direction after passing through the second wedged birefringent plate.

Backward-propagating light incident on the same optical isolator is separated into ordinary and extraordinary beams, whose relationship is reversed with that of a forward light due to the nonreciprocality of the Faraday rotation (see Fig. 9.19b). Eventually, when reaching first birefringent plate, the beams do not become

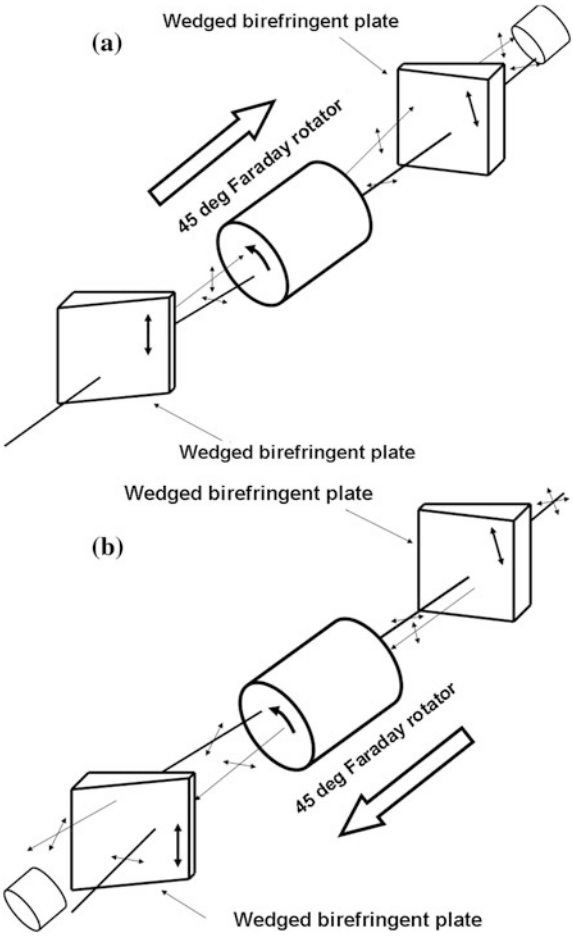

Fig. 9.19 (**a**) Forward propagation and (**b**) backward propagation of light in a polarization insensitive optical isolator. (Images courtesy of FDK Corporation)

parallel to each other (as on the way forward), so they cannot be converged and be coupled into the input fiber (see Fig. 9.19b).

9.2.3 High-Power Fiber-Coupled Isolators

Several companies developed high-power fiber-coupled optical isolators using not only true single-mode fibers but large-mode area fiber as well. Companies such as OFR (Thorlabs) offer fiber-coupled optical isolators with a collimated output, in which the output port of the isolator is replaced by collimating optics. This in turn allows the usage of such a device as the output component of the fiber laser system. These isolators handle over 10 W of pass-through optical power.

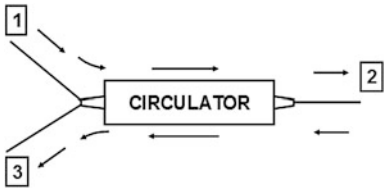

Fig. 9.20 The schematic and light propagation directions of a packaged three-port fiber-coupled optical circulator

Optical Circulators: A fiber-coupled optical circulator is a passive N-port device that couples light from port 1 to port 2, port 2 to port 3, and so on, to port $N - 1$ to port N. It has a high degree of isolation in opposite directions. Optical circulators allow unidirectional propagation of the light traveling in the fiber core and therefore are very useful in ring-fiber resonators.

Two principal structural components are shared by most optical circulators: a polarization rotation device (usually a Faraday rotator) and a polarization beam-splitting device (usually a polarizing prism or set of prisms). In the case of fiber-coupled circulators, each circulator port is effectively fiber coupled. The operation principle of an optical circulator is very similar to that used in an optical isolator. Using a polarization rotation of the light propagating forward through the system, an optical circulator uses the same polarization rotation again when the light is on the way back. Unlike isolators in which the back-propagating beam gets dumped, an optical circulator uses backward-propagating light as an output signal of its output ports (i.e., from port N to port $N + 1$). However, there is approximately 30 dB of isolation between port N and port $N - 1$. A typical view of the packaged fiber-coupled optical circulator is shown in Fig. 9.20.

The main challenge during the design of the optical circulator is to obtain a small insertion loss. Lately, because of growing demand for optical circulators used in high-power fiber laser technology, scaling the power tolerance of optical circulators is an important task. The following sections provide the design structure of some optical circulators as described in the literature.

9.2.4 Polarization-Dependent Circulator

Figure 9.21 shows a conventional polarization-sensitive (polarization-dependent) optical circulator [8]. Forward propagation is similar to that in optical isolator. Because the Faraday rotator rotates the propagating light polarization in the same direction (e.g., clockwise), one can easily reproduce the path of the light beam through the circulator shown in Fig. 9.21. In the case of fiber-coupled circulators, each port is fiber coupled (not shown in the figure).

(Image courtesy of the Optical Society of America)

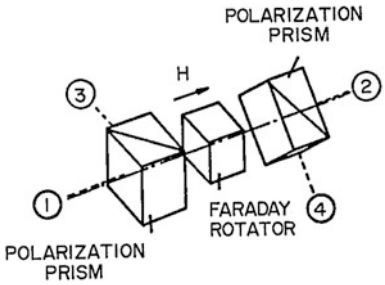

Fig. 9.21 Schematic view of a polarization-dependent four-port optical circulator [8]

9.2.5 Polarization-Independent Circulator

The polarization-independent optical circulator is somewhat more complicated because it must include polarization-insensitive components or set of polarization-sensitive components that produce overall device polarization insensitivity. Figure 9.22 shows an example design of the polarization-insensitive circulator, which uses prism-based polarization separators, a Faraday rotator, and a half-wave plate. Shirasaki et al. [9] used total internal reflection to make ordinary and extraordinary beams adjacent (Fig. 9.23).

The Faraday rotator employs a permanent magnet and Faraday garnet crystal. High-power, compactly packaged fiber-coupled optical circulators still demonstrate challenges. However, some companies (e.g., OFR) have already started commercial development of such circulators.

Fiber Bragg Gratings: The FBG is an optical device that employs a constant period grating (uniform grating) of higher and lower refractive indices in the fiber core (or in the vicinity of the ring surrounding the core) along the light-propagating direction (Fig. 9.24). This technology uses a photosensitive optical fiber that is exposed to deep ultraviolet laser light through a grating, thus creating an interferometric pattern along the light propagation direction in the fiber core and a modulated profile of the fiber core refractive index.

Depending on the refractive index grating period and grating length, FBGs operate as optical filters or mirrors. FBGs play an important role in spectral linewidth control of fiber lasers. The reflectivity of the uniform grating with constant modulation amplitude and constant period can be obtained using the coupled mode theory [10], given by the following formula:

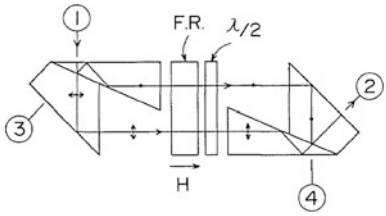

Fig. 9.22 Prism-based polarization separator [9]. (Image courtesy of the Optical Society of America)

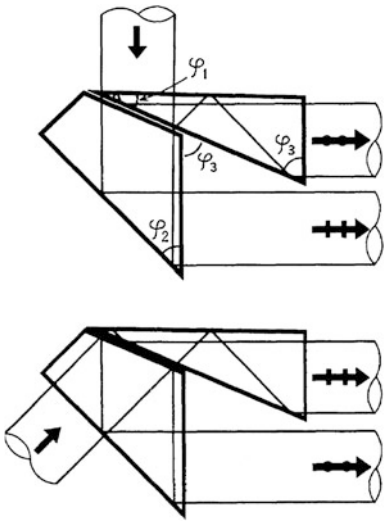

Fig. 9.23 Schematic of a polarization-insensitive optical circulator [9]. (Image courtesy of the Optical Society of America)

$$R(L,\lambda) = \frac{\kappa^2 \sin h^2(s \cdot L)}{\Delta\beta^2 \sin h^2(s \cdot L) + s^2 \cos h^2(s \cdot L)} \tag{9.10}$$

where $\kappa = \frac{\pi \Delta n}{\lambda} M_{\text{power}}$ is the power coupling coefficient for the sinusoidal variation of the refractive index, $\Delta\beta = \beta - {}^{\pi}/_{\Lambda}$ is the detuning wavevector, $\beta = \frac{2\pi n_0}{\lambda}$ is the propagation constant, and M_{power} is the fraction of the fiber mode power contained in the fiber core and $s = \sqrt{\kappa^2 - \Delta\beta^2}$.

The FWHM of the spectral bandwidth for the uniform diffraction grating is as follows [11]:

$$\Delta\lambda = \lambda_B R \sqrt{\left(\frac{\Delta n}{2n_0}\right)^2 + \left(\frac{1}{N}\right)^2} \tag{9.11}$$

where R is the coefficient that determines the grating strength ($R = 1$ for strong grating and $R = 0.5$ for weak grating), Δn is the refractive index modulation, λ_B is the central wavelength of operation (Bragg wavelength), and N is the number of grating lines along the whole length of the grating.

9.2.6 *Chirped FBG as a Self-Phase Modulation Compensator*

In a pulsed fiber laser system as a result of self-phase modulation (SPM; discussed in detail in Chap. 10), the original laser pulse is chirped. Using a special FBG type called chirped FBG (CFBG), one can compensate for the pulse chirp and ensure undisturbed laser pulse propagation in the amplifier. CFBG is an FBG where the

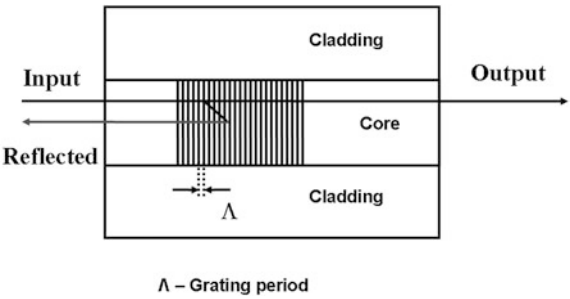

Fig. 9.24 Schematic view of the fiber Bragg grating

regions with high refractive index are not uniformly spaced or are not perpendicular to the length of the fiber (Fig. 9.25).

If we introduce a chirp bandwidth $\Delta\lambda_{\text{chirp}}$ and an effective index of refraction n_{eff} and FBG period Λ, one can express wavelength chirp bandwidth of the gratings as:

$$\Delta\lambda_{\text{chirp}} = 2n_{\text{eff}}\Delta\Lambda_{\text{chirp}} \tag{9.12}$$

where $\Delta\Lambda_{\text{chirp}} = \Lambda_{\text{long}} - \Lambda_{\text{short}}$. FBG dispersion is then described by the following expression:

$$A_D = 2L_{\text{grating}} \times {}^{1}\!/\!_{\left(\Delta\lambda_{\text{chirp}} V_{\text{group}}\right)} \tag{9.13}$$

where L_{grating} is the FBG length and V_{group} is the group velocity. A typical value of the FBG is 10 ns/m/$\Delta\lambda_{\text{chirp}}$.

Depending on the sign of the FBG dispersion, A_D, one can either compress or broaden the optical pulse. For Gaussian-shaped laser pulses, the following expression is used to calculate the pulse width deviation from its original value:

$$t_p = t_p(0)\left[1 + 2\pi c\left(\Delta\lambda_{\text{chirp}} A_D L_{\text{grating}}\right)/\lambda^2\right]^{0.5} \tag{9.14}$$

where $t_p(0)$ is the original pulse width of the laser entering the amplifier. By balancing the grating length, grating dispersion, and chirp bandwidth, one can control the pulse width of the pulse propagating in the amplifier.

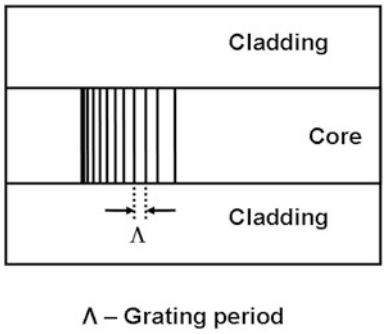

Fig. 9.25 Schematic example of a chirped fiber Bragg grating

9.2.7 A Few Words About Fiber Endface Preparation

In addition to fiber cleaving, there are four common types of fiber end preparations used in fiber lasers, either for fiber-coupled pump diode terminations or in output ports of fiber laser systems (Fig. 9.26):

1. A flat polish of the end face of the fiber, which results in back reflection of about −14 dB (i.e., 4 %).
2. A physical contact polish produces a slightly curved end face that forces the fibers in the mating connectors into contact. This reduces back reflection to about −40 dB by eliminating the fiber-to-air interface. This is the most commonly used preparation.
3. An angled physical contact polish adds 8 degrees or more to a flat polish condition. When used with fiber-to-fiber contact, this type of polishing keeps the fiber ends together. Also, light at the interface is reflected at a large angle, missing the core. Back reflections can be reduced to about −70 dB with this technique, or even more if larger angles are used.
4. A high-power flat-polished end face preparation is typically used for high-power fiber-coupled diode laser termination. The idea is to spatially separate the metallic part of the ferrule from the bare fiber end to prevent the deposition of metal particles on the fiber end face (e.g., in case back-propagating intense laser light hits the area next to the fiber).

Fiber end face preparation (in terms of surface profile) plays an important role in high-power fiber lasers because it determines optical back reflection into the gain material, which in turn may reduce fiber laser performance. Note that a high degree of cleanliness of the termination surface is required in most high-power fiber laser applications due to a high probability of damage to a poorly cleaned surface.

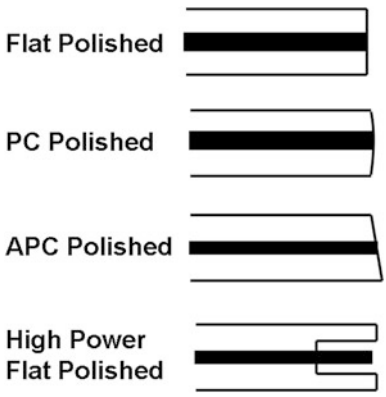

Fig. 9.26 The most commonly used fiber end face preparation types (applied to ferrule-based connectors)

References

1. N.G. Basov, B.M. Vul, YuM Popov, Quantum-mechanical semiconductor generators and amplifiers of electromagnetic oscillations. Sov. Phys. JETP **10**, 416–417 (1959)
2. R.N. Hall, G.E. Fenner, J.D. Kingsley, T.J. Soltys, R.O. Carlson, Coherent light emission from GaAs junctions. Phys. Rev. Lett. **9**(9), 366–369 (1962)
3. S.D. Offsey, J.M. Woodall, A.C. Warren, P.D. Kirchner, T.I. Chappell, G.D. Pettit, Appl. Phys. Lett. vol. **48**, 475 (1986)
4. S.M. Sze, Physics of semiconductor devices (Wiley-Interscience, New York, 1981), pp. 880
5. J.D. Love, Spot size, adiabaticity and diffraction in tapered fibers. Electron. Lett. **23**, 993–994 (1987)
6. A.Wetter, M.Faucher, B.Sévigny, High power cladding light strippers, in *Proceedings of SPIE,* vol. 6873, 687327.1–8, (2008)
7. L. Sun, S. Jiang, J.D. Zuegel, J.R. Marciante, All-fiber optical isolator based on Faraday rotation in highly terbium-doped fiber. Opt. Lett. **35**, 706–708 (2010)
8. T. Matsumoto, K. Sato, Polarization-independent optical circulator: an experiment. Appl. Opt. **19**, 108–112 (1980)
9. M. Shirasaki, H. Kuwahara, T.Obokata, Compact polarization-independent optical circulator. Appl.Opt. **20**, 2683– 2687 (1981)
10. D.K.W. Lam, B.K. Garside, Characterization of single-mode optical fiber filters. Appl. Opt. **20**, 440–445 (1981)
11. P.S. Russell, J.L. Archambault, L. Reekie, Fiber gratings. Physics World, October 1993 issue, pp. 41–46 (1993)
12. I. Gorog, P.V. Goedertier, J.D. Knox, I.Ladany, J.P. Wittke, A.H. Firester, Information scanning technology: applications of CW AlGaAs injection lasers. Appl. Opt. **15**, 1425– (1976)
13. M.I. Nathan, Semiconductor lasers. Appl. Opt. **5**, 1514–1528 (1966)

Chapter 10
High-Power Fiber Lasers

High-power fiber lasers occupy probably the most challenging and demanding place in the whole field of fiber laser technology; they also are state of the art. Both continuous-wave (CW) and pulsed high-power fiber laser systems constantly require technological advances. This chapter describes the main challenges in the development of high-power fiber lasers—the solution of which creates a path to successful laser development.

The main challenges in scaling-up fiber laser power are:

1. Nonlinear effects must be eliminated. For CW fiber lasers, two main nonlinear effects restrict power scaling: stimulated Brillouin scattering (SBS) and stimulated Raman scattering (SRS). Large core size and short fiber length will increase SRS and SBS thresholds.
2. For close to diffraction-limited beam quality (i.e., fundamental LP_{01} mode operation) at high operation powers, large-mode area (LMA), double-clad (DC) fiber with a high doping level of the active ion is required.
3. Core glass and end-facet damage must be eliminated because they may lead to fiber laser efficiency degradation or fatal breakdown.
4. High-power and high-brightness diode laser pumps and pump-coupling systems with high damage thresholds and high pump/signal power coupling efficiency with low thermal load must be developed.
5. Thermal management must occur to avoid heat-induced damage. Thermal effects may cause instability or even reduction in beam quality, change in laser wavelength or line-width, or polarization instability. In the case of challenges related to preservation of good beam quality, LMA fiber should be used with a numerical aperture (NA) below a certain value to discriminate high-order modes using coiling technology. The temperature dependence of the refractive index has a direct influence on the NA and hence the mode-discrimination capabilities of the LMA fiber.
6. Photodarkening must be addressed.
7. Robust, commercially available fiber-optic components and system configurations must be developed, such that the whole laser system maintains its

V. Ter-Mikirtychev, *Fundamentals of Fiber Lasers and Fiber Amplifiers*,
Springer Series in Optical Sciences 181, DOI: 10.1007/978-3-319-02338-0_10,

efficiency, beam quality, and damage-free operation while operating at high average power.
8. Polarization maintenance problems must be addressed to maintain precise phase control for coherent beam combining and nonlinear frequency conversion.

Processes in high-power CW fiber lasers that lead to bulk and surface damage of the fiber material include the following:

- Optical nonlinearities create self-pulsing in high-power fiber lasers. Self-pulsing is thought to be a reason for self-mode locking and self-Q-switching in optical fibers and causes self-focusing, resulting in bulk optical damage of the fiber glass.
- Thermal stress on the output of the fiber produces surface damage. A power level of 200–500 kW/cm^2 (depending on the condition of the fiber end surface) is considered to be the upper limit for damage-free fiber laser operation due to thermal stress.

Prevention strategy

The threshold of SBS and SRS optical processes can be increased by the following:

1. Increasing laser line-width when possible.
2. Decreasing gain fiber length.
3. Increasing gain fiber core diameter.
4. End-capping the fiber.
5. Reducing thermal load.

In most cases, during development of high-power fiber lasers, the following nonlinear processes have to be taken into consideration: SRS, SBS, four-wave mixing (FWM), self-phase modulation (SPM), cross-phase modulation (XPM), and self-focusing. These nonlinear processes play a key role in the development of reliable fiber laser systems and will be discussed later in this chapter.

Some authors have suggested using new fiber materials, such as YAG, to replace silica to ease several challenges of fiber lasers' power scaling. By replacing silica with YAG in the fiber core and optimizing fiber parameters, such as core diameter and fiber length, Parthasarathy et al. [1] showed that the limit for the YAG fiber laser is 6 kW per fiber in a multimode operation (compared to 1.8 kW for a silica-based fiber laser). Because of the smaller SBS gain in YAG (<10–12 m/W), the maximum output power of 30 kW can be achieved from a single fiber without a significant increase in fiber core diameter [1]. Significant improvement is also expected for single-mode laser operation using this approach.

10.1 Gain Fiber Pumping Technology for High-Power Fiber Lasers

The way that pumping radiation is coupled into the gain fiber determines the fiber laser pumping scheme. There are two main types of such coupling: when pumping light is coupled directly into the core (so-called core-pumped gain fibers) and when pumping light is coupled into the cladding (so-called clad-pumped gain fibers). Each pumping scheme has its advantages and disadvantages. Depending on the application, researchers and engineers give preference to one of these pump coupling schemes. This section compares the two fundamental pumping schemes, which should help the reader to understand the pump-type selection strategy.

Core Pumping: This pumping scheme is applied to single-clad gain fibers (Fig. 10.1). Its main advantages include a high core absorption, which allows for a short gain fiber length. However, it is restricted by its limited pump power due to high-brightness (single transverse mode) diode lasers, which are required for successful core pumping. This results in core darkening with creation of parasitic absorption due to high power density.

Clad Pumping: This pumping scheme is applied to DC and triple-clad (TC) gain fibers. A low-index polymer is typically used as a second/third (outer) cladding (Fig. 10.2). Its main advantages include the ability to couple high-power pump radiation from low-brightness diode lasers while maintaining the fundamental mode of the fiber laser radiation emerging from the doped fiber core. The downside is reduced effective pump absorption; therefore, longer fibers are required for effective absorption of the pump, which in turn affects the power threshold of nonlinear processes inside the core. Another limitation is reduced power density due to large clad diameters. For example, high-power densities are required for true three-energy-level lasers, such as Er^{3+}, and may be a limitation when reabsorption saturation is required. Nevertheless, using a DC fiber helps to scale fiber sources to higher power levels, which are not achievable with core-pump geometry, as well as higher pulse energies, because the large multimode inner cladding facilitates the use of higher-power and lower-cost multimode pump sources.

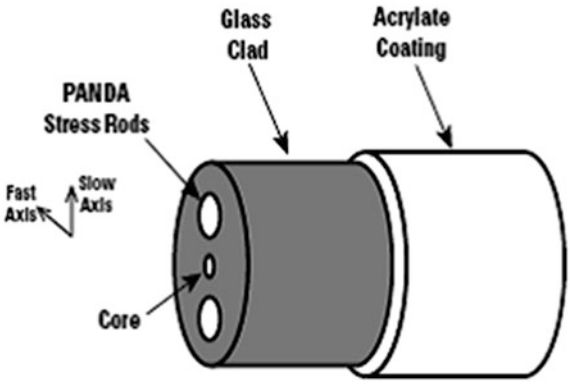

Fig. 10.1 Typical structure of the single-clad Panda-type fiber (Image courtesy of Nufern)

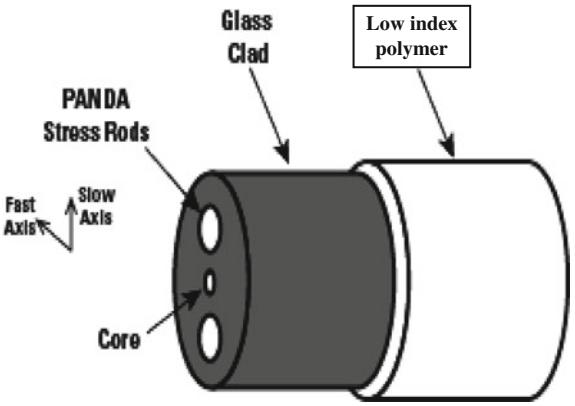

Fig. 10.2 Typical structure of the double-clad Panda-type fiber (Image courtesy of Nufern)

10.2 Double-Clad Fibers and Clad-Pumping Technology

A DC fiber is an optical fiber with two claddings that are equally important for light propagation through it. The main difference between single-clad fiber and DC fiber is the value of the refractive index of the outer cladding. This difference allows the wave-guided propagation of light inside the cladding of DC fiber at the same time that another wavelength of light is propagated in the DC fiber core. At the same time, cladding of the single-clad fiber has a purpose of creating wave-guiding condition for the core propagating light. Cladding of the single-clad fiber is not designed to be a waveguide. Usually in both cases of single- and DC fibers, the outer cladding is made of a polymer, which has a special lower refractive index in the case of DC fibers.

Because the DC fiber can waveguide laser radiation in the cladding and core simultaneously, DC fibers are widely used in fiber lasers and fiber amplifiers, especially with elevated power. Because of the bigger diameter of the cladding compared to that of the core, it is much easier to launch higher pump power into the cladding. In the case of DC fiber, the core is doped and acts as the gain medium of the fiber amplifier or laser. The pump light is coupled into the inner cladding. While propagating along the fiber, the pump light rays cross the core area; in this way, they perform optical pumping of the core, creating population inversion. The effective absorption coefficient of the light propagating along the cladding at the wavelength of the absorption for the ions in the doped core is reduced by a factor of the ratio of cladding-to-core areas.

The so-called clad-pumping technology was developed in the mid-1980s, basically revolutionizing the power scaling of fiber lasers and amplifiers with close to diffraction-limited beam quality. There is only one main disadvantage in the design of practical fiber laser systems: a reduced (by a factor of cladding-to-core area ratio) $x = S_{\text{clad}}/S_{\text{core}}$ effective absorption coefficient, which in turn requires an increased length of gain fiber to achieve full pump absorption. In addition to the increased cost of the longer gain fiber, this disadvantage also reduces the threshold

of nonlinear processes inside the core. Therefore, for high peak power applications, one may preserve short, single-clad, highly doped fiber. Note that the usage of a modified shape of the first cladding geometry (as opposed to round) was used to aid absorption of pump light by the doped fiber core. OFS (Furukawa, Avon, CT) introduced the so-called star cladding geometry to optimize cladding pump absorption.

For a typical true single-mode DC fiber with 5 and 125-μm core and clad diameters, respectively, effective absorption of the core at the pump wavelength is reduced by a factor of $(125/5)^2 = 625$. For example, in Yb^{3+}-doped DC 5/125 fiber developed by Nufern, this effective absorption coefficient reduction leads to about 10 m of gain fiber required to absorb 99 % of pump power propagating in cladding. However, the ability to launch several tens of watts into the DC 125 micron cladding makes this type of fiber very popular and widely used.

10.2.1 Clad-Pumping Schemes

Several pumping schemes to launch pump light into DC fiber have been developed. These schemes include end pumping, which launches pump light into one or both opposite ends of the fiber; fused fiber bundling, in which several multimode fibers are fusion-spliced to the inner cladding; and V-groove side pumping, in which the pump beam is launched by total internal reflection from a V-shaped groove cut into the inner cladding of the fiber. The main challenges of these pumping schemes include obstruction of the fiber ends and limited scalability for end pumping; the need for DC fiber and a fused bundle with matching dimensions for the fused fiber combiner; and relatively high alignment sensitivity for V-groove side pumping geometry.

On the other hand, wavelength division multiplexing (WDM) is a technique in which optical signals with different wavelengths transmitted together are separated or combined while being transmitted separately. This technique was mostly used for optical fiber communications because of the power restrictions of these devices. However, they are more and more often used in fiber laser technology. Because of the free space optics that are a core technology of the free space, micro-optics based WDM, until recently this method was mostly used for core-pumping geometry. With the development of TC fibers, which can tolerate high incident pump powers, WDM devices are also being used in clad-pumping configurations.

Among all mentioned DC fiber pump-coupling techniques, probably the most widely used in medium- to high-power fiber lasers and amplifiers is fused-fiber bundling, which can be manufactured with or without a signal fiber incorporated into the bundle of several multimode fibers. Sometimes, the signal fiber (which can be an LMA or single-mode fiber) is called a through fiber or signal-though fiber. Typical pump power transmission from pump fiber ports to the DC fiber cladding is more than 90 %, whereas signal fiber power transmission through a fiber combiner is more than 80 %.

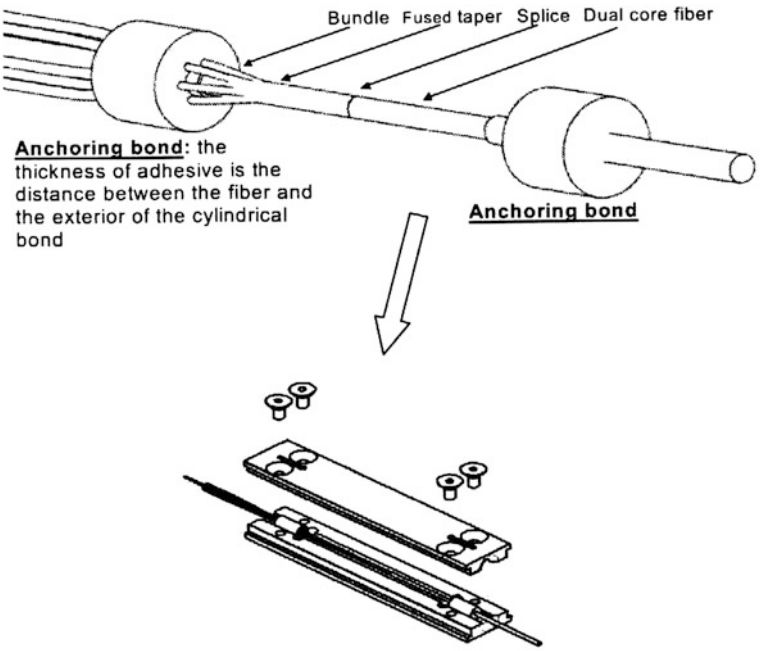

Fig. 10.3 Typical tapered fused-bundle structure with anchoring bonds [2] (Image courtesy of SPIE)

Currently, commercially available fused pump combiners developed by ITF can couple more than 1 kW of total pump power into the cladding of DC fiber [2], which can lead to more than 2 kW of launched pump power if a simultaneous counter and copropagating pumping scheme is employed. Figure 10.3 demonstrates a typical tapered fused-bundle (TFB) structure used by Wetter et al. [2]. The authors used so-called anchoring bonds and the metallic package in which the structure is embedded. The anchoring bonds absorb most of the heat in TFB devices; along with an optimized metallic package, they help the combiner to withhold such high optical power. Figure 10.4 shows some examples of fiber laser and fiber amplifier designs using TFB devices [2].

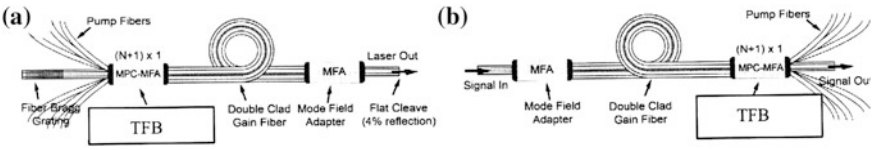

Fig. 10.4 Examples of tapered fused-bundle (*TFB*)-based fiber laser (**a**) and fiber amplifier (**b**) [2] (Image courtesy of SPIE)

10.2.2 Clad-Pumping and Triple-Clad Fibers

TC fibers are all-glass DC fiber configurations in which the core, inner cladding, and outer cladding are all made of optical glass (Fig. 10.5). Similar to ordinary DC fibers, a polymer is used as a protection for the outer glass layer. The pumping light propagates inside the inner cladding, whereas the glass outer cladding serves as a reliable and rugged outer guiding layer with a low refractive index. This is a state-of-the-art gain fiber technology for high-power DC fibers.

Using TC fibers in fiber laser design and development has the following advantages:

1. Reliable pump guiding.
2. No need for index matching during fiber recoating.
3. High power tolerance for end-face pump coupling in fiber-optic devices, such as WDM.

TC fiber is also a good solution for some clad-pumping applications in which pumping light experiences optical absorption in the polymer cladding at the pump wavelength, such as when induced by water absorption bands.

10.2.3 Free Space

Free-space pumping technology was historically first used in fiber lasers. Today, it is still a good option, especially for applications such as high-power fiber lasers, in which some of the fiber-coupled components are not readily available. Free-space pump coupling can work well for both core- and clad-pumping applications.

With the appearance of DC fibers and clad-pumping technology, free-space pump beam coupling regained popularity because of more relaxed requirements for focusing conditions. Among issues and challenges that have to be addressed in the use of free-space pumping are fiber and lens holders, heat dissipating mounts, and other heat management problems. With a continuing reduction in prices for lens optics, such as aspheric lenses, the free-space pumping approach still attracts

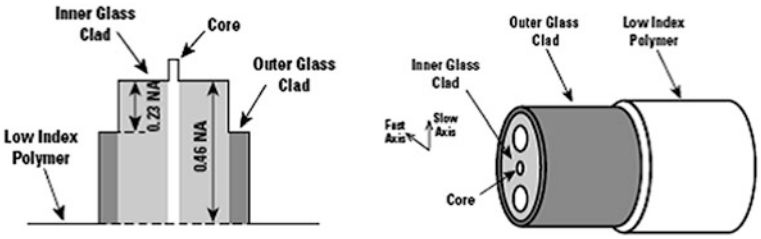

Fig. 10.5 Typical structure of the triple-clad Panda-type fiber (Image courtesy of Nufern)

the attention of researchers. However, for many applications, such as military applications or those with harsh operational conditions, an alignment-free approach (i.e., all-fiber solution) looks more attractive, although at a higher cost for the all-fiber components and splicing equipment.

Today's filter-based, fiber-coupled WDM components are free-space pump-coupling components packaged in a very compact enclosure with fiber pigtails at each connection port (also with fused WDM fiber components). Several free-space solutions have been suggested in recent years, in addition to straightforward end free-space pump coupling—namely, the embedded V-groove, prism coupler, and embedded mirror. Figure 10.6 summarizes these techniques. Most of the suggested

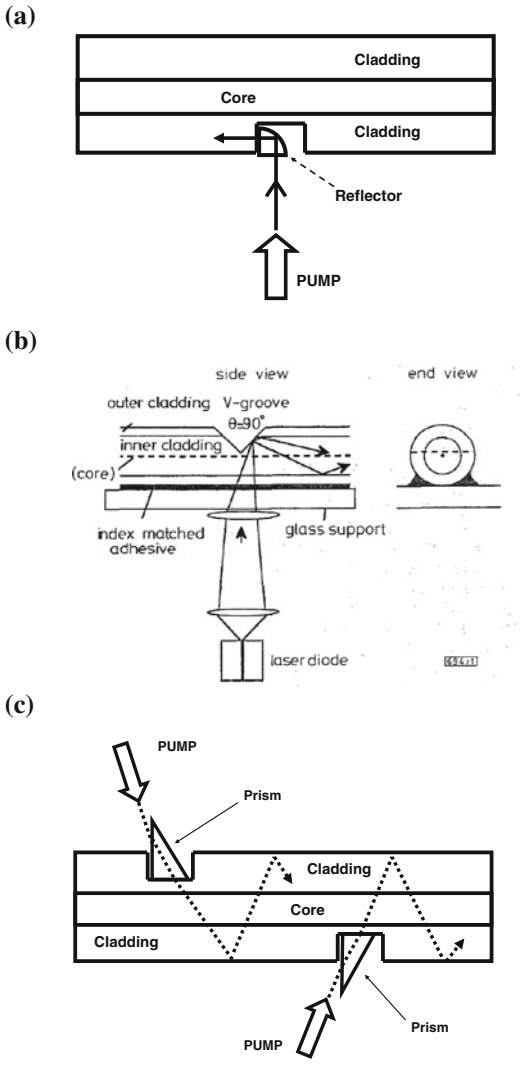

Fig. 10.6 **a** Diagram of an embedded mirror side-pumping technique (*cross-sectional side view*). **b** Fiber V-groove configuration [4] (Image courtesy of IET IEE). **c** Prism-based pump-coupler configuration for double-clad fibers

techniques are applicable for clad pumping of gain fibers. More detailed descriptions of the experimental implementation of these techniques can be found elsewhere [3–5].

10.2.4 Fused-Pump Combiners

Fused-fiber technology is a method in which one or several individual fibers are integrated together in a new fiber-optic device by a heating, fusing, or melting process. Fused fiber-optic pump or signal couplers are created by fusing and tapering two or more fibers together. This technology is one of the most simple, rugged, and cost-effective approaches to split or combine optical signals/pumps propagating in the fiber. Typical excess loss is as low as 0.2 dB. The split/combine ratio is very accurate and can be manufactured with tolerance between several percentages and a fraction of a percent.

These devices are bidirectional. Although they offer low back reflection and insertion losses, they still should be used with great care in high-power fiber laser and fiber amplifier systems. In the case of pump-combining devices with a through signal, companies who manufacture these components usually guarantee more than 30 dB of signal to pump port back-reflection isolation. However, this isolation does not prevent core to clad power coupling from fiber termination or bending, which in turn may be a reason for optical damage of pump diode lasers from back reflection in many cases. However, properly designed terminating fiber ends as well as output power optical isolation (e.g., using in-line fiber-coupled Faraday isolators) make fused-pump combiners irreplaceable for most applications. Figure 10.7 shows a typical fused pump to polarization-maintaining (PM) fiber signal combiner.

The number of pumping ports and device performance depends on several factors, including clad and core diameters of input and output fibers as well as their NAs. Fused pump–beam combiners are one of the most widely used devices in current fiber laser systems.

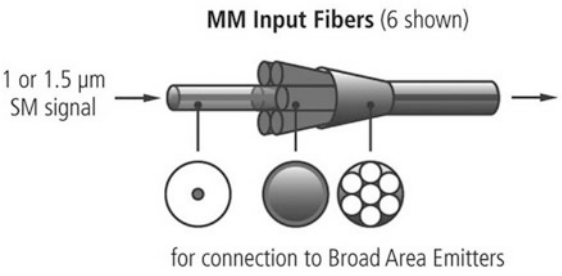

Fig. 10.7 Polarization-maintaining pump combiner developed by OFS. *MM* multimode, *SM* single mode (Reproduced with permission from Specialty Photonics Division, OFS Fitel LLC)

10.3 Large-Mode Area Fibers for High-Power, Diffraction-Limited Operation

An LMA fiber can be defined as an optical fiber that has a larger than true single-mode fiber core diameter, supporting only one or a few propagating spatial modes. The concept of LMA fibers was developed in the 1990s and mainly was inspired by researchers who worked in the field of high peak power and single-frequency fiber lasers and amplifiers. For these applications, it is desirable to use optical fibers with increased core areas, but preserving their single spatial-mode propagation as in many cases. LMA fibers have a much higher threshold of practically all nonlinearities due to the reduced intensities of the light propagating in the core, as well as a higher optical damage threshold. These features of LMA fibers make them irreplaceable for several applications, such as amplification of high peak power pulses or for amplification or oscillation of single-frequency laser radiation in gain fibers.

It may seem that the easiest way to design such an LMA fiber is to create a small difference between the core and cladding refractive indexes, which in turn decreases the NA of the core. However, because of the weaker guidance of the light waves inside the core in this case, the propagating losses can become high from small imperfections of the inner fiber or from fiber bending. Therefore, such an approach is very limited. Among existing reliable and bend loss-insensitive LMA fibers (both doped and undoped) with close to one propagating spatial mode, the biggest core diameter is 10–15 μm with a NA of 0.06–0.08. Figure 10.8 shows the typical panda-type PM LMA fiber profile, pictured from the fiber end.

To make LMA fibers more practical, several other techniques have been suggested. One of them is to achieve specially optimized refractive index profiles, which suppresses high-order mode propagation. This approach currently allows the achievement of up to a 30-μm LMA fiber core diameter. Note that fiber manufacturing with a sophisticated refractive index profile is a common challenge.

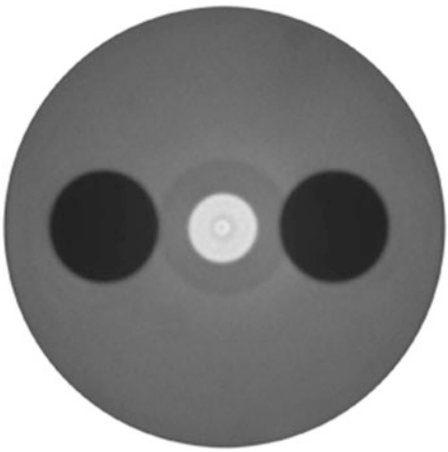

Fig. 10.8 Typical polarization-maintaining large-area mode 20/125 double-clad fiber profile. This magnified photograph is taken from the fiber end (Image courtesy of nLight/Liekki)

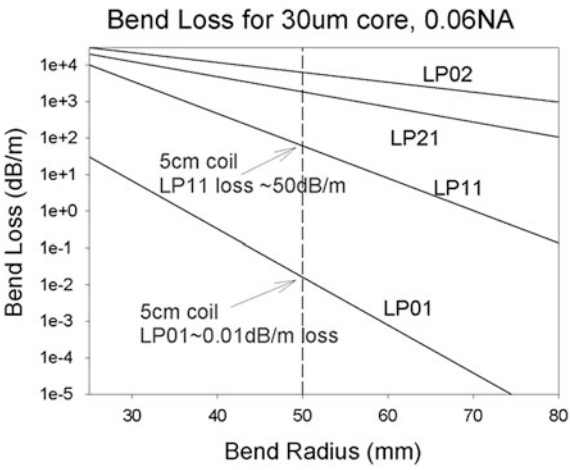

Fig. 10.9 Calculated loss dependence of the 30-μm core LMA fiber on the coil diameter for different fiber spatial modes (Image courtesy of Nufern)

Another technique suggests an excitation of the fundamental mode of multimode fiber during light coupling into the fiber. However, this approach requires precise determination of the light to fiber-coupling conditions, which become very critical. Because of this limitation, along with possible mode mixing in the fiber, more academic exploration of this technology is required.

In 2000, researchers from the Naval Research Laboratory and Sandia Research Laboratory proposed an interesting and practically important method for achieving single spatial-mode propagation in multimode optical fibers. Within this approach, it is suggested to induce significant bend loss to all high-order spatial modes of the fiber while preserving the minimum bend loss of its fundamental mode. This technology uses the fact that the fiber fundamental mode LP_{01} has the smallest bend loss sensitivities compared with higher-order LP modes. In addition, the bend loss attenuation coefficient depends exponentially on the radius of curvature of the bent fiber.

For all modes, the fundamental waveguide mode loss is less sensitive to bend and the bend-loss attenuation coefficient (expressed in dB/m) depends exponentially on the radius of coiling curvature (see Fig. 10.9). In practical applications, to introduce very high loss for all higher-order modes and at the same time little loss for LP_{01}, one needs to choose certain diameters of the fiber spool. The mode-filtering technique suppresses propagation of higher-order modes along the entire length of the fiber amplifier, and at the same time results in improved beam quality without loss of power and efficiency. The laser energy is extracted mostly to the LP_{01} mode. This technology is currently most widely used in research laboratories and commercial fiber laser systems.

Figure 10.10 demonstrates the distribution of intensity of LMA fiber for coiled and noncoiled conditions. Improvements in beam profile and beam quality are evident. However, that although LMA fibers can be coiled to obtain the single transverse mode operation, the coiling itself can cause instabilities and mode distortion in the fiber core [6].

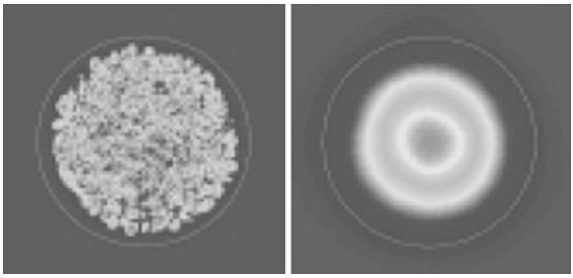

Fig. 10.10 Near–field spatial profile of the output from a multimode fiber amplifier ($d_{core} = 25$ μm) when the fiber is coiled (*right*) and not coiled (*left*) [46] (Image courtesy of SPIE)

10.4 Nonlinear Processes in Optical Fibers and Their Role in Fiber Laser and Fiber Amplifiers Technology Development

All nonlinear processes that take place in optical fibers can be grouped into two main categories: nonlinear scattering processes and nonlinear power dependence of the fiber refractive index. Nonlinear processes that belong to first group include SBS and SRS. The second group combines the processes of SPM, XPM, and FWM. From a practical viewpoint, SBS, SRS, and FWM mostly affect power distribution among several spectral lines corresponding to individual propagating waves, whereas SPM and XPM mostly affect spectral parameters of the propagating signals. Because of the crucial importance of nonlinear processes in fiber lasers design and development, each individual nonlinear process is described in more detail below.

To review the main nonlinear processes that take place in fibers and play an important role in the design and development of high-power fiber laser and fiber amplifier systems, several important parameters of optical fibers are introduced here. First, consider the so-called effective length (L_{eff}), which is determined by the absorption characteristics of the fiber:

$$L_{\text{eff}} = \frac{1}{P_0}\int P(z)\mathrm{d}z = \int \exp(-\mu z)\mathrm{d}z = \frac{1-\exp(-\mu L)}{\mu} \tag{10.1}$$

where P_0 is the original optical power entering fiber, $P(z)$ is the optical power inside the fiber at given point z along the fiber length, L is the total fiber length, and μ is the fiber absorption coefficient at the wavelength of light propagation.

Another important fiber parameter is the effective area A_{eff}, which is defined as:

$$A_{\text{eff}} = \frac{\left(\int_0^\infty |E_a(r)|^2 r\,\mathrm{d}r\right)^2}{\int_0^\infty |E_a(r)|^4 r\,\mathrm{d}r} \tag{10.2}$$

where E_a is the amplitude of the fundamental fiber mode and $|E_a(r)|^2 = I(r)$ is the intensity of the fiber fundamental mode at radius r from the axis of the fiber.

In the case of conventional step index fibers, the field distribution of the fundamental mode is very well approximated by a Gaussian function. Therefore, the effective area of the fiber core is equal to:

$$A_{\text{eff}} = \pi w(\lambda)^2 \tag{10.3}$$

where $2w(\lambda)$ is the so-called mode field diameter (MFD) of the fiber core at wavelength λ. Note that for fibers other than step index fibers (i.e., dispersion-shifted or dispersion-flattened fibers), the MFD cannot be approximated by a Gaussian function and one should use other methods to determine MFD. But in the first approximation estimate of the effective core area of the fiber, in most practical cases of high-power fiber lasers, MFD gives a good value that can be taken to determine A_{eff}.

Also, recall the power dependence of the glass refractive index, which plays an important role in understanding the optical nonlinearities in fibers. As is well known, the glass refractive index can be expressed as:

$$n = n_0 + n_2 \frac{P}{A_{\text{eff}}} \tag{10.4}$$

where n_0 is the linear refractive index of the fiber core (measured at low optical power levels), n_2 is the nonlinear refractive index coefficient (which has a value of 2.35×10^{-20} m^2/W for silica), and P is the optical power of the propagating light wave in watts.

10.4.1 Threshold Power of the Stimulated Scattering Process

It is useful here to review the basic formulas that determine the threshold of the stimulated scattering process. For the general case of a stimulated scattering process (SRS or SBS) with an arbitrary pulse width of excitation (CW; i.e., stationery or pulsed), one can derive an analytical expression for the scattering process power threshold in a nonstationary regime of excitation. Following Ya et al. [7], one can obtain:

$$g \frac{P_{\text{thpeak}}}{A_{\text{eff}}} L_{\text{eff}} = M \quad \text{when} \quad \Gamma t_p \gg 15 \tag{10.5}$$

and

$$g \frac{P_{\text{thpeak}}}{A_{\text{eff}}} L_{\text{eff}} = \frac{\left(\frac{M}{2} + \Gamma t_{\text{p}}\right)^2}{2\Gamma t_{\text{p}}} \quad \text{when} \quad \Gamma t_{\text{p}} \ll 15 \tag{10.6}$$

where g is a stimulated scattering gain given in cm/W, $P_{\text{th peak}}$ is the threshold peak power of the scattering process given in watts, L_{eff} is the effective length of the fiber given in centimeters, A_{eff} is the effective area of the fiber core given in cm^2, Γ is the spectral line-width of spontaneous scattering process given in hertz, t_p is the propagating optical pulse width given in seconds, and M is a numerical factor that

determines a gain value of exp(M), which is usually considered as sufficient to amplify noise photons that shifted during stimulated scattering process optical frequency to the detectable level. The value of M is typically 30 for the general theory of stimulated scattering. For SRS, $M = 16$, whereas $M = 21$ for SBS.

10.4.2 Stimulated Raman Scattering

Raman scattering is an important and interesting phenomenon that was discovered in 1928 independently in Russia (by Landsberg and Mandelstam) and India (by Raman and Krishnan) in crystals and liquids, respectively. Historically, the process is named after Sir C.V. Raman, the Indian scientist who made this important discovery in liquids.

Unlike many applications of Raman scattering in spectroscopy and optics, in the field of fiber lasers—especially high-power fiber lasers—the Raman scattering phenomenon is often considered to be an obstacle rather than an opportunity (except for Raman fiber lasers or special cases when the Raman effect is used to control other nonlinear processes). Therefore, this important nonlinear process is discussed in detail here.

The basic physical idea behind Raman scattering is an interaction of an incident light wave with intrinsic vibrations of molecules. When a light wave is propagating in the medium, it scatters, creating a phonon through excitation of the molecule vibrations. As in any scattering process, both energy and momentum (or wave vector) have to be preserved. Raman scattering, similar to Brillouin scattering (with respect to the photon–phonon interaction), is an inelastic scattering process of light photons propagating inside the medium with optical phonons of the medium (more detailed information about optical and acoustical phonons in solids can be found in different textbooks on solid-state physics). The result of this photon–phonon interaction is a number of new photons with energy equal to the sum or difference between the energy of the original photon and integer number of phonon energy. Therefore, when the light is propagating inside the Raman active medium, new frequencies appear in the spectrum of scattered waves. This spectrum consists of frequency components shifted with respect to the incident photon. These frequency separations between individual spectral components of the so-called Raman spectrum correspond to the intrinsic phonon energy of the medium. Shifted frequency components are located on both sides of the spectral position of the incident light wave. Those spectral components that appear on the low-energy side from the original light wave frequency are called Stokes components, whereas whose located on the high-energy side are anti-Stokes components. Anti-Stokes components correspond with the added phonon energy to the original light-wave photon energy and Stokes components correspond with the subtracted phonon energy. Separation from the original signal light-wave frequency with one phonon called the first Stokes (or first anti-Stokes), with two phonons is called second stokes (or second anti-Stokes), and so on.

In crystalline solids, where wave vector selection rules have to be strictly followed, the Raman spectrum consists of very narrow bands; in glasses, where wave vector selection rules are practically absent and which are disordered materials, Raman scattering response is a series of broad bands that demonstrate a spectral distribution of the scattering process rather than a strictly defined frequency shift. At room temperature (close to 300 K), anti-Stokes components are greatly weaker than Stokes components.

The study of the Raman scattering phenomenon changed drastically with the appearance of lasers in 1961, when high-intensity laser beams became available to researchers. A new process was observed by Woodbury and Ng in 1962 using laser light as an excitation source in Raman scattering experiments. When a weak optical signal at a frequency corresponding to a Stokes Raman scattering component is injected into the medium together with strong pump light, it will be amplified with gain that is proportional to the pump power. This is called SRS.

In laser physics, SRS gain is a measure of the signal wave amplification in the field of high-power pump radiation. SRS also has a so-called critical power or threshold power, which corresponds to the appearance of scattered optical power and is comparable to that of the pump power (usually in the first Stokes component). If positive feedback is provided (Fabry–Perot optical resonators are commonly used for such applications), a coherent Raman wave can be obtained. The device that employs a Raman active material and an optical resonator to produce coherent emission at Raman Stokes and anti-Stokes spectral components is called a Raman laser.

In optical fibers where large pump intensities and long interaction lengths are easily available, a weak spontaneous Raman scattering signal is amplified to the power level of input laser intensities, and the process becomes SRS. Figure 10.11 demonstrates a typical Raman gain spectral dependence for different glasses. The slightly different spectral position of the first Stokes component near 440 cm^{-1} is a result of different phonon energy of different materials shown in the figure. These phonon energies correspond to different energies of intrinsic vibration.

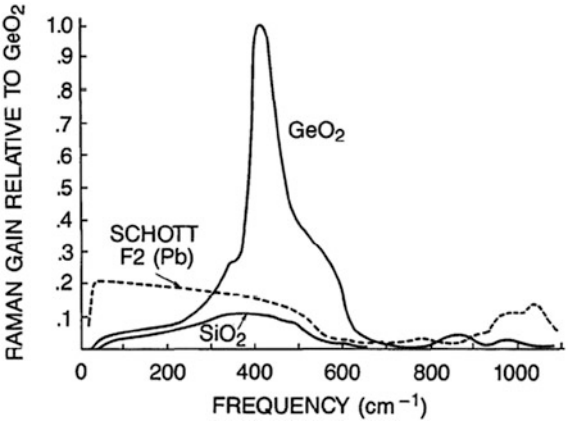

Fig. 10.11 Raman gain in different glasses [47] (Image courtesy of the Optical Society of America)

10.4.3 Continuous-Wave SRS

In the case of CW pump in the SRS process, the critical power (or threshold) is determined by the following expression:

$$P_{\text{thSRS}} = \frac{16\,A_{\text{eff}}}{g_{\text{R}} L_{\text{eff}}} \tag{10.7}$$

where g_{R} is Raman gain measured in cm/W. It has the following value in fused silica at a 1-μm wavelength of pump light:

$$g_{\text{R}} = 9.8 \times 10^{-11}\,\text{cm/W} \tag{10.8}$$

Note that Raman gain is inversely proportional to the pump wavelength:

$$g_{\text{R}} \propto \frac{1}{\lambda_{\text{p}}} \tag{10.9}$$

For an arbitrary pump signal spectral bandwidth ($\Delta\omega_{\text{p}}$), Raman gain is determined as:

$$g_{\text{RARB}}(\Delta\omega_{\text{p}}) = g_{\text{R}}\left(1 + \frac{\Delta\omega_{\text{p}}}{\Gamma_{\text{R}}}\right)^{-1} \tag{10.10}$$

Γ_{R} is the homogeneous width of the Raman line, which in silica fibers is:

$$\Gamma_{\text{R}} = 6 \times 10^{12}\,\text{Hz} \tag{10.11}$$

Therefore, the SRS threshold power for an arbitrary spectral line-width of the pump beam is:

$$P_{\text{thSRS}}(\Delta\omega_{\text{p}}) = \frac{16A_{\text{eff}}}{g_{\text{RARB}}(\Delta\omega_{\text{p}})L_{\text{eff}}} \tag{10.12}$$

As shown in Fig. 10.11, in GeO_2-doped fibers, Raman gain is about 10 times higher than in fused silica. From above formula to determine SRS threshold power, one can easily calculate this important parameter. For silica fiber with effective length of 10 m and core diameter of 6 μm, where CW laser light with 1-μm wavelength propagates in the core, this critical power is approximately 550 W.

10.4.4 Pulsed SRS

From the previous analysis, the threshold peak power of the SRS in silica fiber can be calculated using the following formulas:

$$g_{\text{R}} \frac{P_{\text{thpeak}}}{A_{\text{eff}}} L_{\text{eff}} = 16 \quad \text{when} \quad t_{\text{p}} \gg 1.3\,\text{ps} \tag{10.13}$$

and

$$g_R \frac{P_{thpeak}}{A_{eff}} L_{eff} = \frac{(8 + \Gamma_R t_p)^2}{2\Gamma_R t_p} \quad \text{when} \quad t_p \ll 1.3\,\text{ps}, \quad \Gamma_R = 6 \times 10^{12}\,\text{Hz} \quad (10.14)$$

The calculation of the SRS threshold power is very important in fiber laser design and development because it is one of those threshold powers that may restrict power scaling of the fiber laser or amplifier. From the analysis in this section, one can see that shortening fiber length, increasing fiber core diameter, and increasing propagating laser signal spectral line-width result in increasing SRS threshold.

10.4.5 Stimulated Brillouin Scattering

The physical nature of the Brillouin scattering phenomenon is very similar to that of Raman scattering. The main difference is that Brillouin scattering defines a process where an incident (or propagating) light wave interacts with acoustical phonons of the medium (i.e., with its lattice vibration modes). This process was predicted by Mandelstam in 1918 (published in 1926) and Brillouin in 1922. It describes an inelastic scattering of an incident optical wave on the thermally excited acoustical waves/phonons. Historically, the effect is named after Brillouin. Gross was the first to demonstrate this effect experimentally in crystals and liquids.

Brillouin scattering demonstrates a similar picture of frequency shifts of the scattered light to that of Raman scattering with all notations of Stokes and anti-Stokes given in the previous section. Because the optical phonon energy is much smaller than acoustical phonon energy, Brillouin scattering shifts are much smaller than that of Raman scattering.

The Brillouin scattering frequency shift that appears in the Brillouin scattering spectra corresponds to the energy of vibration modes of the lattice, which belong to the medium of the light propagation and can be expressed as:

$$h\nu_B = h\frac{2nV_a}{\lambda_p}\sqrt{\left(\frac{1 - \cos\theta_B}{2}\right)} \quad (10.15)$$

where n is the medium refractive index at pump wavelength, V_a is the acoustic velocity of the medium, and θ_B is the angle between the scattered wave vector and the initial pump wave vector. This frequency shift is approximately 11.25 GHz for silica fiber at a 1.5-μm wavelength of pump light, which corresponds to the energy of acoustic vibration mode in silica. ν_B varies inversely with λ_p.

From the previous formula, one can see that in case of single mode fibers, nonzero frequency shift is possible only for one value of phase-matching angle θ_B:

$$\theta_B = \pi \quad (10.16)$$

The physical meaning of this solution is that the SBS phase-matching condition is possible in case of counter propagating waves. In other words, the SBS Stokes component is expected to emerge from the fiber at the input end (i.e., backscattering). In the SRS case, the Stokes component copropagates with the pump (i.e., forward scattering).

10.4.6 Continuous-Wave SBS

Following the same logic as in the case of SRS for CW pumping in the SBS process, a critical power (or threshold) is determined by the following expression:

$$P_{\text{thSBS}}(\Delta\omega_{\text{p}}) = \frac{21A_{\text{eff}}}{g_{\text{BARB}}(\Delta\omega_{\text{p}})L_{\text{eff}}}$$

where g_{BARB} is the Brillouin gain measured in cm/W for an arbitrary spectral line-width of the pump signal.

As it was shown in Ref. [8], SBS gain coefficient in a steady-state regime can be expressed as:

$$g_{\text{Bst}} = g_{\text{B}} = \frac{4\pi^2 n^7 p^2 \Gamma_{\text{B}}}{c\upsilon\rho\lambda^2} \tag{10.17}$$

where n is the refractive index of the medium, p is the elastooptic coefficient, Γ_{B} is the lifetime of the SBS active acoustic phonon, υ is the acoustic phonon speed of propagation, ρ is the density of the medium, and λ is the laser wavelength in a vacuum. It has the following value in fused silica at a 1.5-μm wavelength of pump light:

$$g_{\text{B}} = 4.3 \times 10^{-9}\ \text{cm/W} \tag{10.18}$$

This result is almost three orders of magnitude larger than that of the Raman scattering. Unlike Raman gain, it is almost independent of the wavelength.

Figure 10.12 shows a measured SBS gain spectrum for pure silica fiber measured at 828-nm pump wavelength.

The 20-GHz spectral shift in Fig. 10.10 at a 826-nm pump wavelength gives an 11 GHz shift at a 1,500-nm wavelength according to the following relationship:

$$\nu_{\text{B}} \propto \frac{1}{\lambda_{\text{p}}}$$

As shown in Fig. 10.12, a Brillouin line-width of 275 MHz at 826-nm excitation wavelength should give an $\sim$80 MHz Brillouin line-width at 1,500-nm excitation wavelength. Brillouin scattering line-width is inversely proportional to the square of the excitation wavelength.

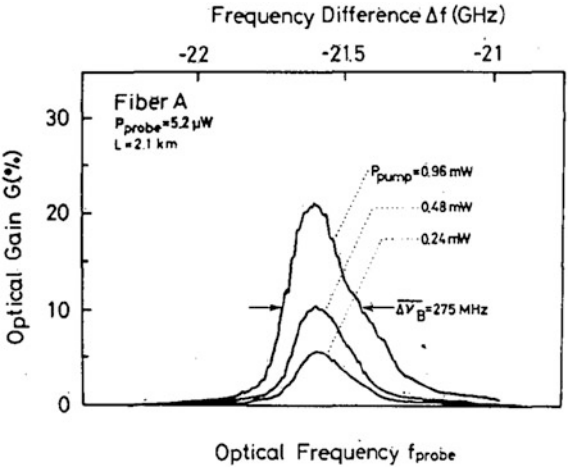

Fig. 10.12 Gain spectra of pure silica fiber measured with 828-nm wavelength of excitation [48] (Image courtesy of the Optical Society of America)

For arbitrary pump-signal spectral bandwidth ($\Delta\omega_p$), Brillouin gain is determined as:

$$g_{BARB}(\Delta\omega_p) = g_B\left(1 + \frac{\Delta\omega_p}{\Gamma_B}\right)^{-1} \tag{10.19}$$

Γ_B^{-1} is the phonon lifetime of the medium, which in silica fibers is:

$$\Gamma_B^{-1} = 10\,\text{ns} \tag{10.20}$$

The expected spectral dependence of Γ_B is inversely proportionality to the square of pump wavelength:

$$\Gamma_B \propto \frac{1}{\lambda_p^2} \tag{10.21}$$

As one can see, the SBS threshold in fibers in most cases (unless the pump laser line-width is very broad) is much lower than that of the SRS. This is why SBS usually appears much earlier in scaling up the fiber laser power and is more dangerous because of its back-propagating nature. For 10 m of silica fiber with a core diameter of 6 μm and propagating pump signal spectral line-width in the sub-MHz range, the SBS threshold is few watts, which is the limit for straightforward design of single-frequency CW fiber lasers using conventional Yb^{3+}-doped DC fibers pumped at 976 nm with about 2 dB/m pump absorption.

10.4.7 Pulsed SBS

Similarly to SRS, the following formulas can be used for an SBS power threshold calculation in the case of optical pulse excitation for both stationary (long-pulse) and nonstationary (short-pulse excitation):

$$g_B \frac{P_{thpeak}}{A_{eff}} L_{eff} = 21 \quad \text{when} \quad t_p \gg 100\,\text{ns} \tag{10.22}$$

and

$$g_B \frac{P_{thpeak}}{A_{eff}} L_{eff} = \frac{\left(\frac{21}{2} + \Gamma_B t_p\right)^2}{2\Gamma_B t_p} \quad \text{when} \quad t_p \ll 100\,\text{ns},\ \Gamma_B \approx 100 \times 10^6\,\text{Hz} \tag{10.23}$$

where $M = 21$ for the SBS process in silica fibers.

Knowing the transient SBS gain coefficient gives a path to calculate the threshold of SBS in pulsed fiber lasers and amplifiers.

10.4.8 Optical Kerr Effect

The three processes described in this section are based on the optical Kerr effect in fibers. This important optical phenomenon is devoted to the process of instantaneous nonlinear optical response of the dielectric medium to the propagating light. This process describes a change in the refractive index of the medium due to the propagating of high-intensity electromagnetic radiation.

The basic formula of the optical Kerr effect is expressed in the following relationship:

$$\Delta n = n_2 I \equiv n_2 \frac{P}{A_{eff}} \tag{10.24}$$

where n_2 is the nonlinear refractive index of the optical medium where high-intensity light is propagating, expressed in cm^2/W; I is the intensity of the light beam, expressed in W/cm^2; and P is the optical power of the propagating beam, expressed in watts. The typical value for the nonlinear refractive index in glass fibers varies in the range of 2–5 $\times$ 10^{-16} cm^2/W, depending on the fiber glass composition.

10.4.9 Self-Phase Modulation

SPM is a phenomenon caused by nonlinear phase modulation of the optical beam induced by its own intensity. The optical Kerr effect plays central role in the SPM

phenomenon, which creates a different phase condition for the peak of the pulse as compared to its rising and falling edges. The latter process results in the direct change of the pulse spectral characteristics. In addition to the distortion of spectral characteristics of the fiber laser pulses, SPM causes power instability and intensifies the self-mode-locking effect.

Consider an optical pulse propagating in a fiber with Kerr nonlinearity. If we assume that the propagating pulse has a uniform intensity profile, the phase acquired by the pulse after propagating length L_{eff} of the fiber can be expressed as:

$$\varphi(t, L) = \omega_0 t - \frac{\omega_0 \left[n_0 + n_2 \frac{P(t)}{A_{\text{eff}}} \right] L_{\text{eff}}}{c} \tag{10.25}$$

where ω_0 is the carrier frequency of the propagating in the fiber pulse. The instantaneous carrier frequency of the propagating pulse is then:

$$\omega(t, L) = \frac{\mathrm{d}\varphi(t, L)}{\mathrm{d}t} = \omega_0 - \frac{\omega_0 n_2 L_{\text{eff}}}{c} \frac{\mathrm{d}P(t)}{\mathrm{d}t} \tag{10.26}$$

For the important case of Gaussian pulse shape, intensity of the pulse varies according to the following Gaussian function:

$$P(t) = P_0 \exp\left(-\frac{t^2}{\tau_0^2} \right) \tag{10.27}$$

One can obtain the following expression for the propagating signal-pulse duration at full width, half maximum:

$$t_{\text{p}} = 2\sqrt{\ln 2} \times \tau_0 \tag{10.28}$$

Spectral broadening of the Gaussian pulse propagating inside a fiber due to SPM can be determined as follows:

$$\delta\omega(t, L) = \omega(t, L) - \omega_0 = \frac{2\omega_0 n_2 L_{\text{eff}} P_0}{c\tau_0^2 A_{\text{eff}}} t \exp\left(-\frac{t^2}{\tau_0^2} \right) \tag{10.29}$$

By zeroing a time derivative of the above function, one can determine the maximum spectral broadening due to SPM of the propagating Gaussian pulse as follows:

$$\delta\omega_{\max} = 0.86\tau_0^{-1} \frac{n_2 \omega_0}{c A_{\text{eff}}} P_0 L_{\text{eff}} \tag{10.30}$$

If one considers general case of a super-Gaussian pulse shape, the SPM-induced chirp $\delta\omega(t)$ can be derived from the temporally varying phase with the following expression [9]:

$$\delta\omega(t) = \frac{2m}{\tau_0} \frac{L_{\text{eff}}}{L_{\text{NL}}} \left(\frac{t}{\tau_0} \right)^{2m-1} \exp\left(-\left(\frac{t}{\tau_0} \right)^{2m} \right) \tag{10.31}$$

L_{NL} is nonlinear fiber length, which is:

$$L_{NL} = (\gamma P_0)^{-1} \tag{10.32}$$

The nonlinear parameter γ is defined as:

$$\gamma = \frac{n_2 \omega_0}{c A_{eff}} \tag{10.33}$$

For Gaussian pulse shape, $m = 1$, whereas $m = 3$ for the super-Gaussian pulse shape.

For an unchirped Gaussian pulse, $\Delta\omega_0 = \tau_0^{-1}$ where $\Delta\omega_0$ is the spectral width of the pulse at $1/\exp(+1)$ level. Therefore, for the Gaussian pulse width with $m = 1$, the maximum spectral broadening factor is:

$$\delta\omega_{max} = 0.86\,\Delta\omega_0\,\varphi_{max} = 0.86\tau_0^{-1}\frac{n_2\omega_0}{cA_{eff}}P_0 L_{eff}. \tag{10.34}$$

10.4.10 Cross-Phase Modulation

Unlike SPM, XPM takes place in the case of multiple-beam co-propagation along the fiber. Particularly, XPM is a phenomenon in which intensity of one propagating optical signal influences the phase of another co-propagating optical signal. An analytical expression that describes a refractive index change of one co-propagating signal Δn_1 in the field of I_2 intensity of the second co-propagating signal is as follows:

$$\Delta n_1 = 2 \times n_2 \times I_2 \tag{10.35}$$

For certainty, one can assume that indexes 1 and 2 correspond to the individual wavelength of the co-propagating beams (i.e., λ_1 and λ_2. One can see from the expression for the phase change that XPM is twice as effective as SPM for the same intensity of interacting signal waves.

In fibers, there are two main contributions of the XPM phenomenon to the propagating signal pulses along the fiber length: spectral broadening enhancement and frequency shift. For the case of Gaussian pulse shape with spectral frequency ω_1, combined spectral broadening of this pulse induced by another co-propagating pulse (i.e., pump pulse) with spectral frequency ω_2 is given by the following expression [10]:

$$\Delta\omega_{1SPM+XPM} \approx \frac{\omega_1}{c} n_2 (I_1 + 2I_2)\frac{L}{\tau_0} \tag{10.36}$$

Spectral broadening enhancement therefore is:

$$\frac{\Delta\omega_{1\mathrm{SPM}+\mathrm{XPM}}}{\Delta\omega_{1\mathrm{SPM}}} = \left(1 + 2\frac{I_2}{I_1}\right) \tag{10.37}$$

On the other hand, the maximum XPM-induced frequency chirp is:

$$\delta\omega_{1\max} = 2\frac{\omega_1}{c} n_2 I_2 \frac{L_w}{\tau_0} \tag{10.38}$$

where L_w is the walkoff length and τ_0 is the pulse width. The walkoff length L_w is determined by the following expression:

$$L_w = \frac{\tau_0}{|d|} \tag{10.39}$$

where $d = \dfrac{v_{g1} - v_{g2}}{v_{g1} v_{g2}}$ is a group velocity mismatch between the two pulses and v_{gi} is the group velocity of an individual traveling signal pulse.

In fiber lasers, XPM is used for synchronization of individual mode-locked fiber lasers, as well as some other applications.

10.4.11 Four-Wave Mixing

FWM is a third-order nonlinear process in silica fibers. As in the case of SBS and SRS, this process results in redistribution of power among several spectral components that appear during propagation of high-intensity light in the fiber.

Due to the phase sensitivity of this nonlinear process, there are several ways to achieve efficient FWM. Unlike FWM process in bulk media, where FWM phase-matching may be achieved by choosing appropriate angles between interacting beams, in fibers high efficiency of the FWM can be achieved over long distances of individual signal propagation under conditions of phase matching. Obviously, this in turn can be achieved either by small spectral separation of individual signals participating in the FWM process or by choosing the appropriate dispersion dependence of the fiber in which FWM expected to take place.

In fibers under certain dispersion conditions (i.e., near zero-dispersion point), three optical frequencies (v_α, v_β, and v_γ) mix up to produce a fourth frequency $v_{\alpha\beta\gamma}$ as follows:

$$v_{\alpha\beta\gamma} = v_\alpha + v_\beta - v_\gamma \tag{10.40}$$

where $\alpha, \beta \neq \gamma$.

The number of generated mixing products K during the process of FWM for a number of wavelengths N launched into the fiber is expressed by the following:

$$K = \frac{N^2(N-1)}{2} \tag{10.41}$$

To calculate the optical power of the signal created by the FWM process, one should consider several factors that influence this value, including the spectral spacing of individual signals participating in FWM process and the dispersion of the fiber material where FWM takes place.

The optical power of the signal appearing as a result of the FWM process can be calculated using following expression:

$$P_{\alpha\beta\gamma} = \eta_{\text{FWM}} D_{\text{deg}}^2 \gamma^2 P_\alpha P_\beta P_\gamma \exp(-\mu L_{\text{eff}}) \tag{10.42}$$

Here, γ is a nonlinear interaction constant that represents the strength of the Kerr nonlinearity in the fiber, given by:

$$\gamma = 2\pi n_2 \frac{1}{A_{\text{eff}} \lambda} \tag{10.43}$$

In these equations, n_2 is the nonlinear refractive index (typical value is 3 W^{-1} km^{-1}), L_{eff} is the effective length of the fiber, D_{deg}^2 is the degeneracy factor (which is equal to 3 for two mixing waves or 6 for three distinct mixing waves), μ is the loss coefficient (typical value is 4.5×10^{-7} cm^{-1}, which corresponds to 0.2 dB/km for telecom fibers and ~5–10 dB/m for gain fibers), A_{eff} is the effective cross-section area of the fiber core, and $P_{\alpha,\beta,\gamma}$ is the individual channel power. η_{FWM} is the FWM process efficiency in gain fiber (i.e., EDFA, YDFA or TmDFA), which can be expressed as:

$$\eta_{\text{FWM}} = \frac{\mu^2}{\mu^2 + \Delta\beta_{\text{FWM}}^2} \left[1 + \frac{4 \exp(-\mu L_{\text{eff}}) \sin^2\left(\Delta\beta_{\text{FWM}} L_{\text{eff}} / 2\right)}{(1 - \exp(-\mu L_{\text{eff}}))^2} \right] \tag{10.44}$$

where A_{eff} is the effective area (i.e., fiber core area) and $\Delta\beta_{\text{FWM}}$ is the phase mismatch between interacting waves, which in turn depends on chromatic dispersion D_{chrom} (typical value for telecom fibers is 17 ps × nm^{-1} × km^{-1}), its slope $\partial D_{\text{chrom}} / \partial\lambda$ (typical value is 0.8 ps × nm^{-2} × km^{-1}), and spectral spacing between channels $\Delta\nu$ (i.e., individual signals):

$$\Delta\beta_{\text{FWM}} = \frac{2\pi\lambda^2}{c} \Delta\nu^2 \left(D_{\text{chrom}} + \Delta\nu \frac{\lambda^2}{c} \frac{\partial D_{\text{chrom}}}{\partial\lambda} \right) \tag{10.45}$$

In the case of high signal attenuation—that is, when $[1 - \exp(-\mu L_{\text{eff}}) \ll 1]$—FWM efficiency becomes:

$$\eta_{\text{FWM}} = \frac{\mu^2}{\mu^2 + \Delta\beta_{\text{FWM}}^2} \tag{10.46}$$

Note that FWM is essentially a phase-matching process. That is, for energy to be interchanged between individual channels, all channels must operate in phase, which in turn requires a small value of $\Delta\beta_{\text{FWM}}$. The above expression for FWM efficiency indicates also that smaller spectral separation between channels results in higher FWM efficiency.

10.5 Self-Focusing and Self-Trapping in Optical Fibers

Self-focusing was theoretically predicted by Askarian in the USSR [11] in 1962, who studied the phenomenon of high-power electromagnetic field propagation in plasma. In the following years, several groups in the USSR and USA carried out experimental verification of this phenomenon as well as its further theoretical consideration. The main idea behind this interesting and very important physical process is in the nonlinear optical response of the medium refractive index to the propagating electromagnetic wave. This section presents basic formulas that describe the self-focusing and self-trapping phenomena and their importance in the field of fiber lasers, especially high-power fiber lasers and amplifiers.

One of the important parameters of the self-focusing phenomenon is the so-called critical power of the process. It determines the threshold of self-focusing and can be calculated using following expression, which can be obtained by consideration of total internal reflection from the wall of the nonlinear waveguide created in the field of the high-power beam [12]:

$$P_{\mathrm{cr}} = P_{\mathrm{selftr}} \approx (1.22\lambda)^2 \frac{1}{32\, n_0 n_2} \tag{10.47}$$

where λ is the wavelength of propagating electromagnetic wave in vacuum (given in centimeters) and n_0 and n_2 are the linear and nonlinear refractive indexes, respectively. (In glass, $n_2 \approx 2.5 \times 10^{-16}$ cm^2/W). With variations of the nonlinear refractive index in different glasses of optical fibers, the range of P_{cr} is usually 1–3 MW. Note that the critical power of self-focusing depends only on the wavelength, linear refractive index, and nonlinear refractive index.

The physical meaning of this power can be described as the condition when the light beams with power greater than P_{cr} experience focusing; with power less than this value, they will become defocused due to diffraction. As it is known, for cylindrical geometry the angle of diffraction θ is:

$$\theta \approx 1.22 \frac{\lambda}{n_0 D} \tag{10.48}$$

where D is the beam diameter. When the light wave has a power of $P = P_{\mathrm{cr}}$, a so-called autocollimation or self-trapping takes place (i.e., when divergence of the beam is compensated by self-focusing) [13].

Exceeding the optical power of the propagating beam above the critical power determines the mechanism of self-focusing, which dominates in this process. When the optical power exceeds the critical power by approximately <10 times, a so-called large-scale self-focusing (LSS) takes place, with a characteristic distance between the surface of the medium and the first self-focus which is as follows (in passive medium without loss) [14]:

$$L_{\mathrm{LSS}} \approx \frac{\pi D^2 n_0}{2\lambda \sqrt{\frac{P - P_{\mathrm{cr}}}{P_{\mathrm{cr}}}}} \approx D^2 \times \sqrt{\frac{n_0}{n_2 (P - P_{\mathrm{cr}})}} \tag{10.49}$$

When exceeding of the critical power is high ($>10^4$ times), then small-scale perturbations of the beam intensity create instabilities of the propagating beam, which in turn cause a so-called small scale self-focusing with a characteristic length, where the electrical field of the beam increases $\exp(\pi) = 23$ times [15, 16]:

$$L_{\text{sss}} = \frac{\lambda n_0 A_{\text{eff}}}{8\pi n_2 P} \tag{10.50}$$

In glass, when $P/A_{\text{eff}} \approx 3$ GW/cm^2, the small-scale self-focusing length is $L_{\text{sss}} \sim 8$ cm. Small-scale self-focusing appears first when $P > P_{\text{cr}}$, which is a common situation in high-power Q-switched or mode-locked fiber lasers.

The ratio of the characteristic lengths for these two limits is [16]:

$$\frac{L_{\text{sss}}}{L_{\text{LSS}}} \approx \sqrt{\frac{P_{\text{cr}}}{P}} \tag{10.51}$$

Using this expression, one can determine smallest characteristic length. That is, the first self-focus appeared during high peak-power beam propagation, which in turn determines the dominant self-focusing mechanism. Note that the characteristic length of self-focusing is smaller in an amplifying medium compared with an attenuating medium [17].

Self-focusing plays an important role in the design of high-power fiber laser systems because it is one of the main mechanism for bulk damage of fiber glass under conditions of high peak-power pulse propagation. This phenomenon also plays an important role in the design and development of bulk solid-state lasers with high peak power.

10.6 High-Power Fiber Laser Oscillators Versus Low-Power Master Oscillator–Power Fiber Amplifier Geometry

A straightforward way to achieve high-power laser radiation is to build a single and powerful laser oscillator with a required set of parameters. Being the oldest solution, this approach may look like the simplest way to achieve the goal. However, as it is known from traditional solid-state laser technology based on crystalline, ceramic, or bulk glass laser-active elements, an increased pump level dramatically changes the picture of fundamental physical processes that take place inside the laser cavity. Most of these processes fall into two categories: thermal management and nonlinear optical phenomena. These processes deteriorate laser parameters and therefore have to be taken into consideration during laser design and development.

Taking these problems into account, one may need to find a means to preserve the original or required laser parameters and at the same time be able to scale power of the whole laser system. The main idea behind such an alternative technology would be to create a relatively low-power master oscillator (MO),

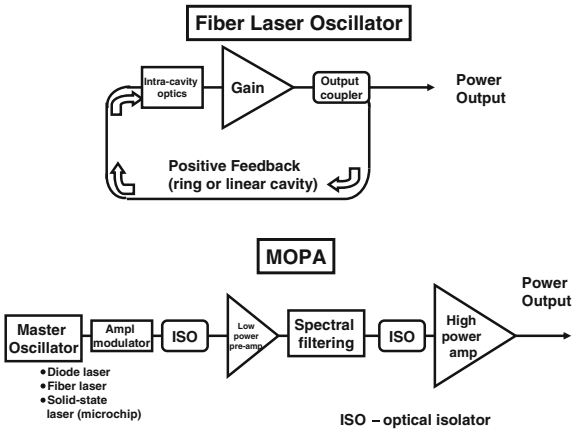

Fig. 10.13 Schematics of fiber laser oscillator (*top*) and master oscillator–power fiber amplifier (MOPA; *bottom*) configurations. *Note* In fiber lasers, MOPA optical isolators are placed in between each amplification stage

where physical processes that may deteriorate laser parameters are not evident. This allows one to achieve all required laser parameters from a single laser except power. The "ideal" laser beam from the MO is then injected into the system of laser amplifiers to eventually achieve the required level of power. Figure 10.13 shows a general schematic of these two approaches.

The second approach is called master oscillator–power amplifier (MOPA) geometry, which is very widely used in laboratories for scaling-up the power of laser systems. This approach was implemented in commercial solid-state and other laser products decades ago. Today, the MOPA is a well-known configuration in laser physics. It consists of a master laser oscillator (seed laser) and a power amplifier (booster) to boost the output power.

The following sections describe several examples of fiber laser systems, using each of the approach modes to solve the problem of laser power scaling.

10.6.1 High-Power Fiber Laser Single Oscillators

Despite the challenges associated with high intracavity optical power, high-power fiber laser oscillators still play an important role in the fiber laser field, especially in those branches where certain laser parameters have to be achieved directly from the laser source and would be problematic in the case of a MOPA. For example, such laser parameters may involve wavelength tunability, intracavity nonlinear frequency conversion, or high-power, tunable ASE-free operation.

Figure 10.14 shows an example schematic of a highly efficient and widely tunable narrow line-width ring fiber laser [18]. The laser is based on Yb^{3+}-doped

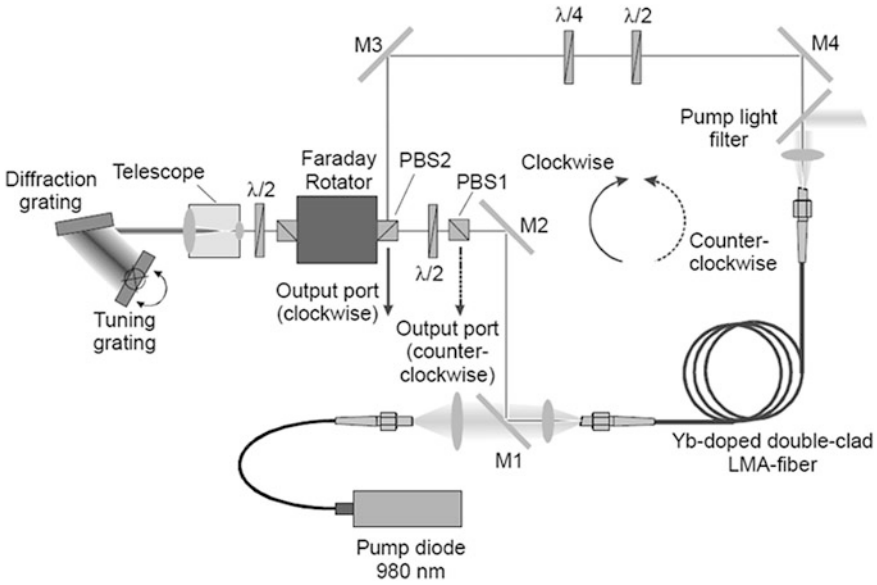

Fig. 10.14 High-power unidirectional Yb^{3+}-based fiber laser [18] (Image courtesy of the Optical Society of America)

DC fiber free-space pumped by a fiber-coupled high-power diode laser. The laser uses a unidirectional ring cavity and produces a linearly polarized beam with an output power of 10 W. The laser is wavelength tunable in the spectral range between 1,032 and 1,124 nm using a diffraction-grating pair in a Littrow–Littman configuration (described earlier in the chapter on tunable lasers). In a mode without any measurable ASE with a linearly polarized beam, the laser delivered 3 W of output power with slope efficiency of 23 % at 1,080-nm wavelength.

Another example of a fiber laser oscillator is illustrated in Fig. 10.15 [19], this time based on Er:Yb-doped gain fiber. The laser produced up to 188 W of CW output at 1.57 μm with $M^2 = 1.9$ and 41 % slope efficiency with respect to launched pump power. When the grating was used, tunable operation was demonstrated with a maximum output power of 108 W at 1,538 nm for a launched pump power of 336 W. The achieved tunability was between 1,531 and 1,571 nm.

A kW-level Yb^{3+} fiber laser was built by Auerbach et al. [18]. The laser schematic is shown in Fig. 10.16. The authors demonstrated a highly-efficient cladding-pumped Yb^{3+}-doped CW fiber laser with output power 1.36 kW at 1.1 μm with 83 % slope efficiency.

The laser produced near diffraction-limited beam quality with $M^2 = 1.4$. The authors [20] end-pumped the laser through both ends of a 12-m DC fiber with 1.6 kW of pump power. Absence of rollover in the output versus input plot indicated that the achieved laser performance was only pump power limited.

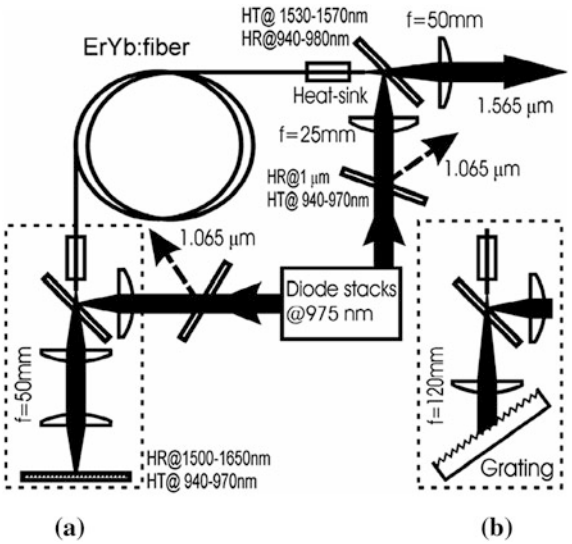

Fig. 10.15 Schematic diagram of co- and counter cladding pumped Er:Yb fiber laser configuration in a linear laser cavity. **a** Free running scheme. **b** External cavity of the tunable fiber laser [19] (Image courtesy of the Optical Society of America)

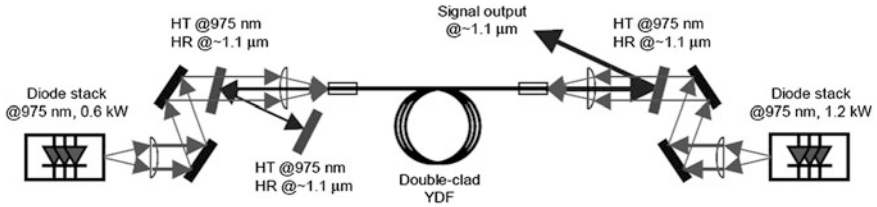

Fig. 10.16 Experimental setup of linear cavity kW-level Yb^{3+} fiber laser [20] (Image courtesy of the Optical Society of America)

10.6.2 High-Power Master Oscillator–Power Fiber Amplifiers

This section presents examples of MOPA-based configurations of fiber lasers. The advantages a of MOPA configuration include the following:

- MOPA allows easier implementation and more control of main laser parameters, especially when they need to be achieved simultaneously. These parameters include variable or certain laser pulse width, laser line width, laser beam quality, and elevated laser power. This is the biggest advantage of MOPA: flexibility.

- The design and structure of the individual subsystem of MOPA (i.e., MO and power amplifier) are usually simpler and reasonably straightforward compared with the design and construction of single high-power laser oscillator.
- All laser parameters can be achieved and controlled at a targeted output power in a MO, then a power amplifier can be used to boost the oscillator power level to what is required. In the case of fiber laser systems, a fiber amplifier design can be a challenge because of numerous optical nonlinear processes that may restrict laser power scaling and alter the original laser parameters.
- There is no high-power intracavity laser field, which in turn requires high power tolerance of fiber-coupled and free-space resonator optical components.

The disadvantages a of MOPA configuration include the following:

- Because more components are involved, the complexity of the system is higher.
- There is amplifier noise, which is the excess noise from residual spontaneous emission in the amplifier gain medium. (For four-energy-level excitation, the amplifier noise is lower than that of the three-level-excitation scheme.)
- A MOPA system can be vulnerable to the back-reflection intensities because they can lead to optical damages through additional amplification on the reflection path and subsequently enter the MO.
- The absence of high-power intracavity laser fields does not allow highly efficient nonlinear frequency conversion, such as intracavity optical harmonic generation, which is widely used in high-power laser oscillators.

There is no principal difference in the physics of traditional, bulk laser MOPA system operation compared with fiber or waveguide MOPA. The only principal difference is the small fiber core diameter and long length of the amplifier, which creates a condition for optical nonlinearities to take place in the fiber amplifiers as well as extremely high gain. These nonlinearities (which affect power scaling, laser parameter degradation, and power tolerance) have to be addressed during a fiber laser design and development process.

Being quite flexible approach, the MOPA configuration does not restrict the choices of selecting seed lasers or subsystems for power amplifiers. To achieve high energy and high peak power oscillation at the level of output of MOPAs whose parameters are not as easily achievable by purely fiber design, hybrid configurations started attracting the attention of many research groups. Such attention has been motivated by a high level of maturity of diode-pumped laser technology using bulk solid-state laser materials as well as microchip lasers.

To demonstrate the effectiveness of the hybrid geometry, Fig. 10.17 shows a MOPA system similar to that built by Liem et al. [21]. The authors employed a low-power diode-pumped, solid-state monolithic nonplanar ring oscillator as a single-frequency seed laser, which has been amplified in 9.4 m of LMA Yb^{3+}-doped DC fiber. The hybrid MOPA system produced more than 100 W of single-frequency laser power that was SBS limited. The ASE power level was estimated at 20 mW, corresponding to 0.02 % of the main laser output. This hybrid MOPA

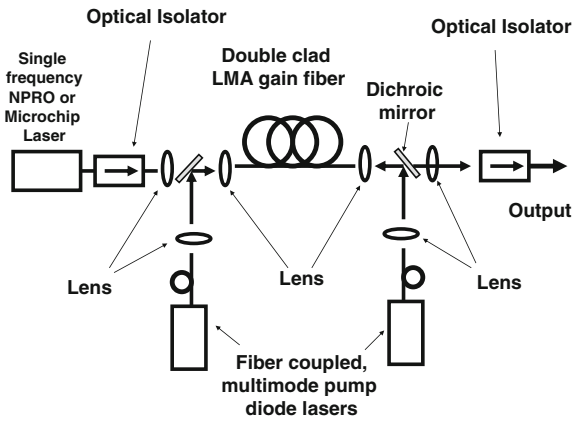

Fig. 10.17 Schematic setup of the single-frequency master oscillator–fiber power amplifier. *LMA* large mode area, *NPRO* nonplanar ring oscillator

configuration preserves excellent beam quality, a high degree of polarization, and single-frequency nature of the seed laser. The system is scalable to a power level of more than 200 W.

Figure 10.18 shows an example of high-power pulsed MOPA design in which a Yb^{3+}-doped DC fiber amplifier was used by Dupriez et al. [22]. The MOPA consists of a current modulated seed laser diode, three-stage preamplifier, and a

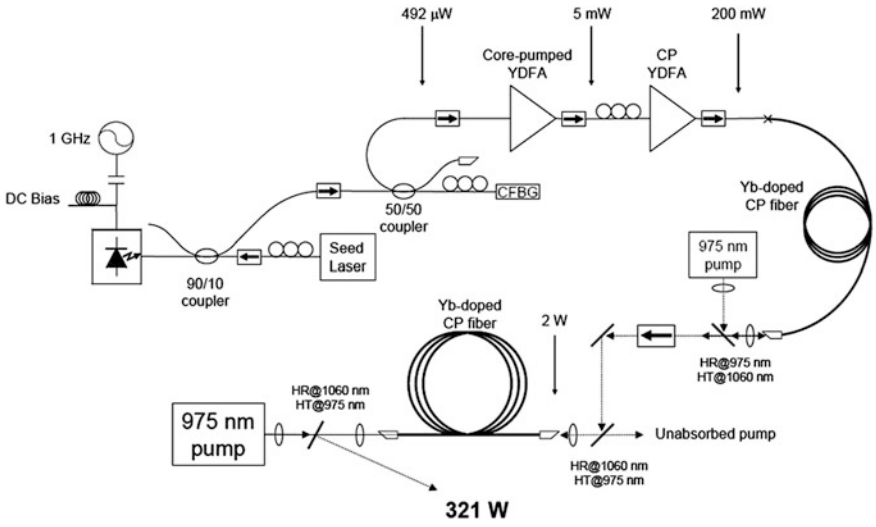

Fig. 10.18 Experimental setup of a 321-W average power pulse MOPA-based Yb^{3+} fiber laser [22]. *CP* cladding pumped, *CFBG* chirped fiber Bragg grating (Image courtesy of the Optical Society of America)

high-power amplifier. In total, 492 μW of diode laser power is injected into the three-stage preamplifier and is boosted to 2 W of output power before it enters the last high-power amplifier stage. The final high-power amplifier is counter-pumped with a high-power 975-nm diode laser and produces 321 W of average power at 1,060-nm wavelength. The laser demonstrates 20-ps pulses at a 1-GHz repetition rate. Despite high peak power of the laser pulses, the observed SPM was moderate and no Raman scattering has been detected at the output of fiber power amplifier.

Another example of a high peak power nanosecond MOPA was developed by Nufern [23], as shown in Fig. 10.19. The authors [23] demonstrated a monolithic linearly-polarized pulsed Yb^{3+}-doped fiber laser, with >10 kW peak power, tunable pulse duration of 2 ns to 0.2 μs, tunable repetition rate of 50 kHz to 50 MHz, and 50 W average power in a diffraction-limited, linearly polarized, and stabilized 0.8 nm line-width output beam operating at 106 nm.

A high average power, femtosecond Yb^{3+} fiber MOPA was reported by Roser et al. [24]. Using the fiber laser schematic shown in Fig. 10.20, the authors [24] demonstrated 90.4 W average power of 500-fs pulses while the laser operated at a 0.9 MHz pulse repetition rate. The femtosecond pulse peak power from such a fiber laser system reached the 200-MW level.

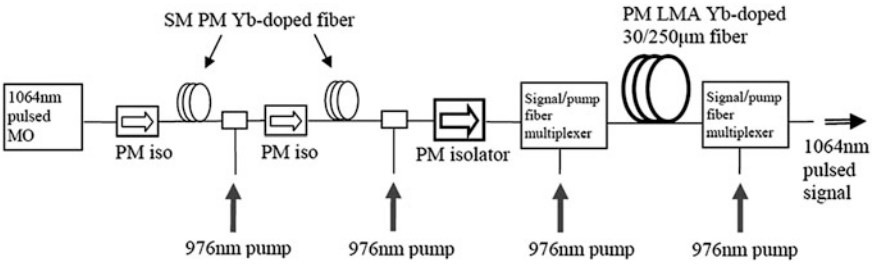

Fig. 10.19 Linearly polarized, nanosecond fiber laser design [23]. *LMA* large mode area, *MO* master oscillator PM, polarization maintained; SM, single mode. (Image courtesy of The international Society for Optics and Photonics (SPIE).)

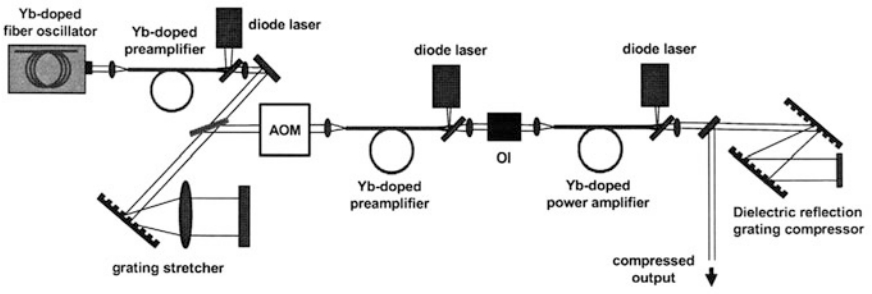

Fig. 10.20 Experimental setup of a high average power femtosecond MOPA system [24]. *AOM* acousto-optical modulator, *OI* optical isolator (Image courtesy of SPIE)

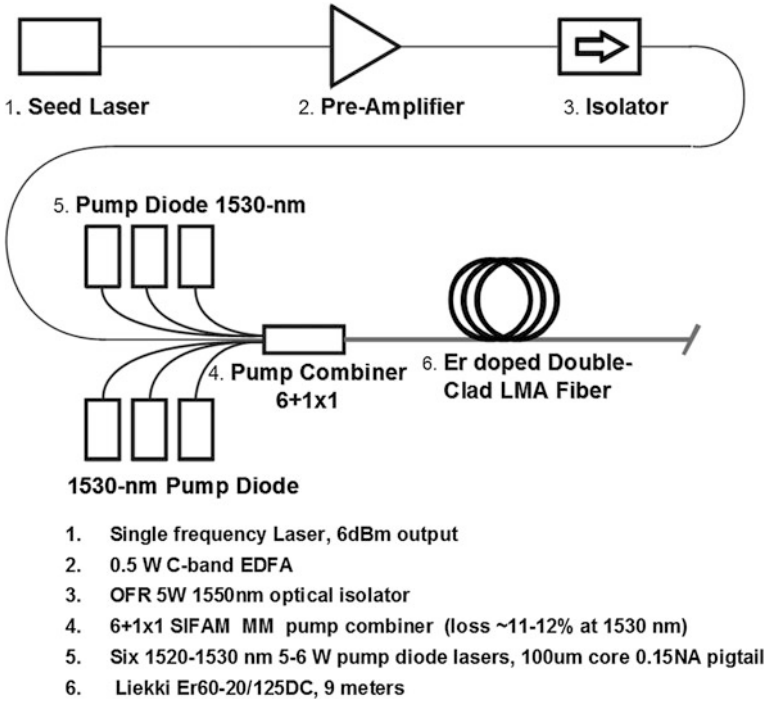

Fig. 10.21 Schematic of resonantly pumped Yb^{3+}-free, Er^{3+} fiber amplifier [26]. *LMA* large mode area (Image courtesy of SPIE)

The MOPA configuration has also been employed for resonantly pumped Er-only high-power amplifiers. The approach is considered to be a power-scalable, eye-safe, highly efficient alternative to existing high-power Yb^{3+} fiber lasers in the 1-μm range of the optical spectrum). Dubinskii et al. [25] implemented the high-power cladding-pumped Yb^{3+}-free Er^{3+} amplifier system resonantly pumped at 1,480 and 1,530 nm, as shown in Fig. 10.21. The authors [25] designed a single-frequency Er^{3+} fiber laser using a single-frequency diode laser as a MO, one preamplifier, and a high-power cladding-pumped amplifier. Using a Liekki Er^{3+}-doped 20/125 LMA gain fiber in a booster stage, the authors achieved 46 % slope efficiency versus absorbed power when cladding pumped with 1,520–1,530-nm fiber-coupled laser diodes, as well as more than 9 W of CW optical power with diffraction-limited beam quality at a 1,570-nm wavelength.

An interesting approach to scale output power of single-frequency fiber lasers was introduced by Zeringue et al. [26]. The authors used monolithic PM Yb^{3+}-doped fiber amplifier seeded with a combination of broad (tunable in the 1,035–1,045-nm range) and single-frequency (1,065-nm) laser signals, as shown in Fig. 10.22. This two-tone concept was used in conjunction with externally applied or intrinsically formed thermal gradients to achieve SBS suppression factors of up to 7 dB in a 7-m-long Yb^{3+}-doped 25/400 fiber. Achieved output power of the

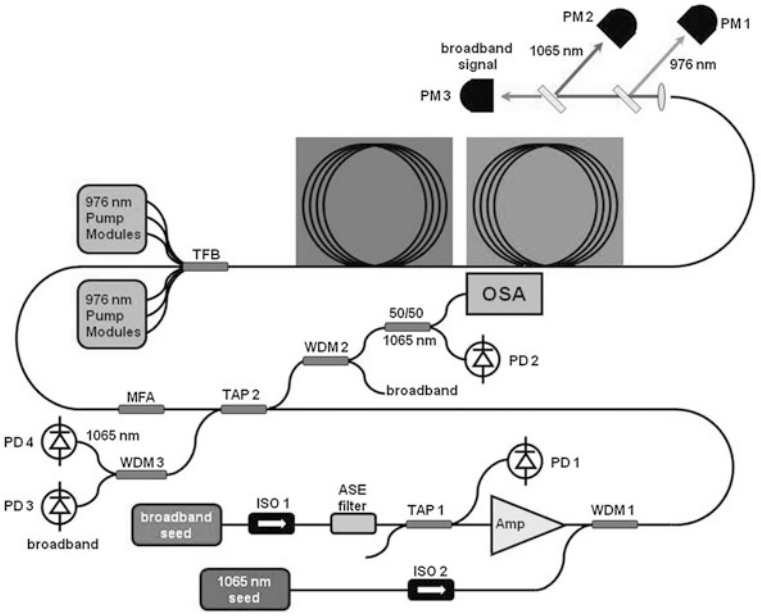

Fig. 10.22 Experimental setup used in Zeringue et al. [26]. *PD* photodiode, *ISO* isolator; *PM* power meter, *OSA* optical spectrum analyzer, *WDM* wavelength-division multiplexer. The ASE filter is used to suppress noise introduced by the broadband laser [23] (Image courtesy of SPIE)

single-frequency laser ranged from 80 to 203 W, with slope efficiencies of 70–80 %. Using an external thermal gradient, the authors measured 100 kHz nominal line-width at 203 W of output power of the laser.

Goodno et al. [27] built a four-stage, Tm^{3+}-doped fiber amplifier chain that emitted 608 W of single-frequency output power. The laser showed an optical gain of 53 dB, 54 % slope efficiency, and beam quality with M^2 of 1.05, as shown in Fig. 10.23. The output power was limited by available pump power and showed now saturation with increasing pump power level. The laser system preserved the input <5-MHz line width, imposing negligible phase noise above 3 kHz. A comparison of the measured SBS limit as well as analytically analyzed thermal

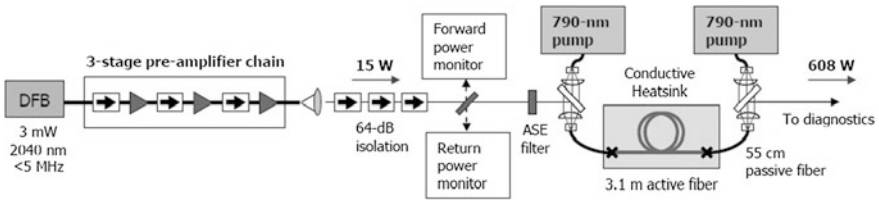

Fig. 10.23 Experimental setup of a four-stage, single-frequency Tm^{3+}-fiber laser MOPA [27]. ASE, amplified spontaneous emission; DFB, distributed feedback laser. (Image courtesy of The international Society for Optics and Photonics (SPIE).)

limit suggests a maximum possible achievable single-frequency power of ~750 W from this fiber laser, scalable to the 1-kW level [27].

It is important to note that selection of the approach used in the design and development of a high-power fiber laser system depends on many factors, which have to be taken into consideration during the decision-making process in selecting a schematic. These factors include the fundamental allowance of the theoretical modeling, required flexibility of the targeted output laser parameters, and allocated cost. This decision also involves information on the availability of the fiber-coupled and free-space optical components used in both MOPA and oscillator systems.

10.7 Beam Combining of High-Power Fiber Lasers

The unique advantages of fiber laser systems—high efficiency, high beam quality, relaxed thermal management issues, and low cost of ownership—helped them to capture several industrial markets as well as some military applications. The latter applications, however, requires a high level of average or CW powers in the order of 50–100 kW, while at the same time maintaining high beam quality of diffraction-limited operation.

Two ways to scale the power of laser systems have been implemented into practice: (a) scaling power of an individual oscillator without degradation of important laser parameters and (b) beam combination of already constructed lasers. By pushing the capabilities to the maximum possible level, both methods can usually be implemented by researchers and engineers. This section reviews the main approaches for high-power beam combing.

The most important parameters of the individual high-power fiber laser sources and their control when considering laser beam combinations include wavelength control, line-width control, and polarization control. By exploring these laser parameters, one may achieve different beam combinations to scale the fiber laser system output power. By combining several laser beams while preserving the beam parameter product (i.e., the product of the beam diameter and the angle of divergence), one may not only scale the output power but also increase the beam brightness.

There are three main approaches for beam combining to increase the output laser beam power (see [28] for a review):

1. Spectral beam combining (sometimes called wavelength beam combining, or WBC).
2. Coherent beam combining.
3. Side-by-side beam combining.

The traditional polarization beam combining technique (PBC; see Fig. 10.24), which combines two linear polarized beams and uses polarization beam splitters/combiners, increases brightness. However, it also results in an unpolarized output beam and therefore cannot be used for repeatable beam combiners based on the polarization control principle. Another reason that restricts the use of PBC in

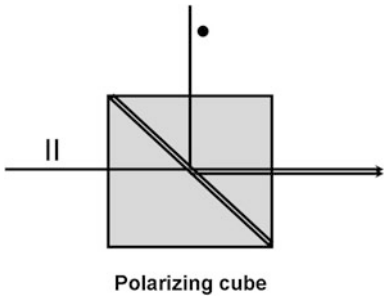

Fig. 10.24 Polarization beam combining using a polarizing cube

high-power fiber laser scaling technology aimed at the 50–100 kW level is limited power tolerance of the polarization beam splitters/combiners.

Within each of these approaches, *N* individual emitters sum up with added power from each individual source. However, unlike WBC and coherent beam combining, side-by-side beam combining approach provides only power scaling but not an increase in brightness. This approach is usually used for diode laser power scaling (i.e., for diode-pumped solid-state laser applications). The first two approaches provide an increase not only in overall power but also in the overall brightness of resultant source (i.e., power per solid angle over a resultant beam aperture). Unlike polarization beam combining, WBC and coherent combining techniques are really scalable approaches theoretically, without a limit on the number of combined elements in the system. Therefore, this review focuses on WBC and coherent beam combining techniques only, because they reflect the most-demanded applications. Fiber lasers are ideal elements (i.e., building blocks) for beam-combining technology because of their size and flexibility of packaging.

10.7.1 Spectral Beam Combining

This approach combines beams of individual laser emitters with different wavelengths of operation into a single, higher-power beam using different types of wavelength-multiplexing devices. Within this technique, the resultant beam aperture and far-field divergence angle remain the same as in original beams, which results in a proportional increase of the output beam brightness.

The most commonly used spectral beam combiners are dichroic mirrors, prisms, and diffraction gratings. Most of the challenges are in really high-power applications (kW level or more). All wavelength control devices that employ thin-film technology often fail to tolerate propagating optical powers. This section concentrates on the review of high-power tolerable and most widely used solutions for wavelength beam combinations.

With the requirements to spectrally combine exceptionally high-power beams with power levels exceeding the kilowatt level, so-called volume Bragg grating—also called volume holographic grating (VHG)—has been successfully used in this

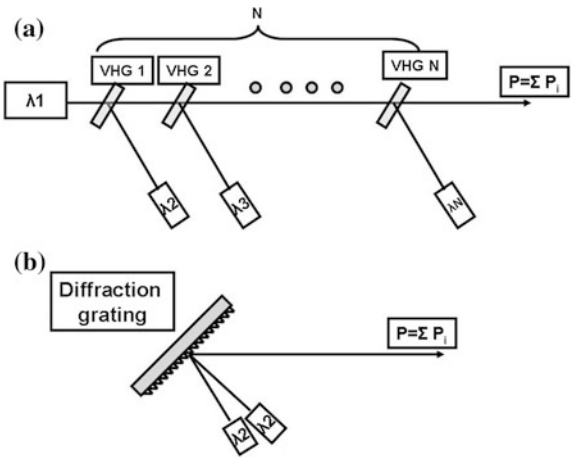

Fig. 10.25 Spectral beam combining using a volume holographic (Bragg) grating (**a**) and a diffraction grating (**b**)

application [29]. Figure 10.25a shows a schematic view of a spectral beam-combining technique using VHG (For comparison, diffraction-grating WBC is shown in Fig. 10.25b).

Being a repeatable device (i.e., the device allows a consequent beam combination of a theoretically unlimited number of single beams), VHG are the most widely used multiplexers, particularly for high-power fiber laser systems [29]. Highly efficient diffractive Bragg gratings in photo-thermo-refractive (PTR) inorganic glass have been applied for high-power laser systems [30, 31]. PTR glass demonstrates high diffraction efficiency (>95 %) in both the transmitting and reflecting types of Bragg gratings. This material demonstrates exceptional thermal and mechanical stability as well as high optical quality. Ciapurin et al. [31] reported low PTR absorption in of 1 μm spectral range with power density tolerance of 100 kW/cm^2.

10.7.2 Volume Holographic Grating

Because of the very important role that VHG plays in the beam combination technology, it is useful here to present some overview on general properties of VHG [32–36]. VHG is a thick Bragg diffraction grating recorded in a PTR glass (Note that VHG can be fabricated in other materials, such as photo-refractive crystals or gelatin). In addition to WBC applications, VHG are widely used for highly efficient spectral narrowing of high- and low-power diode lasers. Generally, VHGs can be categorized into transmission and reflection types (see Fig. 10.26), depending on the direction of incident and diffracted light.

The simplest nonslanted transmission and reflection gratings demonstrate the common characteristics of the VHG. Consider a nonslanted transmission grating

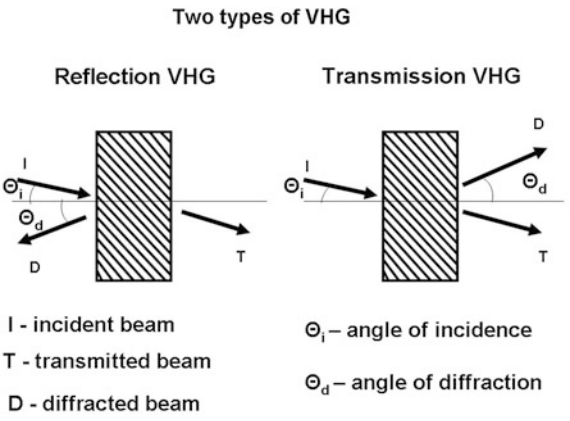

Fig. 10.26 Two types of volume holographic grating (*VHG*): reflection holographic grating (*left*) and transmission holographic grating (*right*) (Image courtesy of Ondax)

with index modulation Δn, with typical values between $(100 \div 300) \times 10^{-6}$ and thickness d. The diffraction efficiency is defined as the ratio between the diffracted intensity and the incident intensity, without considering absorption and Fresnel reflections at the surfaces. When the Bragg condition is satisfied for wavelength λ_B, the diffraction efficiency eff_B is given as:

$$\text{eff}_B = \sin^2\left(\frac{\pi \times \Delta n \times d}{\lambda_B \cos \Theta_n}\right) \tag{10.52}$$

where θ_n is the incident angle inside the medium of index n. When the grating strength Δn increases from zero, the diffraction efficiency increases from 0 to 100 % when:

$$\Delta n = \frac{\lambda_B \cos \Theta_n}{2d} \tag{10.53}$$

For even stronger gratings, the diffraction efficiency eff_B will decrease from 100 % because the diffracted beam is diffracted again by the same grating and coupled back into the original incident beam.

Due to the volume hologram, Bragg-matching condition VHGs have highly sensitive wavelength and angle selectivity. Consider a weak nonslanted transmission grating (i.e., eff_B <100 %). When the incident wavelength λ is different than the Bragg wavelength λ_B, the diffraction efficiency eff(λ) can be approximated as a typical sinc function:

$$\text{eff}(\lambda) = \text{eff}_B \times \left[\frac{\sin\left(\frac{\lambda_B - \lambda}{\Delta\lambda}\right)}{\left(\frac{\lambda_B - \lambda}{\Delta\lambda}\right)}\right]^2 \tag{10.54}$$

where $\Delta\lambda$ is the wavelength deviation at the first null, as shown in Fig. 10.27 (top).

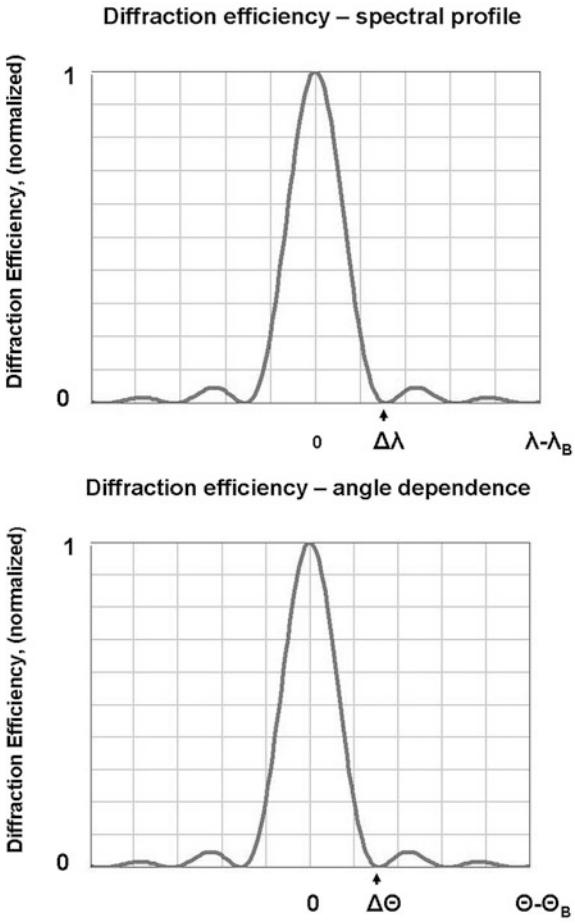

Fig. 10.27 Typical wavelength and angle dependence curves for volume holographic gratings (*VHGs*). When the Bragg condition is equal to wavelengthλ_B and incident angle Θ_B, the diffraction efficiency is eff_B (the central maximum on the figures)

Similarly when the incident angle in air θ is different than the Bragg angle Θ_B, the diffraction efficiency eff_B can be approximated as a typical sinc function:

$$\text{eff}(\Theta) = \text{eff}_B \times \left[\frac{\sin\left(\frac{\Theta_B - \Theta}{\Delta\Theta}\right)}{\left(\frac{\Theta_B - \Theta}{\Delta\Theta}\right)} \right]^2 \tag{10.55}$$

where $\Delta\Theta$ is the incident angle deviation at the first null, as shown in Fig. 10.27 (right).

Using this analysis, one can calculate the required Bragg grating parameters for the incident spectrum of a multichannel laser system. Calculation and manufacturability analyses show that practical minimum spectral separation of individual laser channels should be 2 nm or more to avoid cross-talk. For a more detailed theory of VHG, please see Ref. [36].

VHG can be used not only in spectral but in coherent combiners as well. VHGs recorded in glass have been first suggested for use in coherent coupling of diode lasers in Refs. [37, 38]. The basic idea of this approach is to use volume Bragg gratings to create extremely dispersive external resonators for coherently combining individual lasers. The VHG is acting within this approach as a common output coupler. Venus et al. [37, 38] coherently coupled two 980-nm diode lasers and produced single wavelength output for both diodes with spectral width narrowed to <30 pm. Similar technology can be applied for high-power fiber lasers using coherent beam combining and is potentially capable of achieving 100-kW level of coherent fiber laser radiation.

10.7.3 Coherent Beam Combining

Coherent beam combining adds beams emerging from different individual laser sources (or gain sections) passively or actively phase-locked to each other, usually by some intracavity element or external force to each of the laser resonators (i.e., compensation of phase errors using phase-conjugate elements such as SBS and phase detection with active compensation), with beams interacting externally to the individual laser. In other words, this beam-combining approach forces individual sources to operate with the same frequency spectrum and with the same phase. Using a spatial overlapping of individual emitters' electrical fields, coherent beam combining results in power scaling of the output laser emission.

There are two basic approaches for coherent laser coupling. The first is to inject coherent radiation to the separate lasers and force them to emit coherently. This approach allows for the oscillation of all components of the system in the same mode. However, this approach involves certain risk in systems such as MOPA because back-seeding power may produce optical damage to all in-line laser components; it also requires subsequent coherent coupling of the individual lasers even if individual locking is successful.

The second approach is to design a multichannel high-power laser resonator that provides coherent emission of all its components. This approach allows phase control to be obviated in the channels, but the main problem that prevents stable and efficient coupling is a tendency of a multichannel system to switch between different modes of a complex laser resonator. However, if one achieves high spectral and angle selectivity in the combining device, the second approach may become very effective.

For example, consider two designs. In the approach shown in Fig. 10.28, a so-called all-fiber approach for coherent beam combining was proposed [39]. Here, the authors demonstrated the use of half of a fused-taper single-mode fiber coupler as an output mirror–beam combiner for two fiber lasers. The approach can be used for combining high-power fiber lasers. By tuning one of the fiber laser's Bragg grating mirrors, the authors observed fiber laser injection locking. They demonstrated both spatial and spectral combination of two fiber lasers. Later, a similar approach (see Fig. 10.29) was implemented by another group [40], who demonstrated highly efficient coherent beam combining of N fiber lasers by Y-shaped fused fiber couplers. The authors [40] obtained 2.65 W of combined

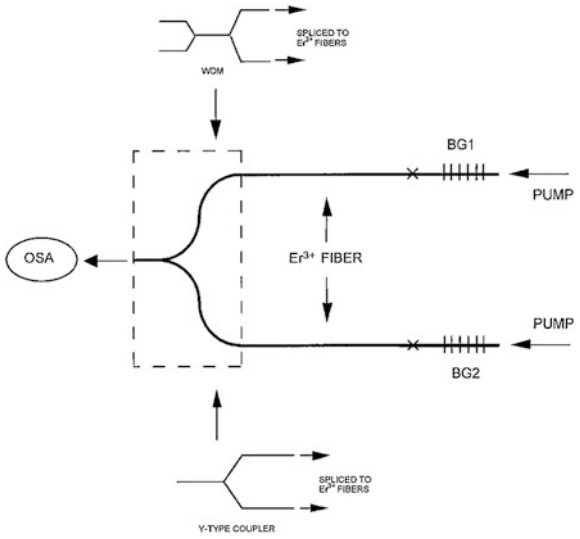

Fig. 10.28 Experimental setup. *OSA* optical spectrum analyzer, *WDM* wavelength-division multiplexer [39] (Image courtesy of the Optical Society of America)

fiber laser emission by combining eight erbium-doped fiber lasers with an 85 % combining efficiency.

For the multielement intracavity beam combination, an interesting design has been suggested and implemented [41], as shown in Fig. 10.30. The authors used the design to scale the power of the fiber laser system consisting of large numbers of elements while maintaining good beam quality. As one can see from Fig. 10.30, the authors used a MOPA configuration as a building block of the system, which defined temporal and spectral characteristics of the individual source.

Each fiber oscillator is placed at the focal plane of the MO array lens; therefore, every oscillator radiation is collimated before falling onto the diffraction grating [41]. The end mirror and grating in the MO array section act as a complex mirror

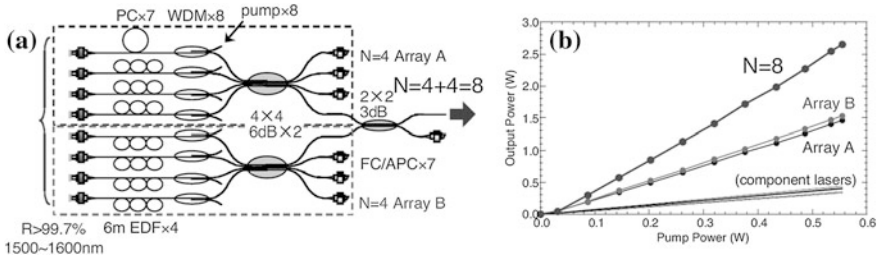

Fig. 10.29 **a** Experimental setup and **b** power evolution of the $N = 8$ fiber laser coherent array [40]. *WDM* wavelength-division multiplexer; PC, polarization controller; EDF,erbium doped fiber; FC, fiber connector, APC, angle-polished connector. (Imagecourtesy of the Optical Society of America.)

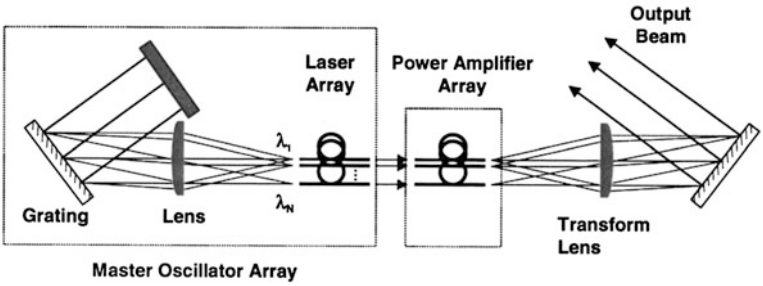

Fig. 10.30 MOPA implementation of a wavelength beam combining system. Each element in the master oscillator operates at a unique wavelength determined by the grating. Part of the light from each oscillator element is used to seed its own amplifier and the amplifier outputs are combined with an identical transform lens and grating [41] (Image courtesy of the Optical Society of America)

and provide feedback at different wavelengths for each fiber oscillator. Subsequently reflected emissions then seed each oscillator on its individual wavelength, which then follow with its own amplifier. Using a similar approach, amplified beams are combined on the second diffraction grating; after recollimation, they are coupled out of the system as an output beam (Fig. 10.30).

Shay et al. [42] experimentally demonstrated an original technique for coherent beam combining of laser beams. Using a so-called Locking of Optical Coherence by Single-detector Electronic-frequency Tagging (LOCSET), the authors achieved phase locking of an array of five 145-W fiber amplifiers. The resultant laser beam produced a record 725-W optical power as a result of coherent beam combination (see Fig. 10.31).

As shown in Fig. 10.31, the MO is coupled into two single-mode PM 1 × 8 power splitters, which have separate phase modulators in each of the eight legs. The output of the modulators is coupled into eight single-mode PM optical fibers.

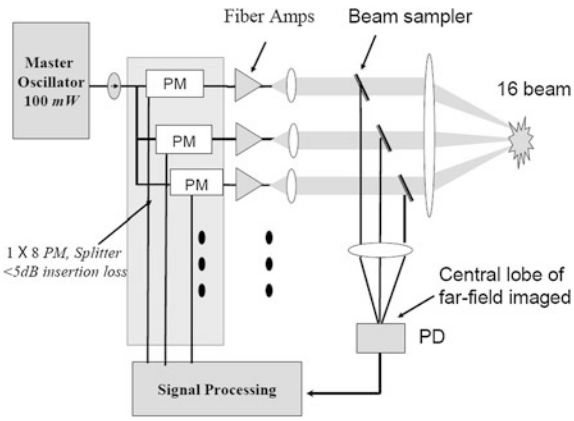

Fig. 10.31 Block diagram of Locking of Optical Coherence by Single-detector Electronic-frequency Tagging (*LOCSET*) beam-combining experiment [42]. *PM* phase modulator, *PD* photodetector (Image courtesy of SPIE)

After each modulator, the light gets coupled into fiber amplifiers. Each amplifier output is collimated by the lens optics and, after passing through a beam splitter, is directed onto a single photodetector by a focusing lens. A small-amplitude radio-frequency (RF) phase modulator is applied to each of the phase modulators at a unique individual RF frequency. The photodetector produces a photocurrent that contains the RF phase modulation frequencies of each beam. In addition, the amplitude of each RF frequency component contains the optical phase error signal for each of the array elements. By electronically extracting the optical phase error for each array element and feeding it back to the corresponding phase modulator, the authors [42] were able to lock each array element to the same phase as the other element in the system.

Unlike other approaches, this technique does not require a reference beam. Avoiding the use of an external reference beam from the electronic phase-locking system simplifies the optical alignment and allows the usage of a single photodetector for the whole system of N combining channels. Mechanical and environmental tolerance of the approach may lead to reliable and practical multi-kilowatt laser systems.

An interesting approach has been demonstrated by Fridman et al. [43], who achieved simultaneous coherent and spectral beam combination in one system (Fig. 10.32). Coherent combination was achieved in the horizontal direction using an interferometric combiner, while spectral combining was implemented in the vertical direction using linear diffraction grating. The authors [43] experimentally demonstrated a combining efficiency of more than 80 % with resultant beam quality of $M^2 = 1.15$.

Ludewigt et al. [44] demonstrated the spectral beam combination of four narrow line-width LMA photonic crystal fiber amplifiers (Fig. 10.33). Each individual beam had a spectral width of $\sim$90 pm at an output power of $\sim$2.1 kW and a beam quality of $M^2 \sim 4$. The polarization-independent grating allowed an efficiency of 99 %. The combined beam has an average power of 8.2 kW (pump power limited) with a good beam quality, practically preserving the beam quality of the individual fiber amplifiers.

Drachenberg et al. [45] presented high-power, high-spectral-density beam combining using VBG of five 150-W beams with a spectral separation of 0.25 nm

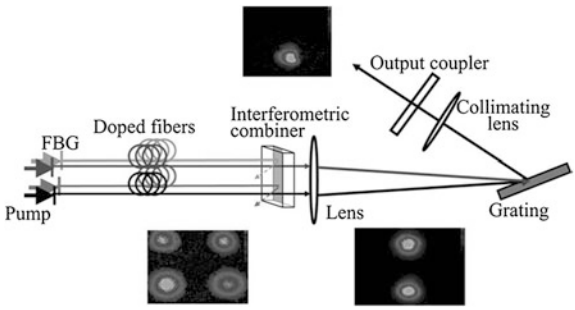

Fig. 10.32 A schematic used for simultaneous coherent and spectral combination of four fiber laser beams [43]. *FBG* fiber Bragg grating (Image courtesy of SPIE)

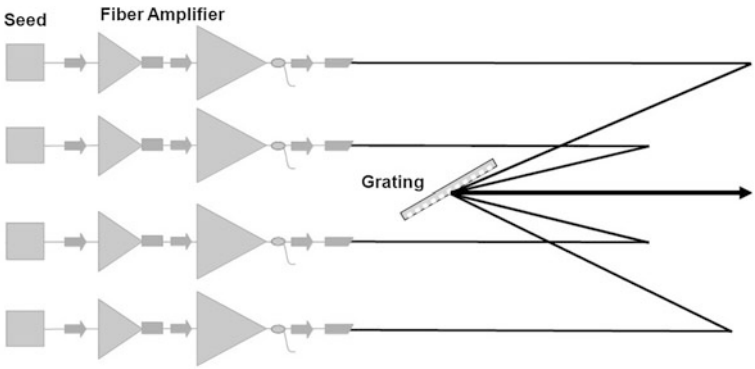

Fig. 10.33 Experimental setup. Spectral beam combining using a polarization-independent dielectric reflective diffraction grating [44] (Image courtesy of SPIE)

between beams—the narrowest to date for high power using heated VBG. Within 1 nm, the authors achieved 750 W of total power, combined with greater than 90 % efficiency (Fig. 10.34).

High-power beams transmitting through or diffracting from a VBG can experience different distortions resulting from thermal effects induced in the VBGs. Each beam also experiences a different aberration, because no two beams pass through the same number of identical VBGs. Each VBG therefore experiences different heating conditions and has a different Bragg wavelength shift. This shift is corrected by thermal tuning. Drachenberg et al. [45] developed a theoretical model of the observed processes and compared it with experiments.

In summary, the main advantages and disadvantages of each of the beam-combining techniques are as follows:

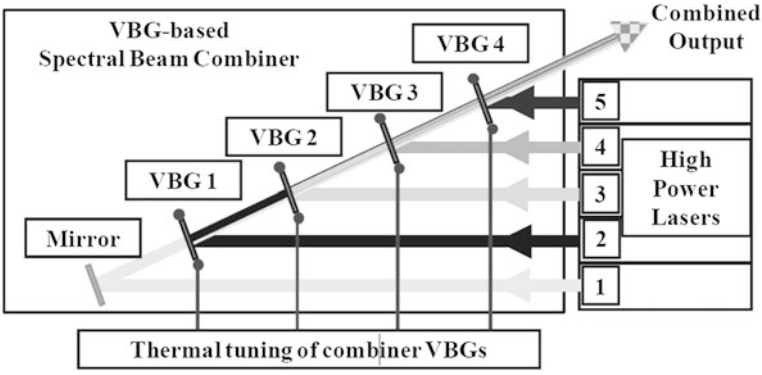

Fig. 10.34 Spectral beam combining geometry used by Drachenberg et al. [45]. *VBG* volume Bragg grating (Image courtesy of SPIE)

10.7.3.1 Spectral Beam Combining

- Does not require coherency of individual beams to be combined beams.
- Because of an increased spectral width of the resultant beam, the spectral brightness (i.e., brightness per unit spectral bandwidth $[W/\text{cm}^2 \times \text{steradian} \times \text{nm}]$) is reduced.
- Reasonably preserves the original beam quality.
- Is an additive technique in terms of power scaling (i.e., except for the power reduction, failure of one source does not affect the performance of other sources and the resultant beam).
- Requires narrower possible line-width of individual laser emitters, especially if a large number of beams has to be combined. In turn, this often requires single-frequency operation of individual lasers, which may be a challenging task—particularly for high-power systems due to being detrimental for power-scaling nonlinear optical processes.

10.7.3.2 Coherent Beam Combining

- Often requires individual sources to share laser resonator components to achieve coherency of the output combined beam, which in turn complicates the whole system design. Particularly, increased intracavity power applies additional power tolerance requirements to laser cavity optics.
- Usually demonstrates increased spectral brightness because the technique either preserves or even reduces individual laser spectral line-width while adding optical power in the resultant beam.
- Reasonably preserves the original beam quality.
- Not an additive technique in terms of power scaling (i.e., failure of one source affects the performance of other sources and the resultant beam, including beam quality).
- Does not necessary require single frequency (i.e., very narrow spectral line-width) of individual laser emitters.

At the current stage of technology development (except for the cases when the resultant output beam spectral bandwidth is of concern, such as in the case of nonlinear frequency conversion or applications where long coherence length is required), spectral beam combing shows great promise for the power scaling of fiber lasers.

References

1. T.A. Parthasarathy, R.S. Hay, G.E. Fair, F.K. Hopkins, Predicted performance limits of yttrium aluminum garnet fiber lasers. Opt. Eng. **49**(9), 094302 (2010)
2. A. Wetter, M. Faucher, M. Lovelady, F. Seguin, Tapered fused-bundle splitter capable of 1 kW CW operation. Proc. SPIE **6453**, 64530I.1–64530I.10 (2007)
3. J.P. Koplow, S.W. Moore, D.A.V. Kliner, A new method for side pumping of double-clad fiber sources. IEEE J. Quantum Electron. **39**(4), 529–540 (2003)
4. D.J. Ropin, L. Goldberg, High efficiency side-coupling of light into optical fibres using imbedded v-grooves. Electron. Lett. **31**(25), 2204–2205 (1995)
5. H. Weber, W. Luthy, H.P. Weber, V. Neuman, H. Berthou, G. Kotrotsios, A longitudinal and side-pumped single transverse mode double-clad fiber laser with a special silicone coating. Opt. Commun. **115**, 99–104 (1995)
6. J.M. Fini, Bend distortion in large-mode-area amplifier fiber design, Proc. SPIE **6781** (2007)
7. B.Y. Zel'Dovich, N.F. Pilipetsky, V.V. Shkunov, *Principles of Phase Conjugation* (Springer Series in Optical Sciences, Berlin, 1985), p. 250 (Hardcover)
8. G.W. Faris et al., High–resolution stimulated Brillouin gain spectroscopy in glasses and crystals. JOSA B **10**(4), 587–599 (1993)
9. G.P. Agrawal, *Nonlinear Fiber Optics*, 3rd edn. (Academic Press, New York, 2001), p. 466
10. R.R. Alfano et al., Cross-phase modulation and induced focusing due to optical nonlinearities in optical fibers and bulk materials. J. Opt. Soc. Am. B. **6**(4), 824–829 (1989)
11. G.A. Askarian, Effect of the gradient of a strong electromagnetic ray on electrons and atoms. Zh. Eksp. Teor. Fiz. **42**, 1361–1570 (1962)
12. G.M. Zverev, V.A. Pashkov, Self-focusing of laser radiation in solid dielectrics. Sov. Phys. JETP **30**(4), 616–621 (1970)
13. R.Y. Chiao, E. Garmire, C.H. Townes, Self-trapping of optical beams. Phys. Rev. Lett. **13**, 479–482 (1964)
14. S.A. Akhmanov, A.P. Sukhorukov, R.V. Khokhlov, Self focusing and diffraction of light in a nonlinear medium. Sov. Phys. Uspekhi **93**, 609–636 (1968)
15. V.I. Bespalov, V.I. Talanov, Filamentary structure of light beams in nonlinear liquids. JETP Lett. **3**, 307–310 (1966)
16. A.A. Mak, L.N. Soms, V.A. Fromzel, V.E. Yashiin, *Lasers Based on Neodymium Glass* (Nauka, Moscow, 1990), pp. 1–288
17. S.A. Akhmanov, A.P. Sukhorukov, R.V. Khokhlov, Self-focusing and diffraction of light in a nonlinear medium. Phys. Uspekhi **10**, 609–636 (1968)
18. M. Auerbach, P. Adel, D. Wandt, C. Fallnich, S. Unger, S. Jetschke, H. Mueller, 10 W widely tunable narrow linewidth double-clad fiber ring laser. Opt. Express **10**, 139–144 (2002)
19. D.Y. Shen, J.K. Sahu, W.A. Clarkson, Highly efficient Er, Yb-doped fiber laser with 188 W free-running and >100 W tunable output power. Opt. Express **13**, 4916–4921 (2005)
20. Y. Jeong, J. Sahu, D. Payne, J. Nilsson, Ytterbium-doped large-core fiber laser with 1.36 kW continuous-wave output power. Opt. Express **12**, 6088–6092 (2004)
21. A. Liem, J. Limpert, H. Zellmer, A. Tünnermann, 100-W single-frequency master-oscillator fiber power amplifier. Opt. Lett. **28**, 1537–1539 (2003)
22. P. Dupriez, A. Piper, A. Malinowski, J.K. Sahu, M. Ibsen, Y. Jeong, L.M.B. Hickey, M.N. Zervas, J. Nilsson, D.J. Richardson, 321 W average power, 1 GHz, 20 ps, 1060 nm pulsed fiber MOPA source, in *Optical Fiber Communication Conference and Exposition and The National Fiber Optic Engineers Conference*, Technical Digest (CD) (Optical Society of America, 2005), paper PDP3
23. V. Khitrov, B. Samson, D. Machewirth, K. Tankala, 50 W single-mode linearly polarized high peak power pulsed fiber laser with tunable ns-μs pulse durations and kHz-MHz repetition. Proc. SPIE **6873**, 68730C1–68730C6 (2008)

24. F. Roser, D. Schimpf, O. Schmidt, B. Ortac, K. Rademaker, J. Limpert, A. Tunnermann, 90 W average power high energy femtosecond fiber laser system. Proc. SPIE **6453**, 645310.1–645310.4 (2007)
25. M. Dubinskii, V. Ter-Mikirtychev, J. Zhang, I. Kudryashov, Yb-free, SLM EDFA: comparison of 980-, 1470- and 1530-nm excitation for the core-and clad-pumping. Proc. SPIE **6952**, 695205 (2008)
26. C. Zeringue, I. Dajani, C. Vergien, C. Robin, Pump limited 203 W monolithic single frequency fiber amplifier: a two-tone approach. Proc. SPIE **7914**, paper 7914-115 (2011)
27. G.D. Goodno, L.D. Book, J.E. Rothenberg, 600-W, single-mode, single-frequency thulium fiber laser amplifier. Proc. SPIE **7195**, paper 71950Y-1-10 (2009)
28. T.Y. Fan, Laser beam combining for high-power, high radiance sources. IEEE J. Sel. Top. Quantum Electron. **11**, 567–577 (2005)
29. I. Ciapurin, L. Glebov, E. Rotari, V. Smirnov, Spectral beam combining by PTR Bragg gratings, in *Proceedings of Solid State and Diode Lasers Technical Review* (*SSDLTR*) (2003), pp. HPFib—4
30. L.B. Glebov, V.I. Smirnov, M.C. Stickley, I.V. Ciapurin, Laser weapons technology III. Proc. SPIE **4724**, 101–109 (2002)
31. I.V. Ciapurin, L.B. Glebov, C.M. Stickley, in *Proceedings of Solid State and Diode Lasers Technical Review*. Albuquerque, Paper HPFIB4 (2002)
32. O. Andrusyak, D. Drachenberg, V. Smirnov, G. Venus, L. Glebov, Fiber laser system with kW-level spectrally-combined output, in *21st Annual Solid State and Diode Laser Technology Review*, *SSDLTR-2008 Technical Digest*, Albuquerque, NM (June 2008), pp. 2–6
33. O. Andrusyak, I. Ciapurin, V. Smirnov, G.Venus, N. Vorobiev, L. Glebov, External and common-cavity high spectral density beam combining of high power fiber lasers, fiber lasers V: technology, systems, and applications, ed. by J. Broeng, C. Headley, *Proceedings of SPIE*, vol. 6873 (2008), p. 685314
34. A. Sevian, O. Andrusyak, I. Ciapurin, G. Venus, V. Smirnov, L. Glebov, Efficient power scaling of laser radiation by spectral beam combining. Opt. Lett. **33**, 384–386 (2008)
35. A. Sevian, O. Andrusyak, I. Ciapurin, G. Venus, V. Smirnov, L. Glebov, Efficient power scaling of laser radiation by spectral beam combining: erratum. Opt. Lett. **33**, 760 (2008)
36. I.V. Ciapurin, L.B. Glebov, V.I. Smirnov, Modeling of Gaussian beam diffraction on volume Bragg gratings in PTR glass. Proc. SPIE 5742, 183–194 (2005), See also Introduction to Volume Holographic Gratings (VHG), Ondax, white paper (www.ondax.com)
37. G. Venus, A. Sevian, V. Smirnov, L. Glebov, Stable coherent coupling of laser diodes by a volume Bragg grating in photothermorefractive glass. Opt. Lett. **31**, 1453–1455 (2006)
38. G. Venus, A. Sevian, L. Glebov, in *Stable Coherent Coupling of Laser Diodes by a Volume Bragg Rating in PTR Glass. High-Power Diode Laser Technology and Applications IV*, ed. by M. Zediker, Proceedings of SPIE, vol. 6104 (2006), p. 61040S
39. V.A. Kozlov, J. Hernández-Cordero, T.F. Morse, All-fiber coherent beam combining of fiber lasers. Opt. Lett. **24**, 1814–1816 (1999)
40. A. Shirakawa, K. Matsuo, K. Ueda, Fiber laser coherent array for power scaling, bandwidth narrowing and beam direction control, in *Advanced Solid-State Photonics, Technical Digest* (Optical Society of America, 2005), paper MC3, pp. 553–558
41. S.J. Augst, J.K. Ranka, T.Y. Fan, A. Sanchez, Beam combining of ytterbium fiber amplifiers. J. Opt. Soc. Am. B **24**, 1707–1715 (2007)
42. T. Shay, J. Baker, A. Sanchez, C. Robin, C. Vergien, C. Zeringue, D. Gallant, C. Lu, B. Pulford, T. Bronder, A. Lucero, in *High-Power Phase Locking of a Fiber Amplifier Array, Fiber Lasers VI: Technology, Systems, and Applications*, ed. by D.V. Gapontsev, D.A. Kliner, J.W. Dawson, K. Tankala, Proceedings of SPIE, vol. 7195, 71951M
43. M. Fridman, V. Eckhouse, N. Davidson, A.A. Friesem, Simultaneous coherent and spectral addition of fiber lasers. Opt. Lett. **33**, 648–650 (2008)
44. K. Ludewigt, M. Gowin, E.T Have1, M. Jung, C. Wirth, O. Schmidt, I. Tsybin, T. Schreiber, R. Eberhardt, J. Limpert, A. Tünnermann, High brightness spectral beam combining to 8.2 kW. Proc. SPIE **7914**, Paper 7914-115 (2011)

45. D. Drachenberg, I. Divliansky, V. Smirnov, G. Venus, L. Glebov, High power spectral beam combining of fiber lasers with ultra high spectral density by thermal tuning of volume bragg gratings. Proc. SPIE **7914**, 79141F1–79141F10 (2011)
46. D. Kliner et al., Fiber technology reels in high power results. SPIE oemagazine, Jan 2004, pp. 32–35
47. G.I. Stegeman, R.H. Stolen, Waveguides and fibers for nonlinear optics. J. Opt. Soc. Am. B **6**, 652–662 (1989)
48. N. Shibata, R.G. Waarts, R.P. Braun, Brillouin-gain spectra for single-mode fibers having pure-silica, GeO_2-doped, and $P2O_5$-doped cores. Opt. Lett. **12**, 269–271 (1987)

Chapter 11
Fiber Industrial Applications of Fiber Lasers

As is evident from the material presented in earlier chapters, fiber lasers in general and high-power fiber lasers in particular are at a crossroads of two important directions in the field of lasers: laser diode pumping technology (including high-power diode laser development) and laser-active optical fiber technology.

In the early twentyfirst century, commercially available fiber lasers—operating in continuous-wave (CW) and pulse modes, with high CW, average, and peak power and short pulse widths—started a new era for fiber laser industrial applications. The combination of diode laser development and state-of-the-art gain fiber technology resulted in unbeatable fiber laser system parameters: high reliability, long lifetime, low cost of ownership, high wall plug efficiency, compact design, and all-fiber architecture (with practically no free-space optics involved, therefore providing increased immunity to environmental conditions). All of these qualities together overtake traditional laser technology in many aspects, including high-power diode-pumped solid-state lasers (DPSS) and some gas lasers.

The industrial laser market includes laser sources with average power levels, usually greater than $\sim$10 W and extending to 30–50 kW. Most 10 W systems are used for marking applications, whereas kilowatt lasers are traditionally used for welding and metal cutting. Because of the closeness of the fundamental frequencies (i.e., laser wavelengths) between widely used neodymium lasers (mostly Nd:YAG, Yb^{3+}:YAG, and Nd:YVO4) and that of Yb^{3+} fiber lasers, which are the most powerful and the most developed high-power fiber lasers, the fiber laser is an excellent substitute for the DPSS laser. A wide range of industrial applications are being explored using DPSS lasers. However, because of several unique features, fiber lasers are expected to penetrate in other fields of industrial use where, for example, diode lasers are the primary sources of light.

Of all fiber laser architectures, the master oscillator–power amplifier (MOPA) configuration is probably one of the most often sought for industrial applications, pushing DPSS lasers aside in many applications because of its unique features (especially for power scaling and flexibility of pulse management). With MOPA, industrial laser users are given a very attractive option to substitute for traditional technologies in the 1,064 nm spectral range (and its harmonics). Currently, MOPA technology offers not only CW single-transverse mode lasers with close to

V. Ter-Mikirtychev, *Fundamentals of Fiber Lasers and Fiber Amplifiers*,
Springer Series in Optical Sciences 181, DOI: 10.1007/978-3-319-02338-0_11,

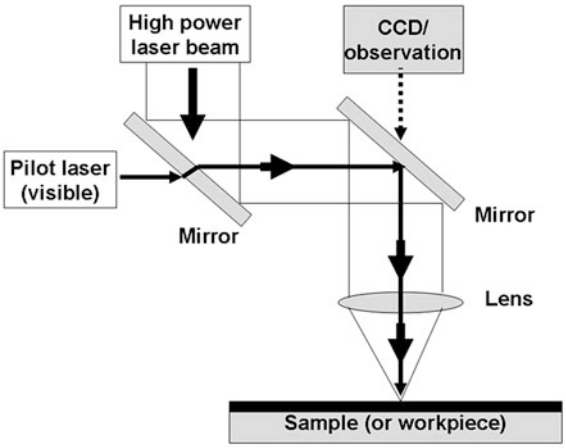

Fig. 11.1 General schematic of laser material processing

diffraction-limited beam quality, but also quasi-CW, pulse Yb^{3+} laser systems with kilowatts of output power and close to diffraction-limited beams—which were never before available from fiber lasers for industrial uses.

In the industrial sector, MOPAs offer a wide range of pulse widths, usually between 10 and 200 ns and pulse repetition rates (PRR) in the hundreds of kilohertz, which are very important for several material processing applications that require high-speed processing, such as some types of marking. The most widely used MOPA design employs a directly modulated master oscillator (often a diode laser) or amplitude-modulated output of a master oscillator with subsequent amplification in fiber amplifiers (usually several amplifier stages). This approach allows practically complete control of the PRR, pulse duration, and pulse waveform of the output beam, which is required in several applications where control of peak power and pulse profile is a concern. Most material processing applications [1–3] are sensitive to the laser power level, laser peak power, wavelength, and laser beam quality (which in turn affect the focusing capability of the beam).

Figure 11.1 shows a typical schematic for laser material processing. As one can see from the figure, the material processing setup usually has a visible pilot laser for alignment purposes; an observation system; optics that includes windows, mirrors, prisms, and a lens system; a high-power laser; and a workpiece with translation capability.

11.1 Laser–Material Interaction for Material Processing

Laser material processing explores certain physical processes during the laser's interaction with the matter. The central process that makes laser material processing possible is light absorption in the sample. Absorbed light transfers energy to electrons and phonons of the material and in such a way converts laser photon

energy into heat. Prolonging the interaction between the laser beam and the material leads to increased heat dissipation and therefore is responsible for the material's temperature increase. Some applications, such as polymer processing, restrict significant heat dissipation; therefore, short-pulse, limited average power lasers with elevated peak power are required. Processes that take place in the sample illuminated by the laser beam (both positively and negatively affecting the desired material treatment) require the laser to operate with certain pulse durations, PRRs, and pulse energies.

Because of the importance of the light absorption process in laser material processing, the optical absorption depth has to be defined. Attenuation of the laser power inside the processing material by 63 % determines a volume where this power is dissipated, which in turn produces a heat that diffuses to the following distance [4]:

$$L = \sqrt{(4D_m t_p)} \tag{11.1}$$

where L is the heat diffusion distance (or depth) in meters, D_m is the thermal diffusivity of the material in m^2/s (see Table 11.1), and t_p is the laser pulse width in seconds.

Thermal diffusion length plays an important role in the optimization and design of laser material processing for given materials. For example, the light penetration length (i.e., absorption length) is shorter than the diffusivity length, so the local temperature rise at the spot of laser–material interaction will be limited. However, if the diffusion length is shorter than the light absorption length, the temperature will increase fast with subsequent melting. To balance between overheating and targeted material treatment, one should optimize both the laser wavelength of operation as well as the laser pulse duration (or time of interaction). For materials that demonstrate low thermal conductivity, one may use longer laser pulses.

A good example of the light absorption length is the case of CO_2 lasers (operating wavelength is 10,600 nm) as used for material processing of metal samples. Because metals are not transparent to most infrared laser light (rather reflecting and absorbing it), CO_2 lasers do not seem to be the best choice for applications such as metal welding and cutting. However, particularly because of the high operating powers and power densities that can be achieved on a metal surface with CO_2 lasers, this type of laser is still widely used for such important applications.

In general, metals have a high degree of electrical conductivity, which in turn strongly affects their surface reflectivity properties. However, because of a large

Table 11.1 Thermal diffusivity of certain metals at room temperature (some data is taken from [4, 5])

Material	Thermal diffusivity, D_m (m^2/s)
Steel	4.2×10^{-6}
Aluminum	8.418×10^{-5}
Copper	1.1234×10^{-4}

electrical conductivity, metals also demonstrate a complex value of its refraction. Both the real part (which is the refractive index) and the imaginary part (which is an absorption coefficient) increase with wavelength and become close in value to each other at longer wavelengths (i.e., >1,000 nm), where the metal's reflectivity can be expressed as the Hagen-Rubens relation [4, 5]:

$$R \approx 1 - \frac{2}{\sqrt{0.003\lambda\sigma_{\mathrm{DC}}}} \tag{11.2}$$

where λ is the wavelength in micrometers and σ_{DC} is the material direct current conductivity in Ω^{-1} cm^{-1}. In other words, materials with high electrical conductivity demonstrate high reflectance at longer wavelengths.

Unlike metals, ceramic and glass materials demonstrate high absorption, not only in infrared but also in the ultraviolet (UV) spectral range. However, the high melting points of these materials as well as poor thermal conductivity make their processing harder.

11.2 Important Laser Parameters for Industrial Application

A deep understanding of laser parameters and how they affect the laser–material interaction process allows for many opportunities to use lasers in material processing. Several laser parameters are usually considered during the design and optimization of material processing, which in turn affects not only laser parameter selection but also choosing the right laser type or system.

11.2.1 Wavelength

Because of the importance of the absorption process in laser material processing, laser wavelength is probably one of the first parameters to be considered. Table 11.2 shows the most widely used types of lasers and corresponding operation wavelengths.

11.2.2 Pulse Energy

The pulse energy delivered by the laser beam into the interaction zone is one of the most important parameters during material processing evaluation. Pulse energy affects the energy density and together with pulse profile (i.e., pulse shaping) provides control of the process, including desired heating and cooling times.

Table 11.2 Laser types and operating wavelengths most commonly used in material processing

Laser type	Operating wavelength (nm)
CO_2 laser	10,600
Yb^{3+} fiber laser (fundamental frequency and harmonics)	1,030–1,100; 515–550; 343–366; 257–275
Nd:YAG laser (fundamental frequency and harmonics)	1,064; 355, 266
Copper vapor laser	511–578
Excimer laser	126–259

11.2.3 Pulse Width and Pulse Repetition Rate

The length of time that the laser energy continues to deliver to the beam–material interaction zone is defined as the pulse width. The majority of laser processing applications require a pulse operating mode. When the laser is pulsed, it delivers energy in each pulse with a certain PRR. (Note that the product of pulse energy and PRR defines the laser average power, which in turn affects the heat transfer in the interaction zone.) Pulse width variation is required at times to balance thermal diffusion distance-to-absorption length. Duty cycle, which was introduced earlier in the book, is also directly related to the pulse duration and pulse width laser parameters; it is basically the ratio of the pulse width over the time between pulses. A duty cycle equal to 1 defines a CW laser (i.e., continuous laser operation) and is the most heat-intensive regime. Certain applications, such as welding and soldering, benefit greatly from CW operation regime of the laser.

Note that ultra short pulses available from mode-locked laser systems deliver picosecond to femtosecond pulse widths. Reducing the laser material interaction to such a short time interval changes the interaction process significantly. When combined with high pulse energy and tight focusing, femtosecond lasers initiate highly nonlinear processes by delivering high power densities but at the same time with reduced heating. Some applications, such as micromachining or polymer processing, often use ultrashort laser sources.

11.2.4 Power

Laser power is one of the most important laser parameters and it is explored in many industrial laser applications. Laser power is defined as the energy delivered by the laser within a unit of time. The power of the CW laser, which is measured in watts, basically says how many Joules are delivered every second of laser operation. For pulse lasers, power is defined as a peak power, which is also measured in watts, which says how many Joules the laser delivers within the laser pulse it emits. Laser power affects material processing in several ways: through average power (or CW power), peak power, and power density (W/cm^2). Laser average power is the parameter that is mostly responsible for heat delivery to the laser–material interaction zone.

11.2.5 Power Density

Power density is determined as the laser beam power over an area of the beam focal spot in the processing zone. It basically says how many photons (and their energies) travel to the beam–material interaction area every second. Power density is measured in terms of watts per centimeters squared and is calculated as pulse energy divided by spot size. Even in a single spot, the power density can vary significantly depending on the beam quality of the laser. Table 11.3 demonstrates several examples of required power densities for most important laser material processing applications.

11.2.6 Laser Beam Quality

Laser beam quality is a measure of the beam quality deviation from the "ideal" diffraction-limited Gaussian beam. At the same time, in the context of material processing applications, the beam quality also implies an energy distribution in the laser beam, which in turn affects the laser–material interaction process and the result of material treatment. A beam, as it was discussed earlier in the book, is characterized using an M^2 value, which is equal to 1 for a perfect Gaussian beam (i.e., its fundamental transverse mode). Most desired beam qualities for material processing applications are close to those with an M^2 of 1 (usually between 1 and 1.5) and demonstrate a central lobe of intensity distribution close to that of a Gaussian profile.

Applications such as micromachining or small-hole drilling require an M^2 of ~ 1, whereas applications such as welding and cutting may benefit from high M^2 values of ~ 50. Taking into account that most lasers with a high value of the M^2 parameter have higher beam power, one may consider the beam quality together with power required for the particular application (i.e., temperature rise). Note that M^2 affects the focusing capability of the beam and more accurately the beam Rayleigh range, which in turn affects the depth of the focus.

As an example, UV excimer lasers, which have very poor beam quality but high pulse energy, cannot be tightly focused. However, because of the uniqueness of this laser type to operate in the UV spectral range with high pulse energies, excimer lasers are widely used by masking their beams to produce a desired pattern at the interaction zone. Excimer lasers are commonly used for etching

Table 11.3 Power density values for several material processing applications

Material treatment process with lasers	Power density (MW/cm^2)
Welding	~ 0.1
Cutting	1–100
Marking	10
Micromachining	10–1,000

(i.e., silicon chips) and Bragg fiber grating manufacturing, which in turn plays a very important role in fiber laser development. This spectral range (i.e., 126–259 nm) is a challenging one for fiber lasers.

11.2.7 Spot Diameter

A laser beam is usually focused onto the interaction zone. The focused laser beam size is determined by a focal spot diameter. Focal spot diameter is a function of the focusing lens focal length, the laser beam quality, the laser wavelength of operation, and the laser beam diameter before focusing:

$$d_{\text{spot}} = 4F_{\text{lens}}M^2\frac{\lambda}{\pi * D} \tag{11.3}$$

where F_{lens} is the focal length of the lens, M^2 is the beam quality parameter, λ is the laser wavelength, and D is the laser beam diameter before focusing.

11.3 Fiber-Optic Power Delivery Systems

Several important applications (e.g., material processing, medicine, imaging, military) require reliable, flexible, and high-quality laser beam delivery systems. As a result, fiber-optic power delivery systems are considered to be some of the most promising solutions. At the same time, the widespread use of the fiber laser technology creates a potential for a unique combination of fiber lasers and fiber power-delivery systems. Fiber-optic delivery systems demonstrate a number of important advantages compared with traditional free-space solutions, including the following:

1. Mechanical flexibility of the optical guide
2. Separation in the space of the laser source and the workplace (the target)
3. Elimination of complex and often expensive opto-mechanics
4. Access to small spaces
5. The possibility to affect (homogenize) an intensity profile of multimode laser beams
6. The possibility of spatial mode filtering
7. Improvement of beam pointing stability (spatial jitter)
8. The possibility of compact bundling of several fiber-optic sources due to a small diameter of individual fibers
9. Easy field servicing of the power transport systems (replacement and repair)
10. Reduced cost of some components

There are also challenges in the fiber type of the optical power delivery system. The main challenges are:

1. Propagating power/energy limitations
2. Polarization preservation of high-power guided beams
3. Beam quality preservation of high-power beams

This section reviews the primary elements of fiber-optic power delivery systems and the fiber laser output, as well as the main types of optical fiber devices used for optical power transfer.

As was described earlier in the book, high beam–quality fiber lasers (particularly in commercially available systems) typically use either single-mode optical fibers or large-mode area fibers. Both of these types of fibers allow for an optional polarization-maintaining feature. The typical core mode field diameters of the optical fibers of high beam–quality fiber lasers are between 6 and 35 μm. Using the square root law, one may calculate the optical damage threshold for propagating nanosecond pulses in these fibers, which gives the damage threshold value on the order of several J/cm^2. This, in turn, gives the maximum propagating in the fiber pulse energy of a fraction of a millijoule. At the same time, the nonlinear scattering processes described earlier, such as stimulated Brillouin scattering and stimulated Raman scattering, also limit the peak power of propagating pulses to several tens of kilowatts. Therefore, for safe and reliable operation, optical power delivery systems based on optical fibers need to be carefully designed. For applications where sub-millijoule, nanosecond optical pulses are sufficient, one may use a properly terminated single-fiber laser source to bring the required optical power to the workplace. However, other applications may require higher pulse energies and average powers.

Examples of fiber-optic delivery systems

Several solutions have been suggested and experimentally demonstrated to increase the damage threshold and therefore increase the power level of fiber-optic beam delivery systems. The most adopted approaches are using fiber bundles, using photonics fibers, and using hollow fibers. This section reviews the fundamental properties of each of these approaches.

Fiber Bundles:

As mentioned, the individual single optical fiber has a limited capacity to transmit a high-power and high-pulse energy beam. It is therefore reasonable to expect that with a closely packed array of single fibers, one can scale the transmitted power practically linearly with the number of used individual fibers. This is exactly the idea behind a system called a fiber bundle. Typically, the fiber bundle consists of an array of several multimode fibers packed together (usually glued). Each individual fiber carries light independently. Therefore, in most cases, optical damage and power limitation conditions have to be considered separately for each fiber.

(a) Manufacturing of fiber-optic bundles

The first step in manufacturing a fiber optic bundle is the creation of a single fiber. The single fiber is manufactured/drawn from a preform (see Chap. 4 for details). After the single fiber is created, a number of these fibers (typically between 40 and 200) are bundled together. The bundled fibers are then packed together, heated, and again drawn, creating a very robust array of such multifibers, which are a few millimeters in diameter. Lastly, the created multifibers (about 200) are again packed together following heating and drawing processes, which result in a fiber bundle consisting thousands of single fibers (Fig. 11.2).

It is important to note that each individual fiber has its own cladding, which is basically preserved during the bundle manufacturing process. During the light injection at the input port of the bundle, some light gets trapped in the fiber cladding. The bundle design usually takes this into consideration by creating layers between individual fibers (which acts as an outer cladding) to dump (absorb) the cladding propagating light. Cladding propagating power limits the overall transmission efficiency of the fiber bundle. Typical power attenuation of the fiber bundle in the visible-infrared spectral range is in the order of a few dB/m (usually around 1–1.2 dB/m). Spectrally, glass fiber bundles operate at between 400 and 2,200 nm. Fiber bundles, which are used for UV applications (such as UV curing devices), employ special UV-transmitting individual fibers; the bundle operates in the wavelength range below 400 nm with better than 45 % optical transmission [6]. There are fiber bundles created by the utilization of plastic individual fibers. Such bundles are typically used in the visible range of optical spectrum ($\sim$400–700 nm).

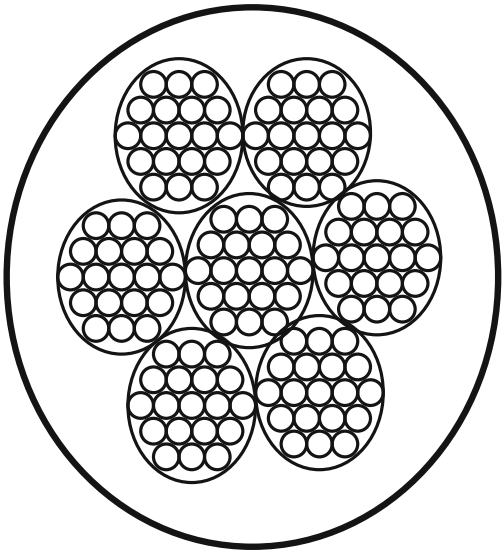

Fig. 11.2 Multibundle fiber-optic structure

(b) Coherent and noncoherent fiber-optic bundles

There are a number of applications where one requires the transmission of images through a mechanically flexible waveguide, rather than optical power. In these applications, it is very important to preserve the relative position of individual fibers within the bundle at both ends of the device. Because a structured fiber bundle preserves the original image at the output port, the fiber bundles are referred to as "coherent bundles". Coherent bundles preserve spatial variation of the injected intensity of the optical beam at the input port of the bundle. As one can expect, the image's spatial resolution is basically determined by the center-to-center spacing of individual fibers in the bundle (Δd) and the transverse magnification of the lens system (M_{lens}), which couples and decouples an optical beam in and from the fiber-optic bundle [6]:

$$\Delta x = \frac{\Delta d}{M_{\text{lens}}} \tag{11.4}$$

Figure 11.3 illustrates a basic cross-sectional structure of the fiber-optic bundle. Note that an alternative way to achieve a lateral magnification in the fiber bundle is to use a tapered individual fiber.

(c) Power transmission by fiber-optic bundles

In addition to the transfer mentioned above, fiber-optic bundles are used for power/energy delivery. Fiber bundles may also be used to divide light from a single source into several beams or to reshape an original beam in order to couple it between different optical devices. For energy transmission applications, the individual fiber requirements are more lenient because the transmitted pulse energy scales with the number of fibers in the bundle, allowing one to keep the propagating energy fluence along the bundle below the damage threshold for individual fibers. Exploring a particle image velocimetry application. Stephens et al. [7] demonstrated a high energy delivery of nanosecond optical pulses from a frequency-doubled Nd:YAG laser source. Using the fiber-optic bundle, the authors [7] delivered 25 mJ of 532 nm pulse energy to the target.

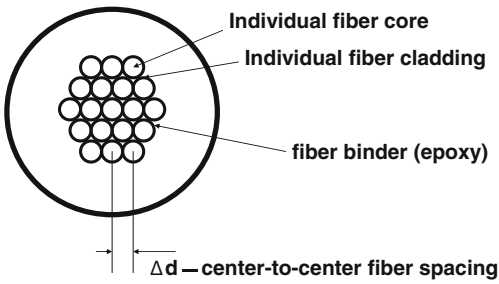

Fig. 11.3 Cross sectional structure of a single fiber-optic bundle

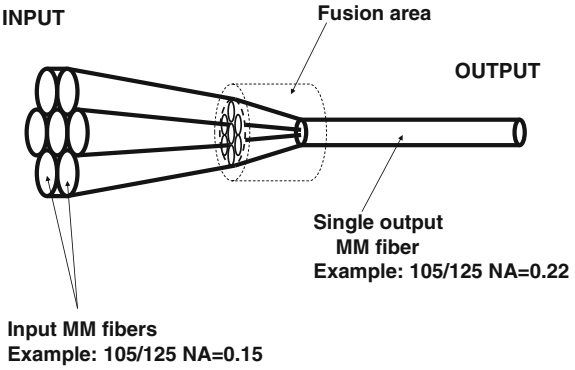

Fig. 11.4 Fused optical pump-coupler structure. Numerical aperture (NA)

(d) Pump combiner/coupler

Chapter 10 described so-called fused pump combiners. Such polarization-maintaining and single-mode pump combiners with feed-through double-clad fibers play a very important role in fiber laser and fiber amplifier technologies. A variation of fiber-optic bundling technology, namely a fused modification of it, plays a very important role in combining and transferring optical power from several fiber-coupled laser sources. A fused-fiber pump combiner without a feed-through fiber but with an output multimode fiber may act as an $N \rightarrow 1$ type of optical coupler/combiner (Fig. 11.4) and is widely used for direct pumping applications in fiber laser and fiber amplifier systems.

In several applications, such as material processing, in which it is required to deliver an average power to the target with relaxed requirements for the polarization and beam quality, such pump couplers are very useful. Fused-pump couplers/combiners deliver several hundred watts of optical power from a single output fiber. The advantage of such a coupler is in a single-fiber (round) output, high pump laser-coupling efficiency (>90 %), and mechanical flexibility of the power delivery system. Note that, as in any optical system, it is necessary to consider brightness preservation during the design of such $N \rightarrow 1$ optical couplers.

Photonics Fibers:

Photonics crystal fibers (PCF) (Holley fibers), which appeared in the early 1990s, have a special place in the fiber science and technology. Due to their unique properties (mainly versatility), they are widely used and have become unique players in several important applications, ranging from fiber laser sources to optical power guides.

Following Tünnermann et al. [8], we will review the main technical characteristics of this type of optical fiber. Figure 11.5a shows a fundamental cross-sectional view of the PCF. The basic idea behind PCF technology is to achieve a controllable refractive index profile in the fiber cladding by creating an array of air holes in the fiber cladding. The air holes have diameter d and pitch Λ. The holes' orientation follows a triangular geometry, as shown in Fig. 11.5a, b.

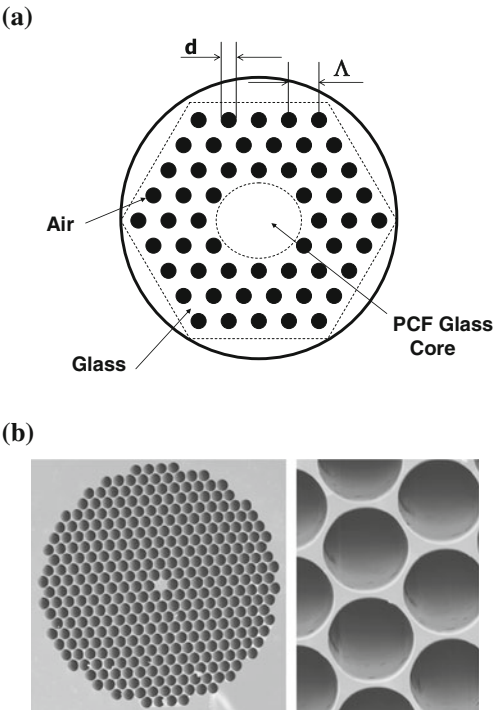

Fig. 11.5 **a** Fundamental, cross-sectional structure of a PCF. **b** Scanning electron microscope micrographs of a PCF produced by the Naval Research laboratory (*left*). The diameter of the solid core at the center of the fiber is 5 μm, whereas the diameter of the holes is 4 μm (*right*). (Reproduced from US Naval Research Laboratory at http://www.nrl.navy.mil/techtransfer/viewpdf_st.php?id=70)

As one can expect, filling the fiber cladding with multiple air holes reduces an average (or effective) refractive index of the cladding glass. This in turn should affect both the propagating condition of the optical waves inside the fiber core (condition of the total internal reflection) as well as the numerical aperture (NA) of the fiber core.

The V-parameter of the PCF can be expressed as follows [9]:

$$V_{\mathrm{PCF}}(\lambda) = \frac{2\pi}{\lambda}\Lambda\sqrt{n(\lambda)_{\mathrm{core}}^2 - n(\lambda)_{\mathrm{clad}}^2} \tag{11.5}$$

For $V_{\mathrm{PCF}} > \pi$, the fiber starts supporting high-order propagating modes (cutoff condition) [9]. Unlike conventional step-index fibers, where wavelength dependence of the refractive index of the cladding material follows the conventional dispersion trend, the effective refractive index of the PCF has a very strong wavelength dependence (Fig. 11.6).

As shown in Fig. 11.6, for a very big pitch value Λ compared with the whole diameter d (more glass mass in the cladding structure), the effective refractive index basically approaches the refractive index of the solid glass. In the opposite case—that is, when the value of the pitch is close to that of the air hole diameter—the effective refractive index decreases (more air in the cladding structure). When addressing the condition of single-mode propagation in PCF, it is useful to illustrate a plot, as shown in Fig. 11.7.

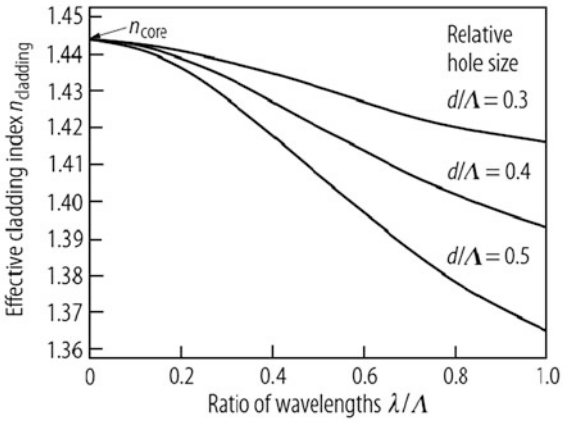

Fig. 11.6 Effective index of refraction of a photonics crystal fiber cladding. (Image courtesy of Springer)

Figure 11.7 demonstrates a dependence of the wavelength to the pitch ratio λ/Λ versus the relative hole diameter d/Λ. As one can see from Fig. 11.7, when the relative air hole diameter is less than 0.45, the PCF demonstrates a single spatial mode propagation for any wavelength (endlessly single-mode PCF) [10]. An important conclusion can be made when PCF demonstrates a relative hole diameter less than 0.45. In this case, one may achieve a single mode propagation with theoretically any core size, provided that the pitch value is chosen accordingly. Note, however, that if the value λ/Λ becomes too small (<0.1), scattering loss due to longitudinal nonuniformities such as microbending, macrobending, and dielectric imperfections increases [11].

Preserving a single spatial propagating mode in a wide range of the fiber core sizes is a very useful property of the PCF for high-energy and high-power fiber laser and optical power transfer applications, for which achieving a high energy of a single transverse mode propagation in a conventional rare-earth-doped glass fiber

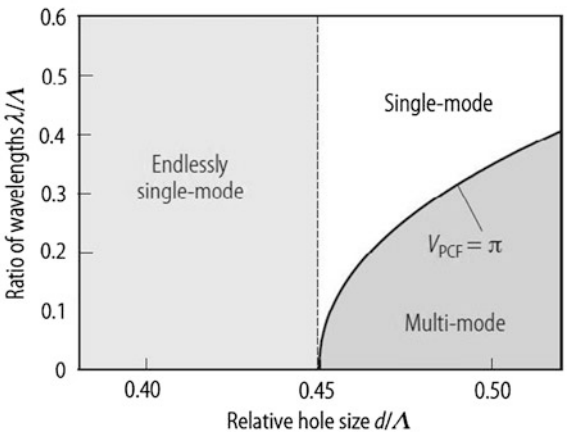

Fig. 11.7 Single-mode versus multimode conditions in photonics crystal fiber. (Image courtesy of Springer)

core has always been a challenge. This property opened up a wide range of opportunities to scale up the pulse energy of the fiber lasers as well as PCF optical power guides. In the case of conventional rare-earth-doped glass fibers, which are typically manufactured by the modified chemical vapor deposition technique, the smallest achievable refraction index difference that is needed for an increased fiber core diameter to maintain single transverse mode propagation is on the order of 1×10^{-3}. This fact leads to the practically achievable and controllable core refractive index of 0.06. In PCF, the controlled refractive index difference can be achieved down to the value of about 10^{-4}, therefore achieving a corresponding core NA value of 0.02.

By using the ability to control the effective refractive index of the fiber cladding, PCF allows one to achieve a cladding-guided light by creating an air-cladding region surrounding the fiber cladding. This in turn leads to a double-clad PCF. In double-clad PCF, the inner cladding is surrounded by a chain of air holes with silica bridges (Fig. 11.8).

The silica bridges of 400 nm are practically achievable, which in turn preserves manufacturability and mechanical stability of the PCF, leading to the inner cladding NA > 0.6. (Note that a typical NA of polymer-based double-clad glass fibers is ~ 0.45.) This property allows one to control the NA of the inner cladding while reducing its diameter. Higher NAs create additional advantages in using high-brightness pump diode lasers, whose radiation needs to be effectively coupled into the double-clad fiber cladding. Using a 1.5 m long, 40 μm fiber core (35 μm mode field diameter) PCF Yb-doped amplifier with core NA of 0.03 ($d/\Lambda = 0.09$), Xie et al. [6] achieved 48 W of average power output power at 1,064 nm wavelength while amplifying a radiation from a mode-locked ND^{3+}:YVO_4 diode-pumped laser. The amplifier's slope efficiency was 74 %. The amplifier operated at a repetition rate of 80 MHz and pulse duration of 10 ps, creating a corresponding pulse peak power of 60 kW in the fiber core. The beam quality of the amplifier output was close to diffraction limited, with $M^2 < 1.2$ [11].

Hollow fibers:

It is important to mention another type of optical fiber, the so-called hollow fiber, which has a very important application in the high-power infrared laser delivery system. There are several properties of the hollow fibers that allow one to

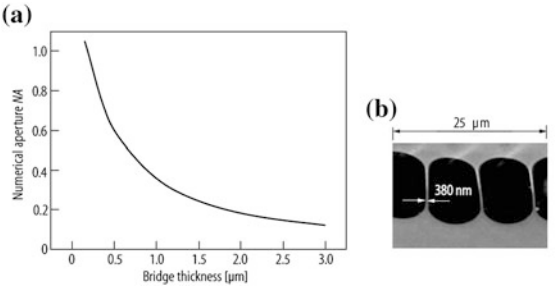

Fig. 11.8 Some characteristics of a double-clad photonics crystal fiber (Image courtesy of Springer)

transmit and deliver optical power where and when traditional solid-core optical fibers show limited performance:

1. The spectral transmittance of hollow fiber is beyond the 20 μm wavelength range.
2. Hollow fiber has a relatively simple structure, which makes this system manufacturable and cost effective.
3. Hollow fiber has an air core, which significantly increases the optical damage threshold (important for high-power applications).

Historically, hollow fibers have been developed and used for optical power delivery of high-power CO_2 lasers operating at the 10.6 μm wavelength. High-power CO_2 lasers are still widely used in laser material processing and occupy a big fraction of the laser market. When properly designed, hollow fibers demonstrate low insertion loss ($\sim$0.1–1 B/m). Note that the high loss nature of hollow fibers compared with all glass telecommunication fibers, where insertion losses are on the order of $\sim$0.2 dB/km, is one of the biggest limiting factors in the widespread use of hollow fibers.

Naturally hollow fibers show no Fresnel reflection at the input and output ports of the waveguide and, because of the air-fill core, the hollow fibers demonstrate low divergence of the output beam (low NA). Mechanically, hollow fibers are generally less flexible (bending strength). Nevertheless, an ability to transmit high-infrared optical power (several kilowatts) [12] makes them irreplaceable in several applications, ranging from laser material processing to laser surgery.

There are two main types of hollow waveguides [13]:

1. "Leaky guides", with an inner core refractive index of $n > 1$.
2. Attenuated total reflectance (ATR) guides, with an inner wall material with a refractive index of $n < 1$.

The two main structures of the hollow waveguides are shown in Fig. 11.9.

The leaky guide, with $n > 1$, employs a metallic and dielectric film deposited on the inside of metallic, plastic, or glass tubing. The ATR type, which has inner wall material with $n < 1$, is composed of dielectric materials and acts as a fiber

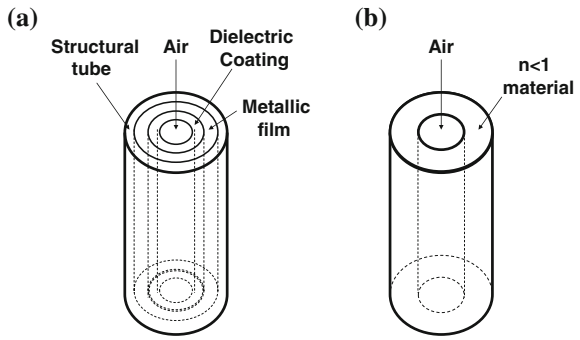

Fig. 11.9 Two types of hollow waveguides. **a** Leaky guide. **b** Attenuated total reflectance guide

with a core refractive index bigger than the refractive index of the cladding. As an example of the ATR type of the hollow waveguide, one may consider sapphire waveguides with $n = 0.67$ at 10.6 μm wavelength. Special oxide glass with $n < 1$ can also be used in the ATR type of hollow waveguides.

Harrington and coworkers [13] developed a hollow glass waveguide structure, consisting of a metallic layer of Ag on the inside of silica glass tubing that is coated by a layer of AgI, a dielectric material. The structure has a simple design, is mechanically very flexible, and demonstrates a smooth inner surface of AgI film [13].

11.4 Main Structure of Fiber-Optic Delivery Systems

The general structure of the fiber-optic delivery system is illustrated in Fig. 11.10. The fiber-optic delivery system generally consists of four main parts: laser source, input coupling optics, fiber-optic waveguide, and output coupling optics. In some cases, when the fiber laser source has a properly designed out-of-the-laser fiber terminating cable, the fiber laser emission can be directly delivered to the target, integrating the laser source, input coupling optics, and fiber-optic waveguide in a single fiber laser unit. Most of the parts used in the fiber laser delivery system have already been reviewed in detail. This section discusses the input coupling optics and output coupling optics.

Input coupling optics couple laser output into the core of the fiber-optic waveguide. This subsystem is usually designed not only to maximize optical coupling efficiency but also to make it a damage-free operation with minimum heat dissipation. The input coupling optics may be of an all-fiber design or a free-space design. In all-fiber designs, one uses fused-pump combiners or fused-beam expanders, for example. These components are usually fusion spliced and each splicing area gets protected. The main advantage of all-fiber designs is the absence

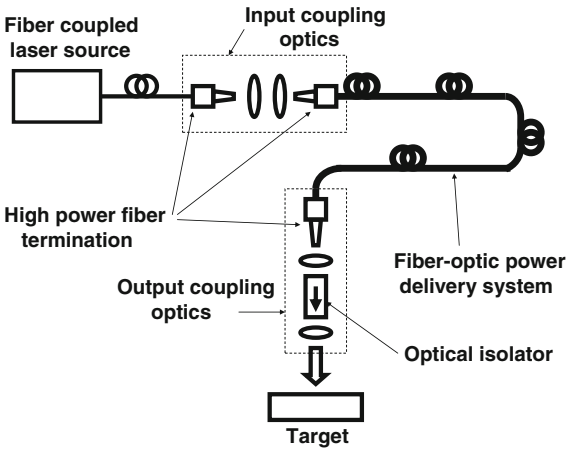

Fig. 11.10 General structure of a fiber-optic delivery system

of free-space zones with high-power beams, mechanical flexibility, and no need for preserving precise alignment of each component during the operation. The main disadvantage is mostly in servicing, for which one needs to use an expensive fusion splicer and, in some cases, optical power limitation of available individual fiber components.

A free-space input optical coupling design offers the greatest flexibility in optical design, flexibility in available free-space components, and the ability to use a free-space laser output beam, which in some cases may have advantages over fiber-coupled lasers. In the case of the free-space input optical coupler design, it is very important to collect most of the laser power into the haul fiber core while taking into account the fiber NA (acceptance angle of the fiber). Any light coupled into the fiber cladding produces the system loss (decreased coupling efficiency) and increases local temperatures, which in turn may lead to a catastrophic failure of the coupling optics and even the fiber-optic waveguide. In the free-space input coupling optics design, each fiber entrance requires proper termination. High-power fiber terminations are commercially available from several vendors. The fiber terminations usually use AR coating as well as angle-polished fiber ends enclosed in high-power fiber sockets. Note that it is extremely important to keep all optical interfaces clean of dust and other contaminations that cause high-power laser beam scattering, burns, and as a sequence, optical damage of the glass surfaces.

Output coupling optics couple out laser beam propagating in the optical waveguide and focus the laser beam on a target for laser processing of the material. It is often important to incorporate a high-power optical isolator into the output coupling optical system because of the danger of back reflection for fiber laser operations. The output coupling optics may include high-power fiber termination, a beam expander, and a beam focusing assembly. The particular design is dictated mostly by the application, which may require a different focal spot, depth of focusing, and beam position precision.

11.5 Main Industrial Applications of Fiber Lasers

11.5.1 Welding

Welding is one of the most widely used applications in laser material processing and is directly related to high-power laser beams. This process requires delivery of certain laser power to the interaction zone within a certain period of time, which in turn is converted to the heat required for the welding process. Deposited heat then softens the material leading to the welding. Because of the well-controlled output power and heating time through laser pulse duration, lasers are considered by many to be an ideal welding tool. Among the advantages that are demonstrated by current state-of-the art current laser welding processes, one may mention precision of welding parameters, high power density, a small interaction zone (which in turn

comes from the capability to deliver high power into a small spot), low distortion of the affected welding area, high speed of the process, and the possibility of laser welding in air.

Disadvantages of laser welding usually come from the cost of laser welding equipment, including high-power lasers (although fiber laser is expected to reduce the cost of ownership), requirements of well-aligned joints of the samples, as well as dealing with high metal reflectivity of the infrared light used from high-power lasers. Temporal regimes required for laser welding span from millisecond to CW laser operations. Lasers with more than 1 kW of average power are usually required for both welding and cutting.

11.5.2 Cutting

Laser cutting is a process that uses a focused laser beam as a heat source to melt and then to vaporize sample material, which in turn during sample (or beam) moving leads to the sample partition. Laser cutting is usually optimized by varying laser power, sample feeding, and power density. Similar to welding, laser cutting usually uses high-power lasers and is considered a fast process when optimized. Laser cutting typically uses microsecond, millisecond, or CW laser operating regimes.

11.5.3 Drilling

During the laser drilling process, the sample material is removed to create via holes. Drilling is usually accomplished by so-called percussion or trepanning drilling processes. The percussion drilling process sets the focal spot diameter close to the targeted hole size. However, there are situations (especially when the laser power is limited) when large holes have to be drilled. In this case, trepanning drilling is a solution. In this technique, the laser focal spot size is set to be smaller than the targeted hole and the laser beam is moved within the targeted hole dimension to "free" the area and create the hole of desired diameter. Laser drilling uses microsecond, nanosecond, and picosecond laser pulses. It is considered to be cost-effective because there is no drill breakage or wear and it is highly reproducible.

11.5.4 Soldering

Soldering uses high-power laser beams and requires local heating of samples. Fiber lasers with controlled pulse widths and controlled high average power produce a fast soldering process. Soldering uses millisecond to CW laser operating regimes when high average powers are achieved.

11.5.5 Marking

Laser marking uses a so-called "thermal shock" or a fast heat dissipation to remove a sample material surface layer. Laser marking has an important role in laser material processing and generates good revenues for material processing companies. Because they are flexible in wavelength selection as well as temporal and energy parameters, lasers are becoming one of the most popular marking tools for many surfaces, including metal and plastic materials. Unlike other marking techniques, such as printing, laser marking is a clean process that does not use hazardous materials, has a low cost of ownership, and is highly flexible for different marking requirements. Laser marking is very stable. Laser marking typically uses nanosecond pulse operating regimes with <100 W of average powers. Fiber lasers are an ideal solution for laser marking applications.

11.5.6 Heat Treating

Because of their high power and tight focusing capabilities, lasers are widely used in material local heating. Some applications require stress removal from the localized area without spreading the heat to the whole workpiece. Laser heating uses localized material treatment and minimizes material distortion and stress. Laser heating uses millisecond to CW laser operation, often with good beam quality, especially when hard-to-access areas have to be heated.

11.5.7 Metal Deposition

Laser metal deposition is the process during which some metal parts are built by injecting metal powders into the focused spot of a high-power CW laser beam. The metal parts created as a result of direct metal deposition vary in mechanical properties depending on the metal alloys used during the process. Metal deposition using high-power CW lasers is a fast process of manufacturing different parts or their repair.

11.5.8 Paint Stripping and Surface Removal

During laser paint stripping, painting material is removed from the sample surface. Basically, because there is no contact operation, lasers offer a clean and safe surface treatment environment with a precisely defined depth of laser–material interaction. (This is unlike chemical stripping, in which special care should be

taken for the waste disposal as well as the non–localized effects of chemicals, which may spread to the other material parts and even removing unintended part of the sample material.) Stripping is implemented though material removal via vaporization of the painted material without significant color change or other sample degradation. Basic requirements for the surface removal or paint stripping are high absorbance of the paint at the laser wavelength and low thermal conductivity.

11.5.9 Micromachining

Micromachining is probably the most precise type of laser material processing. The process results in the production of very small parts. The process requires heat dissipation in a very small area during a very small period of time. Micromachining requires high peak power and very short pulses, but low average power. The speed of the laser should be in the multi-kilohertz range of PRR with picosecond to femtosecond pulse durations. With shorter wavelengths and better beam quality, the process resolution increases. Micromachining is applied to metals, plastics, and composites, among others. The micromachining process using very high peak power femtosecond lasers employs ionization of the material, which takes place in the high-intensity field of the laser beam. Micromachining requires mode-locked lasers, which are costly compared with long-pulse and CW models. However, the advantages achieved by using a femtosecond pulse justify its use in most micromachining applications.

11.5.10 Semiconductor Processing with a Laser Beam

Laser processing of semiconductor materials plays an important role in today's laser applications. Semiconductors generally have strong absorption in the UV, visible, and near infrared region while demonstrating high transparency in the infrared region of the optical spectrum. The 1,064 nm fiber and DPSS lasers are used mostly for silicon marking, whereas UV lasers (e.g., excimer) or harmonics of fiber lasers are used for material processing of wide-bandgap semiconductors, such as gallium arsenide and indium phosphide. The temperature of the semiconductor sample is used as an optimization parameter during processing because of its effect on the light absorption.

Figure 11.11 shows most of the laser material processing applications on a map of beam quality and required laser operating average powers. As one can see, fiber laser sources that demonstrate 3–5 kW power with diffraction-limited beam quality and up to 50 kW in multitransverse mode operation meet most of requirements and are a good fit for numerous applications.

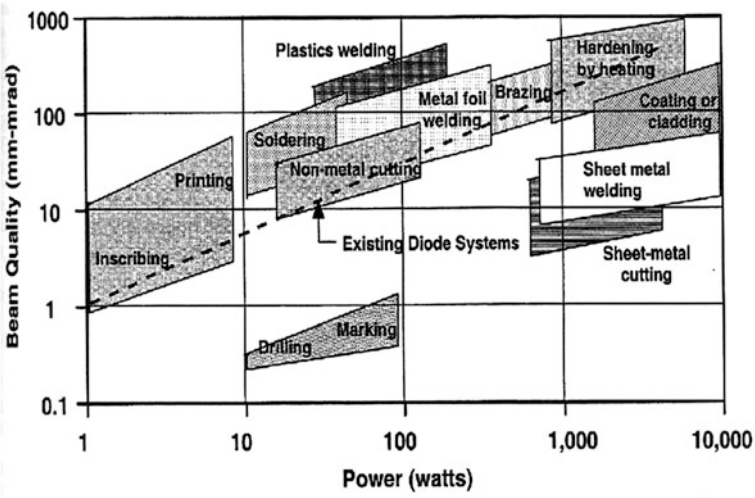

Fig. 11.11 Laser beam quality and average power map for different material processing applications [11, 14] (Image courtesy of SPIE)

11.5.11 Main Competitors of Fiber Lasers in Industrial Laser Applications

This section reviews the main competitors of fiber lasers used in material processing applications. Besides fiber lasers, the most widely used laser types include diode lasers, DPSS (Nd:YAG, Yb^{3+}:YAG, Nd:VO_4), solid-state thin-disk lasers, CO_2 (high cost of ownership), and excimer lasers.

Although fiber laser technology is quickly replacing many diode lasers and DPSS lasers in rod and slab configurations, it still competes with solid-state thin-disk lasers that have appeared during the last decade. Thin-disk lasers have several unique properties and therefore are considered to be one of the main competitors for fiber laser technology in current solid-state laser material processing. Especially in applications requiring high average powers, thin-disk lasers remain in demand, even though industrial fiber lasers have demonstrated multi-kilowatt levels of operation.

Thin-disk lasers have a power-scalable (with the disk area) platform with reasonably good beam quality. Disk lasers provide short (nanosecond) pulses with a high peak power of operation. Currently, disk lasers are superior to fiber lasers in high-energy nanosecond pulses. Disk lasers are very attractive for welding applications in which high beam quality is required along with multi-kilowatt output powers. Disk lasers are not susceptible to back reflection from highly reflecting metal surfaces. They also are more tolerant to high-power and high-energy scaling because their intracavity light fluence is far from the optical

damage threshold, which in turn make them quite reliable in some sensitive (failure intolerant) applications.

The long-existing gas CO_2 lasers also occupy a significant part of the laser material processing market because of their high power availability, especially for applications such as welding and cutting. Using unstable laser resonators, CO_2 lasers may provide diffraction-limited beam quality at elevated optical powers. Some applications that require laser wavelengths in the infrared range benefit from the 10 μm line of this laser. Note, however, that probably the most serious advantage of the CO_2 laser is that they are already installed in many material processing centers and companies. Even if all other parameters of fiber lasers including power, beam quality, and wavelength will satisfy the user, CO_2 lasers will still remain on the market. There is also a discussion currently about the advantages of using CO_2 lasers versus fiber lasers in metal welding and cutting.

Excimer lasers emitting in the 126–259 nm spectral range, with their high pulse energy reaching several hundreds of millijoules and relatively high PRR current, remain out of touch for many applications, such as lithography. Most high-power fiber lasers operate in the near-infrared spectral range and require nonlinear frequency conversion to reach UV wavelengths of operation. This in turn requires high energy and high peak powers. Their small core size (on the order of 30 μm for diffraction-limited systems and several hundreds of micrometers for multimode operation) significantly restricts the fiber laser's pulse energy in the nanosecond range of pulse durations. Excimer lasers will probably remain out of competition from fiber lasers for most lithography applications in the near future.

11.5.12 Summary of Challenges for Fiber Lasers in Industrial Applications

In summary, the challenges facing fiber lasers in industrial applications include the following:

- Back reflection when processing highly reflective materials, such as those with metal-coated surfaces or metal parts.
- Pulse energy scaling for nanosecond fiber lasers systems due to fiber material surface and bulk damage.
- Availability of infrared wavelengths in the vicinity of CO_2 laser sources (i.e., in the 10 μm spectral range) for immediate and painless substitution of gas laser sources.
- Availability of visible (especially blue) and UV wavelengths with power-scalable concepts, which can effectively compete with blue-green solid state and excimer lasers.
- Reliable and high value of polarization extinction ratio at elevated power levels with diffraction beam quality (when nonlinear frequency conversion is considered).

11.5.13 Future of Fiber Lasers in Material Processing

High-power fiber lasers will continue to penetrate the laser material processing market, especially where flexibility in pulse profiles, PRR, and power density are required. The biggest challenge will probably be in penetrating those markets where laser applications require more than 100 mJ of nanosecond pulses in both the UV and infrared spectral range. Even though today the total industrial fiber laser market totals several hundred million dollars and the whole laser material processing market totals a few billion dollars, fiber lasers show great potential and promise. Fiber lasers are already widely used for marking, thin-film ablation, welding, cutting, and semiconductor material processing (e.g., silicon). The unique and flexible fiber laser systems with low cost of ownership and all-fiber architecture definitely make fiber laser technology a top choice for numerous material processing applications.

References

1. W.M. Steen, K. Watkins, *Laser Material Processing*, 3rd edn. (Springer Verlag London Limited, UK, 2003), p. 401
2. R. Iffländer, *Solid-State Lasers for Materials Processing* (Springer Verlag Berlin, 2001), p. 347
3. J.F. Ready, *Industrial Applications of Lasers* (Academic Press, New York City, 1997)
4. J.P. Holman, *Heat Transfer*, 9th edn. (McGraw-Hill, New York, 2002) (which in turn cites A.I. Brown, S.M. Marco, Introduction to Heat Transfer, 3rd edn., McGraw-Hill, New York, 1958 and E.R.G. Eckert, R.M. Drake, Heat and Mass Transfer, McGraw-Hill, New York, 1959)
5. A. Bejan, J. H. Boyett, A.D. Kraus, *Heat Transfer Handbook* (Wiley-IEEE, NJ, 2003), p. 1496
6. T. Xie, D. Mukai, S. Guo, M. Brenner, Z. Chen, Fiber-optic-bundle-based optical coherence tomography. Opt. Lett. **30**, 1803–1805 (2005)
7. T.J. Stephens, M.J. Haste, D.P. Towers, M.J. Thomson, M.R. Taghizadeh, J.D.C. Jones, D.P. Hand, Fiber-optic delivery of high-peak-power q-switched laser pulses for in-cylinder flow measurement. Appl. Opt. **42**, 4307–4314 (2003)
8. A. Tünnermann, J. Limpert, A. Bruns, in *Diode-Pumped Fiber Lasers. Chapter 4.3 in Laser Systems, Part 2, Landolt-Börnstein—Group VIII Advanced Materials and Technologies*, vol. 12 (Springer, 2008), pp. 125–139
9. N.A. Mortensen, J.R. Folkenberg, M.D. Nielsen, K.P. Hansen, Modal cutoff and the V parameter in photonic crystal fibers. Opt. Lett. **28**, 1879–1881 (2003)
10. T.A. Birks, J.C. Knight, P.S.J. Russell, Endlessly single-mode photonic crystal fiber. Opt. Lett. **22**, 961–963 (1997)
11. J. Limpert, A. Liem, M. Reich, T. Schreiber, S. Nolte, H. Zellmer, A. Tünnermann, J. Broeng, A. Petersson, C. Jakobsen, Low-nonlinearity single-transverse-mode ytterbium-doped photonic crystal fiber amplifier. Opt. Express **12**, 1313–1319 (2004)
12. A. Hongo, K. Morosawa, K. Matsumoto, T. Shiota, T. Hashimoto, Transmission of kilowatt-class CO_2 laser light through dielectric-coated metallic hollow waveguides for material processing. Appl. Opt. **31**, 5114–5120 (1992)
13. J.A. Harrington, A review of IR transmitting, hollow waveguides. Fiber Integr. Opt. **19**, 211–217 (2000)
14. W.F. Krupke, Advanced Diode-Pumped Solid-State Lasers (DPSS): Near Term Trends and Future Prospects, in *Proceedings of SPIE*, 2000, vol. 3889, pp. 21–32

Chapter 12
Conclusion

This chapter outlines the major conclusions of the topics reviewed in this book.

1. The physics of fiber lasers and fiber amplifiers are the same as for any other laser type and follow similar theoretical considerations. Most solid-state laser formulas can be used during fiber laser design and development.
2. Unlike bulk lasers, fiber laser resonator modes of optical fibers follow cylindrical geometry waveguide modes. Fundamental mode (LP_{01}) selection techniques in fiber lasers and fiber amplifiers are different from that of open optical resonators.
3. Due to long length and small cross-sectional area of the fiber-active medium, fiber laser gain is enormously high. This has two big impacts on the fiber laser position among other laser systems:

   (a) Pump-to-lasing efficiency is up to 80 %, which in turn results in a high wall plug efficiency.
   (b) Because of the same long gain medium and small fiber-core cross-sectional area, optical nonlinearities and optical damage are serious limitations in scaling up fiber laser powers and essentially peak powers.

4. Special attention has to be paid to nonlinearities and damage issues during fiber laser design.
5. Back-propagating signal powers inside a fiber laser system can be a real danger for several components of the fiber laser or fiber amplifier system. Careful optical isolation of each gain stage of the system is a must for safe operation.
6. Unlike many other laser types, fiber laser and fiber amplifier systems can be made alignment-free due to highly developed fiber-splicing technology and availability of fiber-coupled optical components as well as fused all-fiber components.

V. Ter-Mikirtychev, *Fundamentals of Fiber Lasers and Fiber Amplifiers*,
Springer Series in Optical Sciences 181, DOI: 10.1007/978-3-319-02338-0_12,

7. In the case of high average power (or high CW power), the "thermal immunity" of fiber lasers would be an incorrect assumption during a fiber laser design process. Thermal management has to be considered for reliable operation with preserved laser parameters.
8. The commercial availability of reliable and low-cost fiber-coupled optical components, including pump laser diodes for fiber lasers and amplifiers, are real challenges. Without resolving these issues, the successful development of the fiber laser and fiber amplifier systems (especially high power) will be very problematic.

Index

A

Absorption, 3, 7–9, 11–13, 17–25, 30, 31, 33, 34, 37, 44, 46–47, 50, 51, 53–60, 81, 86, 88, 91, 93, 95, 96, 104, 127, 134, 163–165, 167, 172, 179, 197, 210–213, 228
Absorption band, 3, 23, 24, 46, 47, 50, 51, 53, 56, 57, 59, 167
Absorption characteristics, 172
Absorption coefficient, 21, 23, 24, 35, 164, 165, 172, 212
Absorption cross section, 17, 20, 22, 87, 104
Absorption depth, 211
Absorption frequency, 8
Absorption intensity, 23
Absorption length, 211, 213
Absorption line, 30, 53
Absorption loss, 87, 88
Absorption peak, 50
Absorption process, 7, 8, 12, 211, 212
Absorption saturation, 87, 95
Absorption spectrum, 46, 48, 51, 53, 58, 59
Absorption transition, 47, 87
Acoustic, 10, 174, 177, 178
Acoustic branch, 10
Acoustic phonon, 174, 177, 178
Acoustic phonon energy, 177
Acoustic velocity, 177
Acoustic vibration, 177
Acoustic wave, 10, 174, 177, 178
Active, 1–3, 7, 9, 16, 17, 21, 23–25, 27–29, 32, 34, 37–39, 41, 44, 46, 50, 56, 58, 61, 73, 80, 82, 84, 85, 87, 88, 90, 93, 94, 97, 99–101, 103, 104, 106, 110, 114, 115, 117, 126, 127, 129, 138, 142, 143, 148, 161, 174, 175, 178, 186, 200, 209, 233
Active acoustic phonon, 178
Active and passive techniques, 117
Active centers, 23, 56, 61, 82, 84, 104
Active compensation, 200
Active concentration, 16, 34, 38, 56, 88, 104, 127
Active electronic transition, 9
Active elements, 186
Active fiber, 29, 39, 41
Active glass, 30, 50, 115
Active ion, 2, 3, 7, 16, 17, 21, 24, 32, 34, 37–40, 50, 56, 87, 94, 99, 104, 106, 127, 161
Active laser medium, 85, 100, 110, 114, 127
Active layer, 144
Active level, 28
Active material, 175
Active media, 46, 73, 80, 99, 115
Active medium, 46, 85, 88, 90, 93, 94, 97, 100, 101, 110, 114, 127, 129
Active mode-locking, 117
Active modulation, 101, 110, 157
Active optical center, 21, 23
Active phonon, 27
Active Q-switching, 126
Active rare-earth, 23, 40
Active region, 138, 142, 143
Active transition, 7, 9, 58
Actively phase-locked, 200
Adiabatic, 151
Adiabatically, 151
Adiabaticity, 151
Adiabaticity criteria, 151
Air core, 223
Air holes, 219, 220
Air/solid structure, 73
Air-cladding, 222

V. Ter-Mikirtychev, *Fundamentals of Fiber Lasers and Fiber Amplifiers*, Springer Series in Optical Sciences 181, DOI: 10.1007/978-3-319-02338-0,

Air-fill, 223
Aluminum (Al), 33, 37, 38, 40, 119, 211
Amplification, 1, 37, 79, 80, 82–84, 87, 89, 108, 111, 135, 141, 170, 175, 187, 190, 210
Amplification and oscillation, 37, 79, 135
Amplification and pulse, 89, 109, 170, 210
Amplification and signal wave, 175
Amplification and spontaneous emission, 84
Amplification in double clad fiber, 108
Amplification in fiber amplifier, 210
Amplification of electromagnetic waves, 80
Amplification of light, 135
Amplification principle, 82
Amplification process, 83
Amplification stages, 89
Amplified spontaneous emission (ASE), 84, 85, 105, 108, 144
Amplifier, 191
Amplifier and Yb^{3+}, 191
Amplifier and Er^{3+}, 193
Amplifier and "chopped" seed, 89
Amplifier and Brillouin, 82
Amplifier and DC fiber, 191
Amplifier and fiber, 1, 4, 33, 41, 52, 53, 71, 82–89, 92, 108, 142, 148–150, 153, 164, 166, 169, 171, 172, 186, 187, 190, 191, 193, 194, 202, 203, 210, 219, 233, 234
Amplifier and gain, 83–85, 87, 88, 190
Amplifier and ideal, 85
Amplifier and large-mode-area, 170
Amplifier and laser, 23, 82, 83, 85, 88, 89, 151, 187
Amplifier and length, 49, 85, 88, 171, 190
Amplifier and level, 85
Amplifier and MOPA, 108, 187, 189–191, 193, 202, 209, 210
Amplifier and optical, 83, 83, 85, 86, 89
Amplifier and parametric, 82
Amplifier and power, 108, 130, 187, 190–193, 209
Amplifier and pre-amplifier, 191–193
Amplifier and pulse, 82
Amplifier and pulse propagation, 89, 157
Amplifier and Raman, 4
Amplifier and seeded, 82, 89, 193
Amplifier and solid-state laser, 88
Amplifier and square pulse seeded, 89
Amplifier and type, 88
Amplifier application, 147
Amplifier array, 187, 207
Amplifier chain, 194
Amplifier configuration, 130
Amplifier design, 166, 190
Amplifier energy level, 192
Amplifier FWHM gain bandwidth, 83
Amplifier gain, 83–85, 87, 88, 190
Amplifier gain coefficient, 83–85, 187, 190
Amplifier gain spectrum, 85
Amplifier gain volume, 88
Amplifier geometry, 186, 187
Amplifier inversion, 85
Amplifier loss, 84
Amplifier material, 83, 86, 89
Amplifier noise, 85, 190
Amplifier of electromagnetic oscillations, 79
Amplifier output, 202, 222
Amplifier phase, 85, 86
Amplifier phase shift, 85, 86
Amplifier power, 84
Amplifier pulsing, 86
Amplifier slope efficiency, 222
Amplifier system, 1, 5, 85, 86, 89, 108, 169, 172, 193, 233, 234
Amplifier technologies, 219
Analyzer, 152, 153, 201
Angle alignment, 73
Angle dependence, 199
Angle deviation, 199
Angle of diffraction, 120, 185
Angle of divergence, 73, 76, 195, 196
Angle of incidence, 120
Angle of tapering, 151
Angle of TIR, 65
Angle of total internal reflection, 185
Angle polished, 225
Angle selectivity, 198
Anomalous, 129
Anomalous behavior, 129
Anomalous single frequency, 129
Anti-stokes, 174, 175
APC
APC connector
APC polish
Aperture, 66, 84, 102, 147, 149, 151, 161, 196, 220
Aperture and beam, 196
Aperture and numerical, 219, 220
ASE and fighting, 85
ASE and measurable, 188
ASE and output, 84
ASE and propagating, 84, 85
ASE and spontaneous emission, 84, 85, 128
ASE and suppression, 193
ASE filter, 194

ASE free operation, 105, 187
ASE level, 108
ASE light, 84
ASE noise, 84
ASE photons, 84
ASE power, 84, 190
ASE power level, 190
ASE process, 85, 144
ASE source, 84
Askarian, 185
Astigmatic, 144, 146
Astigmatic nature, 146
Asymptotic, 105
Asymptotic value, 105
Atomic, 7, 10, 12, 79, 83, 86
Atomic chain, 10
Atomic decay, 11
Atomic distance, 7, 10
Atomic energy, 12
Atomic energy level, 12
Atomic line, 83
Atomic line shape, 83
Atomic mass, 83
Atomic masses, 10
Atomic nuclei, 7
Atomic response, 86
Atomic states, 80
Atomic structure, 29
Atomic system, 79
Atomic transition, 83, 86
ATR guides, 223
ATR type, 223, 224
Attenuation profile, 31
Available, 4, 5, 24, 29, 32, 41, 47, 52, 82, 102, 107, 133, 144, 150, 166, 175, 209, 216, 225
Available and commercially, 33, 52, 102, 107, 133, 139, 144, 147, 161, 209, 216, 225
Available CCD, 76
Available components, 5
Available fiber, 161, 209
Available laser diode, 24, 47
Available phonons, 28
Available solution, 4
Axial, 124, 126
Axial mode, 124, 126
Axial mode filter, 126

B

Backscattering, 178
Bandgap, 133, 135, 136, 138, 142, 228
Bandwidth, 23, 59, 68, 83, 110–112 , 114, 115, 123, 125, 126, 128, 157, 158, 176, 179, 205
Bandwidth and chirp, 158
Bandwidth and estimated, 123
Bandwidth and gain, 112
Bandwidth and spectral, 68, 83, 111, 126, 128, 157, 176, 179, 205
Bandwidth and time bandwidth product, 115
Bandwidth limited, 110
Bandwidth product, 111, 115
Beam, 3, 4, 56, 66, 73–77, 82, 88, 91, 102, 107, 109, 119–121, 124, 125, 127, 135, 138, 142, 144, 147–149, 151, 153, 155, 161, 162, 164, 165, 167, 169, 171, 175, 176, 180, 182, 183, 185–189, 191–198, 200–205
Beam and amplified, 88, 175, 202
Beam and amplifying, 82, 88
Beam and arbitrary, 74–76
Beam and astigmatic, 144
Beam and coherent, 162, 195, 196, 200–202, 205
Beam and collimated, 121, 203
Beam and co-propagation, 182
Beam and diffracted, 120, 198
Beam and diffraction limited, 4, 75, 102, 109, 161, 164, 188, 193, 210, 228, 230
Beam and electron, 135, 138
Beam and extraordinary, 153, 156
Beam and focal spot, 77, 214
Beam and Gaussian, 73–77, 214
Beam and gravity, 73, 74
Beam and guided, 216
Beam and incident, 198
Beam and individual, 205
Beam and intra-cavity beam combination, 201
Beam and laser, 73–75, 77, 82, 91, 107, 109, 119, 121, 127, 142, 147–149, 175, 187, 189, 195, 202, 203, 210–212, 214, 215, 225–229
Beam and light, 155, 180, 185
Beam and mirror-beam combination, 200
Beam and multiple, 182
Beam and non-gaussian, 74
Beam and optical, 82, 180, 218
Beam and original, 196, 205, 218
Beam and output, 121, 147, 192, 196, 202, 205, 210, 223, 225
Beam and polarized, 124, 188, 195
Beam and pumping, 138
Beam and rayleigh range, 76, 77, 214

Beam and real, 74
Beam and reference, 203
Beam and resultant, 196, 203, 205
Beam and spectral beam combination, 203
Beam and structure, 144
Beam and wavelength combining, 195, 196, 202
Beam aperture, 196
Beam brightness, 195, 196
Beam combining, 147, 162, 195–197, 200–202, 204, 205
Beam components, 153
Beam coupling, 167
Beam delivery, 147, 215, 216
Beam diameter, 75, 76, 77, 185, 215
Beam divergence, 73, 75, 76
Beam dump, 151
Beam expander, 225
Beam focus, 76, 225
Beam intensity, 73, 74, 186
Beam interaction, 212–215
Beam management, 147
Beam material interaction, 214
Beam overlap, 3
Beam parameter, 73, 74
Beam pass, 153, 204
Beam position, 225
Beam profile, 171
Beam propagating axis, 76
Beam propagation, 73, 186
Beam propagation line, 73
Beam quality, 3, 4, 66, 73, 75, 76, 102, 109, 125, 161, 162, 164, 171, 188, 189, 191, 193–195, 201, 203, 205, 210, 214–216, 219, 222, 228–230
Beam radius, 73
Beam scattering, 225
Beam shape, 144
Beam size, 77
Beam splitter, 149, 195, 196, 203
Beam splitting device, 155
Beam spot size, 73
Beam transformation, 148
Beam waist, 73, 74, 76, 77, 91
Beam wavefront, 73
Beam width, 74
Birefringence, 71, 118
Birefringence plate, 118
Birefringency, 71, 118
Blackbody radiation, 12
Boltzmann, 11, 12, 79, 80
Boltzmann constant, 11
Boltzmann distribution, 79, 80
Boltzmann distribution formula, 79
Boltzmann statistics, 11, 12
Borate, 19, 30, 32, 33, 49
Bragg, 93, 127–129, 142, 143, 152, 156–158, 191, 196–200, 203, 204, 215
Bragg angle, 199
Bragg condition, 198, 199
Bragg diffraction, 197
Bragg grating, 93, 127–129, 152, 156, 158, 191, 196, 197, 199, 200, 203, 204
Bragg matching, 198
Bragg reflection, 127
Bragg reflector, 142, 143
Bragg wavelength, 157, 198, 204
Brewster, 122–124
Brewster angle, 122–124
Brewster condition, 122
Brillouin, 10, 82, 102, 108, 161, 174, 177–179
Brillouin amplifier, 82
Brillouin angle, 199
Brillouin gain, 178, 179
Brillouin gain spectra, 178, 179
Brillouin line-width, 178
Brillouin scattering, 10, 102, 108, 161, 177, 179, 216
Broadening, 13, 14, 16, 17, 68, 71, 80, 82, 87, 97, 107, 109, 181, 182, 183
Broadening and homogeneously broadening, 97
Broadening and inhomogeneously broadening, 14–17, 89, 97, 112
Broadening and line broadening, 13, 14, 80, 109
Broadening and spectral broadening, 87, 181–183
BRT
Bulk damage, 107, 108, 122, 186, 230
Bulk minority diffusion coefficient, 138

C

Carrier, 27, 133–136, 138, 181
Carrier density, 27
Cavity, 34, 90, 93–98, 102–104, 106, 107, 109, 111–114, 116, 117, 121, 124, 126–129, 140–144, 148, 186, 188, 189, 205
Cavity and intra-cavity, 84, 93–96, 100, 101, 103, 104, 108–113, 117, 118, 120–128, 187, 190, 200, 201, 205, 229
Cavity and intra-cavity component, 93, 95, 101
Cavity and intra-cavity device, 108, 110
Cavity and intra-cavity loss, 84, 93, 103, 120–122, 125
Cavity and intra-cavity medium, 104
Cavity and intra-cavity refractive index, 104

Cavity and laser, 90, 94–97, 102–107, 109, 111–114, 116, 117, 121, 124–129, 140, 141, 144, 148, 152, 186, 189, 205
Cavity and linear laser cavity, 95, 189
Cavity and optical cavity, 93, 142, 143
Cavity and ring laser cavity, 97
Cavity and short cavity, 34
Cavity components, 93, 101
Cavity gain, 93, 97
Cavity geometrical parameters, 116
Cavity length, 116
Cavity lifetime, 112
Cavity loss, 126
Cavity mirror, 95, 104, 109, 111, 113, 125, 128, 140, 152
Cavity mode, 97, 126
Cavity mode separation, 126
Cavity Q factor, 103
Cavity Q-switching, 102
Cavity reflectors, 94
Cavity resonance frequency, 97
Cavity roundtrip, 94, 97, 107, 113, 114, 116
Cavity roundtrip time, 107, 116
Cavity transmission, 95
CFBG, 157, 191
Chalcogenide, 32, 33, 37
Chirp, 116, 130, 157, 158, 181–183, 191
Chirp and frequency, 183
Chirp and induced, 181
Chirp and un-chirped, 182
Chirp band-width, 158
Chirp free, 130
Chirped FBG, 157
Chirped fiber Bragg grating, 158, 191
Chirped pulse, 116
Chromatic dispersion, 68–71
Circular, 72, 73, 148
Circular and non-circular cladding profile, 72
Circular core, 72
Circular geometry, 148
Circular optical fiber, 73
Cleaved, 140, 141
Coherence, 202, 205
Coherence and optical, 202
Coherence length, 205
Coherence tomography
Coherent, 56, 74, 84, 127, 162, 175, 195, 196, 200–203, 205, 218
Coherent addition, 203, 205
Coherent and incoherent, 74, 84
Coherent and partially coherent, 74
Coherent array, 201
Coherent beam, 162, 195, 196, 200–202, 205
Coherent beam combining, 162, 195, 196, 200, 201, 205
Coherent bundle, 218
Coherent combination, 203
Coherent coupling, 200
Coherent emission, 56, 175, 200
Coherent fiber laser radiation, 200
Coherent laser coupling, 200
Coherent radiation, 200
Coherent Raman wave, 175
Coherent UV laser beam, 228
Coherently coupled, 200
Coiling, 2, 4, 161, 171
Coiling technology, 2, 161
Collimated, 121, 154, 201, 203
Collimated beam, 121
Collimated output, 154
Collimated port, 121
Complex, 68, 100, 106, 110, 140, 190, 200, 201, 212, 215
Complex combination, 110
Complex exponential form, 68
Complex heterostructures, 140
Complex laser resonator, 200
Complex mirror, 201
Complex opto-mechanics, 215
Complex value, 212
Complexity, 190
Conduction band, 133–136
Confined, 84, 141
Continuous, 4, 30, 99, 101, 117, 139, 161, 176, 178, 209, 213
Continuous laser, 213
Continuous pumping, 101
Continuous transparency, 30
Continuous-wave, 99, 139, 161, 176, 178, 209
Conversion efficiency, 2, 57, 145
Cooling, 29, 126, 145, 212
Cooling configuration, 145
Cooling rate, 29
Cooling time, 212
Coordinates, 74
Coupled, 2, 3, 23, 24, 56, 67, 72, 76, 82, 97, 102, 121, 122, 128, 141, 142, 147–150, 163, 164, 190, 191, 193, 195, 198, 200, 202, 203, 219, 222, 224, 225
Coupled and fiber coupled, 2, 23, 56, 102, 148–150, 152, 154–156, 159, 168, 169, 190, 195, 219

Coupled and fiber coupled circulator, 155, 156
Coupled and fiber coupled components, 167
Coupled and fiber coupled device, 142, 150
Coupled and fiber coupled diode laser, 148–150, 159
Coupled and fiber coupled optical isolator, 152, 154
Coupled and fiber coupled power splitter, 150
Coupled and fiber coupled pump combiner, 150
Coupled and fiber coupled seed laser, 150
Coupled and fiber coupled WDM component, 168
Coupled and power coupled, 3
Coupled diode, 2, 56, 148–150, 159
Coupled into the fiber, 67, 72, 225
Coupled laser source, 219
Coupled mode theory, 156
Coupled pump radiation, 56
CPM
Critical, 28, 38, 65, 67, 73, 87, 107, 147, 171, 175, 176, 178, 185, 186
Critical angle, 65, 67
Critical power, 175, 176, 178, 185, 186
Critical pump, 87
Cross phase modulation, 101, 162, 182
Cross relaxation, 59–61, 89
Cross saturation, 95
Cross section, 17–24, 47, 54–56, 59, 87, 99, 104, 168, 184, 218, 220
Cross talk, 199
Cross-coupling, 72
Crystal fiber, 2, 4, 38, 73, 203, 219, 221, 222
Crystalline quartz, 124
Cut-off, 30, 31, 66, 67, 220

D

Damage, 33, 57, 101, 102, 107, 108, 145, 148, 149, 159, 161, 162, 169, 186, 190, 200, 216, 225, 230, 233
Damage free, 86, 87, 107, 108, 162, 224
Damage issues, 233
Damage mechanism, 89
Damage pattern, 107, 108
Damage problem, 106–108
Damage process, 86
Damage threshold, 33, 100, 107, 108, 118, 122, 161, 170, 216, 218, 230
Decay, 11, 14–16, 28, 80
Decay and luminescence decay, 16
Decay and measured decay, 15
Decay and non-radiative decay, 27, 28, 80
Decay and radiative decay, 14
Decay and room temperature decay, 16
Decay and spontaneous decay, 11, 14, 19, 80, 81, 105
Decay time, 15, 27
Degeneracy, 12, 21, 43, 71, 104, 129, 135, 184
Degeneracy and electron degeneracy, 135
Degeneracy breaks, 71
Degeneracy factors, 129, 184
Degeneracy terms, 12, 21
Density of population, 11, 90
Diagram and b-V diagram, 67
Diagram and energy band diagram, 137
Diagram and energy level diagram, 7, 45, 46, 49, 50, 53, 58, 80, 81
Diagram and franck-condon diagram, 7–9
Diagram of embedded mirror, 168
Dichroic mirror, 121–123, 125, 129, 149, 196
Dielectric film, 223
Dielectric imperfections, 221
Dielectric materials, 107, 223
Dielectric medium, 180
Dielectric mirrors, 144
Dielectric reflective diffraction grating, 204
Dielectric solids, 107
Dielectric waveguide, 65
Diffraction, 118, 120, 142, 185
Diffraction angle, 151
Diffraction effect, 73
Diffraction efficiency, 197–199
Diffraction grating, 118–122, 142, 157, 188, 196, 197, 201–204
Diffraction limited, 4, 73, 75–77, 99, 102, 107, 109, 142, 145, 161, 164, 170–172, 188, 192, 193, 195, 210, 214, 222, 228, 230
Diffraction of light, 210
Diffraction order, 109, 120, 121
Diffusion, 133, 138, 150, 211, 213
Diffusion coefficient, 138
Diffusion length, 138, 211
Diode array, 101, 145
Diode emitting area, 142
Diode emitting surface, 143
Diode laser, 1, 3, 4, 23, 25, 56, 57, 61, 101, 102, 129, 133, 135, 139–150, 159, 161, 163, 169, 187, 192, 193, 196, 197, 200, 209, 210, 222, 229
Diode laser and fiber coupled, 2, 23, 56, 102, 141, 148–150, 159, 167, 187, 193
Diode laser bar, 145–147, 149
Diode laser beam, 147–149
Diode laser emission, 147, 148
Diode laser maintenance, 148

Diode laser power, 144, 145, 192
Diode laser stack, 147–148
Diode laser structure, 140, 142, 143
Diode pumped, 1, 2, 48, 101, 129, 190, 196, 209, 222
Dipole oscillator, 18
Dipole transition, 18
Dirac formula and Fermi-Dirac formula, 134
Dirac probability and Fermi-Dirac probability, 134, 135
Dirac statistics and Fermi-Dirac statistics, 133
Dirac's constant, 27
Disk, 140, 229
Disk area, 229
Disk lasers, 229
Dispersion, 10, 68–71, 110, 117–120, 122, 123, 158, 173, 183, 184, 220
Dispersion and angular dispersion, 120
Dispersion and chromatic dispersion, 68–71
Dispersion and FBG dispersion, 158
Dispersion and fiber dispersion, 68–71
Dispersion and full dispersion, 123
Dispersion and grating dispersion, 158
Dispersion and group velocity dispersion, 118
Dispersion and intra-cavity dispersion, 117
Dispersion and light dispersion, 68
Dispersion and material dispersion, 184
Dispersion and modal dispersion, 68
Dispersion and phonon dispersion, 10
Dispersion and polarization mode dispersion, 71
Dispersion and waveguide dispersion, 70
Dispersion and zero dispersion, 71, 183
Dispersion compensation, 110, 118
Dispersion condition, 183
Dispersion dependence, 183
Dispersion prism, 122
Dispersion trend, 220
Dispersion-flattened, 173
Dispersion-shifted, 173
Dispersive, 118, 122, 123, 126, 200
Dispersive element, 118, 123
Dispersive intra-cavity laser element, 122
Dispersive resonator, 122
Dispersive system, 118
Distributed Bragg, 142–143
Distributed Bragg reflector (DBR), 129, 142–143
Distributed feedback (DFB), 34, 128–130, 142, 143, 149, 153
DND, 40, 42, 87
Dopant, 30, 37–40, 135
Dopant concentration, 3, 16, 24, 136, 137

E

Efficiency, 2, 24, 32, 35, 56, 57, 61, 83, 88, 91, 92, 97, 147, 149, 161, 162, 184, 197, 201, 209, 222, 233
Efficiency and combining efficiency, 203
Efficiency and conversion efficiency, 2, 57, 145
Efficiency and coupling efficiency, 147, 148, 161, 219, 225
Efficiency and diffraction efficiency, 197, 199
Efficiency and energy efficiency, 25
Efficiency and energy extraction efficiency, 83
Efficiency and FWM efficiency, 184
Efficiency and laser efficiency, 28, 32, 56, 90, 161
Efficiency and optical efficiency, 25, 57
Efficiency and overall efficiency, 83
Efficiency and pump efficiency, 93
Efficiency and quantum efficiency, 61, 88, 98
Efficiency and slope efficiency, 25, 35, 92, 96, 188, 194
Efficiency and storage efficiency, 93
Efficiency and transmission efficiency
Efficiency and wall plug efficiency, 209, 233
Einstein, 11–13, 15
Einstein A coefficient, 15, 21
Einstein B coefficient, 12
Einstein coefficient, 11, 13
Einstein analysis, 22
Einstein relations, 13, 19
Electro-magnetic energy, 65
Electron, 7, 9, 13, 18, 28, 44, 133, 135, 136, 138, 202
Electron beam, 135, 138
Electron concentration, 133
Electron degeneracy, 135
Electron exchange, 16
Electron levels, 8
Electron mass, 18
Electron microscope, 220
Electron penetration depth, 138
Electron shell, 13, 44
Electron transition, 8, 133
Electron–hole pair, 133
Electron–hole recombination, 133
Electronic level, 7, 9, 14
Electronic shell, 9
Electronic state, 7, 14
Electronic structure, 18, 20
Electronic transition, 9, 13
Electron–phonon, 9, 13, 28
Electro-optic, 117
Electro-optical modulator, 117

Energy, 3, 7, 10, 11, 12, 16, 18, 24, 25, 32, 35, 44, 46, 53, 59, 79, 90, 95, 104, 107, 133, 135, 136, 171, 177, 218
Energy and propagating, 31, 56, 67, 70, 75, 82, 96, 101
Energy band, 133
Energy band diagram, 137
Energy barrier, 136–138
Energy density, 11, 12, 212
Energy dissipation, 8
Energy exchange, 8
Energy fluence, 107, 218
Energy gap, 16, 27, 28, 135
Energy level, 3, 7, 10, 14, 17, 20, 28, 44, 46, 49, 53, 59, 79, 80, 82, 87, 89, 93, 96, 134, 136
Energy spectral density, 12
Energy states, 10
Energy storage, 99
Energy transfer, 3, 24, 56, 65, 89
Energy transmission, 218
End face, 35, 141, 159, 161, 167
Entropy, 80
Erbium, 53
Erbium-doped, 201
Excitation energy, 8, 20, 89
External cavity, 189
External force, 200
External light, 11
External photon, 11
External polymer, 3
External resonator, 200
Extraction energy, 83, 133

F

Fabry-Perot, 111, 118, 125, 126, 141, 175
Faraday garnet crystal, 156
Faraday isolator, 169
Faraday rotator, 152, 153, 155, 156
FBG, 127, 128, 152, 156, 158, 203
Feedback, 34, 82, 109, 120, 122, 142, 149, 202
Feedback mirror, 122
Fermi energy, 134, 135
Fiber, 3, 23, 28, 30, 33, 37, 39, 41, 44, 50, 53, 56, 57, 62, 66, 68, 71, 75, 82, 84, 87, 92, 99, 108, 141, 151, 155, 162, 166, 171, 180, 201, 215, 216, 218, 219, 224, 229, 233
Fiber absorption, 51, 172
Fiber amplifier, 1, 4, 52, 53, 71, 82, 85, 89, 108, 149, 164, 172, 193, 219, 233
Fiber attenuation, 30
Fiber Bragg grating, 127, 152, 191
Fiber bundle, 216, 217, 218
Fiber cladding, 32, 38, 165, 219, 220, 222
Fiber coiled, 31
Fiber communication, 165
Fiber component, 168, 225
Fiber core, 3, 38, 39, 42, 107, 149, 151, 156, 162, 164, 171, 173, 190, 222
Fiber coupled, 2, 23, 56, 102, 141, 148, 152, 155, 167, 193
Fiber design, 31, 190
Fiber diameter, 107, 149
Fiber dispersion, 68
Fiber entrance, 70, 148, 225
Fiber fabrication, 1, 39
Fiber geometry, 38
Fiber glass, 28, 31, 101, 186
Fiber inspection, 31
Fiber laser, 1–5, 13, 32, 34, 37, 42, 49, 53, 56, 72, 80, 86, 92, 99, 101, 108, 118, 128, 141, 154, 162, 167, 185, 192, 197, 209, 215, 224, 230, 233
Fiber laser resonator, 93, 118, 233
Fiber length, 3, 23, 24, 56, 88, 98, 162, 182
Fiber manufacturing, 2, 40, 51, 61
Fiber materials, 35, 55
Fiber mode, 32, 65, 69, 72, 157, 172
Fiber mode structure, 32
Fiber numerical aperture, 67
Fiber parameters, 66, 162
Fiber perform, 164
Fiber preparation, 2
Fiber production, 40
Fiber pumping, 163
Fiber refractive index, 30, 172
Fiber samples, 35
Fiber spliced, 32
Fiber structure, 2, 31, 39, 72
Fiber technology, 2, 4, 167, 169, 209
Fiber theory, 66
Fiber type, 33, 38, 72, 150, 216
Fiber waveguide, 37
Fiber-to-air interface, 159
Fluorozirconate, 34, 35
Franck–Condon diagram, 7, 9
Franck–Condon principle, 7
Free energy, 20
Free-space, 74, 85, 86, 149, 167, 187, 190, 195, 215, 225
Free spectral range, 126
Frequency, 4, 11, 14, 18, 22, 66, 69, 83, 87, 110, 114, 126, 129, 170, 177, 190, 203
Frequency conversion, 49, 118, 187, 190, 230
Frit, 40
Free spectral range (FSR), 126, 127

Furnace, 39
FWHM, 15, 17, 83, 145

G
Ga, 139
Gain, 23, 25, 27, 40, 44, 59, 80, 84, 86, 93, 109, 110, 138, 175
Gain band, 51, 97, 109, 112, 125, 126
Gain bandwidth, 23, 83, 111, 112, 114, 125
Gain coefficient, 83, 86–88, 94, 180
Gain equalizer, 83
Gain fiber, 1–4, 23, 29, 41, 44, 49, 51, 52, 72, 82, 84, 88, 93, 102, 107, 128, 152, 162, 165, 170, 184, 193
Gain length, 53
Gain material, 32, 99, 102, 141, 159
Gain medium, 27, 83, 86, 88, 93, 99, 103, 104, 125, 126, 142, 164
Gain performance, 41
Gain reduction, 83
Gain saturation, 61, 83
Gaussian beam, 73–77, 214
Gaussian envelope, 15
Gaussian function, 173, 181
Gaussian line, 16
Gaussian mode, 73
Gaussian parameter, 116
Gaussian profile, 214
Gaussian pulse, 111, 114, 130, 181, 182
Gaussian shaped, 115, 158
Gaussian spot size, 74
Ge, 30, 38, 176
Germanate, 19, 28, 32, 50, 51, 60
Germanium, 32
Germanium chloride, 37
Giant pulse, 103
Glass, 2, 9, 9, 14, 16, 22, 27, 30, 35, 44, 173, 180, 200, 220, 223, 225
Glass attenuation, 30
Glass composition, 27, 30, 34, 180
Glass damage, 118
Glass environment, 19
Glass fiber, 35, 180, 217, 241
Glass host, 17, 18, 24, 53, 54, 58, 89
Glass layer, 37, 167
Glass liquid, 29
Glass manufacturing, 29
Glass mass, 220
Glass material, 30, 44, 101, 212
Glass matrix, 17, 19, 29, 32–34, 51
Glass modifier, 33
Glass molecules, 27
Glass perform
Glass refractive index, 173
Glass rod, 38, 40
Glass slab, 147
Glass structure, 9, 27, 29
Glass surface, 35, 225
Glass system, 32, 34, 58
Glass transition, 29
Glass tube, 37, 38
Glass tubing, 223, 224
Glass types, 32, 35, 51
Glass waveguide, 224

H
Half-wave plate, 156
Harmonic generation, 190
Heat, 8, 25, 40, 56, 57, 145, 149, 211, 225, 227
Heat delivery, 213
Heat diffusion, 211
Heat dissipation, 101, 148, 211, 224, 227
Heat load, 145
Heat management, 167
Heat removal, 145, 147
Heat sink, 147, 152
Heat source, 226
Heat transfer, 213
Heat treating, 227
Hole, 94, 97, 134, 135, 220, 226
Hole burning, 94, 97
Hole diameter, 220, 221, 226
Hole dimension, 226
Hole drilling, 214
Hole movement, 136
Hole size, 226
Holley fiber, 219
Hollow fiber, 216, 222, 223
Homogeneous, 13, 14, 17, 111, 176
Homogeneous broadening, 14–16
Homogeneous line-width, 17
Homogeneous nature, 109
Homogeneous width, 176
Host environment, 13
Host glass, 35
Host material, 8, 9, 11, 13, 16, 17, 18, 21, 27, 28, 43, 44
Huang-Rhys factor, 9
Huang-Rhys parameter, 28

I
Inhomogeneous, 109
Inhomogeneous broadening, 14, 16, 17
Inhomogeneous line-width, 17
Inhomogeneous nature, 109

Injection, 70, 126, 135, 138, 217
Injection lasers, 139, 142
Injection locking, 200
Injection of carriers, 135
Injection seeding, 126
Injection type, 138
Injection-lock, 111
Inorganic glass, 197
Intensity, 23, 32, 59, 66, 73, 74, 83, 87, 88, 103, 105, 108, 115, 171, 172, 180–182, 186, 198, 214, 215, 218, 228
Interface, 31, 139, 159, 225
Interferometer, 111
Intra-cavity, 84, 93, 94–96, 100, 101, 103, 108–113, 117, 118, 120, 121–128, 187, 190, 200, 201, 205, 229
Intra-cavity axial mode filter, 126
Intra-cavity beam combination, 201
Intra-cavity component, 93, 95, 101
Intra-cavity device, 108, 110
Intra-cavity dispersion compensating device, 117
Intra-cavity electric field, 112, 113
Intra-cavity etalon, 118
Intra-cavity Fabry-Perot etalon, 126
Intra-cavity fiber, 118, 121
Intra-cavity fiber circulator, 121
Intra-cavity intensity modulator, 117, 118
Intra-cavity laser beam, 109, 121
Intra-cavity laser field, 94, 190
Intra-cavity laser pulse, 110
Intra-cavity light, 96, 229
Intra-cavity light fluence, 229
Intra-cavity loss, 84, 93, 103, 120–122, 125, 126
Intra-cavity loss distribution, 125
Intra-cavity medium, 104
Intra-cavity nonlinear frequency conversion, 190
Intra-cavity optical harmonic generation, 190
Intra-cavity optical modulator, 111
Intra-cavity optical power, 187
Intra-cavity prism, 123
Intra-cavity refractive index, 104
Intra-cavity tuning element, 122
Intra-cavity wavelength dispersive system, 118
Intra-cavity wavelength filter, 123
Intra-cavity wavelength selective element, 124
Inversion, 52, 84–86, 88, 91, 97, 103, 109
Inversion population, 51, 80, 81, 84, 103, 105, 108, 135
Isolator, 102, 155

J

Judd-Ofelt, 18, 19, 48, 59
Judd-Ofelt coefficients, 18
Judd-Ofelt parameters, 18, 48, 59
Judd-Ofelt theory, 18, 19
Junction, 135–138, 141–145

K

Kerr effect, 101, 180
Kerr lens, 117
Kerr nonlinearity, 181
Krishnan, 174

L

Landsberg, 174
Lanthanides, 13
Laser, 2–5, 13, 19, 23, 24, 28, 35, 44, 50, 56, 73, 80, 86, 90, 94, 97, 100, 107, 117, 121, 127, 144, 150, 156, 170, 175, 190, 192
Laser action, 1, 3, 44, 45, 50, 59, 60, 80, 103, 133, 135
Laser active, 2, 9, 21, 23, 24, 25, 28, 29, 32, 34, 37–40, 50, 56, 58, 82, 84, 85, 87, 88, 94, 100, 104, 110, 114, 115, 127, 139, 144, 186, 209
Laser active media, 1
Laser amplifier, 82, 83, 85, 86
Laser applications, 28, 32, 33–35, 37, 48, 72, 73, 80, 124, 147, 159, 196, 213, 228, 231
Laser average power, 101, 106, 213
Laser beam, 73–75, 82, 91, 107, 109, 121, 142, 147–149, 187, 189, 195, 202, 210–212, 214, 215, 225–228
Laser cavity, 90, 94, 95, 102–104, 106, 107, 111–114, 116, 117, 121, 124–129, 140, 141, 144, 148, 152, 186, 205
Laser center, 24
Laser challenges, 49, 51, 56, 59
Laser class, 101
Laser components, 94, 100, 102
Laser concepts, 230
Laser crystals, 1, 49
Laser damage, 106
Laser design, 4, 29, 99, 151, 167, 186, 190, 233
Laser diode, 2, 3, 24, 35, 47, 50, 55, 56, 60, 101, 102, 133, 141, 142, 144, 148, 191, 209, 234

Laser efficiency, 28, 32, 56, 57, 90, 161
Laser emission, 4, 103, 104, 111, 123, 147, 148, 200, 201, 224
Laser energy, 3, 171, 213
Laser excitation, 81, 82
Laser frequency, 87, 129
Laser gain, 13, 72, 94, 97, 99, 100, 110, 111, 115, 125, 126, 233
Laser glass, 3, 24, 25, 27, 30, 44, 50, 109
Laser glass host, 24
Laser host, 16
Laser intensity, 114
Laser level, 44, 81, 85, 90, 96, 104, 106
Laser line, 14, 59, 107, 121, 128
Laser manufacturers, 57
Laser master oscillator, 89
Laser material, 13, 28, 30, 110, 115, 139, 190, 210, 211–214, 223, 225, 227–229, 231
Laser mode, 97, 110, 111, 115, 116, 124
Laser mode-locking, 110
Laser operation, 23, 35, 49, 51, 52, 57, 79–82, 87, 93, 97, 100, 101, 110, 118, 125, 126, 128, 138, 162, 213, 226, 227
Laser oscillation, 1, 88, 110, 112, 115
Laser oscillator, 73, 82, 90, 108, 110, 186–188, 190
Laser output, 90, 96, 98, 106, 107, 118, 121, 128, 129, 149, 190, 216, 224, 225
Laser parameters, 93, 94, 100, 109, 115, 149, 186, 187, 189, 190, 195, 212, 213, 234
Laser performance, 106, 159, 188
Laser photons, 92
Laser physics, 1, 5, 13, 17, 21, 29, 79, 80, 82, 117, 175, 187
Laser power, 57, 97, 102, 106, 129, 144, 145, 161, 179, 187, 189, 190, 192, 210, 213, 225, 226, 233
Laser pulse, 100, 101, 105, 107, 108–111, 115–117, 157, 158, 181, 192, 211, 213, 225
Laser pulse-width, 115
Laser pump, 23, 161
Laser pumping, 56, 148, 163
Laser Q-switched, 103
Laser radiation, 87, 163, 164, 170, 186, 200
Laser regime, 14
Laser resonator, 73, 82, 93, 94, 97, 102–104, 110, 112, 115, 117, 118, 120, 121, 123–127, 141, 143–145, 152, 200, 205, 230, 233
Laser signal, 86, 177, 193
Laser slope efficiency, 92, 96, 97
Laser sources, 53, 195, 209, 213, 219, 228, 230
Laser spectral line-width, 205
Laser threshold, 80, 81, 90, 93, 95, 106, 141
Laser transitions, 16, 23, 46, 50, 53, 58
Laser upper level, 47
Laser wavelength, 23, 87, 102, 104, 143, 178, 209, 211, 212, 215, 228, 230
Leakage losses, 31
Leaky guides, 223
Leaky type
Lifetime, 11, 14, 15, 16, 19, 21, 22, 50, 59, 87, 95, 96, 104, 106, 112, 138, 178, 179
Lifetime measured, 20, 47
Light, 4, 7, 11, 24, 30, 35, 51, 65, 67, 68, 72, 81, 82, 83, 88, 94, 97, 113, 122, 127, 128, 134, 138, 141, 144, 148, 150, 151, 152, 153, 155, 163, 164, 165, 174, 177, 183, 210, 211, 218, 225
Light absorption, 210, 211, 228
Light beam, 155, 180, 185
Light dispersion, 68
Light emission, 11
Light fluence, 229
Light injection, 217
Light intensity, 88, 144
Light path, 94
Light penetration, 211
Light photon, 11
Light polarization, 72, 153, 155
Light propagation, 4, 30, 65, 155, 156, 164, 172, 177
Light pulse, 68
Light quantum, 11
Light ray, 68
Light spectral properties, 68
Light speed, 68
Light strippers, 151
Light wavelength, 71, 142
Light waves, 94, 127, 170
Line, 9, 10, 12–14, 16, 23, 48, 54, 59, 67, 71, 72, 80, 107, 109, 112, 142, 173, 179, 200, 230
Line broadening, 13, 14, 80, 109
Line envelope, 112
Line limit, 130
Line profile, 12, 16
Line shape, 13, 14, 16, 17, 83
Line spectral profile, 15
Linear, 10, 93–96, 116, 124, 145, 173, 185, 195
Linear array, 145
Linear cavity, 96, 189
Linear diatomic chain structure, 10
Linear laser cavity, 95, 189
Linear laser resonator, 94
Linear refractive index, 173, 185

Line-width, 56, 110, 121, 123, 128, 129, 130, 161, 173, 176–179, 187, 192, 194, 203, 205
Logarithmic, 104
Logarithmic loss, 104
Logarithmic output, 104
Longitudinal, 97, 101, 110, 111, 112, 114, 115, 124, 125, 126, 127, 128
Longitudinal mode, 97, 110, 115, 124, 125, 126, 127, 128, 142
Longitudinal non-uniformities
Longitudinally pumped, 90
Lorentzian, 14, 15, 17, 83, 86, 89, 91
Lorentzian function, 14
Loss, 2, 4, 31, 32, 33, 34, 40, 71, 87, 88, 93, 97, 103, 104, 121, 122, 123, 125, 153, 169, 171, 184, 221, 223
Loss attenuation coefficient, 171
Loss coefficient, 83, 93, 184
Loss dependence, 171
Loss distribution, 125
Loss free propagation, 151
Loss limited, 71
Loss mechanism, 87
Loss nature, 223
Loss parameters, 34
Loss peak, 38
Loss sensitivity, 31
Loss spectral distribution, 123
Luminescence quantum yield, 15, 16, 34
Luminescence transition, 8
Lyot Filter, 123, 124, 125

M

Macro bending, 31, 221
Majority carriers, 135, 136
Mandelstam, 174, 177
Manifold, 19, 20, 43, 50
MCVD, 2, 35, 37, 38, 40, 41, 87
Mechanical strength, 30, 34
Metal alloy, 227
Metal deposition, 227
Metal particles, 159
Metal powder, 227
Metal reflectivity, 226
Metal surface, 229
Metal welding, 211, 230
Metastable, 24, 95
Mettalic film, 223
Microbending, 31, 221
Microchip laser, 127, 190
Minority carrier recombination time, 138
Minority carriers, 136
Mirror, 91, 95, 104, 109, 110, 111, 117, 121, 122, 125, 127, 128, 143, 144, 149, 152, 168, 200, 201
Mirror reflectivity, 95, 144
Mirror side pumping, 168
Mirror surface, 144
Mirror-beam combiner, 200
Mode, 3, 4, 10, 11, 23, 24, 32, 42, 56, 65, 66, 67, 69–71, 73, 94, 97, 100, 101, 103, 107, 109–111, 112, 114–117, 119, 124, 125, 127, 141, 145, 150, 154, 157, 170, 171, 173, 177, 188, 213, 219, 221
Mode adaptation, 150
Mode amplitude, 110, 111, 172
Mode area, 42, 85, 154, 191
Mode competition, 112
Mode cut-off, 66
Mode discrimination, 161
Mode discriminator, 126
Mode distance, 115
Mode field, 32, 66, 111, 150, 216
Mode field adaptor, 150, 151
Mode field amplitude, 111
Mode field radii, 32
Mode field radius, 32
Mode field diameter, 32, 66, 173
Mode filtering, 4
Mode frequency, 111
Mode index, 125
Mode intensity, 32, 66
Mode interaction, 112
Mode loss, 171
Mode matching, 151
Mode mixing, 171
Mode nature, 97
Mode notation, 125
Mode oscillation, 94, 112
Mode phases, 112
Mode power, 69, 157
Mode propagation constant, 66, 67
Mode selection, 126
Mode separation, 126
Mode size, 107
Mode spacing, 126
Mode spectral width, 69, 70, 110
Mode structure, 124, 148
Mode theory, 156
Mode transformation, 151
Mode-lock, 100, 110, 116, 117
Mode-locking, 86, 109, 110, 115, 117
MOPA, 108, 127, 187, 189, 190, 191, 192, 193, 194, 201, 202, 209, 210
Multimode, 4, 38, 56, 76, 109, 142, 144, 145, 148, 149, 162, 165, 171, 172, 219, 221

Multimode beam, 75, 77
Multimode conditions, 221
Multimode dimension, 144
Multimode diode, 56, 149
Multimode emitter, 145
Multimode fiber, 109, 172, 219
Multimode gain fiber, 4
Multimode inner cladding, 163
Multimode operation, 145, 162
Multimode pump, 163
Multi-phonon, 28, 33, 58
Multiplexer, 194, 201
Multi-spectral, 83, 94

N

Nanoparticle, 40, 42
Nanoparticle deposition, 40
Nd, 22, 29, 46, 47, 49, 127, 137, 209, 218
Neodymium, 37, 45, 209
Neodymium laser, 209
Neodymium-doped, 22, 33, 47, 49
Nonlinear, 3, 4, 10, 29, 34, 49, 86, 99, 101, 112, 128, 162, 165, 172, 180, 183, 186, 205, 216, 233
Nonlinear absorption, 8
Nonlinear dynamics, 86
Nonlinear effects, 161
Nonlinear fiber length, 182
Nonlinear frequency conversion, 49, 190, 205, 230
Nonlinear interaction, 184
Nonlinear interaction constant, 184
Nonlinear optical processes, 205
Nonlinear optical response, 180, 185
Nonlinear optics, 128
Nonlinear parameter, 182
Nonlinear phase modulation, 180
Nonlinear power dependence, 172
Nonlinear process, 99, 101, 162, 163, 172, 174, 183, 190
Nonlinear refractive index, 34, 173, 180, 184, 185
Nonlinear scattering, 10, 56, 87, 101, 172
Nonlinear waveguide, 185
Non-radiative relaxation, 80
Non-radiative transition, 80
n-type, 136, 137, 141

O

Optical, 2, 7, 9, 10, 14, 27, 72, 82, 106, 110, 142, 145, 149, 152, 175, 178, 203, 216, 225
Optical absorption, 57, 167, 211
Optical amplification, 37, 83
Optical amplifier, 82, 83, 85, 86, 89
Optical axis, 123, 124
Optical back reflection, 159
Optical beam, 82, 180, 218
Optical breakdown, 107
Optical brightness, 149
Optical cavity, 93, 142, 143
Optical center, 7, 9, 10, 13–15, 17, 21, 23, 28, 87, 97, 133
Optical circulator, 155–157
Optical coherence, 202
Optical communication, 33, 37, 38, 53, 71, 128
Optical components, 93, 149, 190, 195, 233
Optical connection loss, 30, 32
Optical constants, 10
Optical contact, 86, 149
Optical conversion efficiency, 145
Optical couplers, 219
Optical damage, 149, 162, 169, 170, 190, 200, 216, 223, 225, 233
Optical efficiency, 25, 57
Optical excitation, 23, 56, 133
Optical feedback, 142, 149
Optical fiber, 1, 2, 4, 29, 30, 33, 37, 39, 66, 68, 70, 72, 75, 82, 85, 148, 156, 164, 170–172, 175, 185, 209, 216, 219, 222
Optical fiber amplifier, 82, 83, 85
Optical fiber communication, 165
Optical filter, 142, 149, 156
Optical frequency, 86
Optical gain, 37, 80, 86, 194
Optical glass, 167
Optical guide, 215
Optical isolator, 97, 142, 149, 152–155, 225
Optical Kerr effect, 101, 180
Optical loss, 2, 110
Optical maser
Optical mode, 141
Optical modulator, 111
Optical nonlinearity, 33
Optical nonlinearities, 82, 93, 162, 173, 190, 233
Optical parametric amplifier, 82
Optical phonon, 27, 174, 177
Optical power, 3, 4, 31, 84, 86, 150, 166, 172, 173, 175, 180, 184, 185, 187, 193, 196, 202, 216, 218, 219, 221, 223, 230
Optical prism, 122
Optical properties, 7, 27, 30, 35, 139
Optical pumping, 54, 56, 135, 138, 147, 164
Optical quality, 72, 197
Optical resonator, 93, 175, 233

Optical response, 180, 185
Optical signal, 53, 151, 165, 169, 175, 182
Optical soliton, 115
Optical spectroscopy, 4
Optical spectrum, 43, 57, 83, 122, 193, 194, 201, 217, 228
Optical switches, 117
Optical telecommunication, 2, 72
Optical transitions, 7, 13, 19, 30, 59, 80
Optical transmission, 30, 34, 71, 217
Optical transparency, 33
Optical waveguide, 65, 93, 141
Optical wavelength, 57
Optical waves, 72, 220
Output energy, 104
OVD, 37, 38, 40
Oxygen, 30, 33, 37

P

Panda, 72, 108, 163, 164, 170
Panda fiber, 72
Panda geometry, 72
Panda profile, 72
Panda stress rods, 72
Panda type, 72, 108, 163, 168, 170
Parasitic absorption, 163
Parasitic lasing, 86, 144
Parasitic reflections, 86
Passive fiber optic coupler, 150
Passive intra-cavity device, 110
Passive losses, 90
Passive medium, 185
Passive mode-locking, 117
Passive nonlinear optical element, 117
Passive Q-switching, 126
Passive resonator, 129
Photonics crystal fibers (PCF), 219–222
Penetration depth, 138
Penetration distance, 138
PER, 128
Periodical change, 127
Periodical pulse, 101
Periodically alternative regions, 127
Periodically polled, xi
Phase, 11, 29, 69, 85, 110, 112, 127, 128, 129, 143, 181, 200, 203
Phase constant, 69
Phase control, 162, 200
Phase detection, 200
Phase difference
Phase errors, 200, 203
Phase locked, 200
Phase matching, 177, 178, 183, 184
Phase modulation, 180
Phase noise, 194
Phase section
Phase sensitivity, 183
Phase separation, 110
Phase shift, 86–87, 128
Phase shifted, 128
Phase transition, 29
Phase variations
Phase velocity, 69
Phosphate, 16, 17, 22, 28, 34, 46, 50
Photo darkening, 51, 52, 61, 163
Photon energy, 28, 104, 105, 174
Photonics crystal fiber, 73, 219, 221, 222
Photostable, 52
Photo-thermo-refractive, 197
Pitch, 142, 219, 221
Plane of junction, 137, 141, 143, 144, 145
Plane reflective diffraction grating, 119
Plasma, 38, 185
PM, 71–73, 107, 118, 150, 169, 170, 202
PM fiber, 71–73
p-n junction, 135–137, 141, 142
POD, 38
Polarization, 56, 72, 118, 128, 149, 153, 195, 196, 230
Polarization beam combining (PBC), 195
Polarization beam splitting, 155, 195, 196
Polarization combined, 56
Polarization control, 195
Polarization degeneracy, 71
Polarization dependence, 118
Polarization direction, 153
Polarization drift, 118
Polarization extinction ratio, 230
Polarization independent, 153, 156, 203, 204
Polarization independent modulator, 118
Polarization insensitive, 153, 154, 156, 157
Polarization instability, 161
Polarization maintained, 149, 150, 169, 193, 202
Polarization mode dispersion, 71
Polarization plane, 72, 153
Polarization preservation, 216
Polarization rotation, 117, 155
Polarization sensitive, 152, 155
Polarization separation, 152, 155
Polarization separator, 156
Polarization state, 128
Polarizer, 72, 123, 152, 153
Population condition, 80
Population density, 11, 90

Population exchange, 12
Population inversion, 91, 103–106, 112, 134, 135
Population of level, 84
Positive feedback, 82, 120, 175, 187
Potential energy, 7
Power, 2–3, 24, 31, 35, 56, 57, 83, 99, 100, 106, 116, 139, 147, 148, 150, 159, 163, 171, 172, 182, 185, 205, 213
Power amplification, 89
Power amplifier, 190, 192
Power attenuation, 217
Power beams, 216, 225
Power combiner, 150
Power conversion efficiency, 87
Power coupling coefficient, 157
Power coupling efficiency, 161
Power delivery, 4, 215, 216, 219
Power density, 3, 51, 145, 197, 213, 214, 231
Power dependence, 52, 173
Power efficient, 110, 121
Power fluctuations, 83
Power guided, 216
Power handling, 150
Power leakage, 31
Power level, 4, 35, 51, 57, 100, 102, 107, 108, 145, 148, 151, 173, 175, 190, 194, 210, 216
Power limit, 188, 203, 216, 217, 225
Power limitation, 216, 225
Power parameter, 95
Power restrictions, 165
Power scalability, 3
Power scaling, 3, 10, 56, 60, 84, 85, 100, 102, 144, 145, 147, 164, 187
Power spectral density, 84
Power splitter, 150
Power stability, 100, 101
Power stripper, 151
Power threshold, 163, 173, 180
Power tolerant, 102, 122
Power transfer, 216, 221
Power transmission, 149, 165, 218
Power transport, 215
PPLN, xi
Prism, 118, 122, 123, 168, 210
Prism based polarization separator, 156
Prism based pump coupler, 168
Prism based resonator, 122, 123
Prism material, 122, 123
Prism pair, 118
Prism refractive index
Prism tuned, 122, 123
Probability of damage, 159
Probability of multi-phonon non-radiative decay, 28
Probability of radiative transition, 15
Probability of spontaneous emission, 11
Probability of the ion interaction, 15
Probability of transition, 15
Propagation axis, 74
Propagation constant, 66–68, 71
Propagation direction, 111, 152, 155, 156
Propagation line, 73
Propagation of light, 65–78
Propagation parameter, 68
Propagation path, 69
PTR, 197
p-type, 135, 136, 138
Pulse amplification, 87, 89
Pulse amplifiers, 82
Pulse broadening, 71
Pulse chirp, 116, 157
Pulse distortion, 87
Pulse duration, 192, 210, 213, 222, 228, 230
Pulse energy, 105, 106, 107, 109, 212, 213, 216, 218, 230
Pulse envelope, 100, 113, 116
Pulse intensity, 87
Pulse laser, 34, 213
Pulse peak power, 116, 192, 222
Pulse production, 99, 108
Pulse profile, 89, 210, 212, 231
Pulse regime, 52
Pulse repetition rate, 192, 210, 211, 213, 228, 230, 231
Pulse repetitive mode, 101
Pulse shape, 89, 93, 181, 182
Pulse spectral bandwidth, 111
Pulse spectrum, 68
Pulse spread, 69, 70
Pulse spreading, 69
Pulse temporal profile, 100
Pulse train, 101, 116, 117
Pulse width, 69, 70, 89, 91, 110, 111, 115, 130, 158, 173, 182, 183, 189, 210, 213
Pump absorption, 3, 24, 56, 95, 96, 163, 164
Pump absorption coefficient, 95
Pump area, 3
Pump beam, 91, 165, 167, 169, 176
Pump combiner, 150, 166, 169, 219
Pump combiner-coupler, 150, 219
Pump conversion efficiency, 14
Pump coupler configuration, 129

Pump couplers, 102, 219
Pump coupling, 56, 117, 161, 165, 167, 168
Pump coupling schemes, 163
Pump coupling techniques, 165
Pump current, 139, 142
Pump diode laser, 3, 23, 56, 169, 222
Pump efficiency, 93
Pump frequency, 87, 95
Pump geometry, 3, 56, 93, 163
Pump internal saturation parameter, 96
Pump intrinsic saturation power, 95
Pump laser, 2, 179, 219
Pump light, 24, 82, 96, 164, 165, 175–177
Pump photons, 8, 92
Pump port, 56, 150, 169
Pump power, 3, 25, 50, 56, 87, 88, 91, 95, 103, 125, 127, 163, 165, 175, 188
Pump power combiner, 150
Pump process, 104
Pump propagation, 3, 82
Pump pulse, 100, 182
Pump pulse duration, 100
Pump radiation, 3, 150, 175
Pump signal, 150, 161, 176, 178, 179
Pump source, 99, 139, 163
Pump to laser efficiency, 61
Pump wave vector, 177
Pump wavelength, 3, 23, 51, 61, 88, 165, 176–179
Pumping absorption, 95, 96, 163, 164, 179
Pumping approach, 54, 138, 167
Pumping architectures, 138
Pumping beam, 56
Pumping circle, 61, 100
Pumping conditions, 51, 100
Pumping configuration, 129, 130, 165
Pumping current flow, 144
Pumping excitation transfer, 24
Pumping geometry, 3, 24, 25, 56, 57, 150, 165
Pumping intensity, 105
Pumping light, 163, 167
Pumping photon, 8, 92
Pumping ports, 169
Pumping process, 56, 80, 88, 100
Pumping pulses, 100
Pumping quantum efficiency, 61, 88
Pumping radiation, 56, 163
Pumping scheme, 51, 57, 61, 80, 130, 163, 165
Pumping sources, 2, 55, 60
Pumping spectral location, 24
Pumping technique, 23, 168
Pumping technology, 1, 55, 56, 60, 163, 164, 167
Pumping wavelength, 87

Q

Q-switch, 103, 107–109
Q-switched fiber laser, 89, 108
Q-switched mode-locked, 100, 116
Q-switched operation, 102
Q-switched pulse, 89, 103
Q-switching, 99–101, 105, 108, 126, 162
Quantum defect, 25, 50, 57, 60, 92
Quantum efficiency, 61, 88, 98
Quantum number, 43
Quantum transition, 28
Quantum yield, 15, 16, 34
Quartz, 122, 124
Quasi four-energy level, 80, 105
Quasi continuous, 30, 101, 131
Quasi phase matching, 177, 178, 183, 184
Quasi three-energy level, 25, 87

R

Rabi frequency, 82
Radiation density, 12
Radiation energy, 11
Radiation spectral density, 12
Radiative decay, 14
Radiative lifetime, 15, 18–23, 47
Radiative transition, 14–16, 18
Raman active material, 175
Raman active medium, 174
Raman amplifiers, 4, 82
Raman effect, 174
Raman fiber lasers, 2, 174
Raman gain, 175, 176, 178
Raman lasers, 4, 59
Raman line, 176
Raman scattering, 10, 102, 161, 174, 175, 177, 192, 216
Raman spectrum, 174, 175
Raman wave, 175
Rare-earth center, 13, 17, 23
Rare-earth doped, 23, 35, 38, 40, 41, 44, 51, 94, 109, 117, 221
Rare-earth doping, 39
Rare-earth ions, 2, 4, 9, 13, 14, 16–19, 21, 23, 33, 35, 37, 40, 41, 44, 45, 53, 62
Rate constant, 52
Rate equation, 105
Rate law, 28
Rayleigh scattering, 31, 34
Recombination, 133, 138
Reflectivity, 87, 93, 95, 104, 119, 128, 144, 156, 211, 212, 226
Relaxation line-width, x
Relaxation oscillations, 112

Relaxation process, 7, 27, 59, 89
Relaxation rate, 27, 28
Resonant absorption, 25, 57
Resonant excitation, 25
Resonant frequency, 79, 99
Resonant nature, 25
Resonant pump, 82
Resonant pumping, 59
Resonator, 73, 82, 93, 94, 96, 97, 102–104, 109, 110, 112, 115, 117–129, 138, 141, 143–145, 152, 155, 175, 190, 200, 205, 230, 233
Resonator axial mode, 126
Resonator axis, 124, 144
Resonator ends, 122
Resonator geometries, 144
Resonator length, 112, 125, 145
Resonator longitudinal mode, 126
Resonator mirror, 109, 118, 121
Resonator mode, 94, 125, 129, 233
Resonator modes, 94, 233
Resonator optical components, 190
Resonator parameters, 117
Resonator Q factor, 102
Resonator round trip, 110
Resonator stability, 144
Resonator transmission, 124
Ring cavity, 96–98, 121, 188
Ring laser resonator, 94, 96, 97, 124
Ring oscillator, 190, 191
Ring resonator, 96, 97
Ring type configuration, 96
Rotation, 117, 121, 123, 124, 153, 155

S

Sapphire, 99, 122, 224
Sapphire waveguides, 224
Saturable absorber, 117
Saturable absorbing mirrors, 117
Saturation parameter, 61, 83, 88, 96
Saturation power, 87, 95
Saturation power parameter, 95
Saturation regime, 85
Schawlow-Townes formula, 129
Schawlow-Townes power dependence, 129
Selective bleaching, 97
Self-focusing, 101, 162, 185, 186
Self-focusing mechanism, 186
Semiconductor, 99, 117, 133–144, 146, 153, 228, 231
Semiconductor boundary, 138
Semiconductor chip, 142
Semiconductor chip sections, 143
Semiconductor compounds, 141
Semiconductor diode, 133
Semiconductor gain material, 141
Semiconductor laser, 17, 99, 133–135, 138, 139, 141–144, 146, 153
Semiconductor layer, 136, 140, 144
Semiconductor materials, 228
Semiconductor saturable absorbing mirror, 117
Silica fiber, 51, 61, 71, 176–180, 183
Silicate, 17, 27, 30, 32–34, 47–51, 53, 55, 153
Slave laser, 99
Spectral bandwidth, 68, 83, 110, 111, 126, 128, 157, 176, 179, 205
Spectral beam combining, 147, 195–197, 204, 205
Spectral broadening, 87, 181–183
Spectral characteristics, 181, 201
Spectral component, 22, 68, 70, 89, 174, 175
Spectral density, 12, 84, 203
Spectral distribution, 18, 20, 84, 123, 175
Spectral domain, 110
Spectral energy, 11
Spectral frequencies, 112
Spectral hole burning, 97
Spectral interval, 11
Spectral line, 12–17, 23, 44, 82, 84, 97, 100, 107, 109, 111, 112, 130, 142, 156, 172, 173, 176–179, 205
Spectral line broadening, 14
Spectral line-width, 173, 176, 177, 179, 205
Spectral mode, 94, 97, 112, 115, 125
Spectral narrowing, 197
Spectral parameters, 17, 29, 142, 172
Spectral position, 54, 111, 174, 175
Spectral profile, 15, 20, 83, 126
Spectral properties, 16, 68, 94, 142
Spectral range, 2, 3, 8, 12, 21, 25, 38, 50, 51, 54, 56, 57, 59, 65, 70, 71, 102, 118, 119, 123, 126, 188, 197, 209, 212, 214, 215, 217, 230, 231
Spectral region, 30
Spectral separation, 111, 127, 183, 184, 199, 203
Spectral shape, 13, 18
Spectral transmission, 120
Spectroscopic parameters, 17, 21, 30, 44, 49, 61, 62, 106
Spin, 43, 133
Self-phase modulation (SPM), 107, 157, 162, 172, 180, 181, 182, 192
Square pulse shape, 89
Standing wave cavity, 117
Standing wave resonator, 97, 121

Stark components, 20
Stark effect, 43
Stark levels, 13
Stark splitting, 13, 82
Stark structure, 13
Stark sub-level, 50
Stark system, 14
Stimulated Brillouin scattering, 10, 108, 161, 177, 216
Stimulated emission, 10, 11, 18–23, 47, 56, 59, 80, 82, 84, 85, 106, 138
Stimulated emission cross section, 20, 22, 23, 47, 59
Stimulated nonlinear scattering, 56
Stimulated processes, 11
Stimulated Raman scattering (SRC), 87, 10, 102, 161, 162, 172–180, 183, 216
Stimulated scattering, 10, 173, 174
Stokes, 8, 174, 175, 177, 178
Storage efficiency, 93
Storage time, 2
Structure tube, 223
Surface, 30, 35, 38, 85, 86, 101, 102, 107, 108, 121, 122, 127, 141, 143, 144, 148, 151, 159, 162, 185, 198, 211, 224, 225, 227, 228–230
Surface damage, 101, 102, 107, 108, 162
Surface emitting semiconductor laser, 143
Surface layer, 227
Surface polishing, 107
Surface profile, 85, 159
Surface reflectivity, 211
Surface removal, 227, 228
Surface treatment, 227

T

Tellurate, 19, 28, 32, 34, 49, 58, 59
Temperature dependent, 20
Thermal conductivity
Thermal diffusion
Thermal diffusivity
Thermal distribution, 19
Thermal effect, 100, 204
Thermal energy, 135
Thermal equilibrium, 1, 12, 19, 79, 133
Thermal expansion, 29
Thermal gradient, 193, 194
Thermal immunity, 233
Thermal injury, 57
Thermal lens, 35, 144
Thermal lensing, 144
Thermal limit, 29, 162
Thermal load, 145, 161, 162
Thermal management, 23, 30, 100–102, 140, 148, 161, 195
Thermal perturbations, 118
Thermal problem, 102
Thermal properties, 28
Thermal shock, 227
Thermal stability, 34
Thermal stress, 162
Thermal tuning, 204
Thin disk, 140, 229
Thin film, 139, 231
Thin layer, 140, 141
Threshold, 31, 33, 56, 80, 81, 90, 91, 93, 95, 97, 100, 104, 106, 107, 108, 118, 119, 122, 125, 135, 141, 161–164, 170, 173, 175, 177–180, 185, 216, 223, 230
Threshold calculation, 83, 177, 180
Threshold condition, 138
Threshold of nonlinear scattering process, 56, 87, 101, 172
Threshold of SBS, 162, 180
Threshold of self-focusing, 185
Threshold of SRS, 87, 176, 177, 180
Threshold peak power, 176
Threshold power, 91, 93, 173, 176, 177
Threshold pump power, 93
Threshold value, 106, 216
Thulium, 37, 57
Thulium-doped, 57
TIR, 65, 67
Total internal reflection, 156, 165, 185, 220
Transition metal, 9
Transition probability, 7

U

Unidirectional, 97, 121, 128, 152, 155, 188
Unidirectional device, 97
Unidirectional output, 121
Unidirectional propagation, 97, 155
Unidirectional ring cavity, 188
Unidirectional ring laser resonator, 97
Unstable fiber laser output, 118
Unstable resonators, 73
Up-conversion, 8, 35
Up-conversion coefficient, 53
Up-conversion lasers, 8, 35
Up-conversion losses, 50, 57
Up-conversion rate, 53
Upper energy levels, 12, 20

Upper level, 15, 16, 20, 47, 53, 59, 80, 81, 87

V
Valence band, 133–136
VBG, 203, 204
Vertical cavity surface-emitting laser (VCSEL), 143, 144
Vertical transition, 7
Vibration energy, 7, 8
Vibration mode, 7, 10, 11, 177
V-number, 151
Voigt fucntion, 17
Volume Bragg grating, 196, 204
Volume defect, 106
Volume glass, 28
Volume hologram, 198
Volume holographic grating (VHG), 196–200
V-parameter, 200

W
Waist, 73, 74, 76, 77, 91
Waist diameter, 76, 77
Waist location, 74, 77
Water absorption, 33, 167
Water content, 38
Water cooled, 147
Wave, 3, 4, 10, 14, 65–71, 79, 86, 93, 94, 97, 101, 111, 112, 117, 121, 139, 156, 161, 162, 164, 173–178, 183, 185, 196, 206, 210
Wave amplification, 79, 175
Wave frequency, 174
Wave front, 69
Wave mixing, 101, 183
Wave number, 14, 67, 69, 111
Wave pattern, 94
Wave propagating, 86, 93
Wave vector, 10, 66, 68, 112, 174, 175, 177
Wavelength, 2, 3, 23, 27, 31, 34, 37, 51, 57–61, 66, 69, 70, 71, 87, 88, 92, 95, 98, 102, 104, 118–124, 128, 141, 142–145, 153, 157, 158, 164, 167, 176–179, 183, 188, 194, 199, 202, 210–213, 215, 220–224, 228, 230
Wavelength dependence, 31, 144, 220
Wavelength deviation, 199
Wavelength dispersive element, 118
wavelength division multiplexing (WDM), 117, 165, 167, 168, 194, 201
Wavelength filter, 123
Wavelength fragment, 59
Wavelength in vacuum, 178
Wavelength of absorption, 164
Wavelength of maximum transmission, 123
Wavelength of operation, 51, 141, 157
Wavelength of radiation, 121
Wavelength of zero dispersion, 71
Wavelength range, 2, 57, 119, 122, 217
Wavelength selectivity, 123
Wavelength shift, 204
Wavelength span, 120
Wavelength stability, 144, 161
Wavelength temperature dependence, 142
Wavelength tunability, 143, 187
Wavelength tunable, 23, 118, 121, 188

Y
Ytterbium, 37, 50
Ytterbium amplifier, 21, 52
Ytterbium laser, 37, 50–52
Ytterbium-doped, 50–52

Z
Zeeman effect, 43
Zero-phonon energy, 20
Zero-phonon line, 14, 50, 54
Zeroth order, 120, 121
ZrF_4-BaF_2-LaF_3-AlF_3-NaF (ZBLAN), 17, 19, 28, 34, 35